Summer 2014

Fundamental studies on copper zeolites for catalytic NO x abatement

Anuj Arun Verma
Purdue University

Graduate School Form 30
(Revised 08/14)

PURDUE UNIVERSITY
GRADUATE SCHOOL
Thesis/Dissertation Acceptance

This is to certify that the thesis/dissertation prepared

By Anuj Arun Verma

Entitled
Fundamental Studies on Copper Zeolites For Catalytic NOx abatement.

For the degree of Doctor of Philosophy

Is approved by the final examining committee:

Fabio H. Ribeiro

Joshua Ratts

W. Nicholas Delgass

Aleksey Yezerets

Stephen Beaudoin

To the best of my knowledge and as understood by the student in the Thesis/Dissertation Agreement, Publication Delay, and Certification/Disclaimer (Graduate School Form 32), this thesis/dissertation adheres to the provisions of Purdue University's "Policy on Integrity in Research" and the use of copyrighted material.

Fabio H. Ribeiro

Approved by Major Professor(s): _____

Approved by: John Morgan 08/20/2014

Head of the Department Graduate Program Date

FUNDAMENTAL STUDIES ON COPPER ZEOLITES FOR CATALYTIC NOX ABATEMENT

A Dissertation

Submitted to the Faculty

of

Purdue University

by

Anuj Arun Verma

In Partial Fulfillment of the

Requirements for the Degree

of

Doctor of Philosophy

December 2014

Purdue University

West Lafayette, Indiana

To my parents, Ashish Dada, Poonam Bhabhi, and Sneha!

ACKNOWLEDGEMENTS

Remain calm during your successes for that calmness will help you overcome your failures. – Adapted from the *Bhagwad Gita*.

As this maxim goes, my journey leading up to PhD has tasted many successes and failures and this proverb has helped me immensely. This journey has enabled me to be a much wiser person than I was when I first arrived in Purdue University four years ago (12 August, 2010). This transformation, however, would have been impossible without me meeting certain people who I would like to acknowledge below.

First and Foremost, I would like to thank Professor Fabio Ribeiro, my advisor. He has stood behind me like a rock during my ups and downs in my PhD life. I especially admire his experimental abilities and his emphasis of data reproducibility. If a data-set passes the 'Fabio' test, then rest assured, it will be reproducible in other laboratories. I am also thankful to Fabio for granting more independence in the DeNOx project than other projects in the catalysis group. This has enabled us to 'own' the project and generate new ideas and hypotheses. Moreover, I would like to apologize to Fabio for pursuing a career in industry rather than in academia. I would also like to thank Professor Nick Delgass for teaching me concepts of catalysis and spectroscopy. His unique ability to process data-sets and provide new information has been invaluable in my career. Moreover, his emphasis on developing a 'mosaic' or a vision of understanding in any field is one of his teachings that I hope to apply in my future career.

I would like to thank Dr. Aleksey Yezerets for his industrial inputs given to the DeNOx group. His ability to gather seemingly disparate concepts and apply it in industrially

relevant scenarios is something I hope to implement in my own career. I would also like to acknowledge his DeNOx team at Cummins Inc. for being very helpful in all the wonderful meetings we had. I would also like to acknowledge Dr. Joshua Ratts for providing me with valuable advice in my research and agreeing to be in my PhD committee. Professor Stephen Beaudoin is gratefully acknowledged for agreeing to take part in my PhD committee. I would also like to thank Dr. Jeffrey Miller from whom I learnt about the intricacies of catalyst synthesis and X-ray absorption spectroscopy. Big thanks to my collaborators, Professor William Schneider, Trunojoyo Anggara, and Christopher Paolucci. I have always viewed you guys (Trunojoyo and Chris) as internal members of the NOx group and Prof. Schneider as my third boss. I still maintain that doing computational work is tougher than doing experiments and you people make that look so easy and elegant. I also want to thank Dr. Raj Gounder for teaching me the art of zeolite synthesis and characterization.

Big thanks to Dr. Yury Zvinevich. He taught me how to build complex equipments and more importantly, how to maintain the same. His teachings will be remembered in my professional life. I also want to acknowledge Robb and Dr. Mike Everly from the Amy Instrument facility in Chemistry department, Purdue University. They implemented the labview program which enabled me to get data in record time.

I thank all my colleagues with whom I worked together in the field of catalysis. In particular, Jun Wang, Atish Parekh, Shane Bates, and Vincent Kispersky are acknowledged. Other members in the catalysis group, Dhairya, Harsha, Vinod, Paul, Shankali, Han-ting, Zhenglong, Jamie, Tej, Mike, Amir, Viktor, and Yanran are also acknowledged. I also wish Arthur Shih, Jonatan Albarracin, and John Di Iorio the very best as the new members of the DeNOx group. I think Fabio and Raj could not have asked for better students. I also acknowledge Austin Tackaberry for help in zeolite synthesis.

I am grateful to all my friends who kept me sane during my PhD study. In particular, a very big thanks to Piyush, Gautham, Ankit, Nitin, Sambit, Raghu, Krishna, and Nitish: The ECE gang. While the ChemE gang included Dhairya, Harsha, Mayank, Ranjita, Shenvi, Dude, Krishnaraj, Karthikeyan, Joglekar, Ravi, Pritish, Sumeet, Tej, and Anuradha.

Last but not the least; I would like to thank my parents, Asha and Arun, and Ashish and Poonam for encouraging me to make my own decisions in life. It is only because of your patience that I am here. My sincere apologies for not being in contact as frequently as desired but your understanding is proof enough that you would do anything to see me healthy and happy. Finally, a very big thanks goes to Sneha, who taught me that there is life outside of research and who has patiently been by my side through all these years.

TABLE OF CONTENTS

Page

LIST OF TABLES

Table Page

Table Page

LIST OF FIGURES

Figure Page

Figure Page

Figure Page

Figure Page

Figure Page

Figure Page

Figure Page

Figure Page

Figure Page

ABSTRACT

Verma, Anuj A. Ph.D., Purdue University, December 2014. Fundamental Studies on Copper Zeolites for Catalytic NOx Abatement. Major Professors: Fabio H. Ribeiro and W. Nicholas Delgass.

Stringent regulations in mobile NOx emissions have resulted in the development of Standard Selective Catalytic Reduction (SCR) as the dominant NOx abatement technology in lean burn diesel engines. Standard SCR is a reaction of nitric oxide (NO) with ammonia (NH_3), in the presence of oxygen (O_2) to form nitrogen (N_2) and water (H_2O). Copper containing zeolites show commercially viable SCR performance. Cu-SSZ-13 (CHA framework), a member of this family, is a preferred catalyst for SCR applications because it shows exceptional hydrothermal stability in addition to commercially viable SCR performance [1]. Our work focuses on 1) determination of the active sites, and 2) elucidation of the dominant reaction steps on active sites, for standard SCR (at 473 K) and catalytic oxidation of NO (at 550 K), over Cu-SSZ-13.

A series of Cu-SSZ-13 catalysts (Si:Al = 4.5) tested for standard SCR kinetics exhibited a linear increase in the rate of nitrogen production (per gram catalyst) with Cu:Al ratio till Cu:Al = 0.2. Separate catalyst characterization tools like Ultra-Violet-Visible-Near Infra-red (UV-Vis-NIR) spectroscopy under ambient conditions, X-ray Absorption Near Edge structure (XANES) of Cu ions during standard SCR, Density Functional Theory (DFT) calculations, and titration of residual acid sites with amine titrants on this series of catalysts established isolated Cu ions ion exchanged at the framework Al sites in six member rings of SSZ-13 as the dominant Cu ion configuration below Cu:Al = 0.2, which we assign as the dominant active sites for low temperature standard SCR (T = 473 K). Above Cu:Al = 0.2, Cu ion clusters (Cu_xO_y) were formed, which stabilized on framework

Al sites at favorable distances, in the eight member cage of SSZ-13. Cu_xO_y was active in catalyzing dry NO oxidation to NO_2 via oxygen activation mediated by local Cu-O_y-Cu bonds. The density of local Cu-O_y-Cu bonds was quantified from *in-situ* XANES under NO oxidation and correlated linearly with the rate of NO oxidation, thereby establishing Cu_xO_y as the active sites for NO oxidation. NO oxidation was also explored on catalysts prepared to contain exclusively isolated Cu(II) ions and the Gibbs free energy of reaction intermediates was shown to be higher than the free energy of similar intermediates formed from local Cu-O_y-Cu bonds, consistent with the experimental observation of experimentally undetectable rate of NO oxidation on isolated Cu(II) ions in the six member rings of SSZ-13. As a result, dry NO oxidation is proposed as a probe reaction to detect Cu ion clustering in Cu-SSZ-13 formulations.

Operando XANES during standard SCR also implicated isolated Cu ions (in the six member SSZ-13 ring) as the active site; however, the +2 oxidation state of Cu is not preserved. Experimental XANES analysis during appropriate reactant cutoff from steady state standard SCR and DFT calculated Gibbs free energy analysis of adsorbates under reaction conditions point toward a Cu ion redox between Cu(I) and Cu(II) to mediate standard SCR. The isolated Cu(II) ion reduction is achieved by both NO and NH_3 to make nitrogen, isolated Cu(I) ions, and experimentally detectable proximal Brønsted acidic sites. These proximal acid sites can stabilize ammonium ions during standard SCR catalysis, while NO and O_2 oxidize the Cu(I) back to Cu(II) via nitrite (NO_2^-) intermediate formation, as predicted by DFT. The close proximity between nitrites (on Cu) and ammonium ions (on proximal Brønsted acid sites) enable the formation of nitrogen and water via an intermediate which resembles ammonium nitrite, thereby completing the catalytic cycle. These findings highlight the bi-functional nature of Cu-SSZ-13 displayed by a close proximity of Bronsted acidic sites and redox metal ion centers which work in concert to catalyze the selective reduction of NO with NH_3 in the presence of oxygen, to form nitrogen and water.

CHAPTER 1. INTRODUCTION

1.1 Introduction

Combustion of fossil fuels, primarily in automobile applications, results in the formation of nitrogen oxides (NO + NO_2, NOx). This is an example of a gas mixture which is responsible for an adverse effect on the environment. As a result, there are stringent regulations on the emissions of these gases from automobile exhaust. For diesel engines, the combustion of fuel usually requires excess oxygen (O_2) concentration (in volume % level). Hence, the primary need of a successful NOx abatement technology (deNOx) applied to diesel exhaust is the ability to reduce NOx in volume % levels of O_2, carbon dioxide (CO_2) and water (H_2O) or a lean burn mixture. For this reason, deNOx technologies such as three way catalysts (TWC), which are commercially viable for gasoline engine exhaust which work best in stoichiometric amounts of O_2, (in ppm concentration, rich phase), fail when applied to a diesel exhaust. As a result, extensive research efforts have been devoted to the development of deNOx technologies applied to diesel exhaust. Currently, two technologies are available commercially. The first one is NOx Storage and Reduction (NSR) technology which involves a cyclic operation between the lean and rich phases over a catalyst. The catalyst is usually composed of two components, a noble metal redox component (for example, platinum) and an alkaline earth storage component (for example barium oxide) dispersed over a high surface area support (for example alumina). The NOx in the exhaust is usually stored in the form of nitrates during a lean operation and eventually, the nitrates are reduced by hydrogen gas (H_2) or ammonia (NH_3) to produce nitrogen (N_2) thereby leading to NOx mitigation. The second technology is the Selective Catalytic Reduction (SCR) of NOx in the presence of a reducing agent such as NH_3, hydrocarbons (HC), or hydrogen. There are many catalyst

formulations suited for this purpose. In particular, copper (Cu) and iron (Fe) containing zeolites are practically relevant Selective Catalytic Reduction of NOx

A typical diesel exhaust contains ppm levels of NOx (mainly in the form of nitric oxide). Upon the introduction of a suitable reducing agent such as NH_3 or HC, it is possible to reduce NOx to N_2 and H_2O, which are environmentally benign products. The word 'selective' refers to the fact that the reduction of NOx occurs even in the presence of % levels of O_2. This is achieved in the presence of a catalyst which catalyzes reaction 1.1.

$$4NH_3 + 4NO + O_2 \rightarrow 4N_2 + 6H_2O \qquad \text{Reaction 1.1}$$

Reaction 1.1 is known as the standard SCR. It is to be noted that NH_3 has been used as the reductant in reaction 1.1, even though other reducing agents can be used. The rate of standard SCR can be increased further by introducing a 1:1 molar ratio of NO: NO_2 in the feed stream and the main chemical reaction in the presence of NO_2 is given by reaction 1.2 (known as fast SCR).

$$4NH_3 + 2NO + 2NO_2 \rightarrow 4N_2 + 6H_2O \qquad \text{Reaction 1.2}$$

This is commercially exploited by installing a diesel oxidation catalyst (DOC) upstream of the SCR catalyst. In addition to other oxidation reactions, the DOC uses feed NO and O_2 and performs NO oxidation in order to increase the relative amount of NO_2 in the feed to the SCR catalyst. This in turn increases the rate of NOx removal and a smaller reactor volume is realized. Other reactions also occur over these catalysts, but SCR is the most important [2].

It should be noted that the SCR technology, applied to automobiles is relatively new. This reaction however is well established commercially for emissions control from stationary power generation sources. The typical catalysts used for this process are V_2O_5-WO_3/TiO_2 and V_2O_5-MoO_3/TiO_2. These catalysts show commercially viable NOx conversion in the range of 573 K- 673 K [3]. The basic chemistry of SCR on these catalysts has been

studied extensively by Topsøe, Dumesic, and coworkers [4] and a series of commercial catalysts are available from Haldor Topsøe Inc. These catalysts, however, are unsuitable for an automobile diesel exhaust deNOx technology (at low temperatures, 473 K) because of additional constraints imposed by the system. Diesel exhaust NOx mitigation from an automobile occurs in a dynamic environment with respect to the temperature of the exhaust. This parameter can vary based on a cold start of an engine or to a very high temperature, usually encountered during acceleration. As a result, a commercially viable catalyst formulation for mobile applications must show acceptable NO conversion in dynamic conditions as well as hydrothermal stability. Cu and Fe loaded zeolites are shown to be hydrothermally stable, and particularly suited for vehicular exhaust NOx abatement.

1.2 Cu-Zeolite As a Catalyst for standard SCR

DeNOx in the form of SCR, has its origins in the form of catalytic decomposition of NO (reaction 3) over Cu-zeolites. The catalyst discovery and process development was pioneered by Iwamoto and coworkers [5]. This process does not need a reductant and the Cu-zeolite which provides the best rate of NO removal is Cu-ZSM-5.

$$2NO \rightarrow 2N_2 + O_2 \qquad \text{Reaction 1.3}$$

This reaction, however, requires at least 673 K (for acceptable NO conversion) and is inhibited severely in the presence of O_2 and H_2O. Differential kinetic measurements reveal that the O_2 order is ~ -0.5 [6], which makes it commercially unattractive because of presence of excess oxygen in a diesel exhaust. This motivated the use of reducing agents, initially in the form of HC, but later, NH_3 was favored (in the form of urea) and is in use currently. Many Cu-zeolite formulations such as Cu-ZSM5 [7, 8], Cu-beta [9, 10], Cu-Y [11, 12] etc. have been investigated for NH_3-SCR. These catalysts, however, do not show acceptable hydrothermal stability and as a result Cu-chabazite (Cu-CHA), a small pore micro-porous solid with ion exchanged Cu has recently received attention [13]. This is an example of a catalyst formulation which has been already been commercialized

(Cu-SSZ13 by BASF and Cu-SAPO34 by Johnson Matthey, both have CHA topology) but the fundamental chemistry of NH_3-SCR is being actively researched by various research groups.

Standard SCR over Cu-zeolites is generally believed to be mediated over ion exchanged Cu ions within the zeolite. In Cu-SSZ-13, the energetically stable isolated Cu ions present near the six member ring of SSZ-13 are shown to be the dominant active sites for low temperature standard SCR (T ~ 473 K) by using a variety of techniques by many research groups. Initial work done by Korhonen et al. [14] showed that their Cu-SSZ-13 catalyst (active for low temperature standard SCR) was composed entirely of isolated Cu(II) ions. This was shown via *ex-situ* X-ray absorption spectroscopy and *in-situ* ultraviolet-near infrared (UV-Vis) spectroscopy during standard SCR, and was active for standard SCR in separate kinetic tests. This conclusion was confirmed by Deka et al. [15] who further reported NH_3 inhibition at low temperatures (< 413K) due to NH_3 coordination on isolated Cu ions, while the apparent lack of this coordination at higher temperatures (> 473K) led to higher catalyst activity. These studies however lacked a 'structure-activity' relation between isolated Cu ions and standard SCR rates, as the conclusions were primarily based over studies done on a single catalyst, i.e. a single data point.

The simple picture of an isolated Cu ion in a six member ring was recently challenged by Kwak et al. [16] who used hydrogen temperature programmed desorption (H_2-TPR) on dehydrated Cu-SSZ-13 catalysts with varying Cu:Al ratios (Si:Al = 6) to show two Cu(II) to Cu(I) reduction events. The high temperature reduction event (653 K) was attributed to a Cu(II) to Cu(I) reduction of an isolated Cu ion present near the six member ring, while the low temperature reduction event was due to isolated Cu ions in the eight member cages of SSZ-13. In addition, recently, Guo et al. [17] used resonance Raman spectroscopy on candidate Cu-SSZ-13 catalysts (Si:Al = 4.3 and Cu:Al = 0.04, 0.09, 0.26, and 0.36) and observed peaks at 350 cm^{-1} and 610 cm^{-1}, which was assigned to single oxygen bridged Cu dimers (Cu-O-Cu) and di-oxo bridged Cu dimers (Cu-O_2-Cu). This

was the first time, multinuclear Cu species were spectroscopically observed on Cu-SSZ-13, thus painting an even more complicated picture of Cu ion speciation within Cu-SSZ-13. In a subsequent contribution, Gao et al. [18] showed that under sub-ambient conditions of electron paramagnetic resonance (EPR, T = 155K), all Cu ions (till Cu:Al = 0.5) were isolated. These authors [18], however, were unable to establish a structure activity relationship of isolated Cu ions with standard SCR because of mass transfer artefacts in their kinetic data. Further, there was a possibility of isolated Cu ions in the eight member cages of SSZ-13, to be active for standard SCR. Convincing structure-activity relations in standard SCR have recently been shown on other small pore micro-porous solids like Cu-SAPO-34. Xue et al. [19] measured the standard SCR rate as a function of Cu loading and used H_2-TPR to quantify the amount of isolated Cu ions on the same catalysts. They showed that the turnover rate (TOR) for standard SCR at 473 K on these catalysts was identical thereby implicating isolated Cu ions within Cu-SAPO-34 to be the dominant active sites for standard SCR. A similar study, however, is missing from the literature of standard SCR over Cu-SSZ-13.

Various plausible reaction steps have been proposed for low temperature standard SCR (473 K) on Cu-zeolites. A typical Cu-zeolite catalyst is believed to be bi-functional in nature. It is believed that Cu ions have the capability of mediating redox reactions of NOx, while residual Brønsted acid sites act as reservoirs of gas phase NH_3 by stabilizing NH_4^+ ions. In particular Cu ions are believed to be the active centers for the reaction between NO and O_2 (NO oxidation) to form NO_2. The NO_2 molecule desorbs and gas phase NO_2 subsequently reacts with NH_4^+ ions to form an unstable ammonium nitrite like complex which decomposes to for N_2 and H_2O [20]. In fact, NO oxidation was viewed as a rate determining step (R.D.S.) for standard SCR on both Cu- and Fe-zeolites [20]. The simple picture of standard SCR, however, is being challenged by recent experiments performed on Cu-zeolites .In particular, the role of NO oxidation during standard SCR turnover. Peden et al. [21] showed that Cu-SSZ-13 catalysts with Cu:Al ratios less than 0.3 showed SCR activity (NO conversion as a function of temperature) which did not correlate with the NO oxidation activity (NO conversion as a function of temperature) on

the same catalysts, thereby showing that NO oxidation need not be required for standard SCR on isolated Cu ions in Cu-SSZ-13. Gao et al. [13] however did not probe into the molecular origins of this difference, and instead proposed possible sequences of catalytically relevant steps of standard SCR which did not require NO oxidation. Two possible sets of catalytically relevant steps are shown below in Figure 1.1 & Figure 1.2.

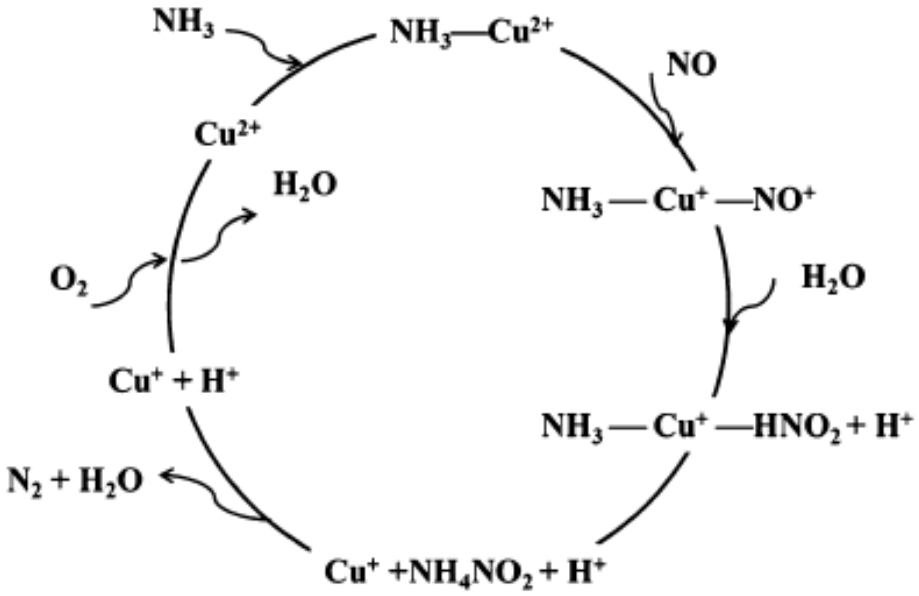

Figure 1.1 Reaction steps of low temperature standard SCR on isolated Cu ions in SSZ-13, proposed by Gao et al [13].

In Figure 1.1, Gao et al. [13] proposed that the first step of standard SCR was NH_3 adsorption on an isolated Cu(II) ion to give Cu(II)-NH_3 complex. This complex was then reduced by NO and H_2O to generate Cu(I) and HNO_2, and subsequently, NH_4NO_2 which decomposed to N_2 and H_2O. In the second set (Figure 1.2), however, NO was treated as a sole reductant of Cu(II) to Cu(I) under standard SCR, independent of NH_3 [22].

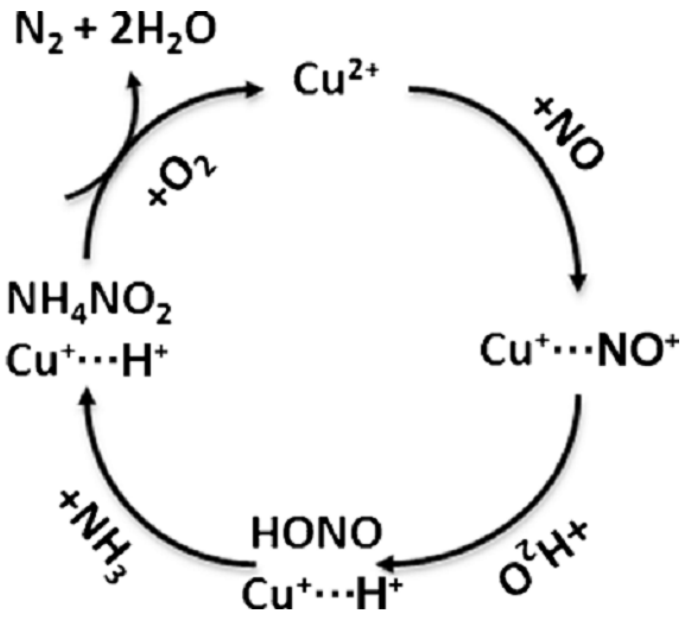

Figure 1.2 An alternate low temperature standard SCR mechanism proposed by Kwak et al. [22] on isolated Cu ions in SSZ-13.

This mechanism was based on ex-situ N^{15}-nuclear magnetic resonance (NMR) results, under ambient conditions which showed stabilization of NO^{+} molecules within the cages of SSZ-13 [22]. Additionally, Ruggeri et al. [23] showed that the SCR activity (measured as NO conversion as a function of temperature) was uninhibited by the presence of water, while the NO oxidation activity (measured as NO conversion as a function of temperature) declined in the presence of water in the feed stream. Based on this observation, Ruggeri et al. [23] concluded that the standard SCR rate determining step did not involve NO oxidation.

Recent *operando* XAS studies by Mcewen et al.[24] and Kispersky et al. [25] on the kinetics of standard SCR over Cu-SSZ-13 revealed a mix of isolated Cu(I) and isolated Cu(II) species during standard SCR. These being true *operando* experiments, they further observed that the rate of standard SCR on Cu-SSZ-13 catalysts did not correlate with either Cu(I) or Cu(II) concentration. This implied that all acceptable catalytic steps on Cu-SSZ-13 (during standard SCR) should involve isolated Cu ions and Cu(I)-Cu(II)

redox pairs. In summary, despite many insights about the nature of the elementary steps of standard SCR on Cu ions in SSZ-13, consensus is lacking and there is a need for further elucidation of kinetically relevant steps which mediate standard SCR over Cu-SSZ-13 which has experimental and theoretical support under reaction conditions.

1.3 Thesis Overview

Through this thesis, a detailed molecular understanding of the standard SCR and NO oxidation will be developed on Cu-SSZ-13. A molecular understanding of these reactions involves an identification of the dominant active site and probable reaction steps on those candidate active sites. With this aim, Chapter 2 is devoted to the identification of isolated Cu ions ion exchanged in place of two protons on Brønsted acidic sites in the six member rings of SSZ-13, as the dominant active sites for standard SCR at 473K. This was accomplished by a combination of reaction kinetics, UV-Vis-NIR spectroscopy, *operando* X-ray absorption near edge structure of Cu ions during standard SCR, DFT calculations of candidate active sites, and statistical analysis of the placement of framework Al atoms as anchors for these isolated Cu ions.

In addition to isolated Cu(II) ions, Cu oxide clusters (Cu_xO_y) can also be stabilized over framework Al pairs at favorable distances in the eight member cages of SSZ-13. These Cu_xO_y species are the active sites for catalytic NO oxidation due to their ability to oxidize NO via oxygen activation on local Cu-O_y-Cu bonds. This conclusion is shown in Chapter 3 via a combination of reaction kinetics, UV-Vis-NIR spectroscopy, *in-situ* XANES analysis during NO oxidation, and DFT calculations on the most probable reaction pathways on different Cu ion configurations. As a result a combination of chapters 2 and 3 teaches us that independent NO oxidation performance cannot act as a surrogate for SCR ability as the site requirements of both reactions are different.

Identification of the active sites for low temperature standard SCR leads us to examine the response of these active sites when individual reactant gas molecules are cut-off from the standard SCR mixture. The response is quantified via *operando* XAS in the form of

Cu ion oxidation states on catalysts which were prepared to contain isolated Cu ions exclusively. Using these results and DFT calculations, we propose a series of reaction steps of standard SCR on isolated Cu ions in SSZ-13. Furthermore, extending the Brønsted acid site counting techniques developed by Bates et al. enables us to count excess Brønsted acidic sites proximal to Cu ions, during the Cu(II) to Cu(I) reduction event (relevant to standard SCR). We propose that these proximal Brønsted acidic sites, which stabilize ammonium ions, are catalytically relevant while residual acid sites, which can also stabilize ammonium ions, are spectators during standard SCR. In this way, through Chapter 4, we describe the molecular origins of standard SCR on isolated Cu ions.

Finally, in order to advance the science of catalysis, the importance of efficient kinetic data collection is emphasized in Chapter 5. Using protocols developed in chemical reaction engineering, a differential reactor is rigorously defined to enable kinetic analysis of chemical reactions wherein product inhibition is evident. We will show the applicability of this kinetic analysis via a case study of catalytic NO oxidation over Cu_xO_y in Cu-SSZ-13 (where NO_2 product order is ~ -0.9).

CHAPTER 2. A KINETIC AND SPECTROSCOPIC STUDY OF STANDARD SCR ON COPPER EXCHANGED SSZ-13

2.1 Abstract

"Copper exchanged SSZ-13 catalysts were used for the standard selective catalytic reduction (SCR) reaction at 473 K with 320 ppm NO, 320 ppm NH_3, 10% O_2, 8% CO_2, and 6% H_2O. The copper to aluminum atomic ratio (Cu:Al) was varied from 0 to 0.35 over seven H- and Cu-SSZ-13 samples with silicon to aluminum atomic ratio (Si:Al) of 4.5, or an effective Si:Al = 6.9 based on the number of Brønsted acid sites per total Al (H^+:Al) of 0.65 in the H-SSZ-13 determined in a previous study [26]. The standard SCR rate per gram was observed to increase linearly up to Cu:Al = 0.2 with a maximum rate of 3.8 x 10^{-6} mol NO g cat^{-1} s^{-1}. The rate per gram was observed to track with a hydrated isolated Cu(II) species in ultraviolet-visible spectroscopy, which was shown to become the active Cu configuration under *operando* x-ray absorption spectroscopy (XAS). Density functional theory calculations showed an exchanged isolated Cu(II) in the six-member ring of SSZ-13 as the most stable position for isolated Cu(II). Statistical analysis of Al distribution in SSZ-13 show a maximum number of isolated Cu in six-membered rings exchanged with 2 Al reach a maximum at Cu:Al = 0.23 for Si:Al = 5, which matched with the maximum observed rate per gram, indicating Cu(II) was the active Cu species. Above Cu:Al = 0.2, a new Cu_xO_y species was observed from ambient XAS measurements which was not active for standard SCR because the Cu:Al = 0.35 rate tracked with the amount of hydrated Cu(II). The number of available Brønsted acid sites in the samples was shown to not be involved in the kinetically relevant steps for standard SCR due to the inverse relationship of the rate per gram and number of Brønsted acid sites.

2.2 Introduction

Metal-exchanged small pore zeolites have recently been adopted for use in the selective catalytic reduction (SCR) of NO with NH_3 reaction for mobile deNOx applications. The metal exchanged chabazite (CHA) structure has been of particular interest, which has two analogues, SSZ-13 and SAPO-34. When exchanged with Cu or Fe, they have been shown to be able to withstand the harsh hydrothermal conditions present in a diesel exhaust system yet still efficiently remove NOx[27-29].

One current area of interest is the role of the exchanged metal in the standard SCR reaction. Fickel et al.[30] using Rietveld refinement of variable temperature XRD identified the location of isolated Cu species in the SSZ-13 structure centered slightly above the six-member ring. A follow-up study by Korhonen et al. [14] ruled out the possibility of Cu dimers in a Cu-SSZ-13 sample with copper to aluminum atomic ratio (Cu:Al) equal to 0.18 and silicon to aluminum atomic ratio (Si:Al) equal to 9, and concluded that isolated Cu(II) near the six-member ring was the active site for standard SCR in Cu-SSZ-13. Kwak et al.[16] suggested multiple positions for isolated Cu(II) rather than only one near the six-member ring based on two different Cu(II) signatures in low Cu loading samples during H_2-TPR and FTIR. Gao et al.[18] used low temperature (155 K) EPR to probe isolated Cu(II) up to near 100% ion exchange and identified two possible positions for hydrated isolated Cu. Wang et al.[31] observed the standard SCR rate per total Cu to be significantly improved in SAPO-34 which contained isolated Cu(II) over a sample which contained extra-framework CuO clusters, even though both catalyst samples had similar total copper content. While most studies have regarded isolated Cu to be in the 2+ oxidation state under reaction conditions, work in our group using *operando* X-ray absorption spectroscopy experiments [24, 25] has demonstrated the appearance of a Cu(I) signature at 8983 eV under standard SCR conditions, indicative of a redox cycle between the two during SCR. In this study, we demonstrate through reaction kinetics, UV-Vis NIR, and *operando* XAS that this isolated Cu is the active site for standard SCR. The Cu species that is the precursor to the active isolated Cu was also identified under ambient conditions using UV-Vis-NIR.

Because exchanged, isolated Cu(II) must be charge-compensated by two framework Al tetrahedral (T-) sites, the density of these species is a function both of the Si:Al ratio and the Cu loading. The distribution of Al T-sites and thus of candidate Cu(II) sites is difficult to assess experimentally. Here we estimate the density of candidate sites by statistical analysis [32] of the SSZ-13 framework under the assumption that the Al obey the Loewenstein's rule [33] prohibition against first-nearest-neighbor Al T-sites. We show that this model gives an estimate of Cu(II) site density consistent with the experimentally observed saturation of these sites.

Kinetic measurements on Cu-SSZ-13 under standard SCR conditions have been reported in the literature[18, 21] and there is a large body of work on other zeolites, including significant contributions on ZSM-5[11, 34-38]. The work by Gao et al.[18] described the possibility of internal mass transfer effects in the SSZ-13 crystal structure, which they believed to occur based on a loss in rate per mole Cu with increasing Cu loading up to 100% ion exchange and calculation of effectiveness factors much less than unity. In the current study, we were able to report differential kinetic information on Cu-SSZ-13 samples for standard SCR in the low temperature region (< 473 K) in the absence of mass transfer effects. Metkar et al.[20, 38] also explored diffusion limitations while varying washcoat thicknesses in Cu and Fe zeolite monoliths in which they concluded were negligible in the lower temperature region.

The role of Brønsted acidity is another important aspect of standard SCR. One reaction mechanism suggests NH_3 is activated on a Brønsted acid site, forming NH_4^+, which then reacts with NOx species [8, 34, 38-41]; however, a study by Brandenberger et al. [42] has suggested that it is only important for binding and dispersing metal ions as they saw similar conversions of NO and NH_3 between 473-573 K in Fe-ZSM-5 with 96% of its Brønsted acid sites poisoned. In this study, ammonia stored under standard SCR conditions will be quantified via transient NH_3 cutoff experiments, which probe the role of Brønsted acidity on the reaction mechanism. The total amount of Brønsted acid sites

will also be determined for each sample and compared with the NH_3 titration experiments and standard SCR rates.

2.3 Experimental Methods

2.3.1 Cu-SSZ-13 Synthesis and Characterization

The H-SSZ-13 was synthesized following a recipe published by Fickel et al. [28, 30], which was derived from the original synthesis by Zones et al. [43-45]. The resulting H-SSZ-13 structure was confirmed via X-ray diffraction (XRD) with a Bruker D8 Focus X-ray Diffractometer with a Cu K (alpha) source. The diffraction pattern was observed to have all the appropriate crystal planes for the CHA structure present [46-49]. BET surface areas for many different batches of H-SSZ-13 ranged in from 580 – 601 $m^2\ g^{-1}$ and t-plot pore volumes ranged from 0.24-0.26 $cm^3\ g^{-1}$[49, 50]. Copper was deposited into the H-SSZ-13 by liquid phase ion exchange with a $Cu(NO_3)_2$ solution at a pH of 5 ±0.2. Atomic absorption spectroscopy experiments gave Si:Al ratios ranging from 4.3-4.5 and Cu:Al ratios ranging from 0.02 to 0.35, depending on the concentration of Cu in the solution. The number of Brønsted acid sites was measured by dosing each sample with 500 ppm NH_3 (from 3.0% NH_3/ Ar, Praxair) in UHP He (99.995%, Indiana Oxygen) at 433 K for two hours until complete saturation. The sample was flushed for eight hours at 433 K [26, 51]. The sample was then placed in U-shaped quartz tube surrounded by quartz wool and inserted into a Micromeritics Autochem II 2920 Chemisorption Analyzer equipped with a thermal conductivity detector (TCD) and Agilent 5975C mass selective detector (MSD). A temperature programmed desorption (TPD) was performed with a 10 $K\ min^{-1}$ temperature ramp from 298 K to 873 K in 50 sccm UHP He. Contributions from fragments of H_2O in m/z = 17 were removed to give a signal only resulting from NH_3. The NH_3 feature in m/z = 17 was quantified to determine the number of available Brønsted acid sites.

2.3.2 Kinetic Data Collection

SCR kinetic experiments were performed via a bench top tubular glass reactor with a quartz frit located in the middle of the tube to hold a catalyst bed. The diameter of the

center section of the reactor was narrowed to 3/8" and catalysts were diluted with silica gel (Fisher Chemical, Catalog No. S817-1) so that the catalyst bed height could be increased to help prevent bypass of any reaction mixture. The standard SCR reaction (conditions are described below) was performed on the silica gel and no conversion of NO or NH_3 was observed; therefore, it was considered inert. Particle sizes used were 125 – 250 μm. A plug of small quartz beads of *ca.* 3 mm diameter were placed on a wire mesh approximately 6 inches above the catalyst bed in order to ensure proper gas mixing before reaching the bed. Thermocouples were placed just above and just below the bed to ensure that no significant temperature gradients existed through the bed. Before entering the reactor, all gases except NH_3 passed through a pre-heater assembly consisting of a helical coil of 3 in. diameter made out of 0.25 in. diameter stainless steel tubing inside a temperature controlled hollow cylindrical Watlow® ceramic fiber heater. Water was introduced into the system by a heated shell-type humidifier (Perma Pure MH-Series) where the diffusion of water across a Nafion membrane into the gas mixture was controlled by the temperature setting. Ammonia was added just above the plug of quartz beads in the reactor in order to remove the possibility of thermal gas phase reactions occurring before reaching the reactor. All kinetic measurements were taken at < 20% conversion, so that all portions of the catalyst bed were exposed to nearly the same gas concentrations and the kinetics remained consistent through the entire bed. Typical gas conditions used were ~320 ppm NO (from 3.6% NO/Ar, Praxair), ~320 ppm NH_3 (from 3.0% NH_3/ Ar, Praxair), 8% CO_2 (liquid, Indiana Oxygen), 10% O_2,(from 99.5%, Indiana Oxygen), 6% H_2O (de-ionized water), and balance He (99.995%, Indiana Oxygen). Total flow rates used were approximately 1.5 L min^{-1}. The effluent gases from the reactor were analyzed online by an MKS Multigas™ 2030 gas phase FT-IR spectrometer. With on-board calibrations provided by MKS, the spectrometer was used to monitor NO, NO_2, N_2O, NH_3, CO_2, and H_2O concentrations with a 0.95 second resolution. Dinitrogen in the effluent gas was measured in initial samples using an Agilent 6890 gas chromatography unit with a series of packed columns including Porapak Q, Carboxen 1000, and Molsieve 5Å. The N_2 value obtained during steady state reaction in initial samples was compared

to the reactants consumed through the reactor to ensure no side reactions were occurring on this set of catalysts, which matched within the 90% confidence interval.

Transient NH_3 cutoff experiments were performed starting under steady state standard SCR conditions at 433 K in the same PFR unit in the absence of CO_2 with a total flowrate of 1.5 L min^{-1}. Ammonia was removed from the standard SCR gas mixture and replaced with an equal flowrate of CO_2 with a 2 position, 6 port, actuated valve (Valco Instrument Company, Inc.; Model E26UWE) to keep the same total feed flowrate. The reverse switch was also performed on a clean catalyst surface by adding NH_3 and removing CO_2. The temperature programmed desorption (TPD) following the cutoff of NH_3 was performed after ~60 minutes of flushing the catalyst in UHP He at 1.5 L min^{-1}. A 5 K min^{-1} ramp was used up to 823 K. The temperature ramp was non-linear due to the system not being built for TPD experiments.

2.3.3 X-Ray Absorption Measurements

The Cu K (8.979 keV) edge XAS data were collected on the insertion-device beam line of the Materials Research Collaborative Access Team (MRCAT, Sector 10 ID) at the Advanced Photon Source, Argonne National Laboratory. A cryogenically cooled double-crystal Si (111) monochromator was used in conjunction with an uncoated glass mirror to minimize the presence of harmonics. Measurements were made in transmission mode with the ionization chambers optimized for the maximum current with linear response (~10^{10} photons detected s^{-1}) using gas mixtures to give 10% absorption in the incident X-ray detector and 70% absorption in the transmission X-ray detector. A Cu foil spectrum was acquired simultaneously with each measurement for energy calibration. The *operando* reactor gave a total absorption (μx) between 1 and 3 and an edge step ($\Delta\mu x$) between 0.5 and 1.5. X-ray absorption near edge structure (XANES) and extended X-ray absorption fine structure (EXAFS) measurements were collected in quick scan mode while the catalyst was exposed to different conditions, which allowed for a spectrum to be collected every 135 seconds. In each case, the data were averaged over three spectra. The Cu K edge has a number of features which were utilized to determine the extent of

Cu reduction under various gas conditions. The peak at 8977 eV is representative of a symmetry forbidden transition from 1s to 3d for Cu(II), which is able to be seen because of mixing of the 3d and 4p orbitals [52]. The peak at 8983 eV represents the 1s to 4p transition for Cu(I) in a two coordinate state [53-60]. The peak at 8987 corresponds to the 1s to 4p transition for Cu(II) [54], and the white line intensity seen at 8995 eV corresponds to Cu(II) [59].

2.3.4 *Operando* XAS Experimental Setup

A low X-ray absorbing carbon tube reactor was utilized to perform *operando* XAS experiments [25, 61]. A 4 mm ID carbon reactor was secured inside an aluminum heating block which had a 25.4 x 2 mm wide slit in the center to allow x-rays to pass through the reactor. Four 100 W heating cartridges (Omega Engineering) were inserted into the aluminum block to provide heating. Wire mesh was used to hold the catalyst bed in the correct position to be analyzed by XAS, and was supported by a 1/16" tube stretching from the wire mesh to the bottom of the reactor. Starting at the bottom of the catalyst bed, a plug of quartz wool was pushed into place for support. Following this, a layer of glassy carbon beads consisting of the same material of the reactor was added to the quartz wool to create a flat surface for the catalyst bed to sit. Next, 8-20 mg of catalyst powder sieved to 125-250 μm was added. Another layer of quartz wool was inserted and finally, a layer of crushed quartz (> 250 μm) was added to help mix the gases entering the bed. A thermocouple was inserted into the top of the catalyst bed to monitor temperature. Gases were introduced sequentially into the lines going to the reactor. Helium carrier gas flowed through a heated shell-type humidifier (Perma Pure MH-Series) to bring DI H_2O into the system. Following this, NO (3000 ppm in N_2, Matheson Tri-Gas) was introduced. Next, O_2 (20% in He, Airgas, Inc.) was added once the NOx gas was diluted in the mixture to avoid any gas phase reactions. The reaction mixture was preheated to 473 K via heat tracing and a preheater coil designed in-house before entering the reactor. Inside the reactor, just above the bed, NH_3 (3000 ppm in He, Matheson Tri-gas) was allowed to enter to minimize the chance of gas phase reactions, which could produce NH_4NO_3. To measure the gas concentrations without reaction, the

gas flow was switched to a bypass which went directly into the MKS Multi-Gas 2030 gas analyzer FTIR. The cell temperature of the FTIR was kept at 464 K based on company provided calibration files. A total flow rate of 500 ml min^{-1} and a reactor temperature of 463K were kept during the experiments. Under *operando* standard SCR conditions, 300 ppm NO, 300 ppm NH_3, 5% H_2O, 10% O_2, 8% CO_2, and balance He gas was used.

2.3.5 UV-Visible Near IR Measurements

UV-Vis-NIR spectra were taken under ambient conditions with a Varian UV-Vis-NIR spectrophotometer (Cary 5000) and a Harrick-Scientific Praying-Mantis diffuse reflectance cell. Barium sulphate ($BaSO_4$, Sigma-Aldrich, 99%) was used in background scans. Each sample and $BaSO_4$ background reference was sieved to 125-250 μm before use. Spectra were collected from 7000 to 50000 cm^{-1} with a scan speed of 2000 cm^{-1} min^{-1}. Each H- and Cu-SSZ-13 sample were pre-treated in dry air (Comm. grade, Indiana Oxygen) up to 823 K elsewhere and then exposed to ambient conditions. Time of exposure to ambient conditions was not controlled as these samples were used in our lab for months beforehand. Close to 0.1 g of each sample was put in a sample cup where UV-Vis-NIR measurements were then performed.

2.3.6 Density Functional Theory Calculations

Periodic density function theory (DFT) calculations were performed using the Vienna *ab-initio* simulation package (VASP) [62-64]. Core states were treated using the projector augmented wave (PAW) [65] method and exchange and correlation treated within the PW91 generalized gradient approximation (GGA) [66]. Plane waves were included to a cutoff of 400 eV and the Brillouin zone sampled at the Γ-point. Electronic energies were converged to 10^{-8} eV and optimized geometries relaxed using the conjugant gradient method until forces on atoms were less than 0.01 eV/Å.

2.4 Results

2.4.1 Kinetics of standard SCR on Cu-SSZ-13

Kinetic measurements were taken on seven samples with Cu:Al ratios ranging from 0 to 0.35. This range of Cu loading was chosen based on existing studies which suggested isolated Cu was the active site for standard SCR and present initially as Cu loading was increased [14, 16, 28, 30]. The H-SSZ-13 sample exhibited no rate per gram catalyst (within experimental error) at the low temperature SCR range of 433-473 K, indicating that Cu was required for the reaction. Apparent activation energies and associated rates were calculated from the conversion of NO and NH_3, as shown below (Equation 2.1 & Equation 2.2).

$$NO_x\ conversion = \frac{NO_{in} - NO_{out}}{NO_{in}}\ x\ 100 \qquad \text{Equation 2.1}$$

$$NH_3\ conversion = \frac{NH_{3,in} - NH_{3,out}}{NH_{3,in}}\ x\ 100 \qquad \text{Equation 2.2}$$

The N_2O and NO_2 quantities, which are usually present in reported conversion expressions, have been ruled out as the amounts observed were within the error of the FTIR instrument. Dinitrogen was quantified using the GC and compared to the amount of NO and NH_3 converted in initial samples within a 90% confidence interval (See Figure A.1). Figure 2.1a shows the Arrhenius plots for all of the standard SCR active catalysts. The activation energies extracted from Figure 2.1a are located in Table A.1. They range from 42 – 71 kJ mol^{-1} with all but the Cu:Al = 0.02 sample (lowest loading of Cu) falling in between 64-71 kJ mol^{-1}. This higher range (64-71 kJ mol^{-1}) was near what has been reported by Gao et al.[18] for Cu-SSZ-13 and others on metal-ZSM-5 [34]. The Cu:Al = 0.02 sample had an activation energy which fell in line with previously reported metal-exchanged zeolites for standard SCR [35, 37, 38]. The reaction orders obtained for each of these samples are depicted in Figure 2.1b.

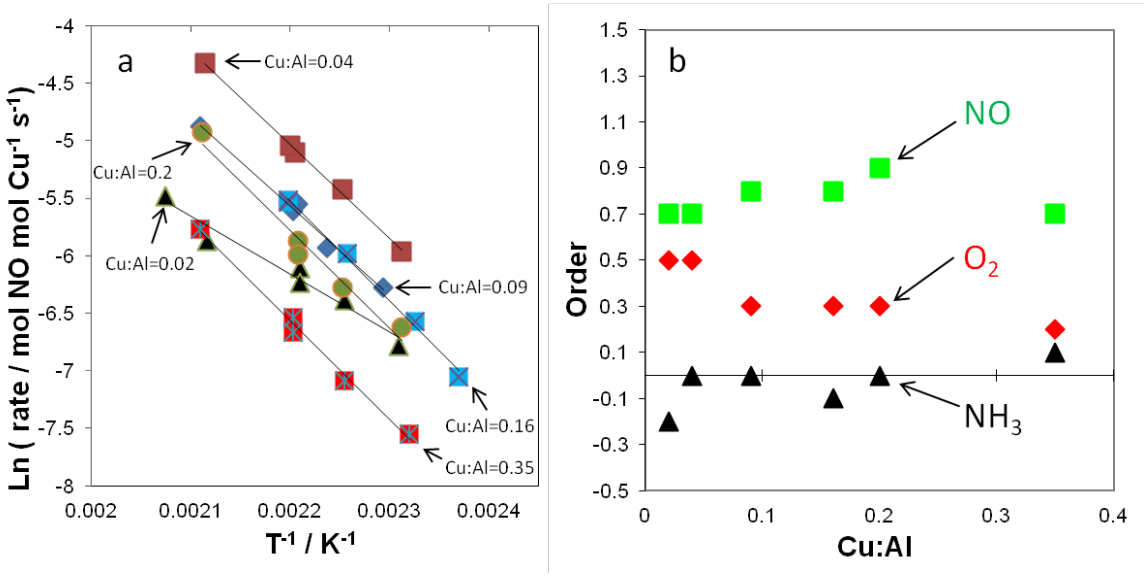

Figure 2.1a-b Arrhenius Plots and reaction orders of the 6 Cu-SSZ-13 catalysts active for standard SCR. The temperature range used for the Arrhenius plots was 433-473K. The standard SCR conditions used are 320 ppm NO, 320 ppm NH_3, 10% O_2, 6% H_2O, and 8% 2. Reaction orders for NO, NH_3, and O_2 shown as a function of Cu:Al ratio. Individual gas concentrations were changed while all other gases were held constant. NO orders were taken with NO concentrations ranging from 75 – 600 ppm, NH_3 orders were taken from 250 ppm – 600 ppm, and O_2 orders were taken from 2.5 – 20% of the feed. 90% confidence interval activation energies and reaction orders were ±5 kJ mol^{-1} and ±0.1, respectively.

The NO reaction order was observed to remain constant across all samples between 0.7-0.9, which is consistent with reports in literature for SCR on zeolites [11, 34, 35, 38]. The NH_3 order above 250 ppm was observed to be between -0.2 – 0.1, which was also consistent with reports in literature that NH_3 order is zero or slightly negative [11, 34, 35, 38]. The O_2 order ranged from 0.2 to 0.5. With the kinetic data presented, the standard SCR reaction can be represented with the following power law model (Equation 2.3).

$$-R_{SCR} = A_o exp\left(\frac{-E_{a,app}}{RT}\right)(NO)^{\alpha}(NH_3)^{\beta}(O_2)^{\gamma} \qquad \text{Equation 2.3}$$

Figure 2.2 shows the standard SCR rate per gram of catalyst which has a linear increase from Cu:Al = 0 to Cu:Al = 0.2 and a maximum rate per gram of 3.8 x 10^{-6} mole NO g cat^{-1} s^{-1}.

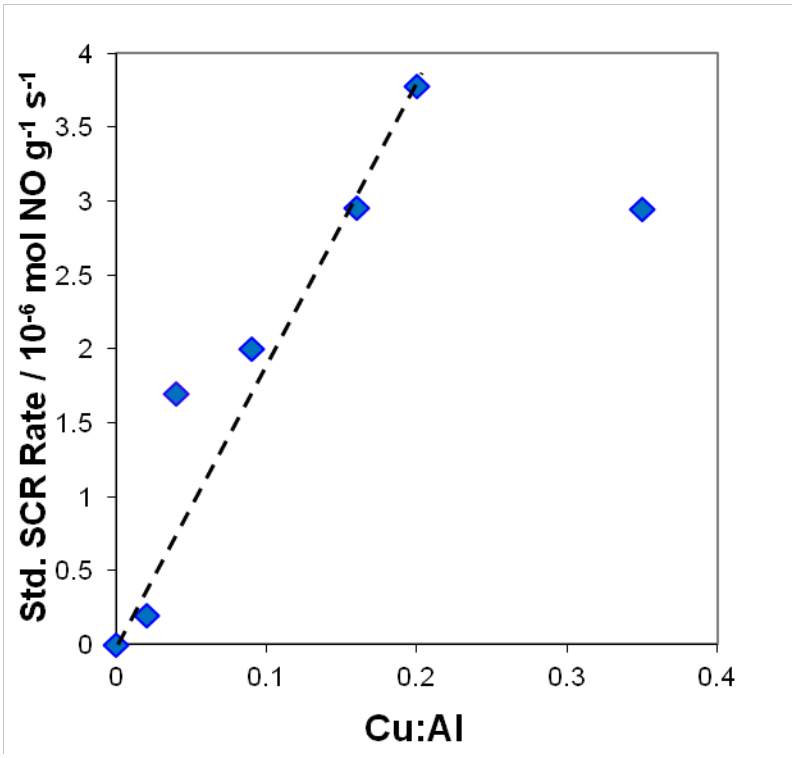

Figure 2.2 Standard SCR rates per gram of catalyst ranging from samples with Cu:Al = 0 to 0.35. Rates are reported at 473 K. Standard SCR conditions used were 320 ppm NO, 320 ppm NH_3, 10% O_2, 8% CO_2, 6% H_2O, and balance Helium at 473 K. 90% confidence interval for rate per gram was ±0.2 mol NO g^{-1} s^{-1}.

The linear trend up to Cu:Al = 0.2 (< 40% theoretical ion exchanged) observed in these samples allowed the Koros-Nowak criterion for mass transfer to be applied. If a linear trend is observed in a series of samples with variable amounts of the same active site on the same support, it indicates that all the active sites can be accessed, thus ruling out any mass transfer limitations and ensuring the catalyst is running in the kinetic regime. These samples met the criterion up to Cu:Al = 0.2. After Cu:Al = 0.2, a drop in rate per gram was observed from 3.8 to 3.0 x 10^{-6} mole NO g cat^{-1} s^{-1} for the sample with Cu:Al = 0.35, which will be explained later as a change in the type of sites available.

2.4.2 Brønsted Acid Site Counting

The number of Brønsted acid sites in each sample was determined using an NH_3 saturation at an intermediate temperature of 433 K, an eight hour flushing step, and a TPD, which was based on our own study [26] of Brønsted acid sites in SSZ-13 and a study by Woolery et al. [51]. By keeping the catalyst at 433 K, all the weakly bound NH_3 which could be in the sample, including on the Cu, was not allowed to adsorb on the surface. Table A.1 shows the H^+:Al determined on each sample and Figure A.2 shows the TPD profiles. The H-form contained 0.65 H^+:Al. Increasing the Cu loading decreased the amount of available Brønsted acid sites until Cu:Al = 0.35 which had H^+:Al=0.24. More explanation on the Brønsted acid site counting technique will be given in the discussion section.

To further investigate the role of Brønsted acid sites in standard SCR, transient NH_3 cutoff experiments were performed on Cu-SSZ-13 samples to probe the different NH_3 species under standard SCR reaction conditions. A "reactive NH_3" species was identified and quantified by tracking the NO concentration in the gas phase IR after removing NH_3 from the standard SCR gas mixture at 433 K. A CO_2 tracer was added into the mixture via a 6-port switching valve to keep the same total flowrate. It was determined that CO_2 did not play a role in the kinetics of the reaction (Figure A.3 and Table A.2); therefore, it could act as an inert tracer to probe the hydrodynamic delay in the system and enable NH_3 quantification associated with the reaction. Figure A.6 shows a representative experiment for the Cu:Al = 0.09 sample. The NO did not stabilize for close to 60 minutes after NH_3 was out of the gas mixture, suggesting an NH_3 species on the surface was still reacting with NO. In the quantification of reactive NH_3 species, one NO molecule reacting was attributed to one reactive NH_3 still present on the catalyst surface based on the stoichiometry of standard SCR. Figure 2.3 shows the quantity of reactive NH_3 determined on several samples. A trend was observed, which showed an increase in reactive NH_3 species up to Cu:Al = 0.2, and had a maximum of 0.16 NH_3:Al. This was also where the maximum standard SCR rate per gram was observed. After Cu:Al = 0.2,

the amount of reactive NH_3 levels off with a value of 0.15 NH_3:Al for the Cu:Al = 0.35 sample.

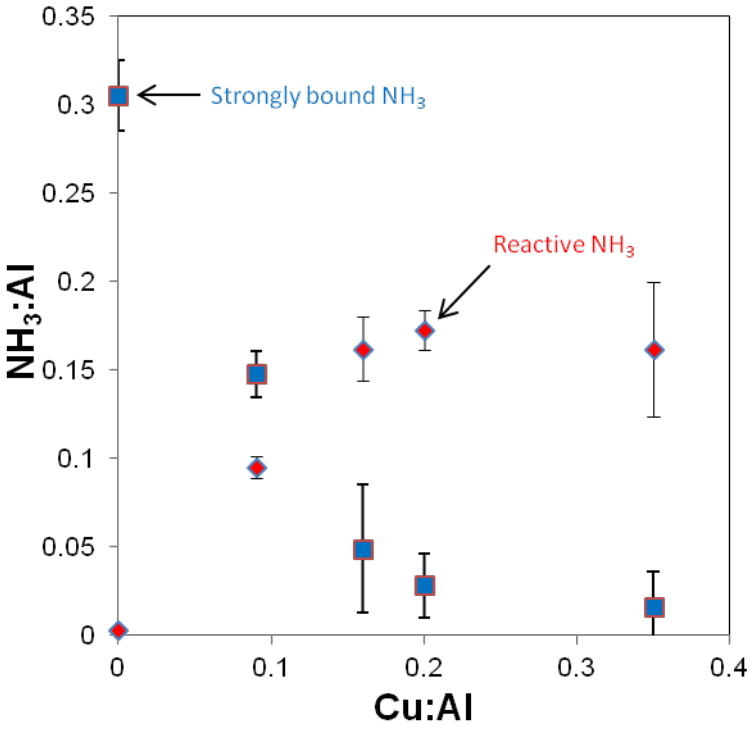

Figure 2.3 Quantities of reactive NH_3 (blue square) and strongly bound NH_3 (red diamond). The amount of reactive NH_3 determined in NH_3 cutoff experiments from standard SCR over different Cu:Al samples. Before NH_3 was removed, standard SCR conditions were present with 320 ppm NO, 320 ppm NH_3, 10% O_2, 6% H_2O, 8% CO_2, and balance Helium at 433 K. Strongly bound NH_3 determined from an NH_3 TPD after NH_3 cutoff experiments and system flush. The TPD had 1500 ml min^{-1} with 5 K min^{-1} temperature ramp to 823 K. 90% confidence interval reported.

After the NH_3 cutoff experiment, the system was flushed for ~60 minutes until the reactants were removed from the gas and only UHP He was present, followed by a temperature programmed desorption. Figure A.7 shows an example of a TPD for the Cu:Al = 0.09 sample This procedure was performed on several samples and the result after NH_3 quantification can be seen in Figure 2.3. The H-form showed 0.28 NH_3:Al. From there, a decrease in the strongly bound species was observed up to Cu:Al = 0.2, at

which point, less than 0.03 NH_3:Al was observed. This species was observed to not vary after several standard SCR conditions on the same sample with different NH_3 gas concentrations. Figure A.8 shows that different SCR gas mixtures played no role in the amount of NH_3 stored in these sites in the Cu:Al = 0.09 sample.

2.4.3 Active Cu Characterization

Figure 2.4 shows UV-Vis-NIR spectra collected in air at ambient conditions for all of the Cu-SSZ-13 samples. Two prominent features were observed. At 12,500 cm^{-1}, a feature corresponding to a d-d transition for isolated, hydrated Cu(II), or $[Cu(H_2O)_6]^{2+}$, was identified [67]. This feature reached a maximum at Cu:Al = 0.2. After Cu:Al = 0.2, the intensity of the feature at 12,500 cm^{-1} saturated (Figure A.11). The second feature observed was close to 42,000 cm^{-1} and first became visible over the transitions associated with the zeolite in the Cu:Al = 0.16 and 0.20. The presence of the second feature was at a maximum for the Cu:Al = 0.35.

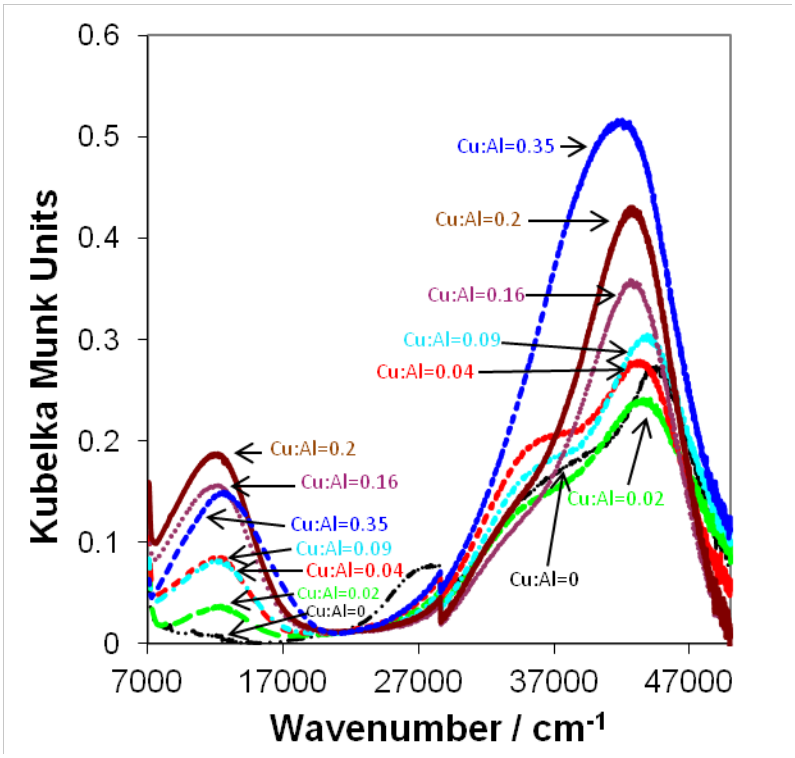

Figure 2.4 UV-Vis-NIR Spectra for each Cu-SSZ-13 sample in this study in air at room temperature.

Hydrated Cu(II) was also observed in XANES spectra in Figure 2.5 for each sample under ambient conditions. A bulk Cu(II)O and hydrated Cu(II) ($[Cu(H_2O)_6]^{2+}$) reference are shown alongside the six Cu-SSZ-13 samples. From the shapes of the XANES spectra, it appears each sample is predominantly in the hydrated Cu(II) form at room temperature, and does not have any bulk Cu(II)O, which has a pre-edge for Cu(II) at 8987 eV and a drop in white line intensity when compared to the hydrated Cu(II) reference. The Cu:Al = 0.35 sample is the only one which has a drop in white line intensity below the hydrated Cu(II) reference. Additionally, the formation of a small pre-edge feature at 8987 eV similar to the bulk Cu(II)O is beginning to form. Linear combination XANES fits were performed using the hydrated Cu(II) and bulk Cu(II)O references as well as isolated Cu(II) and isolated Cu(I) determined from our lowest Cu loading on SSZ-13. Every sample was about 100% hydrated Cu(II) except the Cu:Al = 0.35 sample, which had a 25% contribution from the bulk Cu(II)O reference (Table A.4). No contribution was seen from the isolated Cu(I) or isolated Cu(II) references. The isolated Cu references will be identified in the next paragraph. The corresponding EXAFS spectra and data fits are shown in the Figure A.13 and Table A.5, which exhibit only a first shell Cu-O feature at 1.94Å and a coordination number of 4 for all samples. No second shell was observed, as no features were distinguishable from the noise of the spectra.

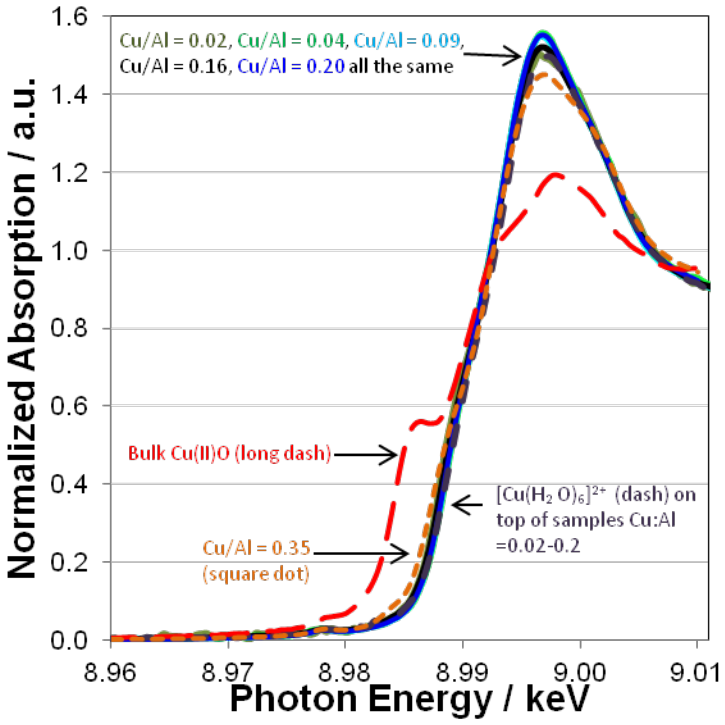

Figure 2.5 XANES spectra for all Cu-SSZ-13 samples in this study in air at room temperature. A $[Cu(H_2O)_6]^{2+}$ was used as the hydrated Cu(II) reference. Bulk Cu(II)O was also shown along side the spectra.

Operando XAS was used to study the state of the catalyst under reaction conditions and observe changes to the Cu while maintaining the concentration of reactants and products approxiamtely constant. Figure 2.6 shows the XANES spectra for two Cu-SSZ-13 samples with Cu:Al = 0.09 and 0.16 under standard SCR reaction conditions.

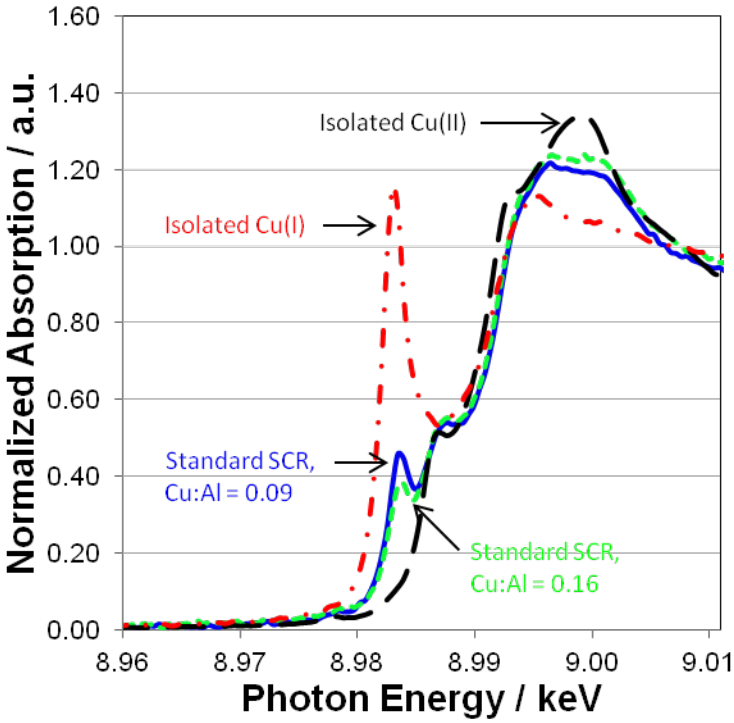

Figure 2.6 XANES spectra for Cu-SSZ-13 samples with Cu:Al = 0.09 and 0.16 under standard SCR reaction conditions compared with the isolated Cu(I) and isolated Cu(II) references. Standard SCR conditions used were 320 ppm NO, 320 ppm NH_3, 10% O_2, 8% CO_2, 6% H_2O, and balance He at 453 K.

The feature observed at 8983 eV for a 2-coordinate Cu(I) is present in both samples. The small pre-edge features corresponding to transitions for Cu(II) are also present at 8977 and 8987 eV. To quantify the extent of isolated Cu, the SSZ-13 sample with Cu:Al = 0.02, which was the lowest loading of Cu obtained, was assumed to contain only isolated Cu based on previous studies in the very low Cu loading regime on Cu-SSZ-13 [16]. This sample was used to create isolated Cu(I) and isolated Cu(II) references with different gas conditions. The isolated Cu(II) reference was made with 10% O_2 in UHP Helium at 473 K while the isolated Cu(I) reference was created with 1000 ppm NO and 1000 ppm NH_3 at 473 K. Each reference exhibited the expected pre-edge features corresponding for Cu(II) and Cu(I) and can be seen in Figure 2.6 along with the samples under standard SCR reaction conditions. When compared side by side with the two isolated Cu references, the samples under reaction conditions were a combination of the two references. The pre-edge at 8983 eV corresponding to the 2-coordinate isolated Cu(I)

was present in both samples. Table A.6 reports linear combination XANES fits for the two Cu-SSZ-13 samples under *operando* standard SCR conditions. The contributions from isolated Cu(I) in the samples were 37% and 26% for the Cu:Al = 0.09 and 0.16, respectively. Both contained negligible amounts of hydrated Cu(II) (<5%) and no bulk Cu(II)O character. The remainder of the fit was the isolated Cu(II) contribution.

The steady state reaction parameters are reported in Table A.6 with a comparison to the rates collected on our laboratory scale plug-flow reactor. An agreement was seen between the rates collected in-house and those collected during the *operando* XAS experiments. The Cu:Al = 0.09 sample exhibited a rate of 4.3 x 10^{-3} mole NO mole Cu^{-1} s^{-1} at 453 K for both the *operando* experiments and in-house experiments. The Cu:Al = 0.16 sample had a rate of 4.7 x 10^{-3} and 3.7 x 10^{-3} mole NO mole Cu^{-1} s^{-1} for *operando* experiments and in house experiments, respectively.

To count the number and type of potential Cu(II) sites, we used a combination of DFT and statistical analysis. The SSZ-13 lattice presents 4-, 6-, and 8-membered rings. In a first set of DFT calculations, we constructed an SSZ-13 supercell containing four Al T-sites (equivalent to an Si:Al ratio of 5) distributed such that two Al are in each of a 4-, 6-, and 8-membered rings. We computed the energy to exchange Cu(II) into each ring according to:

$$Z_4H_4 + Cu^{2+}(aq) \rightarrow Z_4H_2Cu + 2H^+(aq) \qquad (4)$$

We find that the optimized Cu(II) ions uniformally prefer to maintain 4-fold coordination to lattice O in each ring; further, Cu(II) is 1.13 eV more stable in the 6- than the 4-membered ring and 1.5 eV more stable in the 6- than the 8- membered ring. These results support the hypothesis that the 6-ring is the preferred site of Cu(II) exchange, consistent with previous suggestions for this site as the center of standard SCR activity [14, 15, 30].

We next constructed a 768 T site periodic supercell of SSZ-13 using the crystal structure from the International Zeolite Association database [46]. We randomly seeded the lattice with Al up to target Si:Al ratios from approximately 3 to 47, avoiding nearest neighbor Al-O-Al structures in accordance with Loewenstein's rule [32, 68]. Next, random Si to Al swaps were performed that satisfied Loewenstein's rule, and at each iteration the number of six-member rings containing exactly two Al counted. A total of 10^7 iterations were performed, and multiple replicates performed to ensure convergence. Figure 2.7 shows the computed number of six-member rings with two Al per total Al as a function of Si:Al ratio. The density rises rapidly with increasing Si:Al ratio until it maximizes near a ratio of 3, at which point six-member rings with 3 Al T-sites dominate the lattice. At a Si:Al ratio of 5, the density of two-Al six-membered rings is 0.23. Assuming Cu(II) exchange to obey the stoichiometry of Eq. 4, the theoretical maximum six-membered ring Cu:Al ratio is also 0.23 for for a sample in which every Al is a Brønsted acid site.

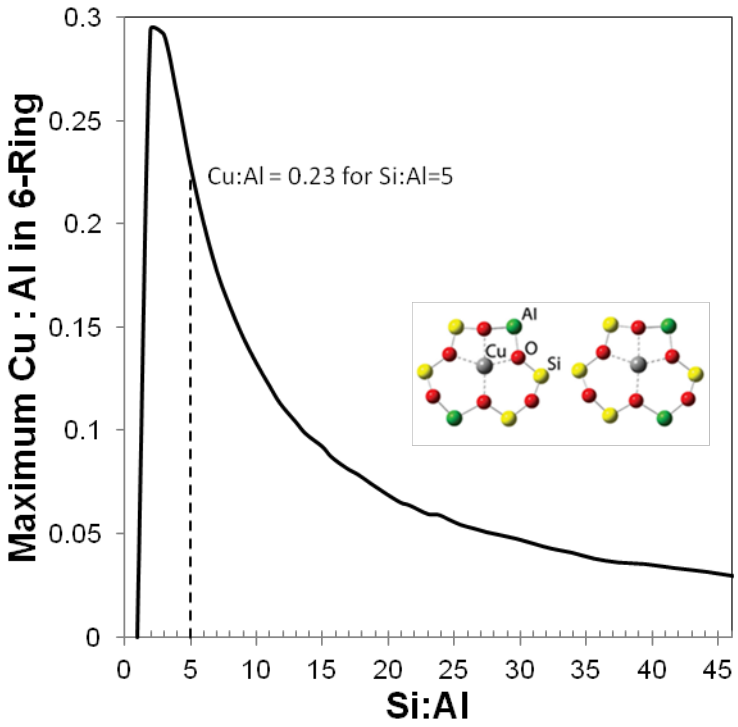

Figure 2.7 The maximum Cu(II) associated with 2 Al in the six-membered ring in SSZ-13 which can theoretically be present for a given Si:Al.

2.5 Discussion

2.5.1 Identification and Location of the Active Cu species

The combination of standard SCR kinetics and spectroscopic techniques used under ambient and reaction conditions allows the active Cu for standard SCR in SSZ-13 to be identified as an isolated Cu species. The linear increase in standard SCR rate per gram up to Cu:Al=0.2 in Figure 2.2 indicates that the active Cu species is populated in the low loading region. Other studies [16, 18] have identified isolated Cu to be present in this regime, suggesting it is the active Cu based on the standard SCR rate that is observed. The linearity of the trend of increasing standard SCR rate per gram also allows the series of Cu-SSZ-13 samples to pass the Koros-Nowak test for mass transfer [69, 70], a debated effect within SSZ-13. Gao et al.[18] have concluded that internal mass transfer can inhibit the reaction by calculating the effectiveness factors from the Thiele modulus and making comparisons of rate per mole Cu in samples with different Cu loadings. However, it is not present in the samples in this study because of the linearity of the rate per gram with the addition of active Cu species up to Cu:Al = 0.2. The Cu:Al = 0.35 sample was also determined to not have any mass transfer issues either, which will be discussed later on.

Figure 2.4 shows an increasing intensity of hydrated (isolated) Cu(II) species based on d-d transitions at 12,500 cm^{-1}. Further confirmation of a hydrated Cu(II) species was seen in Figure 2.5, in which all samples below Cu:Al = 0.2 showed nearly 100% hydrated Cu(II) character when a linear combination fit was used (Table A.4). The intensity in the UV-Vis-NIR measurements was observed to reach a maximum intensity of 0.18 Kubelka Munk units at Cu:Al = 0.2, which suggests there may be a connection between the hydrated Cu(II) species and the active Cu(II). When shown together in Figure 2.8, the rate per gram is seen to track linearly with the intensity of d-d transitions for hydrated Cu(II). The Cu:Al=0.35 sample, which was observed to have a decrease in rate per gram after the Cu:Al=0.2 sample, falls on the line as well. This correlation suggests that hydrated Cu(II) within SSZ-13 is a precursor to the active Cu under standard SCR conditions.

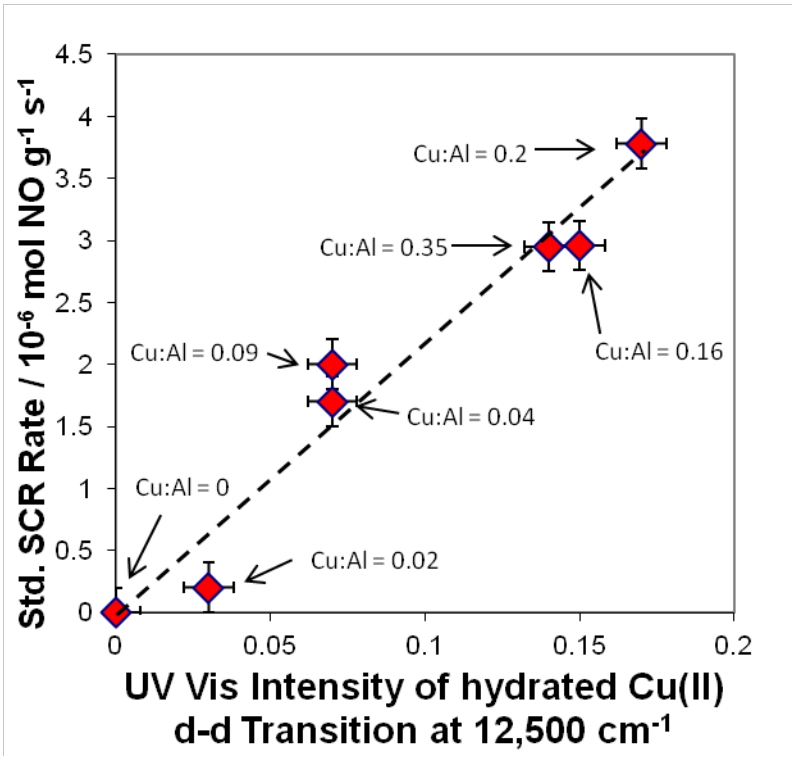

Figure 2.8 Correlation of standard SCR rate per gram with the UV-Vis-NIR intensity of hydrated Cu(II) *d-d* transition at 12500 cm^{-1} in Kubelka-Munk units in air at room temperature in the Cu-SSZ-13 samples. Standard SCR conditions used were 320 ppm NO, 320 ppm NH_3, 10% O_2, 8% CO_2, 6% H_2O, and balance Helium at 473 K. 90% confidence intervals used.

When two of the samples (Cu:Al=0.09 and 0.16) were observed under reaction conditions with *operando* x-ray absorption spectroscopy, several changes took place in the shape of the XANES spectra as shown in Figure 2.6. A feature at 8983 eV for a two-coordinate Cu(I) is present because of the expected Cu redox cycle between Cu(I) and Cu(II) under standard SCR [24, 71]. Other features at 8977 and 8987 eV are indiciative of Cu(II) coordinated to the zeolite. None of these transitions were present under ambient conditions when Cu was surrounded by water, indicating that Cu became coordinated to the zeolite and shed its sphere of hydrated under reaction conditions. Linear combination XANES fits in Table A.6 show that there is now 5% or less contribution from hydrated Cu(II) with only isolated Cu(I) and Cu(II) contributions. This change from 100% hydrated Cu(II) to greater than 95% isolated Cu(I)-Cu(II) under reaction conditions signals two things. The first is that the active Cu is an isolated species since we observe

the active Cu to build in this region based on our kinetic results and this is the only Cu species we see from *operando* XAS. The second is that the hydrated Cu(II) under ambient conditions is the precursor to the active Cu. Using UV-Vis-NIR to look at the precursor under ambient conditions is a very simple experiment and it can give an estimate of the quantity of active Cu present. Based on these new conclusions, the Cu:Al=0.35 sample does not suffer from mass transfer effects because its rate depends on the amount of hydrated Cu, which falls in line with all the other samples.

The location of the active isolated Cu species was determined to be at the six-member ring and exchanged into two Brønsted acid sites. The DFT calculations support a strong Cu(II) preference for six-member rings, and statistical analysis provides a density of these Cu(II) sites consistent with the maximum rate per gram vs. Cu loading observed in the experiments (Figure 2.7). Thus, the active Cu species for standard SCR in Cu-SSZ-13 is isolated and located within the six-member ring of the CHA structure.

2.5.2 Transition to Other Cu species after Cu:Al = 0.2

After Cu:Al = 0.2, several pieces of evidence are present in the data which suggest a new Cu species formed which has multiple Cu in its structure. The linear combinatation XANES fits of Cu-SSZ-13 under ambient conditions (Table A.4) show that the Cu:Al=0.35 sample exhibits a 25% contribution from a bulk Cu(II)O reference. Therefore, it is likely a new Cu species has emerged above the threshold of Cu:Al=0.2 which has multiple Cu, which will be denoted Cu_xO_y. The UV-Vis-NIR spectra (Figure 2.4) reach a maximum amount of *d-d* transitions for hydrated Cu(II) at Cu:Al = 0.2. Following this, a small drop in intensity from 0.18 to 0.14 Kubelka Munk units was seen, suggesting a new Cu species other than hydrated Cu(II) was forming and likely scavenging isolated Cu. It is not clear what has changed in the UV-Vis-NIR in the broad range of wavenumbers from ~27,000 – 50,000 cm^{-1}, but the entire region has reached a maximum in the Cu:Al=0.35 sample. This region was not analyzed for further information.

Another study in our group [72] (CHAPTER 3) used dry NO oxidation reaction conditions over the same set of samples here and found samples with Cu:Al greater than 0.2 to be catalytically active with 300 ppm NO, 150 ppm NO_2, and 10% O_2 at 573 K. Several samples in that study, all with Cu:Al > 0.2, showed increase in rate from zero mol NO mol Cu^{-1} s^{-1} at Cu:Al =0.2 up to 1.7 x 10^{-4} mol NO mol Cu^{-1} s^{-1} in a Cu:Al = 1.6 sample. This indicated a new Cu_xO_y species began to populate after the isolated Cu sites in the six-membered rings were full. Thus, dry NO oxidation was used as a probe reaction to determine the threshold of the formation of new Cu_xO_y species. The new species was inactive for standard SCR because the standard SCR rate per gram in the Cu:Al = 0.35 sample tracked with the amount of hydrated Cu(II) in Figure 2.8.

2.5.3 Choice of Brønsted Acid site Measurement Technique

In a previous study [26], three different NH_3 treatments followed by TPDs were shown to be able to selectively titrate Brønsted acid sites. The NH_3 treatments were compared with an n-propylamine decomposition reaction previously described [73-75] and produced an equivalent result in both H- and Cu-ZSM-5 samples. When the third NH_3 treatment (data used in this study) and n-propylamine decomposition were used in H- and Cu-SSZ-13, we found the n-propylamine unable to access close to 75% of the Brønsted acid sites as calculated from the NH_3 titration. From this, we suggested n-propylamine was unable to accurately count sites in the treatment conditions used because of the combination of the small pore-openings in SSZ-13 and the high aluminum content in ths samples (Si:Al=4.5). Thus, for SSZ-13 in this study, we used NH_3 to titrate the Brønsted acid sites.

The parent H-SSZ-13 sample exhibited ~0.65 H^+:Al from the NH_3 titration, which indicated that one-third of the Al were not contributing to the Brønsted acid sites. This effect has also been observed in other zeolites [76] and the quantity of Al not counted as Brønsted acid sites has typically been identified as extraframework, which is likely the case in our samples.

2.5.4 The Role of Residual Brønsted Acid Sites

The standard SCR rate per gram catalyst did not appear to be affected by the number of Brønsted acid sites measured by intermediate temperature gas phase NH_3 treatment and TPD which are detailed in the previous paragraph. Figure A.16 shows the normalized rate per gram catalyst and normalized H^+:Al together with an inverse correlation to each other. The drop in rate per gram after Cu:Al = 0.2 was not indicative of a shift in kinetically relevant step(s) to the Brønsted acid site. It was only a drop in the number of active Cu species, as indicated by the amount of hydrated Cu(II) tracking with the rate per gram in Figure 2.8. The activation energies and reaction orders in Figure 2.1a-b and Table A.1 also show that the kinetics were not changing over the course of Cu addition into the samples aside from the Cu:Al =0.02 sample.

The amount of strongly bound NH_3 also had an inverse correlation with the standard SCR rate per gram, suggesting it was also part of the total Brønsted acid site quantity. Figure A.17 shows the calculated total number of Brønsted acid sites based on the sum of strongly bound NH_3 and the two Brønsted acid sites for every Cu(II) exchanged. This sum did not include the reactive NH_3 species, which will be discussed next. Each total Brønsted acid site quantity based on the strongly bound species was observed to have a similar offset between 0.23-0.36 H^+:Al lower than the total Brønsted acid sites from the NH_3 titration study [26]. Previous studies [77] have shown that the NH_3 storage capacity can be significantly reduced under reaction conditions due to reaction of the NH_3 species. Since the steady state reactions performed before the NH_3 cutoff and TPD were at 433 K, the rates collected were less than 0.8 x 10^{-6} mol NO g cat^{-1} s^{-1} (Cu:Al = 0.2 sample), which corresponded to less than 4% conversion. The reaction of NH_3 off the Brønsted sites may contribute to the offset, but it is not likely to have much of an effect, or no effect in the case of the H-SSZ-13 sample, which exhibits no rate. A likely scenario is that the partial pressures of the different gases in the mixture shift the equilibrium coverage of NH_3 on Brønsted acid sites. A recent study [78] used NH_3 and H_2O adsorption and desorption experiments and microkinetic modeling to determine coverages over NH_3 on Brønsted acid sites with and without H_2O present on Fe-ZSM-5 at

423 K. The study found the coverage of NH_3 on Brønsted acid sites dropped from ~0.9 to 0.3 when water was present. Based on that study, the combination of 6% H_2O in the reaction mixture along with the other gases could have a profound effect on the NH_3 coverage on Brønsted acid sites under reaction conditions. To prove this was the effect we observed, three different gas conditions were used before an NH_3 cutoff and TPD on the H-SSZ-13 sample. The first was standard SCR as described previously, the second was dry standard SCR (no H_2O), and the third was NH_3 only. Total flowrates during each experiment were kept at 1500 ml min^{-1} just as in the original NH_3 cutoff and TPD experiments. Following the NH_3 cutoff, the TPDs were performed to observe any changes in strongly bound NH_3. Figure A.18 shows water had a large impact on the strongly bound NH_3 coverage. When quantified, the dry standard SCR showed 0.54 NH_3:Al, while the regular standard SCR showed 0.26 NH_3:Al. The final experiment used NH_3 only before the NH_3 cutoff, which gave 0.62 NH_3:Al in the TPD, which was in agreement with our previous study with ~0.65 H^+:Al for the H-SSZ-13 sample [26]. From these results, it appears that the reaction mixture does not allow for all Brønsted acid sites to be occupied under standard SCR conditions, with the presence of 6% H_2O contributing the most to the difference in values obtained. Since the amount of Brønsted acid sites as determined from the strongly bound NH_3 after standard SCR reaction are even smaller in quantity than the NH_3 titration procedures, this is an even stronger indication that the number of sites are not kinetically relevant for the standard SCR rate in these samples.

The reactive NH_3 species may be associated with the active Cu species, a Brønsted acid site, or a combination of both. Recall, the standard SCR rate on each sample correlated with the amount of hydrated Cu(II), a precursor to the active Cu site. The reactive NH_3 also track well with the standard SCR rate seen in Figure A.19, suggesting it is related to the active Cu. A recent mechanism [79] proposed for standard SCR in SSZ-13 suggests the reaction occurs through an intermediate with NH_3 on the active Cu. This also falls in line with our previous study [71] where we suggested NH_3 may react or desorb from Cu, but also keeps water from adsorbing on the active Cu under reaction conditions using

transient cutoff experiments with *operando* XAS. The long time for the NO signal to stabilize in the NH_3 cutoff experiment (~60 min) may suggest there is migration of NH_3 species to an active site, in which case, the Brønsted acid site storage may become important in this transient process. Thus, we cannot rule out the possibility that some or all of the reactive NH_3 comes from Brønsted acid sites surrounding the Cu. Further studies need to be performed to determine the correct position(s) for the reactive NH_3.

2.5.5 The Importance of Cu:Al = 0.2

The agreement of multiple techniques giving a maximum (standard SCR rate per gram, hydrated Cu(II) in UV-Vis-NIR, isolated Cu in six membered ring from statistical calculation) at Cu:Al = 0.2 suggests this is an important transitional region in Cu-SSZ-13 for a Si:Al = 4.5. From the results discussed, the transition is caused by isolated Cu sites in the six-membered rings filling to a maximum value. At this point, the standard SCR rate per gram catalyst is at a maximum, which confirms kinetically that this is the active site for standard SCR. At this transition, another Cu species begins to form which is not located in the six-membered ring, and our results show that multiple Cu are involved. The UV-Vis NIR data show this species may begin to remove isolated Cu after Cu:Al=0.2, which causes a loss in standard SCR rate per gram. The statistical approach used here to confirm experimental results should be used as a road map to make high-performance Cu-SSZ-13 with varying Si:Al for standard SCR.

2.6 Conclusions

Seven H- and Cu-SSZ-13 samples with Si:Al = 4.5 and Cu:Al ranging from 0 to 0.35 were used to determine standard SCR reaction kinetics and probe the active Cu site under standard SCR reaction conditions. The standard SCR rate per gram increased linearly with Cu:Al ratio up to Cu:Al = 0.2, indicating the active site was formed in this regime. This matched with statistical calculations of the maximum amount of isolated Cu occupying 2 Al on the six-membered ring of the SSZ-13 at Cu:Al = 0.23. This linear trend also rules out any mass transfer limitations.

The state of the Cu in SSZ-13 under ambient conditions was tested with UV-Vis-NIR and XAS. The UV-Vis-NIR showed the build up of a hydrated Cu(II) species until Cu:Al = 0.2, which agreed with the trend in standard SCR rate per gram with increasing Cu loading up to Cu:Al = 0.2. Ambient XAS confirmed the state of Cu in all samples with Cu:Al = 0.2 or below to have only this hydrated species. *Operando* XAS showed that all the hydrated Cu became an isolated Cu(I)-Cu(II) mix under standard SCR conditions, confirming the active species of Cu for standard SCR. Hydrated isolated Cu(II) was also determined to be the precursor to the active Cu species because it tracked with the standard SCR rate in all samples and transformed completely to isolated Cu under reaction conditions.

The number of Brønsted acid sites found in each sample were determined to not be involved in the kinetically relevant steps because of an inverse correlation between rate per gram and number of sites. Individual NH_3 species were also quantified under reaction conditions. A strongly bound NH_3 found by TPD after reaction conditions and corresponding to a fraction of the total Brønsted acid sites also showed an inverse correlation with the rate. A reactive NH_3 species found by quantifying the NO reacted after NH_3 was removed from standard SCR mixture tracked with the standard SCR rate suggesting it was on the active Cu or on a nearby Brønsted acid site .

This study suggests a transition region in Cu-SSZ-13 near Cu:Al = 0.2 for our samples which have Si:Al = 4.5, where a Cu_xO_y species not associated with the six-membered ring begins to form. Ambient XAS show the appearance of transitions similar to what have been observed in Cu(II)O in the Cu:Al = 0.35 sample. Thus, the transition region for a given Si:Al in Cu-SSZ-13 must be considered when trying to maximize the isolated Cu for standard SCR and not create other unwanted Cu species."

2.7 Acknowledgements

A lengthy author list is associated with this manuscript. Because this is a dissertation, these people will be listed here. Those people are Shane A. Bates, Christopher Paolucci,

Trunojoyo Anggara, Atish A. Parekh, William F. Schneider, Jeffrey T. Miller, W. Nicholas Delgass and Fabio H. Ribeiro. We would also like to thank Paul Dietrich for his help in executing the XAS experiments at the APS. Use of the Advanced Photon Source is supported by the U. S. Department of Energy, Office of Science, and Office of Basic Energy Sciences, under Contract DE-AC02-06CH11357. MRCAT operations are supported by the Department of Energy and the MRCAT member institutions. Support for JTM was provided under the auspices of the U.S. DOE, Office of Basic Energy Sciences, Division of Chemical Sciences, Geosciences, and Biosciences under contract number DE-AC0-06CH11357. We would also like to thank Sachem, Inc. for their gracious donation of the structure directing agent for SSZ-13 synthesis.

Chapter 2 has been reprinted with permission from (S.A. Bates, A.A. Verma, C. Paolucci, A.A. Parekh, T. Angarra, A. Yezerets, W.F. Schneider, J.T. Miller, W.N. Delgass, and F.H. Ribeiro, Identification of The Active Cu Site in Standard Selective Catalytic Reduction with Ammonia on Cu-SSZ-13, J. Catal., 312 (2014) 87 – 97) Copyright (2014) Elsevier Inc.

CHAPTER 3. KINETICS OF OXIDATION OF NITRIC OXIDE OVER COPPER EXCHANGED SSZ-13

3.1 Abstract

The site requirements and mechanism of dry NO oxidation were examined on a series of Cu-SSZ-13 catalysts (Silicon: total Aluminum ratio = 4.5) with Cu:Al (copper : total Aluminum) ratios ranging from 0.02 to 1.6. Catalysts with Cu:Al ratio < 0.2 exhibit immeasurable NO oxidation rates (per mole Cu), while NO oxidation rates increase monotonically with Cu:Al ratio from 0.2 up to 0.5. Hydrated Cu-SSZ-13 catalysts with Cu:Al < 0.2 exhibit a near infrared feature at 12500 cm^{-1} under ambient conditions that we assign to a *d-d* transition of an isolated, hydrated Cu(II) ion. X-ray absorption near edge structure (XANES) of Cu ions on the same catalysts under ambient conditions quantitatively match a $[Cu(H_2O)_6]^{II}$ reference. The 12500 cm^{-1} feature intensity is constant above Cu:Al ratio = 0.2, implying that the additional Cu ions adopt other configurations. Catalysts with Cu:Al ratio > 0.2 also showed an increasing percentage of Cu_xO_y species (clustered Cu(II) ions $x \geq 2$, $y \geq 1$) as quantified by XANES under ambient conditions. Saturation of these isolated Cu(II) sites at Cu:Al ratio = 0.2 is consistent with the expected number of 6-ring Al_f (framework Al) pair sites available to accommodate them. The hydrated isolated Cu(II) ions in catalysts with Cu:Al ratio < 0.2 are quantitatively converted to dehydrated isolated Cu(II) ions under NO oxidation and do not contribute measurably to the rate of NO oxidation. In contrast, i*n-situ* XANES experiments show that the Cu_xO_y species remain present in the $NO/NO_2/O_2$ environment and contribute linearly to the rate of NO oxidation per mole Cu (at 573K). We used density functional theory (DFT) calculations to compare the ability of isolated Cu ions and Cu dimers (Cu_2O_y) species to support NO oxidation. Only the Cu dimers can accommodate adsorption and dissociation of O_2 necessary to catalyze NO oxidation. We

hypothesize that activated oxygen enables NO to form NO_2 in a catalytically relevant step. These findings reveal that dry NO oxidation (300 ppm NO, 150 ppm NO_2 and 10% O_2) can be used as a probe reaction to identify clustering of Cu ions on Cu-SSZ-13.

3.2 Introduction

Copper-exchanged zeolites form an important class of catalysts that convert NOx (NO and NO_2) pollutants to dinitrogen (N_2) in the presence of ammonia (NH_3) and oxygen (O_2) via selective catalytic reduction (SCR) [2, 80]. In particular, Cu-SSZ-13 shows commercially viable rates for standard SCR ($NO + NH_3 + O_2$) even after hydrothermal aging [1]. However, the location and configuration of the active sites on Cu-SSZ-13 have not been fully characterized. Many research groups have proposed atomically dispersed Cu(II) ions present near the six-member ring of SSZ-13 as the dominant active site for the standard SCR [14, 15, 24]. Fickel et al. [30] used Rietveld refinement of X-ray diffraction patterns at varying temperatures on Cu-SSZ-13 (Cu:Al ratio = 0.35, Si:Al= 6) and proposed that all Cu(II) ions were isolated and present near the six member rings of the zeolite. In addition, Kwak et al. [16] observed another Cu ion configuration in SSZ-13 (Si:Al = 6) at Cu:Al ratio > 0.2, which they assigned to an isolated Cu(II) ion in the 8 member ring. Gao et al. [18] concluded that the active sites for ammonia oxidation were isolated Cu ions in the 8 member cage of SSZ-13 for $0.2 \leq$ Cu:Al ratio ≤ 0.4 and possibly Cu dimers (Cu_2O_y) at Cu:Al ratio > 0.3. Based on increasing ammonia oxidation rates with increasing Cu:Al ratios, Gao et al. speculated that Cu ions in the 8 member ring of Cu-SSZ-13 would be the active sites for generic, non-selective oxidation reactions, while isolated Cu(II) ions near the double 6 member ring in Cu-SSZ-13 would be more suited for selective reactions like standard SCR.

Catalytic NO oxidation is a useful probe reaction to obtain mechanistic information about standard SCR [20, 81]. Available evidence on Cu-SSZ-13 indicates that NO oxidation ($NO + O_2$) rate of reaction is independent of standard SCR ($NO + O_2 + NH_3$) rate. Ruggeri et al. [23] observed that water decreased NO conversion considerably during NO oxidation while not affecting NO conversion during standard SCR. Similarly, Kwak et al.

[21] observed negligible NO conversion during wet NO oxidation (350 ppm NO, 14% O_2, and 10% H_2O) on Cu-SSZ-13 catalysts with Cu:Al ratios varying from 0.1 to 0.3 and increasing wet NO oxidation conversion on Cu:Al ratios > 0.3 at 573 K, even though all catalysts displayed similar NO conversion during Standard SCR. This observation also hints toward the presence of multiple Cu ion configurations as a function of the Cu:Al ratio. Thus, there is a need to understand the distinctions between Cu sites active for NO oxidation and for standard SCR on Cu-SSZ-13.

Density functional theory (DFT) molecular models have been used extensively to study the Cu siting and NOx catalysis on Cu-exchanged zeolites. Most work to-date has employed cluster models containing one or two Al-containing tetrahedral (T-) sites to represent ion exchanged Cu(I) ('ZCu') or Cu(II) ('Z_2Cu'). Schneider et al. [82-84] used single T-site ZCu models on Cu-ZSM-5 to consider an NO oxidation pathway involving successive reactions of two NO molecules with an adsorbed O_2 (Scheme 3.1):

$$\mathrm{ZCu} \xrightarrow{O_2} \mathrm{ZCuO_2} \xrightarrow[-NO_2]{+NO} \mathrm{ZCuO} \xrightarrow[-NO_2]{+NO} \mathrm{ZCu} \qquad \text{Scheme 3.1}$$

Similar intermediates have been considered in DFT studies of NO decomposition [85-87] and N_2O decomposition [88] . Analogous oxygen chemistry can be envisioned involving Cu dimers (Scheme 3.2):

$$\mathrm{ZCu\ldots CuZ} \overset{O_2}{\leftrightarrow} \mathrm{ZCuO_2CuZ} \overset{[O]}{\leftrightarrow} \mathrm{ZCuOCuZ} \overset{[O]}{\leftrightarrow} \mathrm{ZCu\ldots ZCu} \qquad \text{Scheme 3.2}$$

These intermediates have been examined computationally in the context of NO decomposition [32, 89, 90] and methane oxidation [91-93] in Cu-ZSM-5. The stability of these intermediates has been shown to depend on the locations of the charge-compensating T-sites [89, 90, 94]. The large majority of these calculations are based on cluster models, but recently more faithful, fully periodic models have been used to study ZCu(I) and Z_2Cu(II) siting and adsorption in SSZ-13 [24, 95-99]. None have considered

NOx chemistry or the potential relevance of Cu dimers or larger clusters inside Cu-SSZ-13.

In this chapter we report a kinetic and computational study of dry NO oxidation on Cu-SSZ-13 catalysts (Si:Al= 4.5) with varying Cu:Al ratios. Using a combination of steady state reaction kinetics, ultraviolet visible near infrared (UV-Vis-NIR) spectroscopy under ambient conditions and X-ray absorption near edge structure (XANES) under ambient conditions in air, and *in-situ* dry NO oxidation, we show that there is a difference in the dry NO oxidation rate for different Cu ion configurations. We use statistical models to count the number of available sites in SSZ-13 for isolated Cu(II) ions, and use DFT models to contrast O_2 adsorption and reaction on a variety of candidate isolated Cu and Cu dimer sites. We further use DFT to examine the growth of Cu_xO_x ($2 \leq x \leq 8$) particles within SSZ-13. Consistent with experiments, we find that Cu dimers are able to support oxidation catalysis while isolated Cu ions cannot. The result is the aggregate indicator that NO oxidation rate is associated with Cu dimers or larger aggregates and not isolated Cu(II) ions. Dry NO oxidation (300 ppm NO, 150 ppm NO_2, and 10% O_2) is thus a useful probe for Cu ion clustering in Cu-SSZ-13.

3.2 Experimental Methods

3.2.1 Synthesis and Characterization of Cu-SSZ-13

The parent zeolite, H-SSZ-13 was prepared following a recipe detailed by Fickel et al. [30]. The as-synthesized zeolite was in the sodium form with the template within the zeolite. The template was removed by treating the zeolite in 20% O_2/N_2 (Indiana Oxygen, commercial grade) at a flow rate of 100 ml min^{-1}. The temperature was ramped at 0.5 K min^{-1} to 823 K followed by a 480 minute dwell time and subsequent cooling to 298 K. This procedure enabled the formation of Na-SSZ-13. This material was converted into H-SSZ-13 by ion exchanging with 0.2M NH_4OH (Fisher Chemicals, catalog number A669 – 212) at 353 K for 12 hours and treating the decanted and air dried material in 20% O_2/N_2 at a flow rate of 100 ml min^{-1}. The temperature was again ramped 0.5 K min^{-1} to 823 K followed by a 480 minute dwell time and subsequent cooling to 298 K. The

resulting material was confirmed to be H-SSZ-13 via x-ray diffraction using a Bruker D8 Focus X-ray diffractometer with a Cu K α source. The diffraction pattern was in agreement with the literature pattern [26, 100]. A $Cu(NO_3)_2 \cdot xH_2O$ (Sigma Aldrich) precursor salt was used for Cu ion exchange. Approximately 250 ml solution per gram of H-SSZ-13 was used for all the samples. The temperature of copper ion exchange was 338 K. Nine catalysts were ion exchanged at a pH of 5 ± 0.2. The slurry pH was controlled by periodic drop wise addition of a 0.1M NH_4OH solution obtained by mixing an appropriate amount of 28% w/w NH_4OH (Fisher Chemicals, catalog number A669 – 212) with deionized (D.I.) water.

After Cu ion exchange, the solid was separated from the solution by centrifugation for 20 minutes followed by a D.I. water wash for 10 minutes under stirring, and subsequent centrifugation. This procedure was repeated three times. The catalyst was then dried overnight in a vacuum oven (29 psi vacuum) at 293 K. Subsequently, the catalyst was treated in 20% O_2/N_2 and a flow rate of 100 ml min^{-1}, with a temperature ramp of 0.5 K min^{-1} until 823 K and a dwell time of 360 minutes. After the treatment, the catalyst was cooled to 298 K and subsequently used for catalytic testing. The Cu:Al ratio and Si:Al ratio for each sample was measured using a Perkin Elmer AAnalyst 300 atomic absorption spectrometer. Approximately 20 mg of each sample was dissolved in 5 ml aqua regia (HNO_3, 68 – 70 % w/w and HCl, 36.5 – 38 % w/w, both obtained from Mallinckrodt chemicals) and 2 ml HF (48 % w/w, obtained from Macron chemicals) overnight followed by addition of 50 ml D.I. water to dilute the concentrated acid solution. Three standards at approximately 1 ppm, 3 ppm, and 5 ppm were prepared by diluting a 1001 ppm copper in nitric acid solution (Fluka Analytical) for calibrating the instrument. An average of five replicate measurements was reported for each catalyst. Samples for which the Cu:Al ratio measurement was outside the calibration range were diluted further and the measurement repeated on the diluted solution. The details of all Cu-SSZ-13 catalysts used in this study are provided in Table B.1.

The Cu-SSZ-13 catalysts were further characterized by N_2 adsorption and desorption isotherms, aluminum magic angle spinning nuclear magnetic resonance (^{27}Al MAS NMR) spectroscopy and Brønsted acid site counting using ammonia and n-propyl amine. The methodology and results of these characterizations are provided by Bates et al. [26]. The ^{27}Al MAS NMR results showed that the parent SSZ-13 material had 15% Al as extra-framework cations, while, on an average, the ratio of the number of Brønsted acidic protons accessible to ammonia, to the number of framework Al atoms (Al_f) was ~ 0.76 [26].

3.2.2 Kinetic Measurements

The reactor setup used for the steady state NO oxidation experiments was similar to the one used by Pazmiño et al. [101]. The assembly consisted of gas delivery and manifold, reactor, and gas analysis systems. The gas delivery and manifold system was comprised of a series of mass flow controllers (Porter Instruments division), which controlled individual gas flows (NO, NO_2, O_2, CO_2, and N_2). A gas manifold was used to mix all the gases in order to produce the desired gas concentrations and feed them into the reactor system. The reactor system was made up of a down flow vertical Pyrex reactor with an inner diameter of 13 mm and an overall length of 400 mm. A porous glass frit was installed at the midpoint of the reactor, over which a layer of quartz wool was placed in a flattened position. In order to minimize the pressure drop of the flow of gas across the powder catalyst bed, the catalyst particles were sieved to a nominal size of 125 µm - 250 µm and were placed over the top of the quartz wool layer with dilution. All catalysts used in this study were diluted with silica gel (Fisher Scientific) to form a bed of adequate height. Another layer of quartz wool was pressed slightly over the top of the catalyst bed to ensure uniformity of the bed. A metallic mesh was placed 10 mm above the catalyst bed in order to support glass beads (~ 20 mm in height). The temperature across the catalyst bed was measured by placing two K-type thermocouples, one at ~ 2mm above the catalyst bed and the other ~ 2mm below the glass frit. To ensure isothermal conditions across the catalyst bed, (verified by reading the temperatures from the 2 K-type thermocouples), the glass reactor around the catalyst bed was wrapped with

aluminum foil (20 mm by 70 mm) and covered with a 190 mm long aluminum sheath (4 mm thickness). Moreover, the feed gases from the gas manifold were first fed to a gas preheater (maintained at 573 K) and then into the main reactor. The reactor system was built in such a way that the preheated gases could either flow through the catalyst bed or bypass directly into the gas analysis section. Appropriate valves were placed in the reactor setup so that the gas analysis section could receive only one type of gas flow.

The gas-phase concentrations of NO, NO_2, CO_2, H_2O, and N_2O were measured by a Fourier transform infrared (FTIR) analyzer (MKS Multigas™ 2030 gas phase FTIR spectrometer). The FTIR analyzer had a spectral resolution of 0.5 cm^{-1} and factory supplied calibrations were used to quantify the various gas concentrations.

After each experiment, the Pyrex reactor and glass beads were cleaned with a phosphate free cleaning solution and subsequently by freshly prepared aqua regia followed by rinsing in DI water.

3.2.3 X-ray Absorption Measurements

The X-ray absorption spectroscopic (XAS) measurements under *in-situ* and *ex-situ* conditions were made on the insertion-device beam line of the Materials Research Collaborative Access Team (MRCAT, Sector 10 ID) at the Advanced Photon Source, Argonne National Laboratory. The XAS data were collected at the Cu K edge (8,987 eV) in transmission mode. In order to minimize the presence of harmonics, a cryogenically cooled double-crystal Si (111) monochromator was used in conjunction with an uncoated glass mirror. The ionization chambers were optimized for the maximum current with a linear response (10^{10} photons detected s^{-1}). This was accomplished by using gas mixtures to provide for 10% absorption in the incident X-ray detector and 70% absorption in the transmission X-ray detector. The energy calibration for each spectrum was performed by a simultaneous measurement of the XAS spectrum for a Cu foil. The XAS measurements were made in a metallic cylindrical holder which had a capability of containing up to six catalyst pellets. The thickness of catalyst pellets (equivalent to 0.015 – 0.03 g) was

chosen to have an edge step ($\Delta\mu x$) of 1. The cylindrical holder was placed in a quartz tube and the tube was placed in a furnace to enable *in-situ* spectroscopy [101]. For *in-situ* measurements, the catalysts were pelletized and heated to 573 K in 300 ppm NO, 150 ppm NO_2, 10% O_2, and balance He (Ultrahigh Purity, Airgas)

3.2.4 Ex-situ Ultraviolet Visible Near Infra-red (UV-Vis-NIR) Spectroscopy

Ex-situ UV-Vis-NIR spectra under diffuse reflectance conditions were collected on a Varian UV-Vis-NIR spectrophotometer (Cary 5000) equipped with a Harrick-Scientific Praying-Mantis diffuse reflectance accessory (DRA). Barium sulphate ($BaSO_4$, Sigma Aldrich, product number 243353) was used as a reference material for background scans. This material was sieved to a nominal size of 125 μm - 250 μm before taking the background scan. Spectra were collected from 7,000 cm^{-1} to 50,000 cm^{-1} at a scan speed of 2,000 cm^{-1} min^{-1}. Cu-SSZ-13 samples were initially pretreated in 10% O_2/N_2 at 800 K elsewhere and subsequently exposed to ambient conditions. This was done to ensure that these samples were hydrated. Approximately 0.1 g of each sample was placed in the sample cup and spectral measurements were subsequently made.

3.3 Computational Methods

Periodic DFT calculations were performed using the Vienna *ab-initio* simulation package (VASP) [62, 63]. Core states were treated using the projector augmented wave (PAW) [65] method and exchange and correlation treated within the PW91 generalized gradient approximation (GGA) [66]. Valence state plane waves were included to a cutoff of 400 eV and the Brillouin zone sampled at the Γ-point. Electronic energies were converged to 10^{-8} eV and geometries relaxed until atomic forces were less than 0.01 eV/Å. Harmonic vibrational frequencies were calculated by numerical differentiation of atomic forces with differential displacements of 0.01 Å. Tight convergence was necessary to avoid unphysical imaginary frequencies [102]. Most calculations were performed in a 12 SiO_2 formula unit, approximately rhombohedral supercell (Figure 3.1a and Figure 3.1b) [24]. Two Si are replaced by Al to achieve the desired 5:1 Si:Al ratio.

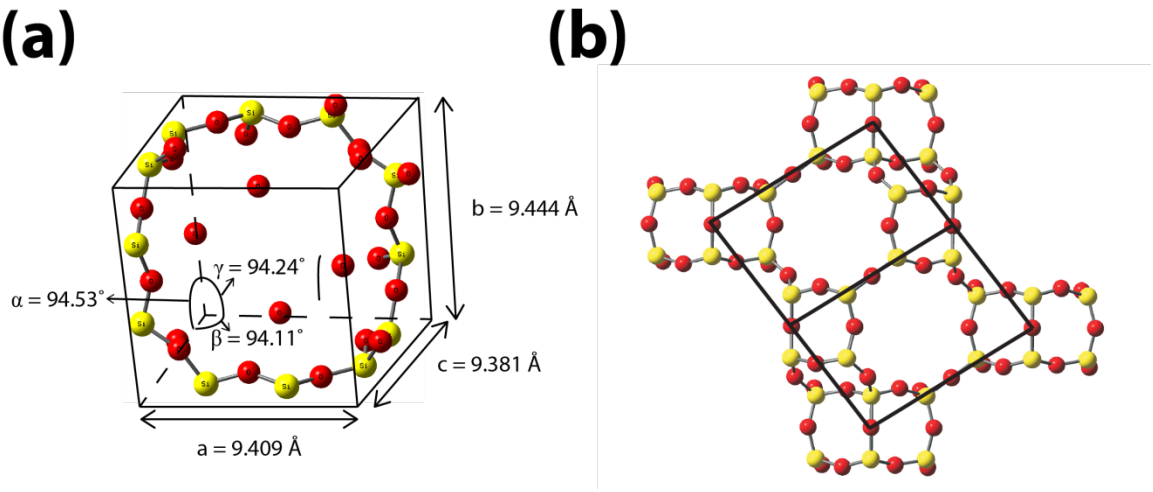

Figure 3.1 SSZ-13 periodic super cell models. (a) The 1 × 1 × 1 supercell model and associated cell parameters. (b) Periodic image illustrating larger 4-, 6-, and 8- ring structures. Yellow and red spheres are Si and O, respectively

The NO oxidation (NO + ½ O_2 → NO_2 , -0.6 eV) energy is exaggerated by the GGA by a factor of two [103], while the hybrid B3LYP [104-106] exchange-correlation functional improves the computed result to -0.68 eV. To take advantage of this improved accuracy, we used a cluster calculation correction scheme similar to that employed by others [107-112] to estimate super cell B3LYP energies as (Equation 3.1):

$$E^{B3LYP}_{supercell} \approx E^{GGA}_{supercell} + (E^{B3LYP}_{cluster} - E^{GGA}_{cluster}) \qquad \text{Equation 3.1}$$

Cluster fragments were extracted from the converged super cell models and included 4- and 6-rings (Figure B.1a) or an 8-membered ring (Figure B.1b). Clusters were terminated with hydroxyl groups with O–H distance fixed at 0.964 Å and oriented as in the optimized periodic structure. Single-point GGA and B3LYP calculations were performed in the Amsterdam Density Functional (ADF) code [113, 114] using an all-electron triple-zeta polarized basis and an integration precision of 10^{-8} [115].

To relate computed energies to experimental conditions, we calculated the Gibbs free energy at 550 K, 10% O_2, 300 ppm NO, and 150 ppm NO_2 as:

$$G_{B3LYP}(T,P) = E_{\mathrm{sup}ercell}^{B3LYP} + E_{ZPE} + \Delta G(T,P) \qquad \text{Equation 3.2}$$

Here E_{ZPE} is the zero point energy of a molecule or adsorbate and $\Delta G(T,P)$ is the free energy difference between 0 K ideal gas and the target temperature and pressure for gaseous as well as adsorbed species. For gas species, we calculated $\Delta G^{\mathrm{gas}}(T,P)$ according to:

$$\Delta G^{\mathrm{gas}}\left(T,P\right) = \Delta G^{o}_{(\mathrm{g})}\left(T\right) + k_B T \ln\left(\frac{P}{P^o}\right) \qquad \text{Equation 3.3}$$

In Equation 3.3 , $\Delta G^{\mathrm{o}}_{(\mathrm{g})}$ was taken from the NIST-JANAF thermochemical table [116] and P^o is 1 bar. The corresponding free energy difference for adsorbed species, $\Delta G^{\mathrm{ads}}(T,P)$, was computed from the harmonic partition function to incorporate vibrational contributions (Equation 3.4).

$$\Delta G^{ads}(T,P) \approx -k_B T ln Q^{vib} \qquad \text{Equation 3.4}$$

3.4 Results

3.4.1 Dry NO Oxidation Kinetics on Varying Cu:Al Ratios over Cu-SSZ-13

The rate of dry NO oxidation per total mole of copper was measured on nine Cu-SSZ-13 catalysts as a function of temperature and various concentrations of NO, NO_2, and O_2. Results are presented in Table 3.1. The H-SSZ-13 catalyst did not display a measurable NO oxidation rate at 573 K. The conversion of NO was measured according toEquation 3.5.

$$NO\,conversion = \frac{NO_{in} - NO_{out}}{NO_{in}} \times 100 \qquad \text{Equation 3.5}$$

The NO conversion was converted to an overall NO oxidation rate by assuming a differential reactor in which the NO conversion was less than 10% and NO_2 was co-fed

with the reactants [101]. Based on the overall rates of NO oxidation ($r_{overall}$), the normalized forward rates (r_{fwd}) were reported in the form of a power law model (Equation 3.6 & Equation 3.7). The approach to equilibrium (β) was included because the NO oxidation rates were possibly limited by equilibrium under the relevant reaction temperature [117].

$$r_{overall} = r_{fwd}(1-\beta) \qquad \text{Equation 3.6}$$

$$r_{fwd} = Ae^{\frac{-E_a}{RT}}[NO]^a[NO_2]^b[O_2]^c \qquad \text{Equation 3.7}$$

Where

$$\beta = \frac{[NO_2]^2}{K[NO]^2[O_2]} \qquad \text{Equation 3.8}$$

For all the kinetic measurements, the value of β was between 0.02 and 0.18, which indicated that equilibrium was not attained under the pertinent temperature range. The apparent pre exponential factor (A / s^{-1}) and activation energy (E_a / kJ mol^{-1}) were also calculated from the forward rate; a, b, and c are forward reaction orders; K is the equilibrium constant for the NO oxidation reaction.

The mass balance, defined as the concentration difference $(NO + NO_2)_{inlet} - (NO + NO_2)_{outlet}$, was less than 3 ppm for all kinetic measurements. This indicated that no side reactions were occurring. Also, N_2O formation was ruled out as its concentration was measured in negligible quantities (< 1 ppm).

For all catalysts active for NO oxidation (Cu:Al ratio > 0.2), the apparent activation energy was 52 ± 5 kJ mol^{-1}. This value is in agreement with Metkar et al. [20] and Kwak et al. [21] who measured an apparent activation energy of 56 kJ mol^{-1} and 58 kJ mol^{-1} respectively, although in their work NO_2 was not co-fed in the feed stream. In the absence of NO_2 co-feeding, Joshi et al. [118], however, obtained an apparent activation

energy of 31 kJ mol^{-1}, which is in line with the expectations from Mulla et al [119]. As a result, the agreement of the value of apparent activation energy by Metkar et al.[20], Kwak et al.[21], and this work may be fortuitous. The NO, NO_2, and O_2 orders (measured at 573 K), for all the catalysts active for NO oxidation, were 1.6 ± 0.2, -0.8 ± 0.1, and 0.9 ± 0.1 respectively. A representative Arrhenius plot and apparent reaction orders (with respect to NO, NO_2 and O_2) for a Cu-SSZ-13 catalyst with Cu:Al ratio of 0.35 is displayed in Figure B.2.

The dry NO oxidation rate (per mole Cu, at 550 K) could not be measured for catalysts with Cu:Al ratio < 0.2, while the NO oxidation rate per mole Cu increased monotonically above Cu:Al ratio = 0.2 and saturated up to Cu:Al ratio = 1.6 (Figure 3.2 and Table 3.1).

These results are in qualitative agreement with Kwak et al. [21] who observed negligible wet NO oxidation conversion for Cu:Al < 0.3, on Cu-SSZ-13 , while higher Cu:Al ratios showed increasing NO conversion during wet NO oxidation (10% H_2O, at 573 K). The similar apparent activation energy and apparent reaction orders observed here for catalysts active for NO oxidation, suggest a similar NO oxidation mechanism. Our observed increase in NO oxidation rates with Cu:Al ratio can thus be attributed to an increase in the number of active sites per gram Cu-SSZ-13

Table 3.1 Summary of dry NO oxidation kinetics, *ex-situ* XANES fitting under ambient condition and *in-situ* XANES fitting under NO oxidation, over Cu-SSZ13 catalysts with varying Cu:Al ratios.

Cu:Al ratio	E_a / kJ mol^{-1}	NO^a Order	$NO_2{}^a$ Order	$O_2{}^a$ Order	$R_{fwd}{}^b$ (10^{-4} mol NO .mol Cu^{-1} s^{-1})	Linear combination *ex-situ* XANES fitting under ambient conditions		Linear combination *in-situ* XANES fitting[f,g]	
						% $[Cu(H_2O)_6](II)$ ions[d]	% Cu_xO_y[e]	% dehydrated isolated Cu(II) ions[e]	% Cu_xO_y[f]
0	N.M.	N.M.	N.M.	N.M.	0	N.M.	N.M.	N.M.	N.M.
0.02	N.M.[c]	N.M.	N.M.	N.M.	0	Reference	0	Reference	0
0.04	N.M.	N.M.	N.M.	N.M.	0	100 ± 5	0 ± 5	100 ± 5	0 ± 5
0.09	N.M.	N.M.	N.M.	N.M.	0	100 ± 5	0 ± 5	100 ± 5	0 ± 5
0.16	N.M.	N.M.	N.M.	N.M.	0	100 ± 5	0 ± 5	100 ± 5	0 ± 5
0.2	N.M.	N.M.	N.M.	N.M.	0	100 ± 5	0 ± 5	100 ± 5	0 ± 5
0.31	45	1.5	-0.8	0.9	0.6	79 ± 5	21 ± 5	65 ± 5	24 ± 5
0.35	51	1.4	-0.7	0.8	1.4	N.M.	N.M.	72 ± 5	28 ± 5
0.39	53	1.5	-0.8	0.8	1.5	N.M.	N.M.	70 ± 5	30 ± 5
1.6	55	1.6	-0.9	0.9	1.7	48 ± 5	52 ± 5	61 ± 5	39 ± 5

a: Measured at 573 K

b: Rate per mole Cu is defined as mol NO . mol Cu^{-1} .s^{-1} and evaluated at 300 ppm NO, 150 ppm NO_2, 10% O_2 and 550 K

c:Cu-SSZ13 catalysts with Cu:Al atomic ratio < 0.2 did not display measurable NO oxidation rate so data are not reported

d: Hydrated $Cu(NO_3)_2$ was used to generate a $[Cu(H_2O)_6]^{(II)}$ reference.

e: Bulk Cu(II)O was used as a reference for Cu_xO_y species in Cu-SSZ13.

f:Feed Conditions: 300 ppm NO, 150 ppm NO_2, 10% O_2 and 573 K.

g:Contribution from dehydrated isolated Cu(I) and $[Cu(H_2O)_6]^{II}$ ions was negligible

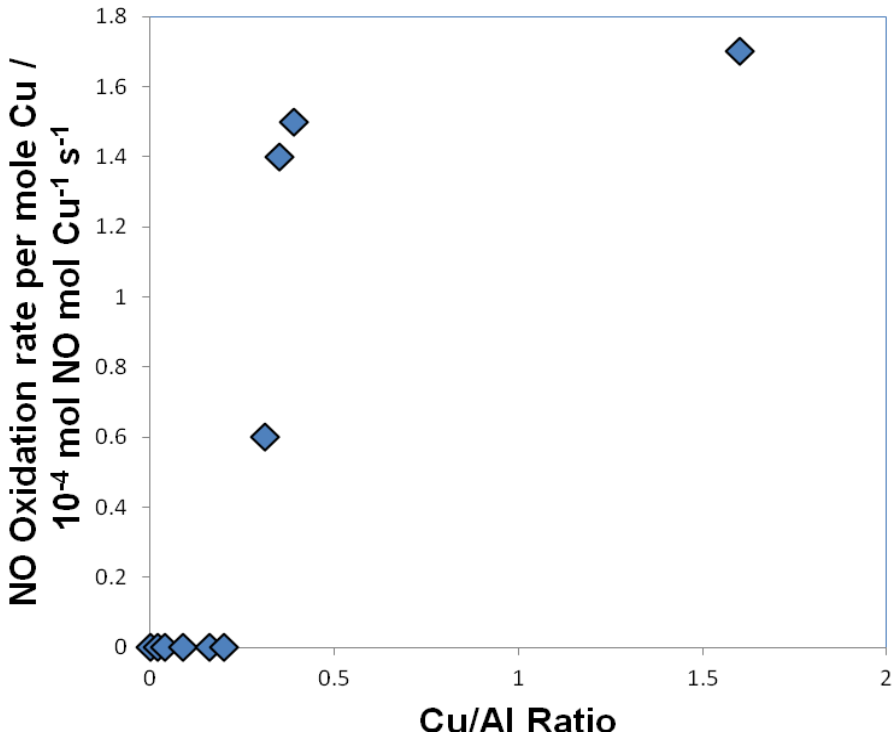

Figure 3.2 Variation of the rate of NO oxidation (10^{-4} mol NO mol $Cu^{-1}.s^{-1}$) with Cu:Al ratio, on Cu-SSZ13. Feed Conditions: 320 ppm NO, 148 ppm NO_2, 10% O_2 and 550 K.

3.4.2 Ex-Situ XANES and UV-Vis-NIR Spectroscopy on Hydrated Cu-SSZ-13 Catalysts under Ambient Conditions

Due to the possibility of multiple Cu ion configurations as probed by NO oxidation kinetics, the state of Cu ions in hydrated Cu-SSZ-13 was investigated using *ex-situ* Cu- K edge XANES and UV-Vis-NIR spectroscopy to obtain complementary information. Traditionally, XANES provides information about the oxidation state of the element of interest. XANES, however, can also probe the local Cu environment. In addition, XANES was measured in the transmission mode which enabled quantification of different Cu ion configurations via linear combination XANES fitting by using references for the candidate states. Based on previous results obtained by McEwen et al. [24], hexa-aquo-Cu ions ($[Cu(H_2O)_6]^{II}$) and bulk Cu(II)O were chosen as appropriate references for hydrated isolated Cu ions in Cu-SSZ-13 and clustered Cu ions (Cu_xO_y species), another

possible configuration of Cu ions in Cu-SSZ-13, respectively. Figure B.3 compares the *ex-situ* XANES spectra (under ambient conditions) of hexa-aquo-Cu ions ($[Cu(H_2O)_6]^{II}$) and bulk Cu(II)O. The XANES spectrum of bulk Cu(II)O has a pre-edge feature at 8,987 eV and is accompanied by a drop in the white line intensity compared to the XANES spectrum of hexa-aquo-Cu ions. The pre-edge feature for bulk Cu(II)O was assigned to the 1s to 4p transition for Cu(II). The edge position for both these Cu ion configurations was 8,995 eV, which indicated a formal oxidation state of +2 for both configurations. Thus, based on different pre-edge features, the XANES signatures for these Cu ions were concluded to be different even though the formal oxidation state was +2 in both configurations.

The *ex-situ* XANES spectra of some of the hydrated Cu-SSZ-13 catalysts under ambient conditions are shown in Figure 3.3. Before the XANES experiments were conducted, the catalysts were hydrated by exposing them to ambient conditions. The spectra of hexa-aquo Cu(II) ions in solution ($[Cu(H_2O)_6]^{II}$) and bulk Cu(II)O are also added as the references used for the linear combination fitting of the XANES spectra for different Cu-SSZ-13 catalysts. The linear combination fitting results revealed a major fraction of hydrated isolated Cu(II) ions within SSZ-13 for Cu:Al ratio below 0.2 (Table 3.1). The XANES region of catalysts with Cu:Al ratio greater than 0.2 exhibited a decrease in the white line intensity and a corresponding appearance of the pre-edge feature at 8,987 eV, consistent with the emergence of Cu_xO_y species in Cu-SSZ-13. This observation quantitatively manifested itself in an increasing percentage of Cu_xO_y species per total mole Cu for increasing Cu:Al ratio above 0.2 (Table 3.1). The corresponding magnitude of the Fourier Transform Extended X-Ray Absorption Fine Structure (FT-EXAFS) is shown in Figure B.4. For each catalyst under ambient conditions (except Cu:Al ratio = 1.6), the first shell Cu – O coordination was evaluated as ~ 4 at a radial distance of 1.94 Å. The measurement of the first shell Cu – O coordination number as 4 instead of 6 (for a hexa –aquo Cu (II) type of ion) was a consequence of the Jahn-Teller distortion around the d^9 Cu(II) ion [24]. Contribution from higher shells was undetectable. This indicated

that under ambient conditions, all Cu ions, irrespective of the configuration, were in +2 formal oxidation states, consistent with the XANES edge position of 8,995 eV.

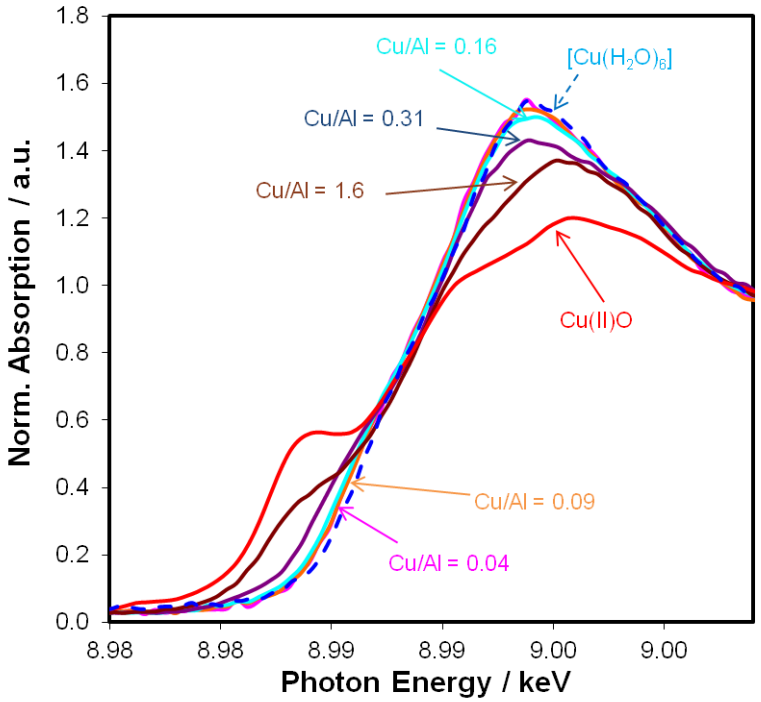

Figure 3.3 *Ex-situ* XANES spectra of various hydrated Cu-SSZ13 catalysts with Cu:Al ranging from 0.04 to 1.6, measured under ambient conditions. XANES of Bulk Cu(II)O and $[Cu(H_2O)_6]^{II}$ measured under ambient conditions, have been added as references to do the linear combination XANES fitting.

From the previous set of experiments, the percentage of hydrated isolated Cu(II) ions per total mole of Cu was quantified for different Cu:Al ratios. To obtain equivalent information about the variation of hydrated isolated Cu(II) ions per gram of catalyst with Cu:Al ratio, UV-Vis-NIR spectroscopy was used on the same set of hydrated Cu-SSZ-13 samples. A Cu(II) *d-d* transition peak centered at ~12500 cm^{-1} was used as a spectroscopic signature of hydrated isolated Cu(II) ions within Cu-SSZ-13 [120]. Additionally, there is a possibility of charge transfer (C.T.) from O (from water) to Cu(II), which is observed at ~ 45000 cm^{-1} for $[Cu(H_2O)_6]^{II}$ ions [15, 120]. The *ex-situ* UV-Vis-NIR spectra of hydrated Cu-SSZ-13 catalysts are shown in Figure 3.4.

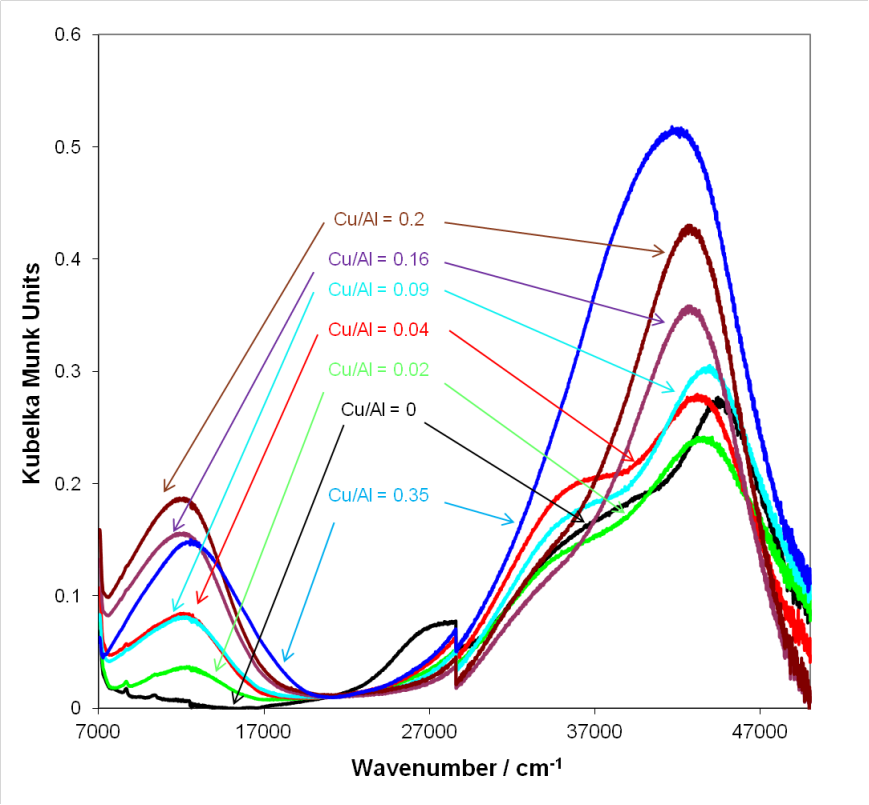

Figure 3.4 *Ex-situ* UV-Vis-NIR spectra of series of hydrated Cu-SSZ13 catalysts with Cu:Al ratio ranging from 0 to 0.35. The peak centered at 12500 cm^{-1} is the contribution from the *d-d* transition of hydrated isolated Cu(II) ions. The peaks between 30000 cm^{-1} and 50000 cm^{-1} have been assigned to a combination of oxygen to Cu(II) charge transfer and a bare zeolite absorption edge.

A reference spectrum of H-SSZ-13 sample was also measured and included. The UV-Vis NIR spectrum of H-SSZ-13 was characterized by an absence of *d-d* transition intensity at ~ 12500 cm^{-1}, although it was characterized by a zeolite absorption edge above 30000 cm^{-1} [121].

Addition of Cu ions as low as 0.3 wt. % (Cu:Al ratio = 0.02) resulted in a finite, non-zero *d-d* transition intensity centered at 12500 cm^{-1}. Quantification of the *d-d* transition peak intensity (Kubelka Munk, K.M. units) for Cu-SSZ-13 catalysts with different Cu:Al ratios revealed a linear increase in the *d-d* intensity with an increase in the Cu:Al ratio up to 0.2 and subsequently, the *d-d* transition intensity saturated, as shown in Figure 3.5.

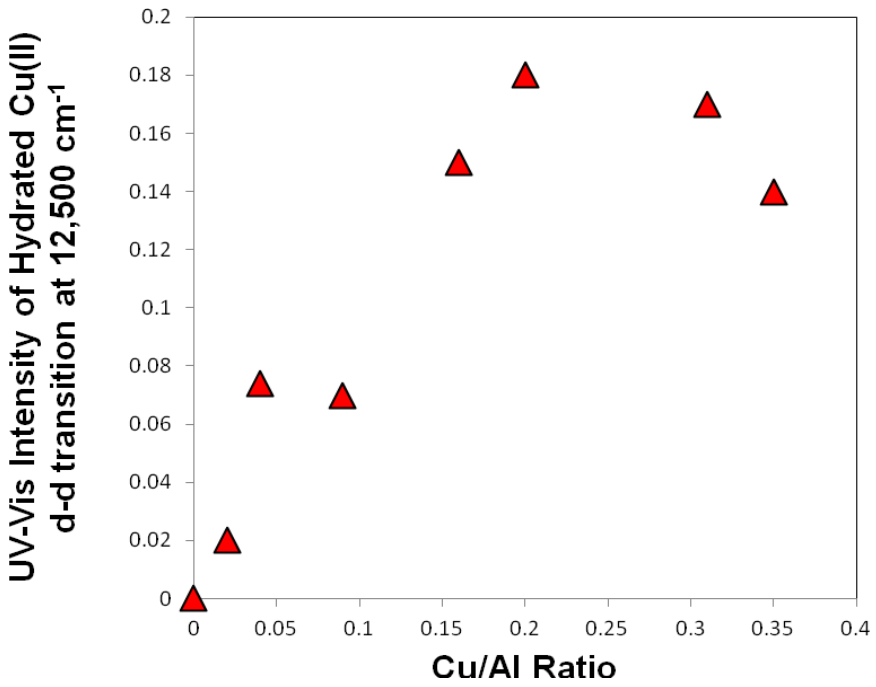

Figure 3.5 Quantification of the *d-d* transition peak intensity centered at 12500 cm^{-1} and obtained from the *ex-situ* UV-Vis-NIR spectra of hydrated Cu-SSZ-13 catalysts under ambient conditions.

This implied that the relative population of hydrated isolated Cu(II) ions per gram catalyst had saturated near Cu:Al ratio = 0.2 and excess Cu ions were deposited in a different configuration. In agreement with the XANES analysis, these excess Cu(II) ions manifested in Cu_xO_y species ($x \geq 2$, $y \geq 1$) under ambient conditions.

3.4.3 XANES analysis of Cu-SSZ-13 Catalysts under *In*-Situ NO Oxidation Condition

To understand the site requirements of dry NO oxidation on Cu-SSZ-13 catalysts, XANES spectra for a series of Cu-SSZ-13 catalysts were measured during *in-situ* dry NO oxidation (300 ppm NO, 150 ppm NO_2, 10% O_2 and 573 K). Once again, the ability of XANES to identify and quantify the local environment of Cu ions was used. The spectra were fitted by a linear combination XANES fit using four different references which signified possible Cu ion configurations under NO oxidation. The reference compounds were hexa-aquo-Cu(II) ions ($[Cu(H_2O)_6]^{II}$), bulk copper oxide (Cu(II)O), dehydrated

isolated Cu(II) ions within SSZ-13 and dehydrated isolated Cu(I) ions within SSZ-13. The corresponding XANES spectra for the references are shown in Figure B.5. The references for the dehydrated isolated Cu(I)/isolated Cu(II) ion within SSZ-13 were generated by treating a Cu-SSZ-13 catalyst (Cu:Al ratio = 0.02) to 1000 ppm NO + 1000 ppm NH_3 at 473 K, and 10 % O_2 at 473 K respectively. The oxidation state of Cu ions was assigned on the basis of fitting the corresponding FT-EXAFS respectively (Figure B.6). The catalyst treated in 1000 ppm NO + 1000 ppm NH_3 at 473 K had a first shell Cu – O coordination number of ~2 at 1.85 Å, consistent with the previous assignment of such species to have a formal oxidation state of +1 [25]. For a similar analysis, moreover, under 10% O_2 at 473 K, the Cu – O coordination number was ~ 4 at 1.96 Å, consistent with a Cu ion formal oxidation state of +2 [25]. Also, for these references, there was no evidence of clustering of Cu ions since the second shell contribution was due to Cu – O – Si type of coordination (Table B.2), consistent with the EXAFS peak assignment by McEwen et al. [24]. This was expected from a Cu-SSZ-13 catalyst with a Cu:Al ratio of 0.02 (Cu weight % = 0.31%) [16, 18].

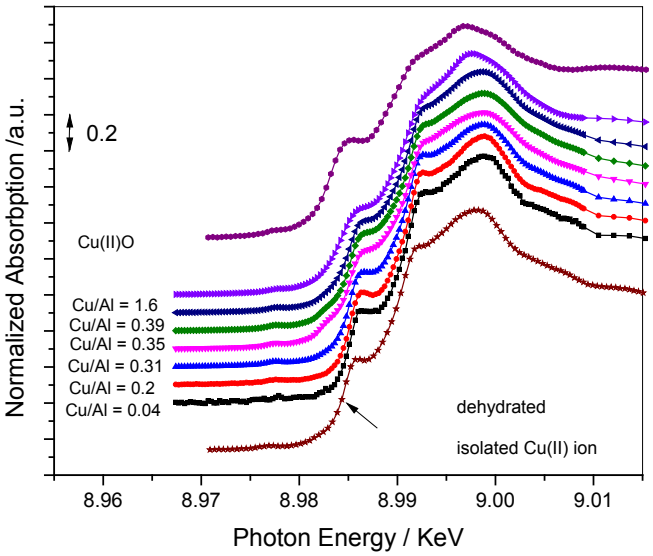

Figure 3.6 *In-situ* XANES spectra, under NO oxidation conditions, of a series of Cu-SSZ13 catalysts with Cu:Al ratio varying from 0.02 to 1.6. Feed Conditions: 300 ppm NO, 150 ppm NO_2, 10% O_2 and 573 K. Bulk Cu(II)O and dehydrated isolated Cu(II) references are included for comparison.

The XANES spectra during *in situ* NO oxidation (300 ppm NO, 150 ppm NO_2, 10% O_2, and 573 K) for the series of Cu-SSZ-13 catalysts are displayed in Figure 3.6. The linear combination fitting results are shown in Table 3.1. For all catalysts, under *in-situ* NO oxidation the contribution due to hydrated isolated Cu^{2+} ions and dehydrated Cu^{1+} ions was negligible. Also, none of the Cu-SSZ-13 XANES spectra could be fitted with a Cu foil XANES spectrum, which showed that metallic Cu did not participate in the catalysis. It was also observed that all Cu-SSZ-13 catalysts with Cu:Al ratio < 0.2 contained a majority of dehydrated isolated Cu^{2+} ions per total mole of Cu under dry NO oxidation, which were shown to be inactive for NO oxidation from separate PFR experiments (Figure 3.2).

Above Cu:Al ratio = 0.2, an increasing contribution of Cu_xO_y species was observed which saturated to a value of ~ 40 % mol Cu_xO_y (mol Cu)$^{-1}$ for the Cu-SSZ-13 catalyst with Cu:Al ratio = 1.6. A linear correlation was obtained between the rate of NO oxidation per mole Cu and the percentage mol Cu_xO_y (mol Cu)$^{-1}$ (Figure 3.7) which indicated that Cu_xO_y species were the active Cu ion configuration for NO oxidation. We note that the slope of the line in Figure 3.7 has units of 10^{-4} mol NO (mole Cu_xO_y)$^{-1}s^{-1}$ indicating that the rate is driven by the amount of Cu_xO_y as expected. The absence of measurable NO oxidation rate at 0% Cu_xO_y shown in Figure 3.7 leads us to conclude that dehydrated isolated Cu(II) ions do not participate in dry NO oxidation (300 ppm NO, 150 ppm NO_2 and 10% O_2).

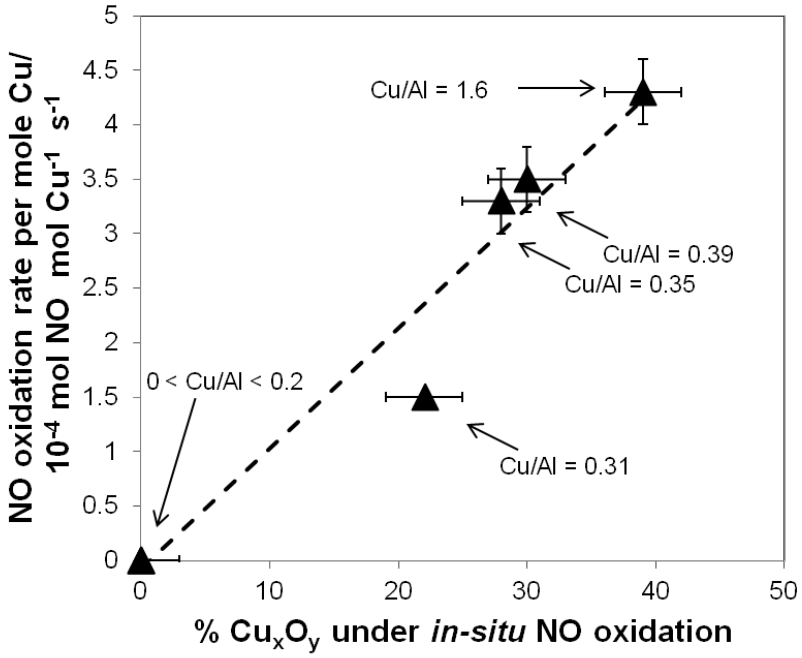

Figure 3.7 Correlation in the rate of NO oxidation (per mole Cu), evaluated at 573 K and the % Cu_xO_y to the total moles of Cu as quantified from *in-situ* XANES under NO oxidation conditions. Feed conditions: 300 ppm NO, 150 ppm NO_2, 10% O_2 and 573 K. All Cu-SSZ13 catalysts with dehydrated isolated Cu(II) ions are included in the origin.

3.4.4 Computational Cu Site Models

The experimental results show that the dry NO oxidation rates do not linearly correlate with total Cu content; thus, multiple Cu species are present in the zeolite. From XANES analysis under *in-situ* NO oxidation conditions (Figure 3.6), dehydrated isolated Cu(II) ions and Cu_xO_y species were identified as two possible Cu ion configurations. Based on the XANES, UV-visible spectroscopy, and wide observation in other zeolites, the CuO_yCu^{II} (y =1, 2) dimers are plausible candidates for the Cu_xO_y species responsible for NO oxidation. We explore that possibility using DFT here.

Both isolated Cu(II) and $Cu_2O_y^{II}$ configurations require two anionic Al-substituted tetrahedral (T-) sites to compensate their charge. To illustrate the types and density of Al pairs available to accommodate isolated Cu(II) or $Cu_2O_y^{II}$ species, we computed the

expected distribution of these pairs within SSZ-13 using an approach similar to that reported previously [32]. This and all zeolites are composed of –O–T–O–T–O– linkages, in which each T-site (Si or Al) is four-fold coordinated to oxygen, and each oxygen then bridges to a different neighbor T-site. Here, we assume that the H^+:Al ratio for the zeolite is equal to 1, which meant that all the Al atoms appear in the zeolite framework and contribute to Bronsted acidity. In real zeolite materials, there might be a possibility of the number of framework Al atoms (Al_f) being less than the total number of Al atoms (Al) and H^+:Al_f < 1 [122]. We term Al_f–O–Al_f first-nearest neighbor (1NN), Al_f–O–Si–O–Al_f second-nearest neighbor (2NN), and so on. For a particular Si:Al ratio, we constructed a 4 × 4 × 4 super cell, seeded with Al up to that Si:Al ratio obeying the Löwenstein's rule prohibition against 1NN Al, and then conducted random Si-Al swaps that retained this rule. We counted the number of Al-Al pairs as a function of Al-Al spatial separation and normalized by the total number of T-site pairs at a given distance. The resultant radial probability distribution identifies the probability of a given Al T-site to have a neighbor Al T-site at a given distance. The result for Si:Al ratio = 5:1 is shown in Figure 3.8.

A first peak at 4.4 Å corresponded to 2NN Al in 4-rings; the next grouping near 5.5 Å corresponded to 2NN Al in 6- and 8-rings. Third-nearest-neighbor (3NN) 6- and 8-ring Al pairs occurred near 6.5 and 7.5 Å, respectively, and fourth-nearest-neighbor (4NN) at 8 Å. The available pairs thus spanned a range of distances and occurred with nearly the same density at this Si:Al ratio as shown in Figure 3.8. At 8.06 Å, the longest Al pair possible was in the 8-member cage. An Al atom was expected to have 4.87 potential partners, and the probability that it had at least one partner was 99.8%.

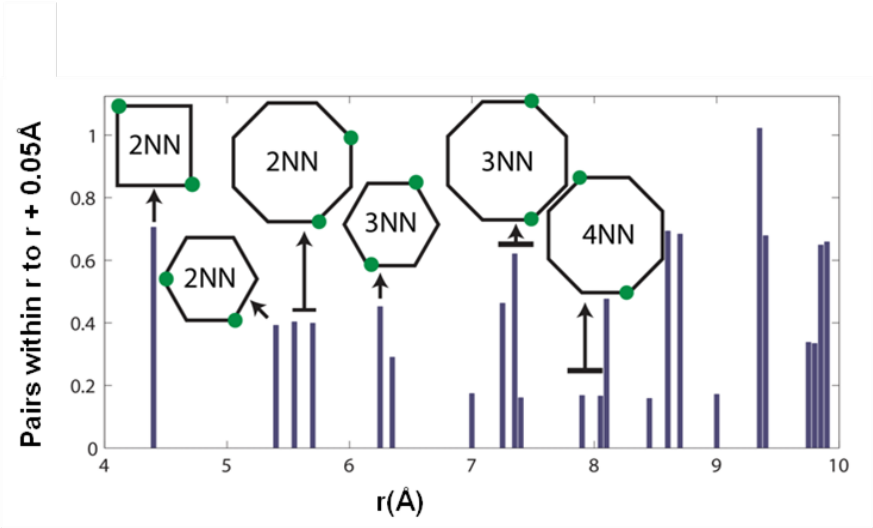

Figure 3.8 Radial distribution of Al-Al pair sites versus. Al-Al separation in SSZ-13 at Si:Al = 5:1. Al are distributed randomly obeying Löwenstein's rule and densities accumulated in 0.05 Å bins.

These calculations were repeated for various Si:Al ratios on SSZ-13. In particular, for each Si:Al ratio, an Al_f pair in the 6 ring was counted as a surrogate for one dehydrated isolated Cu(II) ion. Figure 3.9 shows the maximum amount of dehydrated isolated Cu(II) ion in the six member ring, per Al, calculated for various silicon to framework aluminum (Si:Al) ratios.

We previously showed that Cu(I) charge-compensated by a single Al T-site (ZCu) preferred 6-member ring sites in SSZ-13 [24]. The first column of Table 3.2 reports the relative periodic GGA energies of dehydrated, isolated Cu^{2+} (Z_2Cu) ions in the various ring locations illustrated in Figure 3.8. Energies are referenced to a dehydrated isolated Cu(II) in an 8 member cage with 4NN Al and were determined either in three 1 × 1 × 1 supercell models (Figure 3.1a) that contained 2NN, 3NN, or 4NN Al sites in an 8-ring or in a doubled 2 × 1 × 1 super cell model that simultaneously presents 4-, 6-, and 8-ring sites (Figure B.1 c, d).

Table 3.2 GGA-computed relative energies (eV) of Cu ions and dimers vs. Al-Al pair placement.

	Isolated Cu(II) energy /eV	$CuOCu^{II}$ energy/eV	CuO_2Cu^{II} energy/ eV
4-ring – 2NN	–0.38	0.68	0.65
6-ring – 3NN	–1.51	0.44	0.51
8-ring – 4NN	0	0	0
8-ring – 3NN	0.23	0.46	0.42
8-ring – 2NN	–0.25	0.76	0.88

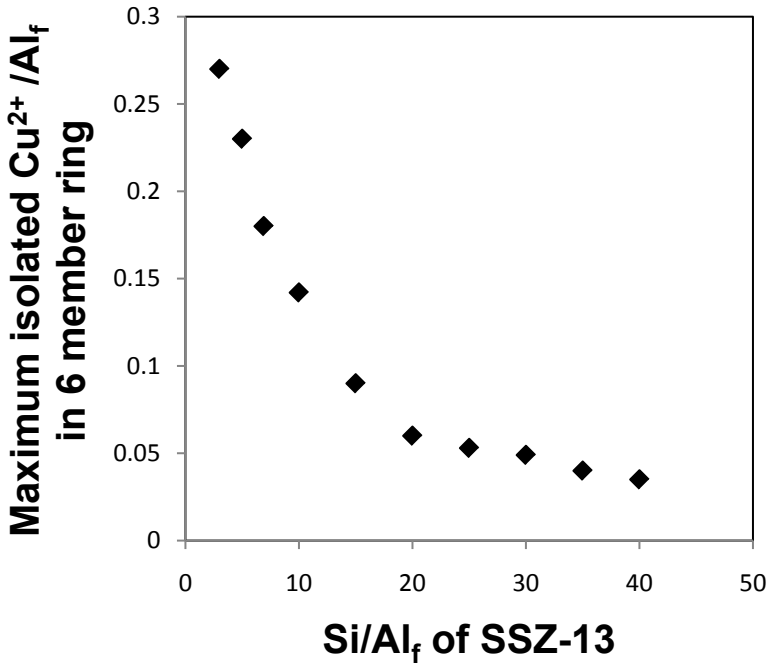

Figure 3.9 The maximum isolated Cu(II) ion to Al ratio that can be accommodated in the 6 member ring of SSZ-13, as a function of Si:Al ratio.

Results from these two structural models differed by less than 0.1 eV, as shown in Table B.4. Geometry optimizations (Figure B.7) showed that a dehydrated isolated Cu(II) ion maintained 4-fold oxygen coordination in the smaller 4- and 6-ring sites but attain only 3-fold coordination in the larger 2NN and 4NN 8-ring sites and 2-fold coordinated in 3NN 8-ring sites. Based on the relative energies in Table 3.2, a dehydrated isolated Cu(II) ion has a strong energetic preference for the 6-ring sites over 4 and 8-ring sites in SSZ-13.

Motivated by the evidence for Cu-O_y-Cu (y = 1, 2) clusters in ZSM-5[91, 123-125], MOR[91], BEA[126], and Y [127] zeolites, we next calculated the structures and relative stabilities of these ZCuO_yCuZ aggregates within our SSZ-13 supercell models. Both y = 1 and y = 2 clusters exhibited singlet and triplet spin states whose relative stability depended on coordination environment [20, 21]. In all cases we optimized both states and report the lower energy results. Figure 3.10a shows triplet ZCuOCuZ optimized in the 4NN 8-ring site. Cu ions adopted a 2-fold coordination to the zeolite lattice and were nearly symmetrically bridged by the central O at Cu–O distance of about 1.75 Å. Figure B.8 and Figure B.9 compare optimized Cu-O-Cu structures computed at the other Al pair sites. The Cu ions in the larger 6- and 8-rings retained two-fold coordination to the zeolite lattice by adjusting the Cu–O–Cu angle from 107-132°. The ZCuOCuZ configuration was too large to be accommodated entirely within a 4-ring; the optimized cluster relaxed to retain two-fold coordination involving O of connected rings. Table 3.2 compares relative energies of ZCuOCuZ referenced to the triplet 4NN 8-ring site. The Cu-O-Cu dimer preferred coordination in an 8-ring over a 4- or 6-ring by 0.44 and 0.68 eV, respectively (Table 3.2). Further, the Cu dimer was more easily accommodated in 4NN Al_f sites than 3NN or 2NN in the 8-ring by 0.46 and 0.76 eV, respectively.

CuO_2Cu^{II} is known to exhibit a coordination chemistry in which the O_2 can end-on bridge the two Cu (μ-1,2-O_2), side-on chelate the two (μ-η^2:η^2-O_2), or dissociate into two oxo bridges (μ-O,μ-O)[89, 90, 92-94] . We found examples of all of these structures during optimizations of the various Al pair models (Figure B.10 & Figure B.11). Nearer Al sites preferred the μ-1,2-O_2 structures while farther sites, like the 8-ring 4NN site shown in Figure 3.10b, preferred singlet μ-η^2:η^2-O_2. Cu again in general preferred to associate with two lattice O near the Al sites in addition to the bridging O_2.

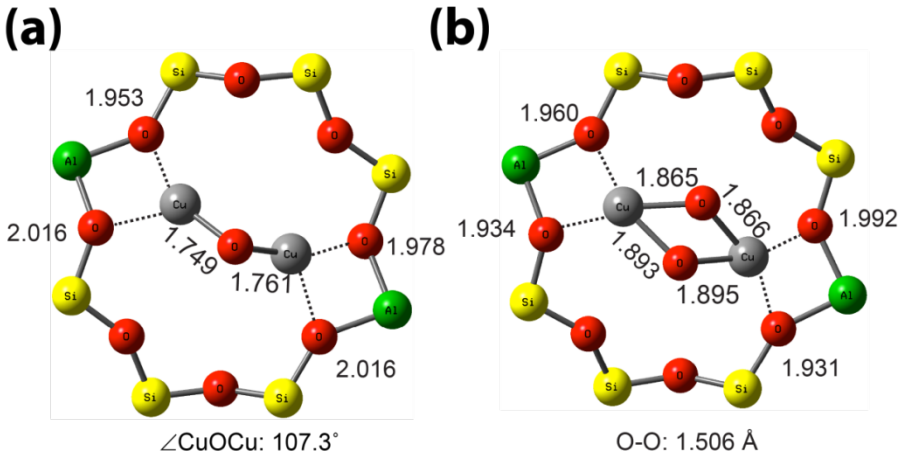

Figure 3.10 The optimized periodic structure of atomic and diatomic oxygen adsorbed in the 8-ring of SSZ-13 of (a) ZCuOCuZ with fourth-nearest-neighbor (4NN) Al pairs and (b) μ-η^2-η^2-Cu_2O_2 with 4NN Al pairs. Cu–O distances indicated in Å. Yellow red, grey, and green spheres are Si, O, Cu, and Al, respectively.

Table 3.2 compares the relative energies of these Cu-O_2-Cu^{II} dimers vs. Al siting; as with the Cu-O-Cu^{II} dimers, the Cu-O_2-Cu^{II} dimers preferred 8-ring sites over 4- and 6-rings by 0.51 and 0.65 eV, respectively, and preferred the 4NN Al sites in 8-rings by 0.42-0.88 eV, respectively.

We can use these results in combination with the redox reaction steps of Scheme 3.1 and Scheme 3.2 to compare the energies of O_2 adsorption and successive NO oxidation on ZCu, Z_2Cu in a 6-ring [24], and Cu dimers in an 8-ring. For the latter we considered 2NN, 3NN, and 4NN Al T-sites, to examine sensitivity to the proximity of these coordination sites, under NO oxidation. We applied a B3LYP cluster correction to the GGA energies to improve agreement with the known overall NO oxidation energy. In some cases, B3LYP reverses the order of singlet and triplet states; we report free energies using the lowest-energy B3LYP results in Figure 3.11.

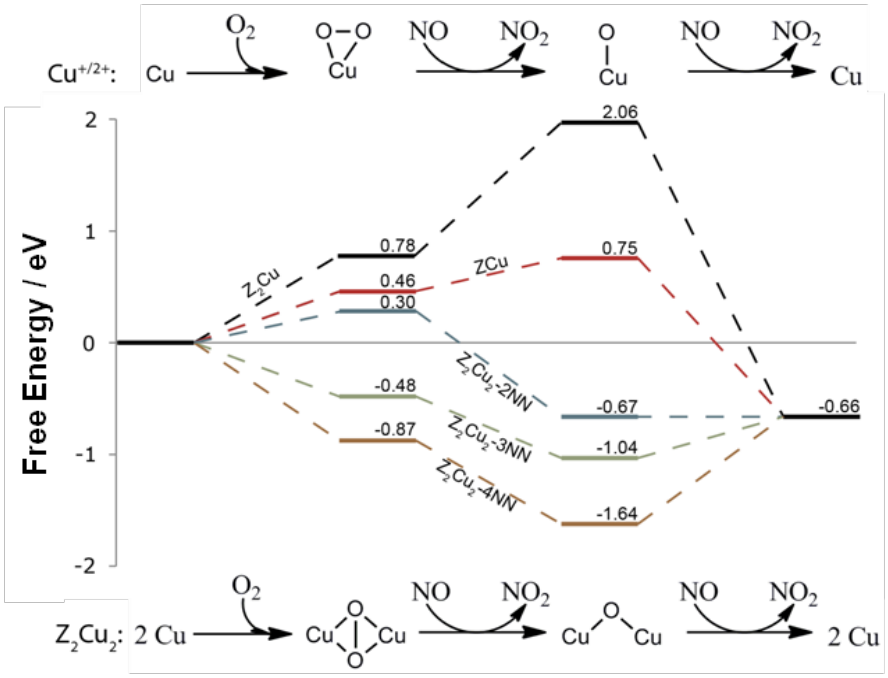

Figure 3.11 B3LYP-calculated relative free energies of O_2 adsorption and sequential reduction on candidate isolated and Cu pair sites. Gibbs free energies are calculated at 500 K, 300 ppm NO, 150 ppm NO_2 and 10% O_2.

We found that O_2 is essentially unbound on Z_2Cu (structures in Figure B.12). Oxygen abstraction from Z_2CuO_2 created a highly oxidized and high energy Z_2CuO intermediate of 2.06 eV in free energy, unlikely to have any role in catalysis. Our calculation [24] and others [84, 85] concluded that an isolated ZCu binds O_2 preferentially as a side-on peroxide (η^2-O_2). The abstraction of O by NO formed a ZCuO intermediate with free energy cost of 0.29 eV. In contrast, O_2 adsorption was increasingly more favorable on 8-ring Cu pairs in 2NN to 3NN to 4NN Al sites (Figure 3.11 and Table B.5). The abstraction of O by NO to form ZCuOCuZ is uniformly downhill in Gibbs free energy by 0.6-1.1 eV. A second O abstraction to complete the catalytic cycle was either flat or uphill in free energy depending on the Al sites.

This free energy analysis of O_2 dissociation intermediates in NO oxidation is consistent with the observed apparent reaction orders and showed that dehydrated isolated Cu(II)

ions are unlikely to participate in this catalysis; dehydrated isolated Cu(I) ions could have a role, but Cu dimers similar to those studied in the context of Cu-ZSM-5 catalysis are likely active sites for NO oxidation. Mathematical analysis of the reaction mechanism on the Cu pair sites (Appendix B, Pg. 147) showed the mechanism to be consistent with the measured reaction orders with respect to NO, NO_2, and O_2. Further, the relationship between the orders and the surface coverage of the kinetically relevant intermediates was obtained by taking the derivative of $\ln(-r_{NO})$ with respect to $\ln(C_i)$ (where C_i is the concentration of either NO, NO_2, or O_2). Based on this analysis, the surface coverage of O^* was found to be 0.6, consistent with the stability of this intermediate (in Figure 3.11). In comparison, the surface coverages of O_2^* , * , and NO_2^* were 0.1, 0.1 and 0.2 respectively.

From Figure 3.2, Cu at Cu:Al ratio > 0.5 contributes to the NO oxidation rate per mole Cu and may reflect the formation of larger Cu aggregates (Cu_xO_y species, x > 2, y > 2). It is difficult to confirm or refute the presence of larger clusters based on a DFT analysis alone; metal oxide clusters can exhibit considerable structural variability and their stability is a strong function of the reaction environment [128-130]. As a simple test of the plausibility of larger Cu_xO_y clusters within SSZ-13, we selected structures for clusters with $x = y = 3 - 9$ from previous DFT optimizations of gas-phase clusters [130] and computed the GGA energy to "grow" such clusters within the 1 × 1 × 1 supercell according to:

$$Z_2H_2 + x\ CuO\ (s) \rightarrow Z_2Cu_xO_x + H_2 \qquad \text{Scheme 3.3}$$

These formation energies were referenced to bulk Cu(II)O, which contains chains of Cu(II) square-planar coordinated by O ions (Figure B.13). Model Cu_xO_x clusters in SSZ-13 were created by inserting the gas-phase structures into the large cage and relaxing; results are shown in Figure B.14, Figure B.15, and Figure B.16.

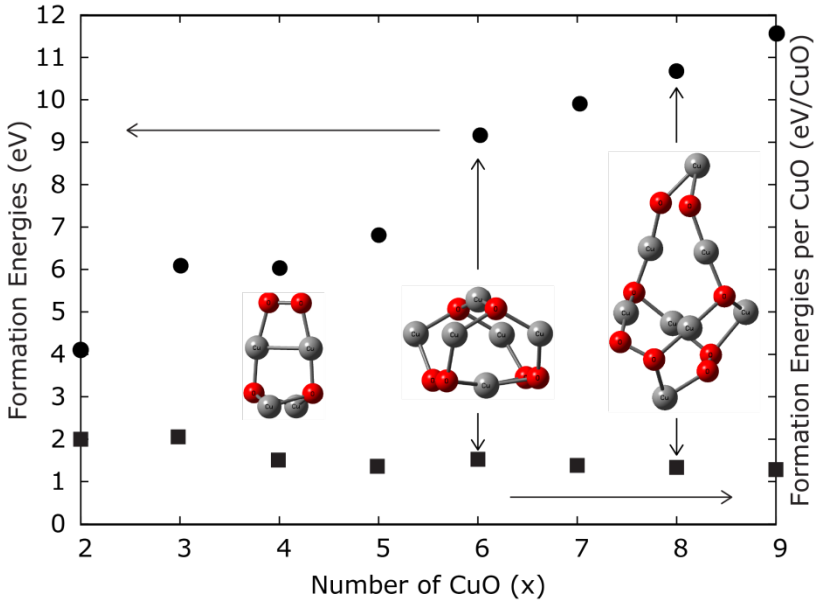

Figure 3.12 GGA-computed Cu_xO_x formation energies in an SSZ-13 cage (left axis) and formation energy per formula unit (right axis).

Clusters up to $x = 8$ fit within a single 8 member ring cage; by $x = 9$ the cluster percolates through a 6-ring window to an adjacent cage. Figure 3.12 shows that formation energies as defined here are uniformly positive relative to bulk Cu(II)O and increase nearly monotonically with cluster size. Formation energies per Cu(II)O formula unit are thus nearly constant. This analysis showed that Cu_xO_x ($x \leq 8$) clusters fit into the 8 member ring cage and were able to grow once nucleated as a Cu dimer.

3.5 Discussion

3.5.1 The Active Cu Ion Configuration for Dry NO Oxidation on Cu-SSZ-13

The change in NO oxidation rate (per mole Cu) from zero to increasing values at Cu:Al ratio of 0.2 on Cu-SSZ-13 catalysts (Si:Al = 4.5) indicated the presence of at least two different Cu(II) ion configurations within the Cu-SSZ-13 catalyst. The difference in Cu ion configuration can be a consequence of either a different location of isolated Cu(II) ions (8 ring versus the 6 ring of SSZ-13) or the presence of clustered Cu ions (Cu_xO_y) or both. Kwak et al. [16] attributed a Cu(II) to Cu(I) H_2-TPR reduction peak (maximum at

513 K) for Cu:Al ratio > 0.2 in Cu-SSZ-13 (Si:Al ratio = 6) to isolated Cu(II) ions in the 8 member cage. In a subsequent contribution, Gao et al.[18] utilized *ex-situ* Electron Paramagnetic Resonance (EPR) to show that hydrated Cu-SSZ-13 catalysts with a Cu:Al ratio less than 0.5 were composed of hydrated isolated Cu(II) ions quantitatively. Thus, they claimed that the dominant Cu ion configuration was isolated Cu(II) ions near the 6 member ring for Cu:Al ratio up to 0.2, and in the 8 ring for Cu:Al ratio above 0.2. The presence of Cu_xO_y species was also excluded by Giordanino et al. [120] by using *in-situ* UV-Vis-NIR spectroscopy under NO oxidation. In the catalysts used in our study, however, *ex-situ* XANES under ambient conditions showed a dominant fraction of hydrated isolated Cu(II) ions below Cu:Al = 0.2, while an increasing fraction of Cu_xO_y ($x \geq 2$, $y \geq 1$) species was observed above Cu:Al ratio = 0.2. The Cu edge position was 8,995 eV and the first shell Cu – O coordination number was ~ 4 which meant that all the Cu species had a formal oxidation state of +2. Even though the second shell coordination (Cu – O – Cu) from FT – EXAFS was undetected within experimental error (Figure B.4), our DFT calculations showed that Cu pairs are stable, therefore Cu_xO_y species were concluded to be highly dispersed under ambient conditions. Similar EXAFS results under NO oxidation were obtained (Figure B.4 for EXAFS under ambient conditions and Figure B.17 for EXAFS during dry NO oxidation). Further evidence of the presence of dispersed Cu_xO_y species above Cu:Al =0.2, was provided by *in-situ* XANES under NO oxidation. We find a linear correlation between dry NO oxidation rates per mole Cu and the percentage of Cu present as Cu_xO_y ($x \geq 2$, $y \geq 1$) species. This observation shows that the active sites for dry NO oxidation were formed in proportion to the percentage of Cu_xO_y species (per mole Cu), thus satisfying the Koros – Nowak test [70] and certifying the rate measurement to be free from internal and external mass transport limitations. With this level of experiment, however, we were unable to state the exact size of the active copper oxide cluster required for NO oxidation, because of unavailability of appropriate XANES references of Cu_xO_y clusters with $2 \leq x, y \leq 8$, which would be used for linear combination fitting of spectra obtained under in-situ conditions.

The linear correlation between NO oxidation rate (per mole Cu) and the % of Cu_xO_y species (Figure 3.7), without specifying a particular size or type of Cu_xO_y cluster, implies that either the NO oxidation rate is independent of the Cu_xO_y cluster or the current catalyst synthesis strategy produces the same distribution of Cu_xO_y cluster types in all catalysts active for NO oxidation. Figure 3.11 argues that the rate depends even on the orientation of a cluster within a pore. Thus, Figure 3.7 cannot be used as a calibration curve for backing out the absolute number of Cu_xO_y species in Cu-SSZ-13 based on a measured NO oxidation rate. The data presented in Figure 3.7 confirm the local nature of the active site for NO oxidation, i.e. the requirement of a local Cu-O_y-Cu bond during NO oxidation catalysis over Cu-SSZ-13. The DFT results, moreover, demonstrated that the formation of Cu_xO_x ($x \leq 8$) clusters is plausible inside the SSZ-13 cage structure.

The integrated experimental and computational results indicate that dry NO oxidation would be favored over a local Cu – O_y – Cu bond and would be unfavorable on a dehydrated isolated Cu(II) ion, within Cu-SSZ-13. Hence, bulk Cu(II)O, which was also characterized by local Cu – O_y – Cu bonds, was used as an appropriate XANES reference for quantifying the concentration of clustered Cu(II) ions in Cu-SSZ-13. From DFT calculations, moreover, the free energy analysis showed that the Cu_2O_y species were the active sites for NO oxidation and the most energetically favorable location of these Cu_2O_y species was in the 8 member ring of SSZ-13.

3.5.2 On the Dominant Cu Ion Configuration Below Cu:Al Ratio of 0.2

Hydrated Cu-SSZ-13 catalysts with Cu:Al ratio < 0.2, under ambient conditions displayed a XANES spectrum which showed quantitative resemblance to hexa-aquo-Cu(II) ions (Table 3.1). This analysis showed that in addition to the majority of hydrated Cu ions being isolated from each other, they were also screened from zeolite interactions due to a sphere of hydration. We speculate that the hydration sphere of isolated Cu(II) ions was responsible for providing Cu-specific spectroscopic information in terms of *d-d* transition intensity. For Cu-SSZ-13, Giordanino et al. [120] reported that dehydrated

isolated Cu(II) ions interact with the zeolite framework and exhibit *d-d* transition at ~14000 cm^{-1}. Under ambient conditions, however, the maximum intensity of the *d-d* transition of hydrated isolated Cu(II) ions in SSZ-13 was obtained at 12500 cm^{-1} [131]. Under NO oxidation, these isolated Cu(II) ions were dehydrated and displayed a XANES spectrum which showed quantitative resemblance to dehydrated isolated Cu^{2+} ions within SSZ-13 (Table 3.1), which were inactive for NO oxidation.

From DFT calculations, the most stable location of the isolated Cu^{2+} ion was near the 6 member ring of Cu-SSZ-13 (Table 3.2). By counting the number of framework Al pairs in the 6 member ring, in particular, assuming random framework Al distribution, Löwenstein's rule, and H^+:Al = 1, the calculated maximum isolated Cu^{2+} ions per Al_f was 0.23 (for SSZ-13 with Si:Al_f ratio = 5 Figure 3.9). This number obtained from calculations, cannot be directly compared with the experimental results because the set of Cu-SSZ-13 catalysts had an average H^+:Al_f ratio of ~0.76. A fair comparison will involve reporting the experimentally obtained silicon to framework aluminum ratio (Si:Al_f) and a copper to framework Al ratio (Cu:Al_f). For Cu-SSZ-13 catalysts reported in this study, the total silicon to Aluminum ratio was 4.5, while the Si:Al_f was 5.3. From Figure 3.9, the maximum number of isolated Cu(II) in the 6 member ring for SSZ-13 having a Si:Al_f of 5.3, occurs at Cu:Al_f = 0.22. However, by calculating the Cu^{2+}:H^+ ratio (by taking into account, the H^+:Al_f for the parent SSZ-13 = 0.76), the maximum number of isolated Cu^{2+} ions associated with a six member ring, occurs at Cu:Al_f = 0.31. Thus, based on the experimental constraints on the quality of SSZ-13, the range in which Cu-SSZ-13 forms a maximum number of isolated Cu^{2+} ions in the six member ring occurs at Cu:Al_f varying from 0.22 to 0.31. For our catalysts, the onset of NO oxidation rate occurs at Cu:Al ratio = 0.2 when normalized to the number of framework Al atoms, calculated from ^{27}Al MAS NMR, leads to Cu:Al_f ratio = 0.23, which is within the range specified from statistical counting of isolated Cu^{2+} ions in the 6 member rings of Cu-SSZ-13. The lack of a measurable NO oxidation rate up to Cu:Al ratio = 0.2 was thus a catalytic consequence of the saturation of paired framework Al sites in the 6 member ring with dehydrated isolated Cu^{2+} ions under NO oxidation. For catalysts with Cu:Al ratio > 0.2, formation of

Cu_xO_y clusters in the 8 member cage of SSZ-13 occurred because all the Al pairs in the 6 member rings were occupied by isolated Cu(II) ions. These Cu_xO_y clusters were responsible for the monotonic increase and saturation in the NO oxidation rate (per mole Cu) for catalysts with Cu:Al ratios ranging from 0.2 - 1.6.

3.5.3 On the Difference In The Rates of NO Oxidation Between Isolated Cu(II) Ions and Cu_xO_y Species

The Gibbs free energy NO oxidation pathway on isolated Cu(II) ions near the 6 member ring (Z_2Cu) and Cu – O_y – Cu species in the 8 member cage showed that there was a considerable difference with respect to the probable reaction intermediates. In particular, a notable difference was observed in the molecular adsorption and subsequent activation of oxygen on each Cu ion configuration respectively (+0.78 eV for Z_2Cu and -0.87 eV for Z_2Cu_2 – 4NN, as shown in Figure 3.11). Furthermore, the activated oxygen then enabled a catalytically relevant step for NO to form NO_2, which can form nitrates on Cu – O_y – Cu based on the NO_2 disproportionation reaction observed on Cu-SSZ-13 [132]. The overall rate of NO oxidation being measurable on Cu – O_y – Cu species in the 8 member ring than on isolated Cu(II) ions near the 6 member ring was thus a consequence of the higher stability of the most probable intermediates under NO oxidation, consistent with the experimental results. With these results, it is plausible that larger Cu_xO_y clusters ($x > 2$, $y > 2$) can also take part in the NO oxidation catalysis. The role of larger Cu_xO_y clusters for NO oxidation kinetics, however, needs to be studied further.

Previous work by our group (Chapter 2) on the standard SCR ability of different Cu ion configurations within Cu-SSZ-13 showed that isolated Cu(II) ions near the six member rings were the dominant active sites for standard SCR (at 473 K) while it was shown that the standard SCR rate on Cu ion configurations with a local Cu-O_y-Cu bond were insignificant in comparison to isolated Cu ions on Cu-SSZ-13 (at 473 K). This was due to the standard SCR rate tracking with the *d-d* transition intensity of hydrated isolated Cu(II) ions in Cu-SSZ-13 even for catalysts that had Cu_xO_y clusters in addition to isolated Cu(II)

ions. This Cu_xO_y configuration is active for dry NO oxidation based on the results provided in this contribution. We propose that dry NO oxidation when analyzed independently of standard SCR shows that NO oxidation rates cannot be correlated to standard SCR rates due to different active site requirements. The kinetic relevance of NO oxidation under standard SCR for Cu-SSZ-13, however, still needs to be investigated.

Commercial catalyst formulations still suffer from deactivation during standard SCR due to breakdown of the zeolite structure, dealumination, and clustering of Cu ions within the zeolite [1, 133]. In the event of Cu ion cluster formation, we propose the use of dry NO oxidation as a probe reaction to qualitatively identify these species. This is due to the ability of dry NO oxidation to be selective to non-isolated Cu(II) species [118, 134].

3.6 Conclusions

A combined experimental and computational kinetic study of dry NO oxidation on Cu–SSZ-13 catalysts revealed at least two Cu ion configurations within SSZ-13. Below the Cu:Al ratio = 0.2 (Si:Al = 4.5), the dominant Cu ion configuration in hydrated catalysts was a hydrated isolated Cu(II) ion. Under dry NO oxidation, these species were quantitatively converted to dehydrated isolated Cu(II) ions in the vicinity of 2 framework Al sites, in the 6 member ring of SSZ-13. In the vicinity of Cu:Al ratio = 0.2, all framework Al pairs in the 6 member rings of SSZ-13 were ion exchanged by dehydrated isolated Cu(II) ions and this configuration did not display a measurable NO oxidation rate (300 ppm NO, 150 ppm NO_2, 10% O_2 and 573 K). Subsequently, catalysts with Cu:Al ratio > 0.2 displayed a linear increase in the NO oxidation rate (per mole Cu) with an increase in the percentage of Cu_xO_y species (per mole Cu, $x \geq 2$, $y \geq 1$) as quantified from *in-situ* XANES, indicating that Cu_xO_y species with local Cu – O_y – Cu bonds were the active sites for dry NO oxidation. The presence of Cu_xO_y species above Cu:Al ratio of 0.2 was rationalized by the availability of Al pairs at larger distances required for stabilization within the 8 member cage, indicating the formation of this second Cu ion configuration in the 8 member cage of SSZ-13. The Cu_xO_y species in the 8 member ring

of SSZ-13 displayed a more facile redox pathway for the oxidation of NO than dehydrated isolated Cu(II) ions near the 6 member ring, consistent with the experimental difference in the rates of NO oxidation between these configurations. The proposed pathway was consistent with the observed reaction orders and identified the molecular adsorption and subsequent activation of oxygen as a kinetically relevant step during NO oxidation catalysis.

These results imply that there is a theoretical limit to the density of dehydrated isolated Cu^{2+} ions near the 6 member rings of SSZ-13, claimed to be the active sites for Standard SCR reaction [14, 24, 30]. This limit depends on the Si:Al ratio of SSZ-13. Excess Cu ion exchange above this limit would manifest in Cu_xO_y species in the 8 member cages of SSZ-13 which would be the likely locus for NO oxidation. Moreover, NO oxidation, being selective to only Cu_xO_y species in Cu-SSZ-13, can also be used as a probe reaction to identify clustering of Cu ions.

3.7 Acknowledgements

A lengthy author list is associated with this manuscript. Because this is a dissertation, these people will be listed here. Those people are Shane A. Bates, Trunojoyo Anggara, Christopher Paolucci, Atish A. Parekh, Krishna Kamasamudram, Aleksey Yezerets, Jeffrey T. Miller, W. Nicholas Delgass, William F. Schneider, and Fabio H. Ribeiro. We would also like to thank Paul Dietrich for his help in executing the XAS experiments at the APS. Use of the Advanced Photon Source is supported by the U. S. Department of Energy, Office of Science, and Office of Basic Energy Sciences, under Contract DE-AC02-06CH11357. MRCAT operations are supported by the Department of Energy and the MRCAT member institutions. Support for JTM was provided under the auspices of the U.S. DOE, Office of Basic Energy Sciences, Division of Chemical Sciences, Geosciences, and Biosciences under contract number DE-AC0-06CH11357. We would also like to thank Sachem, Inc. for their gracious donation of the structure directing agent for SSZ-13 synthesis.

CHAPTER 4. ISOLATION OF THE COPPER REDOX STEPS IN STANDARD SCR ON COPPER EXCHANGED SSZ-13

4.1 Abstract

"We report *operando* X-ray absorption experiments and density functional theory (DFT) calculations that elucidate the role of Cu redox in the selective catalytic reduction (SCR) of NO over Cu-exchanged SSZ-13. Catalysts prepared to contain only isolated, exchanged Cu(II) evidence both Cu(II) and Cu(I) under standard SCR conditions at 473 K. Reactant cutoff experiments show that NO and NH_3 together are necessary for Cu(II) reduction to Cu(I). DFT calculations show that NO-assisted NH_3 dissociation is both energetically favorable and accounts for the observed Cu(II) reduction. The calculations predict in situ generation of Brønsted sites proximal to Cu(I) upon reduction, which we quantify in separate titration experiments. Both NO and O_2 are necessary for oxidation of Cu(I) to Cu(II), which DFT suggests to occur via an NO_2 intermediate. Reaction of Cu-bound NO_2 with proximal NH_4^+ completes the catalytic cycle. N_2 is produced in both reduction and oxidation half-cycles.

4.2 Introduction

NOx selective catalytic reduction (SCR) to N_2 with NH_3 is commonly used to control emissions from stationary combustion sources. Standard SCR is a redox reaction between NO and NH_3:

$$4NO + 4NH_3 + O_2 \rightarrow 4N_2 + 6H_2O \qquad \text{Scheme 4.1}$$

and under useful conditions is selective for NH_3 oxidation by NO over the O_2 that is typically present in great excess [2]. Vanadia catalysts used in stationary applications do not have sufficient hydrothermal stability for mobile applications. Only with the discovery of hydrothermally stable, Cu-exchanged chabazite (CHA) catalysts, including Cu-SSZ-13 (aluminosilicate) and Cu-SAPO-34 (silicoaluminophosphate), has NOx SCR become commercially viable for mobile source emissions control [1].

The CHA framework contains interconnected 4-, 6-, and 8-member rings (4-MR, 6-MR, 8-MR). Substitution of Al for Si in the SSZ-13 and of Si for P in SAPO-34 introduces anionic coordination sites for exchanged Cu(I) and/or Cu(II) ions, H^+, NH_4^+, and other cations. The identities and numbers of exchanged cationic species depend on the framework Si:Al (silicon: total aluminum) ratio, the distribution of Al atoms in the framework, the total Cu content and Cu exchange method, and the treatment history of the material. Furthermore, the Cu coordination environment [15] and oxidation state can change under reaction conditions[24].

The preferred Cu exchange sites at low Cu loading in SSZ-13 are well established. DFT calculations identify a 6-MR containing two framework Al atoms as the most stable exchange site for a Cu(II) ion in SSZ-13 [15, 98, 135]. Temperature programmed reduction experiments [16] and electron paramagnetic resonance spectroscopy [18] both show that these exchange sites are populated first at low Cu:Al (copper : total aluminum) ratios. The number of such exchange sites depends only on the Si:Al ratio if Al atoms are distributed randomly within the SSZ-13 framework. Numerical simulations of such placement show a Cu:Al ratio of 0.2 to correspond to complete population of 6-MR Cu(II) sites at a Si:Al ratio of 4.5 [135]. UV-Visible-NIR spectroscopy [135], X-ray absorption spectroscopy (XAS) [72], and NH_3 titration of residual Brønsted acid sites [26] together show that SSZ-13 samples prepared with Si:Al ratio of 4.5 and loaded with Cu:Al $\leq$ 0.2 contain exclusively Cu(II) ions isolated in the 6-MR. Furthermore, Cu-SSZ-13 samples containing only isolated Cu(II) are active for standard SCR at 473 K,[14, 15, 21, 80, 135]

with SCR rates that are directly proportional to the density of 6-MR Cu(II) ions.[14, 15, 21, 80, 135]

Although standard SCR rates correlate with initial 6-MR Cu(II) content, this oxidation state is not maintained during catalysis. *Operando* XAS show the presence of both Cu(II) and Cu(I) under standard SCR conditions [24, 136] and their proportions have been quantified under differential plug flow conditions in the absence of transport limitations on Cu-SSZ-13 samples that initially contained only 6-MR Cu(II) ions [25]. DFT calculations show that the oxidation state of 6-MR Cu can be changed by adsorbates and that both Cu(I) and Cu(II) forms have comparable thermodynamic stability under SCR conditions [24]. Kwak et al. proposed that Cu-nitrosyls formed by NO chemisorption are responsible for the reduction of Cu(II) to Cu(I), based on *ex-situ* vibrational and ^{15}N nuclear magnetic resonance spectroscopies at ambient temperature [22]. More recently, Gao et al.[13] proposed that Cu(II) is reduced to Cu(I) by co-adsorption of NO and NH_3, based on *ex-situ* diffuse reflectance infrared fourier transform spectroscopy. Taken together, this evidence indicates that Cu redox chemistry occurs during standard SCR.

In this contribution, we report *operando* experiments and DFT computations and analysis that isolate and explain the response of a Cu-SSZ-13 catalyst, initially prepared to contain only 6-MR Cu(II) ions, to standard SCR reaction conditions at 473 K and upon cutoff of each reactant under plug flow conditions. We show that standard SCR is associated with Cu redox between the Cu(II) and Cu(I) states, that the reduction half-cycle requires both NH_3 and NO, that each reduction event generates a Brønsted acid site proximal to Cu(I) that binds a catalytically relevant NH_4^+ species, and that the oxidation half-cycle requires NO and O_2 and consumes this NH_4^+. We use these results to propose a series of plausible redox steps for standard SCR of NO with NH_3, in which N_2 is formed as a product in both the reduction and oxidation half-cycles.

4.3 Results and Discussion

Two Cu-SSZ-13 catalysts (Cu:Al = 0.11 and 0.16, Si:Al = 4.5) were prepared to contain exclusively isolated Cu(II) ions.[26, 135] Preparation details are in Appendix for Chapter 4, (Pg.171) and characterization data presented elsewhere.[26, 135] These catalysts were placed in glassy carbon tubes in a custom-built reactor setup specially developed for collecting *operando* SCR kinetics under plug flow conditions[24, 25] and exposed to standard SCR mixtures at 473 K. The experimental setup is discussed in Appendix for Chapter 4 (Pg. 171 - 174). Under differential conditions (< 20% NO conversion) the observed steady-state SCR rates per mol Cu were 4.8×10^{-3} and 5.1×10^{-3}mol NO (mol Cu s)$^{-1}$ for the Cu:Al 0.11and 0.16 samples, respectively, each within a factor of 1.3 to rates on the same catalysts measured elsewhere (comparison of standard SCR rates detailed in Appendix for Chapter 4, Pg. 175-176) [135]. The reproducibility of the reaction rates confirms the *operando* XAS reactor operates under plug flow, while the constant SCR turnover rate certifies that the kinetic data are not corrupted by heat and mass transfer artifacts by the Koros-Nowak test [69, 70]. The *operando* X-ray absorption near edge structure (XANES) spectra of Cu were fitted with linear combinations of three XANES references, including an isolated Cu(II) ion in SSZ-13, an isolated Cu(I) ion in SSZ-13, and a hydrated isolated Cu(II) ion ($[Cu(H_2O)_6]^{II}$) (details of *operando* XANES measurements and Cu XANES references are in Appendix for Chapter 4, Pg. 177 & 178). The first column of Figure 4.1 shows that nearly 30% of Cu is present as Cu(I) and 70% as Cu(II) under standard SCR conditions in both samples (corresponding XANES spectra and quantification results are in Appendix for Chapter 4, Pg. 181 and Table C.4).

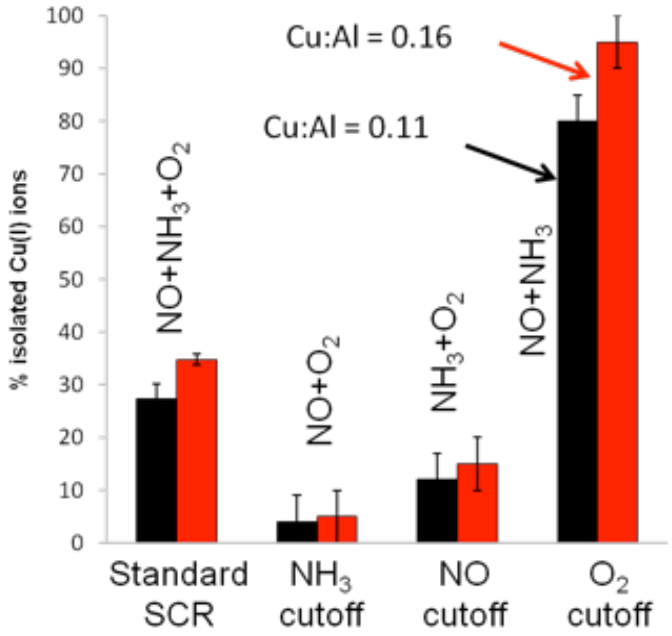

Figure 4.1 Percentage isolated Cu(I) relative to total Cu ions under various steady state flow conditions. 5% H_2O was present in all the cutoff mixtures. Standard SCR conditions are 320 ppm NO, 320 ppm NH_3, 10% O_2, and 5% H_2O, at 473 K.

Reactant cut-off experiments were performed to probe the effect of gas composition on the Cu oxidation states. Starting from steady-state standard SCR conditions, the flow of one reactant was switched to an inert CO_2 tracer to maintain a constant total gas flow rate (experimental details in Appendix for Chapter 4 Pg. 171). NH_3 cut-off experiments left behind a feed mixture of NO and O_2, while NO cut-off left behind a feed of NH_3 and O_2. In both experiments, feed streams contained 5% H_2O and an appropriate amount of balance He gas. After NH_3 or NO cut-off, NO consumption rates decreased with time to undetectable levels. The steady state Cu(I) percentage (Figure 4.1) decreased to ~ 5% after NH_3 cutoff and ~ 12% after NO cutoff (XANES before and after NH_3 and NO cutoffs detailed in Figure C.5 and Figure C.7, respectively), indicating that the feed streams lost their reduction ability when either NH_3 or NO was absent at 473 K. Thus, we conclude that NO or NH_3 separately, at concentrations typical of standard SCR, cannot reduce isolated Cu(II) ions to Cu(I).

To probe why NH_3 and NO are needed together to reduce Cu(II) to Cu(I), we used DFT calculations to compute adsorption free energies and oxidation states on a 6-MR Cu(II) ion. We constructed an SSZ-13 supercell model (nominal Si:Al ratio of 5:1) containing two Al in a 6-MR,and placed a Cu ion in this preferred exchange site [135].

We probed molecular adsorption of NH_3, H_2O, O_2, N_2, and NO at this Cu site using the hybrid screened exchange (HSE06) exchange-correlation functional, which provides superior estimates of reaction energies involving NO [97, 137]. Initial adsorbate geometries were chosen from low-energy structures visited during preliminary *ab-initio* molecular dynamics (AIMD) simulations and were subsequently optimized; relaxed structures and binding energies of all adsorbates are in Appendix for Chapter 4 Pgs. 190 - 198. NH_3 and H_2O bind most exothermically to the Cu site and diatomic binding is only modestly exothermic.

To relate the HSE06 adsorption energies to adsorption free energies at the experimental reaction conditions, ΔG(473 K),we used isothermal AIMD and the PBE functional to construct the potential of mean force (PMF) associated with drawing adsorbed NH_3 from the SSZ-13 central cage to the Cu(II) site (details in Appendix for Chapter 4 Pg. 199). The PBE functional is more cost-effective than HSE06 and provides an NH_3 binding energy within 8 kJ $mol^{-1}$of the HSE06 value. The free energy difference at 473 K is – 62 kJ mol^{-1} from the integrated PMF. The free energy associated with confining an ideal gas within a zeolite cage has been estimated from adsorption experiments [138] and Grand-Canonical Monte Carlo simulations [139]to be +20-30 kJ mol^{-1}. The upper value of 30 kJ $mol^{-1}$is appropriate to the small-pore SSZ-13. Combining these, we estimate the net NH_3 adsorption free energy relative to an NH_3 ideal gas is –32 kJ mol^{-1}. This free energy difference is comparable to that computed for an ideal NH_3 gas that retains the equivalent of 2/3 of its free translational entropy upon adsorption, also in agreement with experimental results for oxygen adsorption in chabazite [140]. Consistent with this picture, the MD simulations reveal an adsorbate that is quite dynamic even at the equilibrium Cu-NH_3 distance.

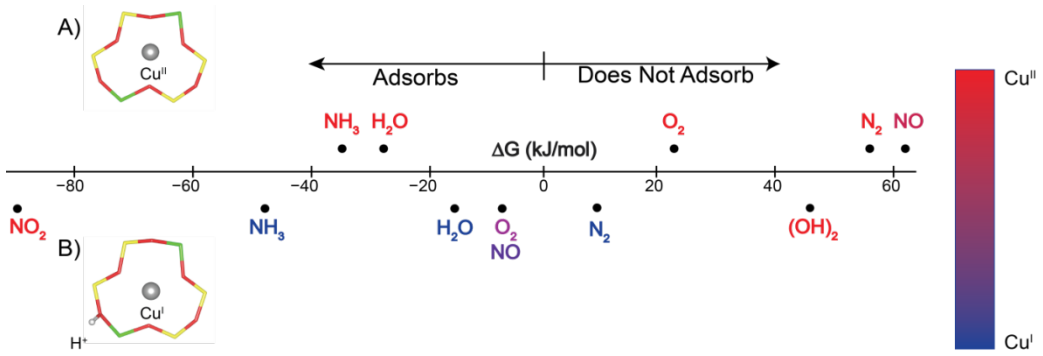

Figure 4.2 DFT-computed adsorption free energy (horizontal scale) and Cu oxidation state (color scale) on A) 6-MR Cu(II)^{I} and B) 6-MR Cu(I) plus Brønsted site. NO_2 and $(OH)_2$ energies referenced to $½O_2$ and NO/H_2O.

Figure 4.2A reports 473 K adsorption free energies computed from the HSE06 energies and the assumption that all adsorbates lose 1/3 of their gas-phase translational entropy. Only NH_3 and H_2O adsorb exergonically and thus competitively onto 6-MR Cu sites under standard SCR conditions. The diatomics (NO, N_2, & O_2) are unlikely to populate these sites. The binding preference computed for NH_3 over H_2O is consistent with XANES spectra collected after NH_3 cut-off experiments, which show the proportions of hydrated Cu(II) to increase from 7 ± 3% to 41 ± 5% on the 0.11 Cu:Al sample and from 3 ± 3% to 48 ± 5% on the 0.16 Cu:Al sample (details in Appendix for Chapter 4, Pg. 185, & Table C.4).

We determined Cu oxidation state from both integrated Cu density of states (DOS) and Bader charges, using the isolated Cu ion in the 6-MR as a Cu(II) standard. Results from both analyses were consistent across all calculations (details in Appendix for Chapter 4, Pgs. 201 - 202). Figure 4.2A summarizes the Bader results in the color-coding of each adsorbate. NH_3 adsorption leaves Cu in the Cu(II) state, consistent with formal charge considerations. Separate calculations show that the Cu Bader charge decreases from 2+ to 1.9+ upon adsorption of four NH_3. This reduction may in part account for the 10% Cu(I) detected in XANES spectra following NO cutoff (Figure 4.1). This reduction, however, is insufficient to account for the 30% Cu(I) detected during standard SCR.

Further, the HSE06 results in Figure 4.2A show that a 6-MR Cu(II) does not bind NO under standard SCR conditions and is not reduced by association with NO.

These DFT results are consistent with the experimental observation that no single reactant reduces Cu(II) to Cu(I). Optimization of NH_3 and NO or NH_3 and O_2 at the 6-MR Cu(II) site produces results unchanged from NH_3 adsorption alone. As we explored NH_3 adsorption, however, we discovered a dissociation that produces Cu-bound NH_2 and a new Brønsted acidic proton, as illustrated in the bottom reaction path in Figure 4.3. This HSE06-computed reaction is endothermic by +119 $kJmol^{-1}$ and thus is unlikely to occur at temperatures as low as 473 K. However, the computed Cu oxidation state is +1.55, intermediate between Cu(I) and Cu(II) and suggesting that NH_3 dissociation is a possible route to Cu reduction. We next explored NO co-adsorbed with this dissociated NH_3 and found that NO binds at the NH_2 nitrogen to form an H_2NNO intermediate

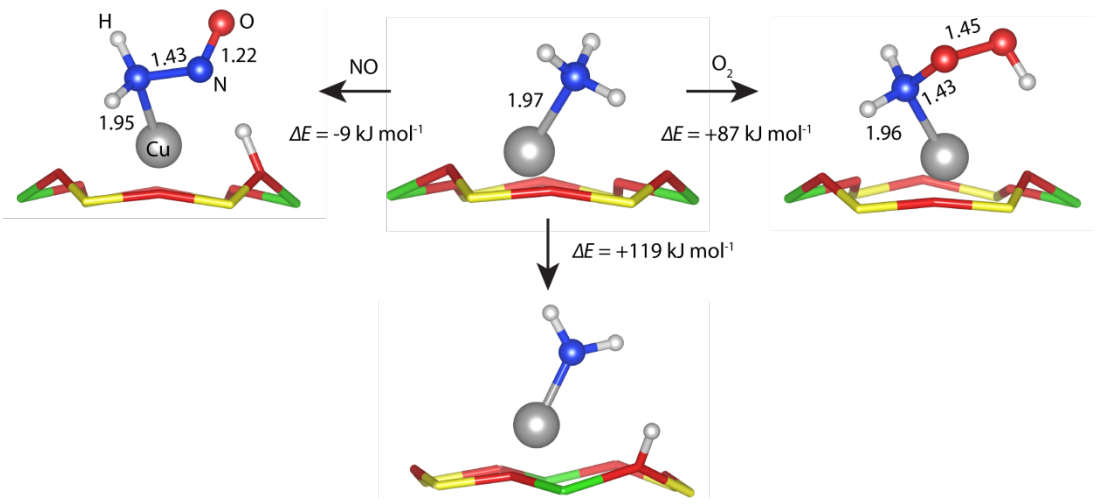

Figure 4.3 HSE06-computed structures and energies of NH_3 dissociation (center), NO-assisted dissociation (left), and O_2-assisted dissociation (right) products

(left path, Figure 4.3) reminiscent of that created from the gas-phase reaction of H_2N and NO radicals. The computed N-N bond energy is 128 kJ mol^{-1}, less than the corresponding gas-phase H_2N–NO bond energy of –226 kJ mol^{-1} [141] and reflecting the geometric distortions associated with adsorbing the intermediate on Cu. Figure 4.4

shows that NH_3 adsorption followed by NO-assisted dissociation has a computed free energy change close to zero and decreases the normalized Cu charge 2+ to 1+. The H_2NNO intermediate has the proper stoichiometry to decompose to N_2 and H_2O; in the gas-phase it does so via successive proton transfers [141]. As shown in Figure 4.4, the decomposition free energy of this intermediate to N_2, H_2O, Cu(I) and a new Brønsted acid site is–288 kJ mol^{-1}.

We compared this NO/NH_3 co-reaction with O_2-assisted NH_3 activation. Starting from dissociated NH_3 and O_2, the Brønsted proton relaxes away from the framework to form an H_2NOOH adduct (Figure 4.3). The net reaction energy is +87 kJ mol^{-1}, the Bader-determined Cu oxidation state remains 2+, and no new Brønsted site is created. The inability of O_2 to activate NH_3 adsorbed on isolated 6-MR Cu(II) ions is likely the underlying reason for the selective nature of NO reduction on this site.

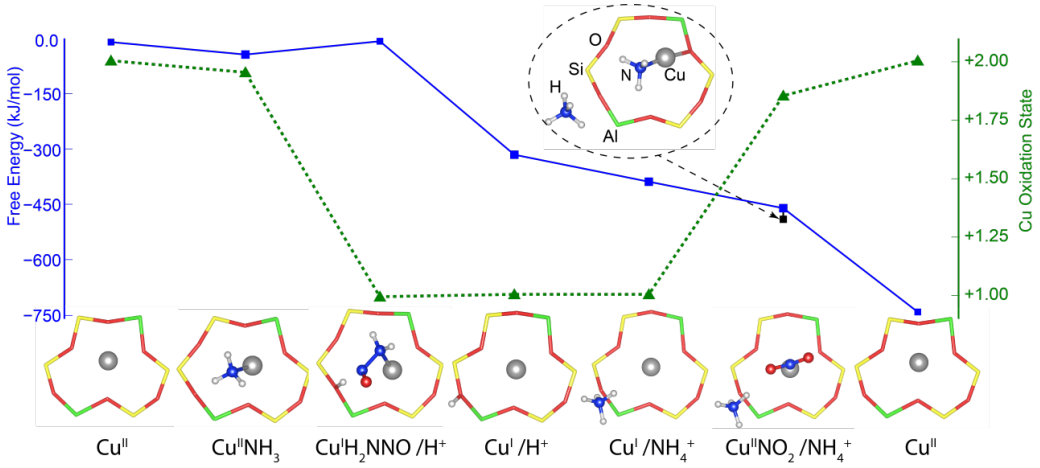

Figure 4.4 HSE06-computed reaction free energies and Cu oxidation states along the standard SCR pathway. Free energies at 473K, 1 atm, 300 ppm NH_3 and NO, 10% O_2, 5% H_2O, and 60 ppm N_2 (20% conversion). Circled species indicates NH_3 co-adsorption on Cu(I) and Brønsted sites.

We used this observation of Cu(II) reduction by NO and NH_3 to test the DFT prediction that one Brønsted acid site is created *in situ* upon each reduction of an isolated Cu(II) to a Cu(I) ion. Experimental details on Cu(I) generation and the titration of excess Brønsted

sites is provided in Appendix for Chapter 4 Pgs. 185 - 188. As shown in Figure 4.5, the number of excess H^+ sites titrated on reduced Cu(I)-SSZ-13 samples were equal, within experimental error, to the total number of Cu(I) sites generated (Figure 4.5), consistent with the stoichimetric reduction of isolated Cu(II) ions to Cu(I)/H^+ site pairs. The direct experimental observation of an additional H^+ site formed during Cu(II) reduction to Cu(I) during standard SCR suggests that NH_4^+ intermediates bound at H^+ sites proximal to Cu(I) ions, but not at distant H^+ sites that remain after Cu exchange, [26] are involved in the standard SCR catalytic cycle.

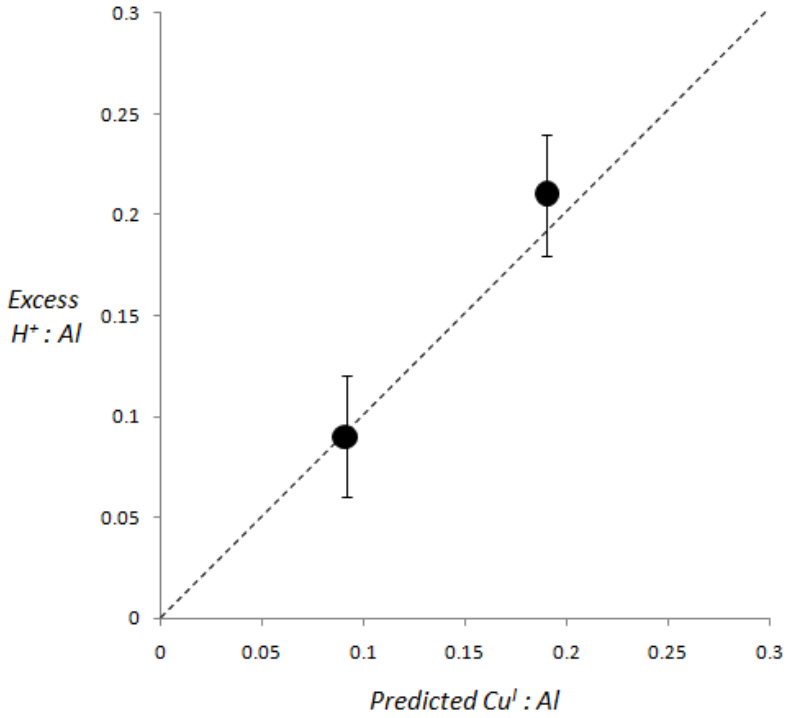

Figure 4.5 NH_3 titration of excess H^+ sites formed upon reduction of Cu-SSZ-13 samples after treatment in flowing NO + NH_3 (473 K).

O_2 cutoff experiments provide complementary information about the re-oxidation of Cu(I). Steady state NO conversion over the Cu-SSZ-13 under SCR conditions decreased to zero after O_2 cut-off from the feed. As shown in Figure 4.1, a gas mixture containing only the NH_3 and NO reactants caused the percentage of Cu(I) species to increase to 75-

95% (corresponding XANES spectra are in Figure C.9, Appendix for Chapter 4). O_2 is thus necessary for catalytic SCR turnovers, and specifically required for the re-oxidation of Cu(I) to Cu(II).

To model the oxidation half-cycle, we began with the same Cu 6-MR model, now starting from the reduced Cu(I) / H^+site. We computed 473 K adsorption free energies of the same reactants following the approach above; results are shown in Figure 4.2B. In general, adsorption is stronger on the Cu(I) than on the Cu(II) site. NH_3 binds most strongly to the Cu(I) site while H_2O, O_2, and NO bind weakly and N_2 does not adsorb (Figure 4.2B). Of these only O_2 oxidizes the Cu to any extent, but its binding is too weak to account for the observed Cu oxidation [24]. NH_3 binds even more strongly to the proximal Brønsted acid site to form the NH_4^+ intermediate shown in Figure 4.4. Computed adsorption free energies on the Brønsted and Cu(I) sites are –78 and –45 kJ mol^{-1}, respectively.

As with Cu(II) reduction to Cu(I), adsorption of individual reactants cannot account for the observed Cu(I) re-oxidation. Thus, we looked for oxidizing species generated from O_2 and another reactant. DFT calculations show that a di-hydroxyl adduct formed from H_2O and ½ O_2 oxidizes Cu(I) to Cu(II) (Figure 4.2, $(OH)_2$,). Similarly, NO_2 formed from NO and ½ O_2 both binds strongly and oxidizes Cu(I) to Cu(II) (Figure 4.2) to form an adsorbed nitrite [84]. The exact mechanism of this NO oxidation remains to be determined but could occur *via* a route similar to the gas-phase, in which two NO and O_2 combine at the site to produce adsorbed nitrite and a second NO_2 that is consumed in a subsequent step through the catalytic cycle. Ruggeri et al.[142] demonstrated through chemical trapping on Fe-ZSM-5 that NO_2 forms on isolated Fe sites, and it seems plausible that NO_2 forms on Cu sites in a similar fashion.

Co-adsorption of NO_2 on the Cu site and NH_3 on the proximal Brønsted site is both energetically favorable (Figure 4.4) and produces an ammonium nitrite-like complex of

the correct stoichiometry to decompose into two H_2O and one N_2, consuming the Brønsted site and leaving behind the original 6-MR Cu(II) site (Figure 4.4). Similar two site mechanisms with one proximal site generated *insitu* have been proposed on supported rhodium-rhenium bimetallic catalysts and supported vanadia domains for selective catalytic reactions [4, 143]. Other NH_4^+ species exist in Cu-SSZ-13, bound at residual H^+ sites that remain after Cu ion-exchange,[26] but only NH_4^+ sites proximal to the Cu site where nitrite species are formed participate directly in the catalytic cycle at the SCR conditions considered here.

Scheme 4.2 summarizes the SCR redox mechanism inferred from the experimental and DFT findings. A 6-MR Cu(II) site is in quasi-equilibrium with bound H_2O and with bound NH_3. NO-assisted dissociation of NH_3 occurs selectively in the presence of excess O_2 and reduces Cu(II) to Cu(I) while producing an H_2NNO intermediate and proximal Brønsted acid site. The H_2NNO intermediate decomposes to H_2O and N_2. The Brønsted acid site, generated *in-situ* and proximal to the Cu site, adsorbs NH_3 to form an NH_4^+ ion. At this point in the catalytic cycle, the active site consists of a Cu(I) site and a NH_4^+ion balancing the two framework Al anionic charges. NH_3 binds strongly to the Cu(I) site, consistent with the NH_3 inhibition observed at over-stoichiometric NH_3 concentrations [135]. NO_2 formed directly on this Cu site or indirectly on other sites competes with adsorbed $NH_3$and oxidizes the Cu site. The adjacent NO_2^- and NH_4^+decompose to generate two H_2O molecules and N_2. In the overall SCR catalytic cycle, the desired product (N_2) is thus formed in both the reduction and oxidation half-cycles, which is an unexpected and unusual finding among known redox catalytic cycles.

Several of the steps in Scheme 4.2 are non-elementary and require further experimental and computational work to fully characterize. Combining the DFT computed equilibrium constants with rate determining step (RDS) assumptions for either the oxidation or reduction half-cycles predicts either 100% Cu(I) or Cu(II) at steady state. We surmise that both half-reactions are kinetically relevant and that a single RDS assumption is not valid for standard SCR at these conditions on the isolated Cu ions of SSZ-13. Consistent

with the kinetic relevance of both half reactions, standard SCR rates do not correlate with either the number of Cu(I) or Cu(II) observed in *operando* XANES [25].

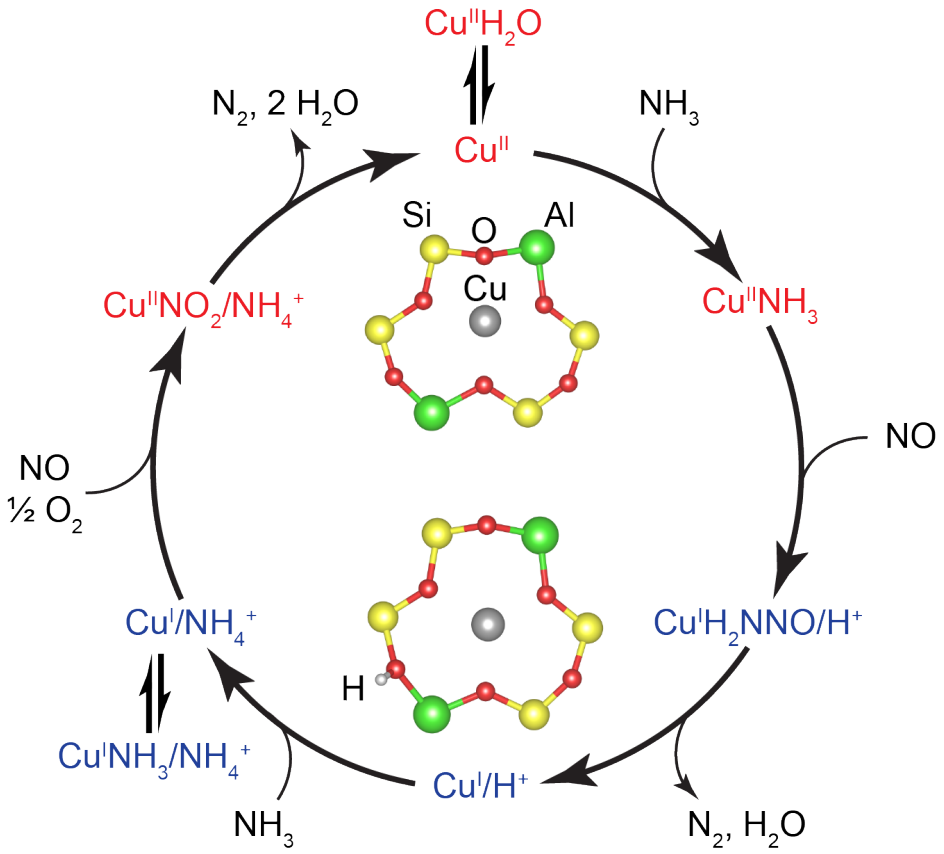

Scheme 4.2 Proposed SCR cycle over Cu-SSZ-13 at 473 K. The reduction and oxidation half-cycles are in red and blue, respectively.

4.4 Conclusions

These experimental and computational findings highlight the redox and bi-functional nature of the Cu-SSZ-13 active site during standard NH_3-SCR. Cu ion reduction requires the NO-assisted dissociation of NH_3 and, as a direct consequence, the reduction becomes selective for NO in the presence of excess O_2. These reduction events generate experimentally detectable Brønsted acid sites that are required for stabilizing reactive NH_4^+ intermediates proximal to Cu ions. It is this dual nature of the active site, composed of the isolated Cu ion and the 6-MR containing two framework Al atoms, that

allows for redox chemistry and is required to close the catalytic cycle. The mixture of Cu(I) and Cu(II) present under differential steady state conditions suggests that the reduction and re-oxidation of Cu play significant roles in SCR kinetics. Similar mechanisms are envisioned for Cu(II) on SAPO-34 and other zeolite supports".

4.5 Acknowledgements

This work is an intricate mix of experiments and computation. I would like to thank Christopher Paolucci and Professor William F. Schneider for performing calculations on the reaction pathway. I would also like to thank Shane A. Bates, Atish A. Parekh, V.F. Kispersky, J.T. Miller, R. Gounder, W. Nicholas Delgass, and F.H. Ribeiro. We would also like to thank Paul Dietrich for his help in executing the XAS experiments at the APS. Use of the Advanced Photon Source is supported by the U. S. Department of Energy, Office of Science, and Office of Basic Energy Sciences, under Contract DE-AC02-06CH11357. MRCAT operations are supported by the Department of Energy and the MRCAT member institutions. Support for JTM was provided under the auspices of the U.S. DOE, Office of Basic Energy Sciences, Division of Chemical Sciences, Geosciences, and Biosciences under contract number DE-AC0-06CH11357. We would also like to thank Sachem, Inc. for their gracious donation of the structure directing agent for SSZ-13 synthesis.

Chapter 4 and Appendix C has been reprinted with permission from C. Paolucci, A.A. Verma, S.A.Bates, V.F.Kispersky, J.T.Miller, R. Gounder, W. Nicholas Delgass, F.H. Ribeiro, and W.F. Schneider, Isolation of the Copper Redox Steps in the Selective Catalytic Reduction on Cu-SSZ-13, Angew. Chem.. doi 10.1002/ange.201407030

CHAPTER 5. PREVENTION OF FALSIFICATION OF REACTION KINETICS BY PRODUCT INHIBITION

5.1 Abstract

While the potential for product inhibition in catalytic reactions is well known, the impact on measured kinetic parameters of unaccounted inhibition seems less appreciated. Product inhibition is common, and when it occurs and is not accounted for, measured rates, apparent activation energies and reaction orders will all be in error by as much as 50% or more. This is illustrated with a case study involving kinetics of NO oxidation over Cu ion clusters (Cu_xO_y) in Cu-SSZ-13, wherein product NO_2 inhibits the forward reaction. Furthermore, in the presence of inhibition, when only reactants are fed to a plug flow reactor or placed in a batch reactor, virtually no practical conversion is low enough to guarantee differential behavior. Inclusion of products along with reactants in the feed solves this problem completely.

5.2 Introduction

The inhibition of the forward reaction by the products of reaction is prevalent in heterogeneous catalysis. Examples include the combustion of methane on Pd [144, 145], hydro-dechlorination of chlorocarbons on Pd [146, 147], the water-gas shift on Pd [148], Pt [149, 150], and $CuO/ZnO/Al_2O_3$ [151], SO_2 oxidation on Pt [152], NO oxidation on Cu, Fe-zeolites [20, 72] and Pt [101, 119], and NO decomposition on Cu-zeolites [6]. Failure to account for product inhibition in the planning and analysis of kinetic experiments can produce significant errors. The source of those errors is easy to understand from the following qualitative argument. Consider an A to B reaction taking place in a well-mixed flow reactor (CSTR) fed by pure A. A typical set of experiments would vary temperature at constant concentration and flow rate of A and vary the

concentration of A ($[A]$) at constant T. The slope of a plot of ln(*rate*) versus T^{-1} would be used to evaluate the apparent rate constant (with the apparent activation energy) and the slope of a plot of ln(*rate*) versus ln$[A]$ would give the apparent reaction order with respect to A. We will assume that even though the total conversion is below 10% for all data gathered, the rate is inverse order in B for all measurements and that this fact not known to the investigator. In the activation energy experiments, as the temperature is increased the conversion will increase, increasing the concentration of B ($[B]$). At higher $[B]$ the rate will be decreased, thus diminishing the increase in rate caused by higher temperature and leading to lower apparent activation energy. This was experimentally verified by Mulla et al. [119] and Hamzehlouyan et al. [152] who studied the effect of product inhibition on the kinetics of NO oxidation and SO_3 oxidation respectively over supported Pt clusters and recorded a lower value of the apparent activation energy in the absence of product co-feeding. Similarly, increases in the concentration of A at constant temperature will yield more B, which will diminish the rate increase caused by A and lead to a lower than expected order in A.

Most commonly, the errors above are generated by the assumption that the reactor is run in the differential regime and that the inhibition effects of products can be ignored. While it is true that there will always be a conversion below which product inhibition can be ignored, we will show in the discussion below that the value of the conversion often is too low for practical experiments and that no reactor type is immune from the problem. We will also show the quantitative effects of overlooking product inhibition for a simple Langmuir-Hinshelwood-Hougen-Watson (LHHW) rate expression and a real kinetic system involving NO oxidation over Cu-SSZ-13. Finally, we will show how the errors can be avoided by adding the products to the reaction mixture.

5.3 Experimental Methods

5.3.1 Catalyst Preparation

We have previously shown that catalytic dry NO oxidation (300 ppm NO, 150 ppm NO_2, and 10% O_2) is significant on Cu ion clusters (Cu_xO_y species, $x \geq 2$, $y \geq 1$) and isolated Cu ions in Cu-SSZ-13, show rates which are within experimental error [72]. As a result, a candidate Cu-SSZ-13 catalyst was selected from a series of Cu-SSZ-13 catalysts prepared by a liquid phase ion exchange method using copper nitrate as the Cu ion precursor. The methods for catalyst synthesis and characterization have been provided in detail elsewhere [72, 135]. In short, the catalyst was prepared by liquid phase ion exchange of H-SSZ-13 (Si:Al = 4.5) and $Cu(NO_3).xH_2O$. The ion exchange was performed at 338 K and at a pH of 5 ± 0.2. This catalyst had 28 ± 5 % of Cu_xO_y species as quantified under *in-situ* NO oxidation (from separate X-ray absorption results) and the Cu:Al (Cu: total Al ratio) was 0.36 [72].

5.3.2 Catalytic Testing

The rector setup used for testing the kinetic effect of product co-feeding on NO oxidation is described in detail by Verma et al [72]. Overall, two sets of experiments were performed. The first set involved testing the kinetics of NO oxidation in the presence of product (NO_2) co-feeding with the feed stream. The standard gas concentrations in this set was 320 ppm NO, 148 ppm NO_2, 10% O_2, and balance N_2 gas, at 200°C. In this set, the NO conversion was kept less than 10%. The NO_2 inhibition was quantified by measuring the apparent reaction order with respect to NO_2, and the rate of reaction was calculated at the respective inlet concentrations on the assumption that a differential plug flow reactor could be treated as a CSTR. The second set of experiments involved no NO_2 co-feeding. The standard gas flow conditions for this set was 320 ppm NO, 10% O_2 and balance N_2, at 200°C. Once again, the NO conversion was less than 10%, the inhibition effect of NO_2 was ignored, and a CSTR model was used to calculate the NO oxidation rates. Furthermore, as a proof of concept, all apparent reaction orders (with respect to NO, O_2, and NO_2, obtained from the first set) were then used to develop an integral plug-

flow reactor (PFR) formalism to test the quantitative effect of product inhibition on kinetic data points in the second set of experiments. In both kinetic data-sets, the NOx mass balance, defined as $(NO + NO_2)_{inlet}$ - $(NO + NO_2)_{outlet}$ was less than 3 ppm. The concentration of N_2O was within experimental error (less than 1 ppm) in all the kinetic data points. Lastly, all experiments were performed far away from equilibrium as quantified by $\beta < 0.01$, where $\beta = \frac{[NO]^2[O_2]}{K[NO_2]^2}$ is the approach to equilibrium and K is the equilibrium constant.

5.4 Results

5.4.1 Kinetic Experiments in Presence of NO_2 in the Feed Stream

In order to show that NO oxidation on Cu-SSZ-13 was indeed inhibited by NO_2, the rate of NO oxidation was first evaluated on the catalyst with NO_2 co-feeding (set 1). The NO conversion was less than 10% and the overall rate of reaction was calculated using the inlet gas concentrations, the residence time (τ) and, assuming a CSTR model, which because of the small variation of concentrations at differential conditions, assumes that the rate is the same at all points in the reactor. For the CSTR model, the following equations were used to calculate the rate of reaction.

$$r_{fwd} = \frac{F_{NO_o} - F_{NO}}{N} = \frac{F_{NO_o} X}{N} = \frac{[NO]_o X}{\tau}, \text{ where } \tau = \frac{N}{Q} \qquad \text{Equation 5.1}$$

F_{NO_o} = Inlet molar flow rate of NO

F_{NO} = outlet molar flow rate of NO

$[NO]_o$ = inlet concentration of NO

N = number of moles of Cu per gram catalyst

Q = volumetric flow rate of total gas in the reactor outlet.

r_{fwd} = moles of NO reacted per mole Cu per second.

The rate was calculated for the standard feed concentrations at each test temperature and the corresponding Arrhenius plot (CSTR model, black squares) is displayed in Figure 5.1. The apparent activation energy was 45 ± 3 kJ mol^{-1}. This value is in agreement with results obtained by Verma et al. [72] In a similar way, the rate of NO oxidation was also investigated with different feed gas concentrations (in presence of NO_2 co-feeding) and the apparent reaction orders with respect to NO, NO_2, and O_2 were measured at 473 K.

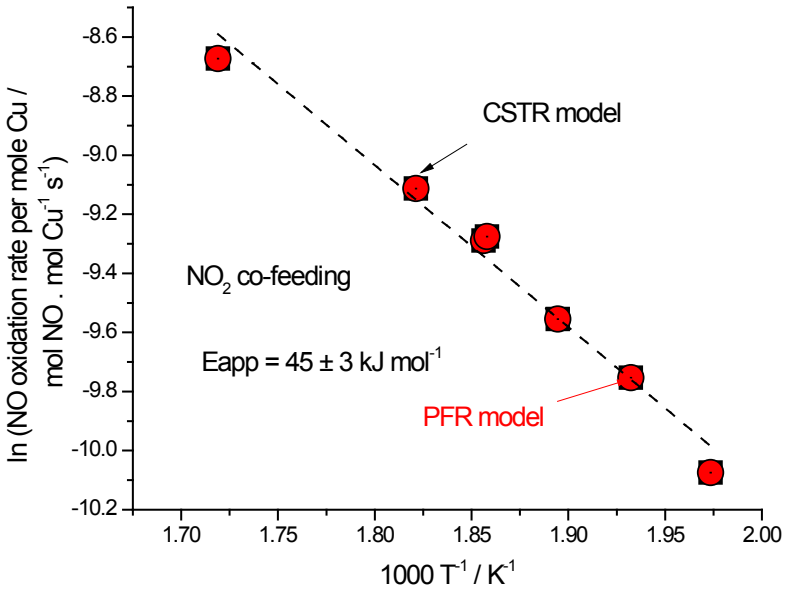

Figure 5.1 Variation of the rate of NO oxidation (per mole Cu) with temperature, with NO_2 in the feed. Feed conditions: 320 ppm NO, 148 ppm NO_2, and 10% O_2. Red circles are data points evaluated from the PFR model, while black squares are evaluated from the CSTR model.

These were 1.5 ± 0.1, -1 ± 0.1, and 0.9 ± 0.1 for NO, NO_2, and O_2 respectively (Figure 5.2). This analysis showed that NO_2 indeed inhibited the forward rate of NO oxidation over Cu-SSZ-13. Now taking the NO_2 inhibition into account, the assumption of the reaction rate not varying along the length of the reactor was relaxed and the reaction rates were re-evaluated using a PFR formalism in which the forward rate (r_{fwd}) of NO

consumption was described by a power law model (Equation 5.2). The lumped kinetic constant is k_{eff} .

$$r_{fwd} = k_{eff}[NO]^{1.5}[NO_2]^{-0.9}[O_2]^{0.9} \qquad \text{Equation 5.2}$$

The governing differential equation for the PFR formalism is detailed in Equation 5.3

$$[NO]_o \frac{dX}{d\tau} = r_{fwd} = k_{eff}[NO]^{1.5}[NO_2]^{-0.9}[O_2]^{0.9} \qquad \text{Where } \tau = \frac{N}{Q} \qquad \text{Equation 5.3}$$

$$\text{And } k_{eff} = \frac{[NO]_o}{\tau}\int_0^X \frac{dX}{[NO]^{1.5}[NO_2]^{-0.9}[O_2]^{0.9}} \qquad \text{Equation 5.4}$$

The concentration terms were written in terms of the inlet concentrations of each gas respectively and the NO conversion (X) and the resulting expression was integrated numerically to give k_{eff}. The Arrhenius plot for rate data points obtained from the PFR formalism (red circles) is also shown in Figure 5.1 for comparison and is shown to be similar to the rates evaluated from the CSTR formalism.

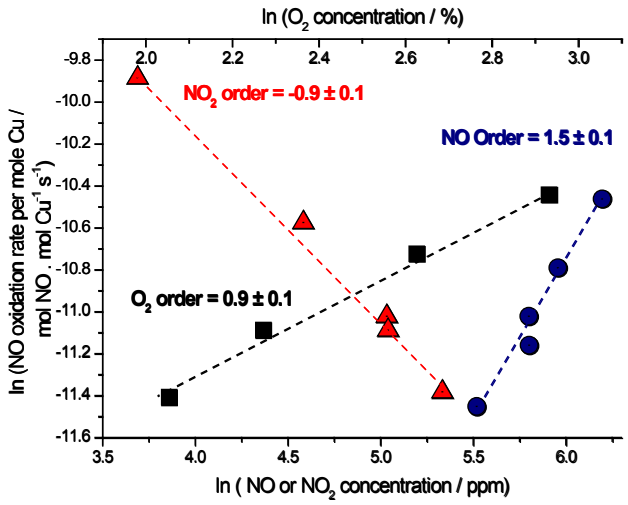

Figure 5.2 Variation of the rate of NO oxidation per mole Cu, with individual gas concentrations, at 473 K. All kinetic data points included in this plot have NO_2 co-feeding.

It should be noted that the rate of NO oxidation in the CSTR formalism, was evaluated without knowledge of the apparent reaction orders beforehand, i.e. the quantitative information regarding NO_2 inhibition was not intrinsically included in the CSTR equation, the result, however, was virtually identical to that from the PFR analysis because of the co-feeding of NO_2 in the feed stream, which renders true differential conditions as the NO_2 concentration ($[NO_2]_o + [_{NO}]_o X$) equals $[NO_2]_o$ at small values of X.

5.4.2 Kinetic Experiments in Absence of NO_2 in the Feed Stream

In the second set of experiments, in order to compare the effect of NO_2 co-feeding on the kinetics, the product was not co-fed with the reactants. Once again, the NO conversion was less than 10% and the rate of NO oxidation was evaluated at the respective reactor outlet concentrations with a CSTR formalism described in Equation 5.1. This analysis ignored the effect of NO_2 inhibition. Using these rates, the Arrhenius plot is shown in Figure 5.3. The value for the apparent activation energy obtained for no NO_2 co-feeding is 22 ± 1 kJ mol^{-1}. This value agrees with similar values of apparent activation energy measured from NO oxidation experiments in the absence of NO_2 co-feeding by Joshi et al. [118] The measured value, however, is lower by a factor of ~ 2 from results obtained by Metkar et al. [20] and Peden et al. [21] who report an apparent activation energy of 54 kJ mol^{-1} and 43 kJ mol^{-1} respectively in the absence of NO_2 co-feeding with the reactants.

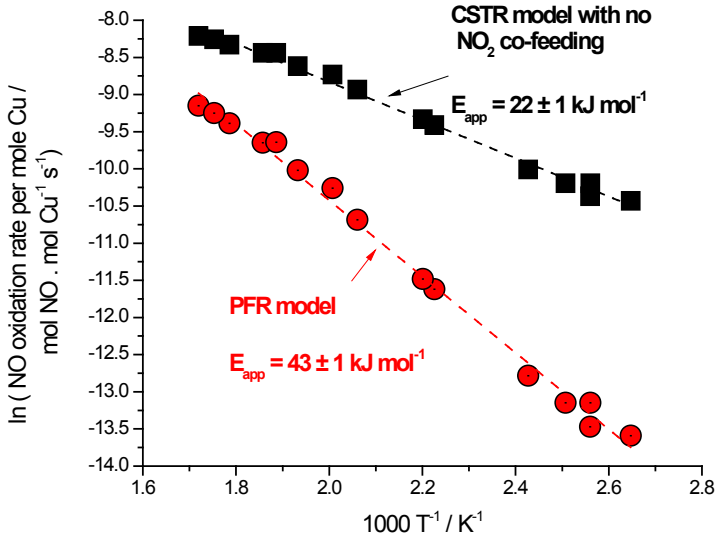

Figure 5.3 Variation of the rate of NO oxidation per mole Cu with temperature, in the absence of NO_2 co-feeding. Feed conditions: 320 ppm NO and 10% O_2. Black squares represent rates which are evaluated from a CSTR model and ignoring product inhibition. Red circles represent rates evaluated from a PFR model which included NO_2 inhibition.

In this set, where NO_2 inhibition was ignored, the apparent reaction orders with respect to NO and O_2 at 473 K shown in Figure 5.4, was 0.8 ± 0.1 and 0.5 ± 0.1 respectively, which matched well with similar kinetic estimations in the absence of NO_2 co-feeding in the literature [20, 21]. These numbers, however, differ markedly from similar kinetic estimations performed with NO_2 co-feeding in the feed stream (set 1). In particular, the ratio of kinetic parameters obtained from NO_2 co-feeding versus no co-feeding ($n_{co\,feed} : n_{nocofeed}$), like apparent activation energy, NO order, and O_2 order are 2 ± 0.2, 1.9 ± 0.2, and 2.2 ± 0.2 respectively. This is a systematic trend and further explanation will be provided in the discussion section.

The analysis of the CSTR model application to set two was based on the premise that the investigator ignored the inhibitory effect of NO_2 on the kinetics of NO oxidation. This can be corrected by using a PFR model which uses the actual dependence on all the reaction orders (including NO_2 inhibition) as shown in the power law model of Equation

5.4. Once again, the same PFR model will be used. Due to possible product inhibition, the reactor outlet concentration at each data point used to evaluate the rate in the black squares of Figure 5.3 was input in Equation 5.4 and the actual k_{eff} which accounted for inhibition, was calculated and re-cast in the Arrhenius plot. These corrected rate data points (red circles) are now shown in Figure 5.3 and compared with the Arrhenius plot prepared by the rate data points which discounted the NO_2 inhibition. As expected, the apparent activation energy of 43 ± 1 kJ mol^{-1} was obtained, which was similar to the apparent activation energy when NO_2 was co-fed with the reactants.

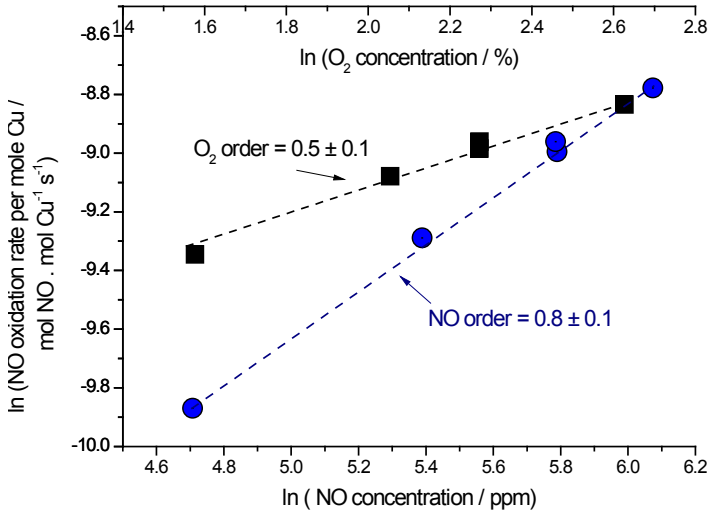

Figure 5.4 Variation of the rate of NO oxidation per mole Cu, with NO and O_2 concentrations, at 473 K. Co-feeding of NO_2 in the feed stream was not done.

5.5 Discussion

In order to evaluate when the inhibition term can and cannot be ignored in the rate expression, we must first examine its origin. We begin with the simplest case. A Langmuir-Hinshelwood-Hougen-Watson analysis of $A \rightarrow B$ on a catalytic surface yields $r_b = \frac{kK_A P_A}{1 + K_A P_A + K_B P_B}$, where k is the rate constant for the rate-determining step of A to B on the surface and K_A and K_B are adsorption equilibrium constants for A and B. For

simplicity, assume that $K_A P_A$ is very much less than 1. If $K_B P_B$ is large with respect to 1, the rate will be first inverse order in B and will be decreased by the presence of B unless P_B is small enough to make $K_B P_B << 1$. Since $P_B = P_{A_o} X_A$, where X_A is the conversion of A, there is a value of X_A below which the rate is independent of B, and that value depends on the value of K_B. To estimate a typical value of K_B in units of atm^{-1}, we take the correlation suggested by Vannice et al. [153] for the upper bound of $-\Delta S^o_{ads}$ as $12.2 - 0.0014\Delta H^o_{ads}$, where the entropy units are cal (mol K)$^{-1}$ and the enthalpy units are cal mol^{-1}. For $-\Delta H^o_{ads}$ of 20 kcal.mol^{-1}, the upper bound for $-\Delta S^o_{ads}$ would be 40.2 cal (mol K)$^{-1}$. If we then take a mid range value of 25 cal (mol K)$^{-1}$ for $-\Delta S^o_{ads}$ and assume, arbitrarily, that the onset of inhibition will occur when $K_B P_B$ = 0.1, the following equation shows the relation between P_B, ΔH^o_{ads}, and T at that point:

$$P_B = 0.1 \exp\left(\left(25 + \frac{\Delta H^o_B}{T}\right) R^{-1}\right) \qquad \text{Equation 5.5}$$

At 600 K, the rate or reaction of 1 atmosphere of A would be product inhibited at a conversion of 0.16%. This example serves to illustrate that the range of differential conversion, where the influence of the products on the rate can be ignored, can be substantially narrower than is usually invoked in the literature (which is usually set at 10% conversion of reactant).

5.5.1 The Problem: Ignoring Inhibition Leads to Substantial Errors

To examine the consequences of unaccounted for inhibition, we choose a CSTR because the rate can be calculated as a simple algebraic function of measured parameters, i.e.

$r = \frac{[A]_o X}{\tau}$. As a specific example, we will use the NO oxidation reaction $2NO + O_2 \rightarrow 2NO_2$ as representative of a power law rate expression. Suppose that only NO and O_2 are fed to the CSTR. The true rate of consumption of NO (r_{NO}) is taken to be

$$r_{NO} = A\exp\left(\frac{-E_A}{RT}\right)\frac{[NO]^a[O_2]^b}{[NO_2]^c}(1-\beta) \qquad \text{Equation 5.6}$$

Where $A\exp\left(\frac{-E_A}{RT}\right)$ is the forward rate constant (k_{eff}), A is the pre-exponential factor, E_a the apparent activation energy, a, b, c are the magnitudes of reaction orders, and $\beta = \frac{[NO]^2[O_2]}{K[NO_2]^2}$ is the dimensionless approach to equilibrium. Since a, b, and c are all positive and we will assume that the reaction is proceeding far from equilibrium so that β is close to zero, the true rate at any point in the reactor will be

$$r_{NO} = A\exp\left(\frac{-E_A}{RT}\right)\frac{[NO]^a[O_2]^b}{[NO_2]^c} = A\exp\left(\frac{-E_A}{RT}\right)\frac{[NO]_o^{a-c}(1-X)^a([O_2]_o - [NO]_o\frac{X}{2})^b}{(X)^c} \qquad \text{Equation 5.7}$$

$$[NO] = [NO]_o(1-X), \qquad [O]_2 = [O_2]_o - [NO]_o\tfrac{X}{2}, \qquad [NO]_o X$$

Here, X is the conversion of NO and $[NO]_o$ and $[O_2]_o$ represent the initial concentrations of species NO and O_2 in the feed. At low conversions such that X is small with respect to 1 and the numerator of Equation 5.7 becomes essentially independent of X, and Equation 5.7 simplifies to:

$$r_{NO} = \frac{\gamma\exp\left(\frac{-E_A}{RT}\right)}{X^c} \qquad \text{Equation 5.8}$$

where γ is $[NO]_o^{a-c}[O_2]_o^b$. It is usually assumed that low conversions will make the reactor differential and the rate independent of X. Examination of Equation 5.8 clearly shows that this is not the case, however. Thus, as long as the product inhibits the reaction, the reactor cannot be differential *at any conversion*.

Combining Equation 5.8 with $r_{NO} = \frac{[NO]_o X}{\tau}$ yields

$$X = \left(\frac{\tau B \exp\left(\frac{-E_a}{RT}\right)}{[NO]_o} \right)^{\frac{1}{1+c}} = \left(\tau [NO]_o^{a-c-1} [O_2]_o^b \exp\left(\frac{-E_a}{RT}\right) \right)^{\frac{1}{1+c}} \qquad \text{Equation 5.9}$$

And the corresponding change in the molar flow rates of NO from the reactor inlet to outlet is given as follows

$$F_{NO_o} - F_{NO} = \frac{[NO]_o X}{Q} = \frac{[NO]_o^{\frac{a}{1+c}}}{Q} \left(\tau [O_2]_o^b \exp\left(\frac{-E_a}{RT}\right) \right)^{\frac{1}{1+c}} \qquad \text{Equation 5.10}$$

A series of experiments run with constant inlet concentrations of NO and O_2 and a constant molar flow rate of NO, but different temperatures would produce $F_{NO_o} - F_{NO}$ as a function of T. Since r_{NO} depends only on $F_{NO_o} - F_{NO}$, in a linear fashion, a plot of $\ln(r_{NO})$ versus T^{-1} gives a straight line with slope $\frac{-E_a}{R(1+c)}$. Thus, the measured apparent activation energy (E_{meas}) would be $\frac{E_a}{1+c}$. If one mistakenly assumed that the rate was not product inhibited, then r_{NO} at low X would appear to be given by $r_{NO} = A \exp\left(\frac{-E_A}{RT}\right)[NO]^a[O_2]^b$ and E_{meas} would appear, mistakenly, to equal E_a. Thus,

ignoring product inhibition would lead to an error of a factor of $\frac{1}{1+c}$ in the activation energy. For experiments run at constant temperature and τ, but varying either $[NO]_o$ or $[O_2]_o$, with the other held constant, would produce $F_{NO_o} - F_{NO}$ as a function of $[C_i]_o$, where C is either NO or O_2. Then, plotting $\ln(r_{NO})$ versus $\ln([C_i])$ would give a slope of $\frac{a}{1+c}$ or $\frac{b}{1+c}$. Again, the measured orders of reaction would be a factor of $\frac{1}{1+c}$ too low.

For a plug flow reactor, the rate changes as X changes down the length of the reactor. If we assume constant density for simplicity, at any point in the reactor, $r_{NO} = [NO]_o \frac{dX}{d\tau}$. Using Equation 5.3 for the rate at low X and integrating down the reaction length, again produces equation Equation 5.4. The mistaken assumption that the reactor is differential and that the rate is independent of X leads to the incorrect conclusion that r_{NO} is equal to $\frac{[NO]_o X}{\tau}$. Thus, one can easily see that the mistaken assumption that a PFR is differential and that product inhibition can be ignored leads to the same error of a factor of $\frac{1}{1+c}$ in the orders and activation energy as for the CSTR. The analysis of a constant density batch reactor is identical to that for the PFR with τ replaced by time.

5.5.2 The Solution: Add Product to the Feed

If one is not sure about the existence of product inhibition, adding a measurable concentration of the products to the feed will guarantee that the rate will be independent of X and that the reactor can be considered to be differential at low X. We illustrate the procedure with the power law kinetics for the NO oxidation reaction. With NO_2 added to the feed ($[NO_2]_o$) the rate equation far from equilibrium becomes:

$$r_{NO} = A\exp\left(\frac{-E_A}{RT}\right)\frac{[NO]^a[O_2]^b}{[NO_2]^c} = A\exp\left(\frac{-E_A}{RT}\right)\frac{[NO]_o^a(1-X)^a([O_2]_o - [NO]_o\frac{X}{2})^b}{([NO_2]_o + [NO]_o X)^c} \quad \text{Equation 5.11}$$

$$= \hat{A}\exp\left(\frac{-E_A}{RT}\right)$$ Equation 5.12

Where Equation 5.12 represents the rate for small X and $\hat{A} = \frac{A[NO]_o^a[O_2]_o^b}{[NO_2]_o^c}$. Combining this rate equation into the design equation of a CSTR, $r_{NO} = \frac{[NO]_o X}{\tau}$ yields $[NO]_o X = \tau \hat{A}\exp\left(\frac{-E_a}{RT}\right)$

And $F_{NO_o} - F_{NO} = \frac{[NO]_o X}{Q} = \frac{\tau \hat{A}\exp\left(\frac{-E_a}{RT}\right)}{Q} = \frac{\tau A[NO]_o^a[O_2]_o^b \exp\left(\frac{-E_a}{RT}\right)}{Q[NO_2]_o^c}$ Equation 5.13

Thus, an investigator who measures $F_{NO_o} - F_{NO}$ with changes in temperature and inlet concentrations separately will be able to recover the true kinetic parameters by assuming a differential reactor. The rate of reaction evaluated at low NO conversion (< 10%), will be the same value everywhere in the reactor for a given set of gas concentrations and τ. This ensures that the rate is independent of conversion (at low conversions) and a separate PFR analysis will yield Equation 5.13. This renders true differential conditions even in a PFR which behaves as a CSTR.

In summary, the analysis presented predicts that $\frac{n_{cofeeding}}{n_{nocofeeding}} = 1 + c$, where $n_{cofeeding}$ is the value of the true kinetic parameter estimated in the presence of NO_2 co-feeding, $n_{nocofeeding}$ is the value of the falsified kinetic parameter in the absence of product co-feeding, and **c** is the absolute value of the apparent product order. This is experimentally demonstrated in the current case study of NO oxidation on Cu-SSZ-13. By computing $n_{cofeed} : n_{nocofeed}$

from the apparent activation energy, NO order, and O_2 order, a value of **c** can be obtained for each which should be equal to the modulus of the NO_2 apparent reaction order. This is demonstrated in Table 5.1 and Figure 5.5, which shows that the value of **c** obtained from each kinetic parameter equals to the absolute value of the NO_2 order. Thus, quantitatively, experiments match the predictions of the theory.

Table 5.1 Estimation of **c** from $n_{cofeed} : n_{nocofeed}$ ratio from various kinetic parameters.

Kinetic parameter[a]	n_{cofeed}	$n_{nocofeed}$	$n_{cofeed} : n_{nocofeed}$	**c**
Apparent activation energy	46 kJ mol^{-1}	22 kJ mol^{-1}	2.1 ± 0.2	1.1 ± 0.2
Apparent NO order	1.5	0.8	1.9 ± 0.2	0.9 ± 0.2
Apparent O_2 order	1.1	0.5	2.2 ± 0.2	1.2 ± 0.2
Apparent NO_2 order	-0.9	--	--	0.9 ± 0.1

[a]All reaction orders measured at 473 K

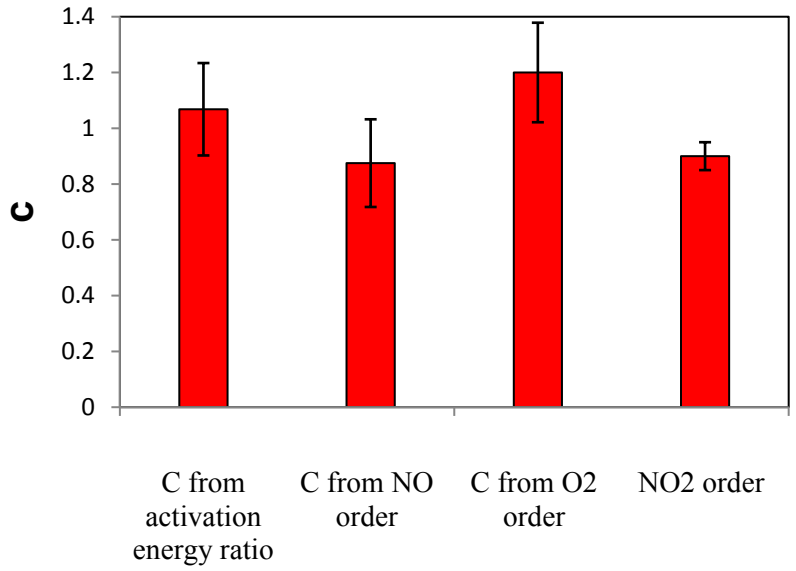

Figure 5.5 Values of c extracted from $n_{cofeed} : n_{nocofeed}$ for apparent activation energy, NO order, and O_2 order. All reaction orders measured at 473 K.

Although we have used catalytic NO oxidation over Cu-SSZ-13 as a case study to describe the effect of product inhibition, the analysis presented is valid for catalytic reactions wherein product inhibition occurs, which only contained inhibition from one product. Inhibition by multiple products can also be accommodated in the calculus of co-feeding. For example, consider the following reaction $A+B \leftrightarrow C+D$ wherein the forward rate of consumption of A (assuming $\beta << 1$) is described by Equation 5.14.

$$r_A = A\exp\left(\frac{-E_A}{RT}\right)\frac{[A]^a[B]^b}{[C]^c[D]^d} \qquad \text{Equation 5.14}$$

Once again, $A\exp\left(\frac{-E_A}{RT}\right)$ is the apparent rate constant and a, b, c, and d are the apparent reaction orders with respect to A, B, C, and D. We shall assume that a, b, c, and d are positive and non-zero, indicating that C and D inhibit the forward reaction. By performing similar analysis one can deduce that $\frac{n_{cofeeding}}{n_{nocofeeding}} = 1+c+d$ i.e, the ratio of the true kinetic parameter obtained in the presence of co-feeding of all products which inhibit the forward rate to the falsified kinetic parameter in the absence of co-feeding is $1+c+d$. Generalizing this result, for the reaction system, $\text{reactants} \leftrightarrow C_1 + C_2 + C_3 + .. + C_i$ wherein all C_i inhibit the forward rate, $\frac{n_{cofeeding}}{n_{nocofeeding}} = 1+\sum_{product} c_i$ where c_i is the absolute value of the apparent reaction order with respect to C_i. Application of this analysis to different catalytic systems in the literature is presented in Table 5.2. Although more potential examples are presented in the literature, the data are incomplete and not easily amenable to this analysis [150, 151].

Possible complications for kinetic analysis in the presence of product gas co-feeding with the reactants involve quantification of the partial pressures of the gases involved in the

reaction. The relative change in reactant and product concentrations will be small since X is small. One way to achieve the higher precision necessary for analysis is to add an internal standard to the feed and to measure the concentrations of reactants and products before and after the reactor for each process condition. Also, adding products might possibly lead to side reactions. For example, NO decomposition on Cu-zeolites to dinitrogen and oxygen is inhibited by oxygen with an apparent reaction order of -0.5 [6]. Co-feeding oxygen with NO in the feed stream produces other products like NO_2 (via NO oxidation) via reactions in parallel. In this scenario, the rate measurements must be strictly in terms of the rate of production of the desirable product, i.e. rate of production of N_2 in the example of NO decomposition, and not the rate of consumption of reactants.

Table 5.2 Literature examples of the quantitative effects of inhibition of products.

Global reaction stoichiometry	Catalyst	Kinetic parameter	n_{cofeed}	$n_{nocofeed}$	$n_{cofeed} : n_{nocofeed}$	$\sum_{product} c_i$
$2NO + O_2 \rightarrow 2NO_2$	Pt/Al_2O_3 & Pt/SiO_2	E_{app}	82	39	2.1	1.1
		NO order	1	0.5 [154]	2	1
		O_2 order	1	0.5 [154]	2	1
		NO_2 order	-1	--	--	1
$2NO + O_2 \rightarrow 2NO_2$	Pt/Al_2O_3	E_{app} [152]	100	59	1.7	0.7
		SO_2 order [152]	0.9	0.7	1.3	0.3
		O_2 order [152]	-0.2	-0.2	--	--
		SO_3 order [152]	-0.4	--	--	0.4

References are marked in square brackets
Gases which inhibit the forward reaction rate are in boldface letters

5.6 Conclusions

In view of the importance of accurate kinetic data to the advancement of catalysis, the prevalence of product inhibition, and the damage to data quality caused by overlooking product inhibition, accounting for the effects of products on the rate for all kinetic measurements would seem prudent. Adding products to the feed is a simple and reliable way to guarantee data integrity at a modest cost in analytical and reactor complexity.

CHAPTER 6. CONCLUSIONS

This thesis is devoted to the detailed understanding of the site requirements of standard ammonia SCR and NO oxidation over different Cu ion configurations within Cu-SSZ-13. Due to a wide variety of framework Al distribution within SSZ-13, many Cu ion configurations can be envisioned. Overlooking complexities, the work in this thesis leads to two types of Cu ion configurations within SSZ-13. The first is an isolated Cu(II) cation co-ordinated by four framework zeolitic oxygen atoms. This Cu ion configuration can be realized in six member rings or eight member cages of SSZ-13. The other configuration of Cu(II) is Cu_xO_y ($x \geq 2$, $y \geq 1$) species. These are exclusively found in eight member cages of SSZ-13, due to steric effects in six member rings (Chapter 3).

Exploring the site requirements of a certain reaction involves the investigation of active sites and elucidation of the dominant reaction steps on those active sites. For catalytic NO oxidation (and other generic non-selective oxidation reactions), the key requirement of an active site is the ability to active di-oxygen. This can be seen by apparent O_2 order being ~ 1 (Figure 6.1), independent of temperature. DFT results in this study (Chapter 3) show that Cu_xO_y species can activate di-oxygen via electron transfer on local Cu-O_y-Cu bonds with a downhill Gibbs free energy change; while isolated Cu(II) ions do not have this ability. This leads to a remarkable difference in the rate of NO oxidation Using *in-situ* X-ray absorption spectroscopy, the rate of NO oxidation was linearly correlated with the density of local Cu-Oy-Cu bonds. As a result the NO oxidation rate was within experimental error on catalysts prepared to contain only isolated Cu(II) ions within SSZ-13. The ability of NO oxidation to discriminate between different Cu ion configurations makes it an ideal probe reaction to detect Cu ion clustering for catalyst diagnostic purposes.

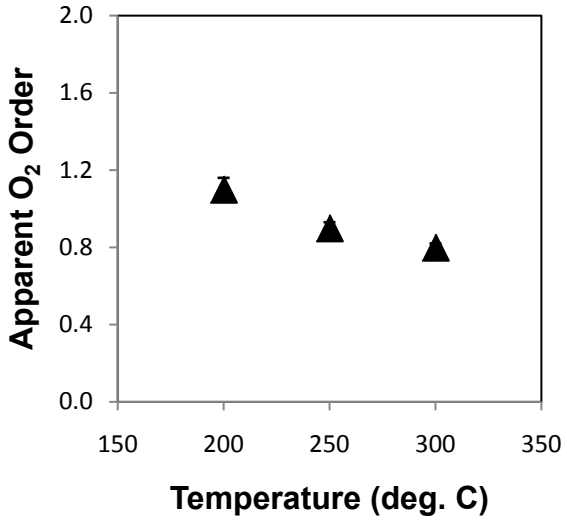

Figure 6.1 Variation of the apparent oxygen order during NO oxidation on Cu-SSZ-13. Feed concentrations : 300 ppm NO, 150 ppm NO_2.

On the other hand, Standard ammonia SCR is mediated primarily by isolated Cu ions within SSZ-13. Results in this thesis only focus on isolated Cu ions stabilized by two framework Al atoms in the six member rings of SSZ-13 (Chapter 2). The active site assignment is based on the linear variation of the SCR rate per gram with total Cu content (mol Cu . g cat^{-1}), and DFT results of energetically most favorable position of isolated Cu(II) ions in SSZ-13. This is supplemented by UV-Vis-NIR spectroscopy and X-ray absorption near edge structure (XANES) of Cu ions during standard SCR. *Operando* XANES also reveal that the +2 oxidation state is not retained on Cu ions during SCR catalysis. A redox between Cu(I) and Cu(II) is observed. Studies in Chapter 3 explored possible ways to explain the molecular origins of the redox nature of isolated Cu ions during standard SCR. Separate residual Brønsted acid site titrations with amine titrants (Chapter 2) revealed that isolated Cu(II) ions are stabilized by removal of two protons from the Brønsted acid sites during synthesis and subsequent pretreatment in dry air. This configuration, however can convert to a Cu(I) which exposes a proximal Brønsted acidic site which is capable of stabilizing ammonia during catalysis. This remarkable arrangement of active isolated Cu ions within SSZ-13 is the primary reason for bi-functional catalytic behavior shown by these active sites during standard SCR. NO + NH_3

have the ability to reduce a Cu(II) to Cu(I) and a proximal Brønsted acid site (during standard SCR). The Cu(I) has the ability to make nitrites (NO_2^-) which reacts with ammonium ions nearby to form water and nitrogen, thereby completing the catalytic cycle and regenerating an isolated Cu(II).

Future studies should concentrate on the role of residual acid sites during standard SCR, effect of zeolite topology on catalytically relevant steps during standard SCR, as well as development of active site titration during SCR catalysis.

LIST OF REFERENCES

LIST OF REFERENCES

[1] J.H. Kwak, D. Tran, S.D. Burton, J. Szanyi, J.H. Lee, C.H.F. Peden, Effects of hydrothermal aging on NH3-SCR reaction over Cu/zeolites, Journal of Catalysis, 287 (2012) 203-209.

[2] S. Brandenberger, O. Kroecher, A. Tissler, R. Althoff, The State of the Art in Selective Catalytic Reduction of NOx by Ammonia Using Metal-Exchanged Zeolite Catalysts, Catalysis Reviews - Science & Engineering, 50 (2008) 492-531.

[3] P. Forzatti, I. Nova, E. Tronconi, A. Kustov, J.R. ThÃ¸gersen, Effect of operating variables on the enhanced SCR reaction over a commercial V2O5/WO3/TiO2 catalyst for stationary applications, Catalysis Today, 184 153-159.

[4] N.Y. Topsoe, J.A. Dumesic, H. Topsoe, Vanadia-Titania Catalysts for Selective Catalytic Reduction of Nitric-Oxide by Ammonia: I.I. Studies of Active Sites and Formulation of Catalytic Cycles, Journal of Catalysis, 151 (1995) 241-252.

[5] M. Iwamoto, H. Hamada, Removal of Nitorgen Monoxide from Exhaust Gases through Novel Catalytic Processes, Catalysis Today, 10 (1991) 57-71.

[6] B. Moden, P. Da Costa, B. Fonfe, D.K. Lee, E. Iglesia, Kinetics and Mechanism of Steady-State Catalytic NO Decomposition Reactions on Cu-ZSM5, Journal of Catalysis, 209 (2002) 75-86.

[7] J.-H. Park, H.J. Park, J.H. Baik, I.-S. Nam, C.-H. Shin, J.-H. Lee, B.K. Cho, S.H. Oh, Hydrothermal stability of CuZSM5 catalyst in reducing NO by NH3 for the urea selective catalytic reduction process, Journal of Catalysis, 240 (2006) 47-57.

[8] H. Sjövall, L. Olsson, E. Fridell, R.J. Blint, Selective catalytic reduction of NOx with NH_3 over Cu-ZSM-5—The effect of changing the gas composition, Applied Catalysis B: Environmental, 64 (2006) 180-188.

[9] C.H.F. Peden, J.H. Kwak, S.D. Burton, R.G. Tonkyn, D.H. Kim, J.-H. Lee, H.-W. Jen, G. Cavataio, Y. Cheng, C.K. Lambert, Possible origin of improved high temperature performance of hydrothermally aged Cu/beta zeolite catalysts, Catalysis Today, 184 245-251.

[10] N. Wilken, K. Wijayanti, K. Kamasamudram, N.W. Currier, R. Vedaiyan, A. Yezerets, L. Olsson, Mechanistic investigation of hydrothermal aging of Cu-Beta for ammonia SCR, Applied Catalysis B: Environmental, 111-112 58-66.

[11] R. Delahay, S. Kieger, N. Tanchoux, P. Trens, B. Coq, Kinetics of the selective catalytic reduction of NO by NH_3 on a Cu-faujasite catalyst, Applied Catalysis B-Environmental, 52 (2004) 251-257.

[12] S.p. Kieger, G.r. Delahay, B. Coq, B. Neveu, Selective Catalytic Reduction of Nitric Oxide by Ammonia over Cu-FAU Catalysts in Oxygen-Rich Atmosphere, Journal of Catalysis, 183 (1999) 267-280.

[13] F. Gao, J.H. Kwak, J. Szanyi, C.H.F. Peden, Current Understanding of Cu-Exchanged Chabazite Molecular Sieves for Use as Commercial Diesel Engine DeNOx Catalysts, Topics in Catalysis, 56 1441-1459.

[14] S.T. Korhonen, D.W. Fickel, R.F. Lobo, B.M. Weckhuysen, A.M. Beale, Isolated Cu(2+) ions: active sites for selective catalytic reduction of NO, Chemical Communications, 47 (2011) 800-802.

[15] U. Deka, A. Juhin, E.A. Eilertsen, H. Emerich, M.A. Green, S.T. Korhonen, B.M. Weckhuysen, A.M. Beale, Confirmation of Isolated Cu^{2+} Ions in SSZ-13 Zeolite as Active Sites in NH_3-Selective Catalytic Reduction, Journal of Physical Chemistry C, 116 (2012) 4809-4818.

[16] J.H. Kwak, H.Y. Zhu, J.H. Lee, C.H.F. Peden, J. Szanyi, Two different cationic positions in Cu-SSZ-13?, Chemical Communications, 48 (2012) 4758.

[17] Q. Guo, F. Fan, D. Ligthart, G. Li, Z. Feng, E.J. Hensen, C. Li, Effect of the Nature and Location of Copper Species on the Catalytic Nitric Oxide Selective Catalytic Reduction Performance of the Copper/SSZ-13 Zeolite, ChemCatChem, 6 (2014) 634-639.

[18] F. Gao, E.D. Walter, E.M. Karp, J. Luo, R.G. Tonkyn, J.H. Kwak, J. Szanyi, C.H.F. Peden, Structure–activity relationships in NH_3-SCR over Cu-SSZ-13 as probed by reaction kinetics and EPR studies, Journal of Catalysis, 300 (2013) 20-29.

[19] J. Xue, X. Wang, G. Qi, J. Wang, M. Shen, W. Li, Characterization of copper species over Cu/SAPO-34 in selective catalytic reduction of NOx with ammonia: Relationships between active Cu sites and de-NOx performance at low temperature, Journal of Catalysis, 297 (2013) 56-64.

[20] P.S. Metkar, V. Balakotaiah, M.P. Harold, Experimental and kinetic modeling study of NO oxidation: Comparison of Fe and Cu-zeolite catalysts, Catalysis Today, 184 (2012) 115-128.

[21] J.H. Kwak, D. Tran, J. Szanyi, C.H.F. Peden, J.H. Lee, The Effect of Copper Loading on the Selective Catalytic Reduction of Nitric Oxide by Ammonia Over Cu-SSZ-13, Catalysis Letters, 142 (2012) 295-301.

[22] J.H. Kwak, J.H. Lee, S.D. Burton, A.S. Lipton, C.H.F. Peden, J.n. Szanyi, A Common Intermediate for N2 Formation in Enzymes and Zeolites: Side-On Cu-Nitrosyl Complexes, Angewandte Chemie, 125 10169-10173.

[23] M. Ruggeri, I. Nova, E. Tronconi, Experimental Study of the NO Oxidation to NO_2 Over Metal Promoted Zeolites Aimed at the Identification of the Standard SCR Rate Determining Step, Topics in Catalysis, 56 (2013) 109-113.

[24] J.-S. McEwen, T. Anggara, W.F. Schneider, V.F. Kispersky, J.T. Miller, W.N. Delgass, F.H. Ribeiro, Integrated operando X-ray absorption and DFT characterization of Cu–SSZ-13 exchange sites during the selective catalytic reduction of NOx with NH_3, Catalysis Today, 184 (2012) 129-144.

[25] V.F. Kispersky, A.J. Kropf, F.H. Ribeiro, J.T. Miller, Low absorption vitreous carbon reactors for operando XAS: a case study on Cu/Zeolites for selective catalytic reduction of NOx by NH3, Physical Chemistry Chemical Physics, 14 (2012) 2229-2238.

[26] S.A. Bates, W.N. Delgass, F.H. Ribeiro, J.T. Miller, R. Gounder, Methods for NH_3 titration of Brønsted acid sites in Cu-zeolites that catalyze the selective catalytic reduction of NO_x with NH_3, Journal of Catalysis, 312 (2014) 26-36.

[27] J.H. Kwak, R.G. Tonkyn, D.H. Kim, J. Szanyi, C.H.F. Peden, Excellent activity and selectivity of Cu-SSZ-13 in the selective catalytic reduction of NOx with NH3, Journal of Catalysis, 275 (2010) 187-190.

[28] D.W. Fickel, E. D'Addio, J.A. Lauterbach, R.F. Lobo, The ammonia selective catalytic reduction activity of copper-exchanged small-pore zeolites, Applied Catalysis B-Environmental, 102 (2011) 441-448.

[29] I. Bull, R.S. Boorse, W.M. Jaglowski, G.S. Koermer, A. Moini, J.A. Patchett, W.M. Xue, P. Burk, J.C. Dettling, M.T. Caudle, 7601662, in, US, 2009.

[30] D.W. Fickel, J.M. Fedeyko, R.F. Lobo, Copper Coordination in Cu-SSZ-13 and Cu-SSZ-16 Investigated by Variable-Temperature XRD, Journal of Physical Chemistry C, 114 (2010) 1633-1640.

[31] L. Wang, W. Li, G. Qi, D. Weng, Location and nature of Cu species in Cu/SAPO-34 for selective catalytic reduction of NO with NH_3, Journal of Catalysis, 289 (2012) 21-29.

[32] B.R. Goodman, K.C. Hass, W.F. Schneider, J.B. Adams, Statistical Analysis of Al Distributions and Metal Ion Pairing Probabilies in Zeolites, Catalysis Letters, 68 (2000) 85-93.

[33] W. Loewenstein, The Distribution of aluminum in the tetrahedra of silicates and aluminates, American Mineralogist, 39 (1954) 92-96.

[34] H.Y. Huang, R.Q. Long, R.T. Yang, Kinetics of selective catalytic reduction of NO with NH_3 on Fe-ZSM-5 catalyst, Applied Catalysis A: General, 235 (2002) 241-251.

[35] T. Komatsu, M. Nunokawa, I.S. Moon, T. Takahara, S. Namba, T. Yashima, Kinetic-Studies of Reduction of Nitric-Oxide With Ammonia on Cu^{2+}-Exchanged Zeolites, Journal of Catalysis, 148 (1994) 427-437.

[36] S.A. Stevenson, J.C. Vartuli, C.F. Brooks, Kinetics of the Selective Catalytic Reduction of NO over HZSM-5, Journal of Catalysis, 190 (2000) 228-239.

[37] J. Eng, Kinetic and Mechanistic Study of NOx Reduction by NH_3 over H-Form Zeolites, Journal of Catalysis, 171 (1997) 27-44.

[38] P.S. Metkar, N. Salazar, R. Muncrief, V. Balakotaiah, M.P. Harold, Selective catalytic reduction of NO with NH3 on iron zeolite monolithic catalysts: Steady-state and transient kinetics, Applied Catalysis B: Environmental, 104 (2011) 110-126.

[39] K. Rahkamaa-Tolonen, T. Maunula, M. Lomma, M. Huuhtanen, R.L. Keiski, The effect of NO_2 on the activity of fresh and aged zeolite catalysts in the NH_3-SCR reaction, Catalysis Today, 100 (2005) 217-222.

[40] R.Q. Long, R.T. Yang, Superior Fe-ZSM-5 catalyst for selective catalytic reduction of nitric oxide by ammonia, Journal of the American Chemical Society, 121 (1999) 5595-5596.

[41] A.L. Kustov, T.W. Hansen, M. Kustova, C.H. Christensen, Selective catalytic reduction of NO by ammonia using mesoporous Fe-containing HZSM-5 and HZSM-12 zeolite catalysts: An option for automotive applications, Applied Catalysis B: Environmental, 76 (2007) 311-319.

[42] S. Brandenberger, O. Kröcher, A. Wokaun, A. Tissler, R. Althoff, The role of Brønsted acidity in the selective catalytic reduction of NO with ammonia over Fe-ZSM-5, Journal of Catalysis, 268 (2009) 297-306.

[43] S.I. Zones, 4544538, in, US, 1985.

[44] S.I. Zones, R.A. Van Nordstrand, Novel zeolite transformations: The template-mediated conversion of Cubic P zeolite to SSZ-13, Zeolites, 8 (1988) 166-174.

[45] S.I. Zones, Conversion of faujasites to high-silica chabazite SSZ-13 in the presence of N,N,N-trimethyl-1-adamantammonium iodide, Journal of the Chemical Society, Faraday Transactions, 87 (1991) 3709-3716.

[46] International Zeolite Association, http://www.iza-online.org/, in.

[47] H. Robson, How to read a patent, Microporous and Mesoporous Materials, 22 (1998) 551-551.

[48] Q. Zhu, J.N. Kondo, T. Tatsumi, S. Inagaki, R. Ohnuma, Y. Kubota, Y. Shimodaira, H. Kobayashi, K. Domen, A comparative study of methanol to olefin over CHA and MTF zeolites, Journal of Physical Chemistry C, 111 (2007) 5409-5415.

[49] A. Zecchina, S. Bordiga, J.G. Vitillo, G. Ricchiardi, C. Lamberti, G. Spoto, M. Bjørgen, K.P. Lillerud, Liquid Hydrogen in Protonic Chabazite, Journal of the American Chemical Society, 127 (2005) 6361-6366.

[50] L. Sommer, D. Mores, S. Svelle, M. Stocker, B.M. Weckhuysen, U. Olsbye, Mesopore formation in zeolite H-SSZ-13 by desilication with NaOH, Microporous and Mesoporous Materials, 132 (2010) 384-394.

[51] G.L. Woolery, G.H. Kuehl, H.C. Timken, A.W. Chester, J.C. Vartuli, On the nature of framework Brønsted and Lewis acid sites in ZSM-5, Zeolites, 19 (1997) 288-296.

[52] L.S. Kau, D.J. Spira-Solomon, J.E. Penner-Hahn, K.O. Hodgson, E.I. Solomon, X-ray absorption edge determination of the oxidation state and coordination number of copper. Application to the type 3 site in Rhus vernicifera laccase and its reaction with oxygen, Journal of the American Chemical Society, 109 (1987) 6433-6442.

[53] D.-J. Liu, H.J. Robota, In situ characterization of Cu-ZSM-5 by X-ray absorption spectroscopy: XANES study of the copper oxidation state during selective catalytic reduction of nitric oxide by hydrocarbons, Applied Catalysis B: Environmental, 4 (1994) 155-165.

[54] K.C.C. Kharas, D.-J. Liu, H.J. Robota, Structure-function properties in Cu-ZSM-5 no decomposition and NO SCR catalysts, Catalysis Today, 26 (1995) 129-145.

[55] D.-J. Liu, H. Robota, In situ XANES characterization of the Cu oxidation state in Cu-ZSM-5 during NO decomposition catalysis, Catalysis Letters, 21 (1993) 291-301.

[56] C. Lamberti, S. Bordiga, M. Salvalaggio, G. Spoto, A. Zecchina, F. Geobaldo, G. Vlaic, M. Bellatreccia, XAFS, IR, and UV-vis study of the Cu-I environment in Cu-I-ZSM-5, Journal of Physical Chemistry B, 101 (1997) 344-360.

[57] I.J. Drake, Y.H. Zhang, M.K. Gilles, C.N.T. Liu, P. Nachimuthu, R.C.C. Perera, H. Wakita, A.T. Bell, An in situ AlK-edge XAS investigation of the local environment of H+- and Cu+-exchanged USY and ZSM-5 zeolites, Journal of Physical Chemistry B, 110 (2006) 11665-11676.

[58] K. Mathisen, M. Stockenhuber, D.G. Nicholson, In situ XAS and IR studies on Cu:SAPO-5 and Cu:SAPO-11: the contributory role of monomeric linear copper(I) species in the selective catalytic reduction of NO(x) by propene, Physical Chemistry Chemical Physics, 11 (2009) 5476-5488.

[59] G. Lamble, A. Moen, D.G. Nicholson, Structure of the diamminecopper(I) ion in solution. An X-ray absorption spectroscopic study, Journal of the Chemical Society, Faraday Transactions, 90 (1994) 2211-2213.

[60] A. Moen, D.G. Nicholson, M. Ronning, Studies on the pre-edge region of the X-ray absorption spectra of copper(I) oxide and the diamminecopper(I) ion, Journal of the Chemical Society, Faraday Transactions, 91 (1995) 3189-3194.

[61] B. Fingland, F. Ribeiro, J. Miller, Simultaneous Measurement of X-ray Absorption Spectra and Kinetics: A Fixed-bed, Plug-flow Operando Reactor, Catalysis Letters, 131 (2009) 1-6.

[62] G. Kresse, J. Furthmüller, Efficiency of ab-initio total energy calculations for metals and semiconductors using a plane-wave basis set, Computational Material Science, 6 (1996) 15-50.

[63] G. Kresse, J. Furthmüller, Efficient iterative schemes for ab initio total-energy calculations using a plane-wave basis set, Physical Review B, 54 (1996) 11169-11186.

[64] VASP, in, http://cms.mpi.univie.ac.at/vasp/.

[65] G. Kresse, D. Joubert, From ultrasoft pseudopotentials to the projector augmented-wave method, Physical Review B, 59 (1999) 1758-1775.

[66] J.P. Perdew, Y. Wang, Accurate and simple analytic representation of the electron-gas correlation energy, Physical Review B, 45 (1992) 13244-13249.

[67] J. Dědeček, B. Wichterlová, Role of Hydrated Cu Ion Complexes and Aluminum Distribution in the Framework on the Cu Ion Siting in ZSM-5, The Journal of Physical Chemistry B, 101 (1997) 10233-10240.

[68] M.J. Rice, A.K. Chakraborty, A.T. Bell, Al Next Nearest Neighbor, Ring Occupation, and Proximity Statistics in ZSM-5, Journal of Catalysis, 186 (1999) 222-227.

[69] R.J. Madon, M. Boudart, Experimental criterion for the absence of artifacts in the measurement of rates of heterogeneous catalytic reactions, Industrial & Engineering Chemistry Fundamentals, 21 (1982) 438-447.

[70] R.M. Koros, E.J. Nowak, A diagnostic test of the kinetic regime in a packed bed reactor, Chem. Eng. Sci., 22 (1967) 470.

[71] S.A. Bates, V.F. Kispersky, A. Yezerets, W.F. Schnieder, J.T. Miller, W.N. Delgass, F.H. Ribeiro, Investigation of the Redox Sites of the Half-reactions of Selective Catalytic Reduction of NOx by NH3 via Operando X-ray Absorption of Cu/SSZ-13, in preparation.

[72] A.A. Verma, S.A. Bates, T. Anggara, C. Paolucci, A.A. Parekh, K. Kamasamudram, A. Yezerets, J.T. Miller, W.N. Delgass, W.F. Schneider, F.H. Ribeiro, NO oxidation: A probe reaction on Cu-SSZ-13, Journal of Catalysis, 312 179-190.

[73] D.J. Parrillo, A.T. Adamo, G.T. Kokotailo, R.J. Gorte, Amine adsorption in H-ZSM-5, Applied Catalysis, 67 (1990) 107-118.

[74] A.G. Palkhiwala, R.J. Gorte, Characterization of H-FER and H-TON using temperature-programmed desorption of alkylamines, Catalysis Letters, 57 (1999) 19-23.

[75] O. Kresnawahjuesa, R.J. Gorte, D.d. Oliveira, L.Y. Lau, A Simple, Inexpensive, and Reliable Method for Measuring Bronsted-acid Site Densities in Solid Acids, Catalysis Letters, 82 (2002) 155-160.

[76] S.M. Campbell, X.-Z. Jiang, R.F. Howe, Methanol to hydrocarbons: spectroscopic studies and the significance of extra-framework aluminium, Microporous and Mesoporous Materials, 29 (1999) 91-108.

[77] K. Kamasamudram, N.W. Currier, X. Chen, A. Yezerets, Overview of the practically important behaviors of zeolite-based urea-SCR catalysts, using compact experimental protocol, Catalysis Today, 151 (2010) 212-222.

[78] H. Sjövall, R.J. Blint, L. Olsson, Detailed Kinetic Modeling of NH_3 and H_2O Adsorption, and NH_3 Oxidation over Cu-ZSM-5, The Journal of Physical Chemistry C, 113 (2009) 1393-1405.

[79] F. Gao, J.H. Kwak, J. Szanyi, C.H.F. Peden, Current Understanding of Cu Exchanged Chabazite Molecular Sieves for Use as Commercial Diesel Engine DeNOx Catalysts, Topics in Catalysis, (2013).

[80] U. Deka, I. Lezcano-Gonzalez, B.M. Weckhuysen, A.M. Beale, Local Environment and Nature of Cu Active Sites in Zeolite-Based Catalysts for the Selective Catalytic Reduction of NOx, ACS Catalysis, 3 (2013) 413-427.

[81] C. Kieffer, J. Lavy, E. Jeudy, N. Bats, G. Delahay, Characterisation of a Commercial Automotive NH_3-SCR Copper–Zeolite Catalyst, Top Catal, 56 (2013) 40-44.

[82] W.F. Schneider, K.C. Hass, R. Ramprasad, J.B. Adams, Cluster Models of Cu Binding and CO and NO Adsorption in Cu-Exchanged Zeolites, Journal of Physical Chemistry 100 (1996) 6032-6046.

[83] W.F. Schneider, K.C. Hass, R. Ramprasad, J.B. Adams, First-Principles Analysis of Elementary Steps in the Catalytic Decomposition of NO by Cu-Exchanged Zeolites, Journal of Physical Chemistry B, 101 (1997) 4353-4357.

[84] W.F. Schneider, K.C. Hass, R. Ramprasad, J.B. Adams, Density Functional Theory Study of Transformations of Nitrogen Oxides Catalyzed by Cu-Exchanged Zeolites, Journal of Physical Chemistry B, 102 (1998) 3692-3705.

[85] B.L. Trout, A.K. Chakraborty, A.T. Bell, Analysis of the Thermochemistry of NOx Decomposition over CuZSM-5 Based on Quantum Chemical and Statistical Mechanical Calculations, Journal of Physical Chemistry 100 (1996) 17582-17592.

[86] B.L. Trout, A.K. Chakraborty, A.T. Bell, Local Spin Density Functional Theory Study of Copper Ion-Exchanged ZSM-5, Journal of Physical Chemistry B, 100 (1996) 4173-4179.

[87] A. Pulido, P. Nachtigall, Correlation Between Catalytic Activity and Metal Cation Coordination: NO Decomposition Over Cu/Zeolites, ChemCatChem, 1 (2009) 449-453.

[88] X. Liu, Z. Yang, R. Zhang, Q. Li, Y. Li, Density Functional Theory Study of Mechanism of N2O Decomposition over Cu-ZSM-5 Zeolites, Journal of Physical Chemistry C, 116 (2012) 20262-20268.

[89] B.R. Goodman, W.F. Schneider, K.C. Hass, J.B. Adams, Theoretical Analysis of oxygen-bridged Cu pairs in Cu-exchanged zeolites, Catalysis Letters, 56 (1998) 183-188.

[90] B.R. Goodman, K.C. Hass, W.F. Schneider, J.B. Adams, Cluster Model Studies of Oxygen-Bridged Cu Pairs in Cu-ZSM-5 Catalysts, Journal of Physical Chemistry B, 103 (1999) 10452-10460.

[91] J.S. Woertink, P.J. Smeets, M.H. Groothaert, M.A. Vance, B.F. Sels, R.A. Schoonheydt, E.I. Solomon, A $[Cu_2O]^{2+}$ core in Cu-ZSM-5, the active site in the oxidation of methane to methanol, Proceedings of the National Academy of Sciences U.S.A., 106 (2009) 18908-18913.

[92] P.J. Smeets, R.G. Hadt, J.S. Woertink, P. Vanelderen, R.A. Schoonheydt, B.F. Sels, E.I. Solomon, Oxygen Precursor to the Reactive Intermediate in Methanol Synthesis by Cu-ZSM-5, The Journal of American Chemical Society, 132 (2010) 14736-14738.

[93] P. Vanelderen, R.G. Hadt, P.J. Smeets, E.I. Solomon, R.A. Schoonheydt, B.F. Sels, Cu-ZSM-5: A biomimetic inorganic model for methane oxidation, Journal of Catalysis, 284 (2011) 157-164.

[94] T. Yumura, M. Takeuchi, H. Kobayashi, Y. Kuroda, Effects of ZSM-5 Zeolite Confinement on Reaction Intermediates during Dioxygen Activation by Enclosed Dicopper Cations, Inorganic Chemistry, 48 (2008) 508-517.

[95] F. Göltl, J. Hafner, Structure and properties of metal-exchanged zeolites studies using gradient-corrected and hybrid functionals. I. Structure and energetics, Journal of Chemical Physics, 136 (2012) 064501.

[96] F. Goltl, J. Hafner, Structure and properties of metal-exchanged zeolites studied using gradient-corrected and hybrid functionals. II. Electronic structure and photoluminescence spectra, Journal of Chemical Physics, 136 (2012) 064502-064517.

[97] F. Goltl, J. Hafner, Structure and properties of metal-exchanged zeolites studied using gradient-corrected and hybrid functionals. III. Energetics and vibrational spectroscopy of adsorbates, Journal of Chemical Physics, 136 (2012) 064503-064531.

[98] F. Göltl, R.E. Bulo, J. Hafner, P. Sautet, What Makes Copper-Exchanged SSZ-13 Zeolite Efficient at Cleaning Car Exhaust Gases?, Journal of Physical Chemistry Letters, 4 (2013) 2244-2249.

[99] E.A. Pidko, E.J.M. Hensen, R.A. van Santen, Self-organization of extraframework cations in zeolites, Proceedings of the Royal Society A, 468 (2012) 2070-2086.

[100] www.iza-online.org, International Zeolite Association (IZA), in.

[101] J.H. Pazmino, J.T. Miller, S.S. Mulla, W.N. Delgass, F.H. Ribeiro, Kinetic studies of the stability of Pt for NO oxidation: Effect of sulfur and long-term aging, Journal of Catalysis, 282 (2011) 13-24.

[102] B.A. De Moor, A. Ghysels, M.-F.o. Reyniers, V. Van Speybroeck, M. Waroquier, G.B. Marin, Normal Mode Analysis in Zeolites: Toward an Efficient Calculation of Adsorption Entropies, Journal of Chemical Theory and Computation, 7 (2011) 1090-1101.

[103] R.B. Getman, W.F. Schneider, DFT-Based Coverage-Dependent Model of Pt-Catalyzed NO Oxidation, ChemCatChem, 2 (2010) 1450-1460.

[104] A.D. Becke, Density-functional exchange-energy approximation with correct asymptotic behavior, Physical Review A, 38 (1988) 3098-3100.

[105] A.D. Becke, Density-functional thermochemistry. III. The role of exact exchange, J. Chemical Physics, 98 (1993) 5648-5652.

[106] C. Lee, W. Yang, R.G. Parr, Development of the Colle-Salvetti correlation-energy formula into a functional of the electron density, Physical Review B, 37 (1988) 785-789.

[107] R. Bulanek, H. Drobna, P. Nachtigall, M. Rubes, O. Bludsky, On the site-specificity of polycarbonyl complexes in Cu/zeolites: combined experimental and DFT study, Physical Chemistry Chemical Physics, 8 (2006) 5535-5542.

[108] C. Tuma, J. Sauer, A hybrid MP2/planewave-DFT scheme for large chemical systems: proton jumps in zeolites, Chemical Physics Letters, 387 (2004) 388-394.

[109] C. Tuma, J. Sauer, Treating dispersion effects in extended systems by hybrid MP2:DFT calculations-protonation of isobutene in zeolite ferrierite, Physical Chemistry Chemical Physics, 8 (2006) 3955-3965.

[110] N. Hansen, T. Kerber, J. Sauer, A.T. Bell, F.J. Keil, Quantum Chemical Modeling of Benzene Ethylation over H-ZSM-5 Approaching Chemical Accuracy: A Hybrid MP2:DFT Study, Journal of the American Chemical Society, 132 (2010) 11525-11538.

[111] S. Svelle, C. Tuma, X. Rozanska, T. Kerber, J. Sauer, Quantum Chemical Modeling of Zeolite-Catalyzed Methylation Reactions: Toward Chemical Accuracy for Barriers, Journal of American Chemical Society, 131 (2008) 816-825.

[112] O. Bludský, M. Rubeš, P. Soldán, P. Nachtigall, Investigation of the benzene-dimer potential energy surface: DFT/CCSD(T) correction scheme, Journal of Chemical Physics, 128 (2008) -.

[113] C. Fonseca Guerra, J.G. Snijders, G. te Velde, E.J. Baerends, Towards an order-N DFT method, Theoretical Chemistry accounts, 99 (1998) 391-403.

[114] G. te Velde, F.M. Bickelhaupt, E.J. Baerends, C. Fonseca Guerra, S.J.A. van Gisbergen, J.G. Snijders, T. Ziegler, Chemistry with ADF, Journal of Computational Chemistry, 22 (2001) 931-967.

[115] G. te Velde, E.J. Baerends, Numerical integration for polyatomic systems, Journal of Computational Physics, 99 (1992) 84-98.

[116] NIST-JANAF Thermochemical Tables, in: http://kinetics.nist.gov/janaf/. .

[117] B.M. Weiss, E. Iglesia, Mechanism and site requirements for NO oxidation on Pd catalysts, Journal of Catalysis, 272 (2010) 74-81.

[118] S. Joshi, Diagnostic of Zeolite-based SCR catalyst deactivation modes using NO oxidation as a probe reaction, in: 23rd North American Catalysis Society Meeting, NAM, 2013.

[119] S.S. Mulla, N. Chen, W.N. Delgass, W.S. Epling, F.H. Ribeiro, NO_2 inhibits the catalytic reaction of NO and O_2 over Pt, Catalysis Letters, 100 (2005) 267-270.

[120] F. Giordanino, P.N.R. Vennestrom, L.F. Lundegaard, F.N. Stappen, S. Mossin, P. Beato, S. Bordiga, C. Lamberti, Characterization of Cu-exchanged SSZ-13: a comparative FTIR, UV-Vis, and EPR study with Cu-ZSM-5 and Cu-[small beta] with similar Si/Al and Cu/Al ratios, Dalton Transactions, (2013).

[121] L. Wang, J.R. Gaudet, W. Li, D. Weng, Migration of Cu species in Cu/SAPO-34 during hydrothermal aging, Journal of Catalysis, 306 (2013) 68-77.

[122] R. Gounder, A.J. Jones, R.T. Carr, E. Iglesia, Solvation and acid strength effects on catalysis by faujasite zeolites, Journal of Catalysis, 286 (2012) 214-223.

[123] M.H. Groothaert, K. Lievens, H. Leeman, B.M. Weckhuysen, R.A. Schoonheydt, An operando optical fiber UV–vis spectroscopic study of the catalytic decomposition of NO and N_2O over Cu-ZSM-5, Journal of Catalysis, 220 (2003) 500-512.

[124] M.H. Groothaert, J.A. van Bokhoven, A.A. Battiston, B.M. Weckhuysen, R.A. Schoonheydt, Bis(m-oxo)dicopper in Cu-ZSM-5 and its role in the decomposition of NO: a combined *in situ* XAFS, UV-vis-NIR and kinetic study, Journal of the American Chemical Society, 125 (2003) 7629-7640.

[125] M.H. Groothaert, P.J. Smeets, B.F. Sels, P.A. Jacobs, R.A. Schoonheydt, Selective Oxidation of Methane by the Bis(μ-oxo)dicopper Core Stabilized on ZSM-5 and Mordenite Zeolites, The Journal of American Chemical Society, 127 (2005) 1394-1395.

[126] K.-i. Shimizu, R. Maruyama, T. Hatamachi, T. Kodama, O2-Bridged Multicopper(II) Complex in Zeolite for Catalytic Direct Photo-oxidation of Benzene to Diphenols, Journal of Physical Chemistry C, 111 (2007) 6440-6446.

[127] K.-i. Shimizu, Y. Murata, A. Satsuma, Dicopper(II)−Dioxygen Complexes in Y Zeolite for Selective Catalytic Oxidation of Cyclohexane under Photoirradiation, Journal of Physical Chemistry C, 111 (2007) 19043-19051.

[128] Y. Xu, W.A. Shelton, W.F. Schneider, Effect of Particle Size on the Oxidizability of Platinum Clusters, Journal of Physical Chemistry A, 110 (2006) 5839-5846.

[129] S. Bennici, A. Gervasini, N. Ravasio, F. Zaccheria, Optimization of Tailoring of CuO_xSpecies of Silica Alumina Supported Catalysts for the Selective Catalytic Reduction of NO*x*, Journal of Physical Chemistry B, 107 (2003) 5168-5176.

[130] G.-T. Bae, B. Dellinger, R.W. Hall, Density Functional Calculation of the Structure and Electronic Properties of CunOn (n = 1−8) Clusters, Journal of Physical Chemistry A, 115 (2011) 2087-2095.

[131] J. Dědeček, O. Bortnovsky, A. Vondrová, B. Wichterlová, Catalytic Activity of Cu-Beta Zeolite in NO Decomposition: Effect of Copper and Aluminium Distribution, Journal of Catalysis, 200 (2001) 160-170.

[132] M. Colombo, I. Nova, E. Tronconi, NO_2 adsorption on Fe- and Cu-zeolite catalysts: The effect of the catalyst red–ox state, Applied Catalysis B, 111–112 (2012) 433-444.

[133] L. Ma, Y. Cheng, G. Cavataio, R.W. McCabe, L. Fu, J. Li, Characterization of commercial Cu-SSZ-13 and Cu-SAPO-34 catalysts with hydrothermal treatment for NH3-SCR of NOx in diesel exhaust, Chemical Engineering Journal, 225 (2013) 323-330.

[134] A. Kumar, Effect of Hydrothermal Aging on Various Catalytic Functions of a Small-Pore Cu-Zeolite Catalyst with CHA-type Structure, in: 23rd North American Catalysis Society Meeting, NAM, 2013.

[135] S.A. Bates, A.A. Verma, C. Paolucci, A.A. Parekh, T. Anggara, A. Yezerets, W.F. Schneider, J.T. Miller, W.N. Delgass, F.H. Ribeiro, Identification of the active Cu site in standard selective catalytic reduction with ammonia on Cu-SSZ-13, Journal of Catalysis, 312 (2014) 87-97.

[136] D.E. Doronkin, M. Casapu, T. Günter, O. Müller, R. Frahm, J.-D. Grunwaldt, Operando Spatially and Time Resolved XAS Study on Zeolite Catalysts for Selective Catalytic Reduction of NOx by NH3, The Journal of Physical Chemistry C, (2014).

[137] R.B. Getman, Y. Xu, W.F. Schneider, Thermodynamics of Environment-Dependent Oxygen Chemisorption on Pt (111)†, The Journal of Physical Chemistry C, 112 (2008) 9559-9572.

[138] A.L. Myers, Characterization of nanopores by standard enthalpy and entropy of adsorption of probe molecules, Colloids and Surfaces A: Physicochemical and Engineering Aspects, 241 (2004) 9-14.

[139] B. Hunger, M. Heuchel, L.A. Clark, R.Q. Snurr, Characterization of acidic OH groups in zeolites of different types: An interpretation of NH3-TPD results in the light of confinement effects, The Journal of Physical Chemistry B, 106 (2002) 3882-3889.

[140] L. Garden, G. Kington, The thermodynamic properties of oxygen sorbed in chabazite, Trans. Faraday Soc., 52 (1956) 1397-1408.

[141] D. Sun, W.F. Schneider, J.B. Adams, D. Sengupta, The Molecular Origins of Selectivity in the Reduction of NOx by NH3, Journal of Physical Chemistry A, 108 (2004) 9365-9374.

[142] M.P. Ruggeri, T. Selleri, M. Colombo, I. Nova, E. Tronconi, Identification of nitrites/HONO as primary products of NO oxidation over Fe-ZSM-5 and their role in the Standard SCR mechanism: A chemical trapping study, Journal of Catalysis, 311 266-270.

[143] M. Chia, Y.J. Pagan-Torres, D. Hibbitts, Q. Tan, H.N. Pham, A.K. Datye, M. Neurock, R.J. Davis, J.A. Dumesic, Selective hydrogenolysis of polyols and cyclic ethers

over bifunctional surface sites on rhodium–rhenium catalysts, Journal of the American Chemical Society, 133 (2011) 12675-12689.

[144] Y.-H. Chin, C. Buda, M. Neurock, E. Iglesia, Selectivity of chemisorbed oxygen in C-H bond activation and CO oxidation and kinetic consequences for CH_4-O_2 catalysis on Pt and Rh clusters, Journal of Catalysis, 283 10-24.

[145] F.H. Ribeiro, M. Chow, R.A. Dallabetta, Kinetics of the complete oxidation of methane over supported palladium catalysts, Journal of Catalysis, 146 (1994) 537-544.

[146] F.H. Ribeiro, C.A. Gerken, G. Rupprechter, G.A. Somorjai, C.S. Kellner, G.W. Coulston, L.E. Manzer, L. Abrams, Structure Insensitivity and Effect of Sulfur in the Reaction of Hydrodechlorination of 1, 1-Dichlorotetrafluoroethane (CF_3CFCl_2) over Pd Catalysts, Journal of Catalysis, 176 (1998) 352-357.

[147] C.D. Thompson, R.M. Rioux, N. Chen, F.H. Ribeiro, Turnover rate, reaction order, and elementary steps for the hydrodechlorination of chlorofluorocarbon compounds on palladium catalysts, The Journal of Physical Chemistry B, 104 (2000) 3067-3077.

[148] L. Bollmann, J.L. Ratts, A.M. Joshi, W.D. Williams, J. Pazmino, Y.V. Joshi, J.T. Miller, A.J. Kropf, W.N. Delgass, F.H. Ribeiro, Effect of Zn addition on the water-gas shift reaction over supported palladium catalysts, Journal of Catalysis, 257 (2008) 43-54.

[149] B. Zugic, S. Zhang, D.C. Bell, F. Tao, M. Flytzani-Stephanopoulos, Probing the Low-Temperature Water-Gas Shift Activity of Alkali-Promoted Platinum Catalysts Stabilized on Carbon Supports, Journal of the American Chemical Society, 136 3238-3245.

[150] A.A. Phatak, N. Koryabkina, S. Rai, J.L. Ratts, W. Ruettinger, R.J. Farrauto, G.E. Blau, W.N. Delgass, F.H. Ribeiro, Kinetics of the water-gas shift reaction on Pt catalysts supported on alumina and ceria, Catalysis today, 123 (2007) 224-234.

[151] N.A. Koryabkina, A.A. Phatak, W.F. Ruettinger, R.J. Farrauto, F.H. Ribeiro, Determination of kinetic parameters for the water-gas shift reaction on copper catalysts under realistic conditions for fuel cell applications, Journal of Catalysis, 217 (2003) 233-239.

[152] T. Hamzehlouyan, C. Sampara, J. Li, A. Kumar, W. Epling, Experimental and kinetic study of SO_2 oxidation on a Pt-Al_2O_3 catalyst, Applied Catalysis B: Environmental, 152-153 108-116.

[153] M.A. Vannice, S.H. Hyun, B. Kalpakci, W.C. Liauh, Entropies of adsorption in heterogeneous catalytic reactions, Journal of Catalysis, 56 (1979) 358-362.

[154] Y. Ji, T. Toops, U. Graham, G. Jacobs, M. Crocker, A kinetic and DRIFTS study of supported Pt catalysts for NO oxidation, Catalysis Letters, 110 (2006) 29-37.

[155] Handbook of Chemistry and Physics, in.

[156] D.E. Mears, Diagnostic criteria for heat transport limitations in fixed bed reactors, Journal of Catalysis, 20 (1971) 127-&.

[157] S. Yagi, D. Kunii, Studies on heat transfer near wall surface in packed beds, AIChE Journal, 6 (1960) 97-104.

[158] I.J. Drake, Y.H. Zhang, D. Briggs, B. Lim, T. Chau, A.T. Bell, The local environment of Cu+ in Cu-Y zeolite and its relationship to the synthesis of dimethyl carbonate, Journal of Physical Chemistry B, 110 (2006) 11654-11664.

APPENDICES

Appendix A Appendix for Chapter 2

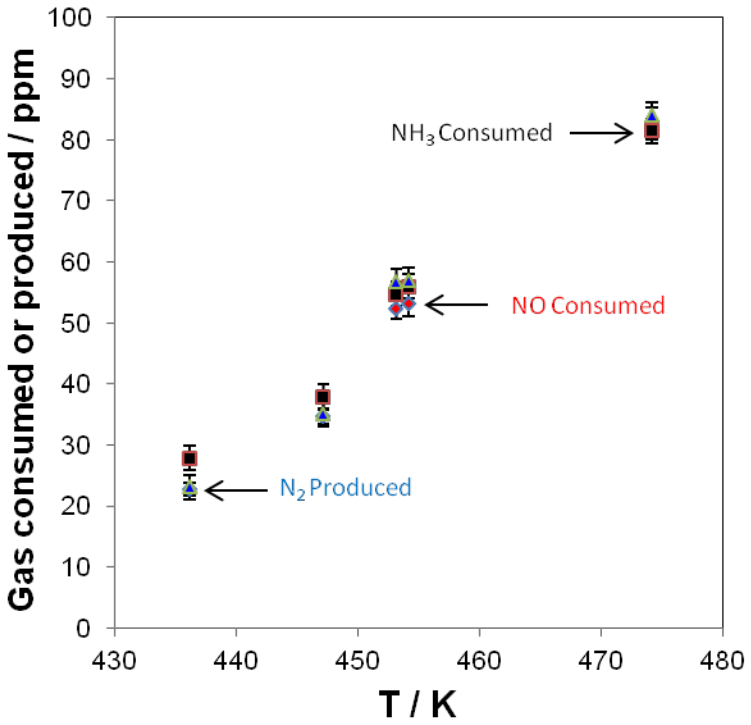

Figure A.2 Mass balance data collected for the Cu-SSZ-13 sample with Cu:Al=0.09 using gas chromatography to quantify N2 produced and gas phase FTIR to determine NO and NH_3 consumed in the standard SCR reaction. ±2 ppm reported for noise in FTIR signals for NO and NH_3, Standard deviation reported for N_2 produced.

Table A.1 Summary of kinetic data collected on each Cu-SSZ-13 sample.

Cu Wt%	Si:Al Ratio*	Cu:Al Ratio*	$E_{a,app}$ / kJ mol^{-1}	A_o / s^{-1}	Rate / 10^{-4} mol NO mol Cu^{-1} s^{-1}	Rate / 10^{-6} mol NO g cat^{-1} s^{-1}	NO Order	NH_3 Order	O_2 Order	Brønsted Acid Sites / H^+ Al^{-1}
0	4.5	0	-	-	-	0	-	-	-	0.65
0.31	4.3	0.02	42	1.35E2	32.4	0.2	0.7	-0.2	0.5	0.45
0.82	4.3	0.04	68	4.29E5	132	1.7	0.7	0	0.5	0.60
1.74	4.5	0.09	64	9.74E4	74.3	2.0	0.8	0	0.3	0.42
3.04	4.5	0.16	70	8.5E5	61.9	3.0	0.8	-0.1	0.3	0.32
3.75	4.5	0.2	71	4.24E5	66.0	3.8	0.9	0	0.3	0.30
6.39	4.5	0.35	71	2.16E5	29.4	3.0	0.7	0.1	0.2	0.24

*Atomic compositions and ratio determined by Atomic Absorption Spectroscopy.
Rated measured at 473 K. Associated Errors in measurements with 90% confidence interval: Ea,app = ±5 kJ mol^{-1}, Rate per gram catalysts = ± 0.2 x 10^{-6} mol NO g^{-1} $s^{-1,}$ Rate per mole Cu = ± 0.2 x 10^{-4} mol NO mol Cu^{-1} s^{-1}, Reaction orders = ±0.1, Brønsted Acid Sites = ±0.08 H^+:Al.

Additional Information on Brønsted Acid Site Count Quantification

For a complete summary of the Brønsted acid site count determinations on H-and Cu-SSZ-13, please refer to our previous study [26] (Chapter 4). Three NH_3 titration procedures and an n-propylamine decomposition [73-75] were compared for Brønsted acid site counts in H- and Cu-ZSM-5. The results showed that the NH_3 titrations were able to selectively titrate Brønsted acid sites as they gave equivalent results to the n-propylamine decomposition. Ammonia was determined to be a better titrant of Brønsted acid sites in H- and Cu-SSZ-13 than n-propylamine as it gave consistent total Brønsted acid site counts, while n-propylamine Brønsted acid site counts nearly four times lower because of mass transport limitations and spatial constraints of close proximity of acid sites. Figure A.2 below shows the result of the third NH_3 titration procedure on H- and Cu-SSZ-13 samples in this study. The samples were treated with ~500 ppm NH_3 in UHP-He at 433 K with a total flowrate of 350 ml min^{-1} for two hours. At the end of the saturation, the NH_3 signal was constant in the FTIR (MKS Multi-gas 2030 Gas Analyzer). Following this, the sample was flushed in UHP-He for eight hours at 433 K with a total flowrate of 350 ml min^{-1}. A TPD was performed on ~30 mg of sample in an

Micrimeritics Autochem II unit with 50 sccm UHP-He flowing and 10 K min^{-1} temperature ramp up to 873 K. One feature resulted in all the experiments corresponding to the Brønsted acid sites.

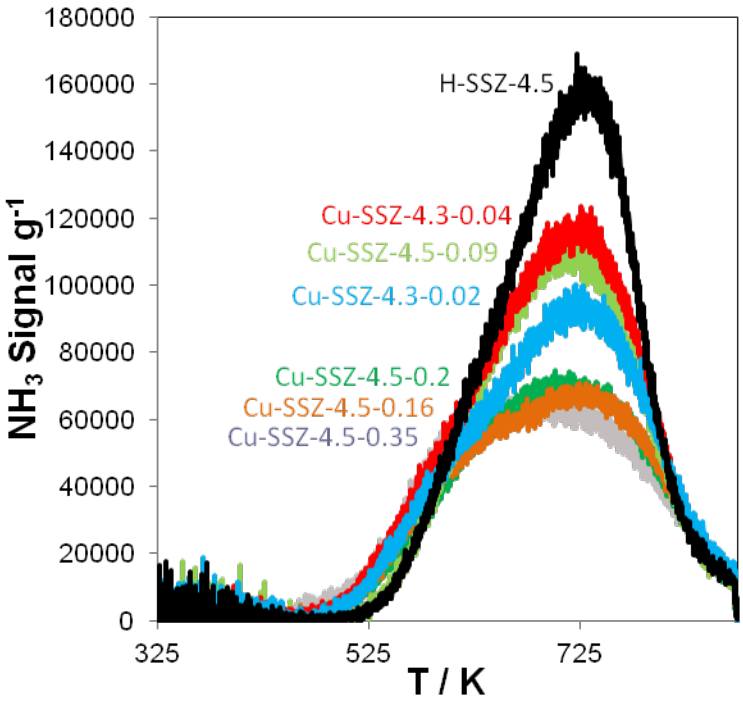

Figure A.3 NH_3 TPD experiments over Cu-SSZ-13 samples ranging from Cu:Al = 0 to 0.35 using NH_3 titration procedure #3 from our previous work [26].

Effect of CO_2 on kinetics for Cu-SSZ-13

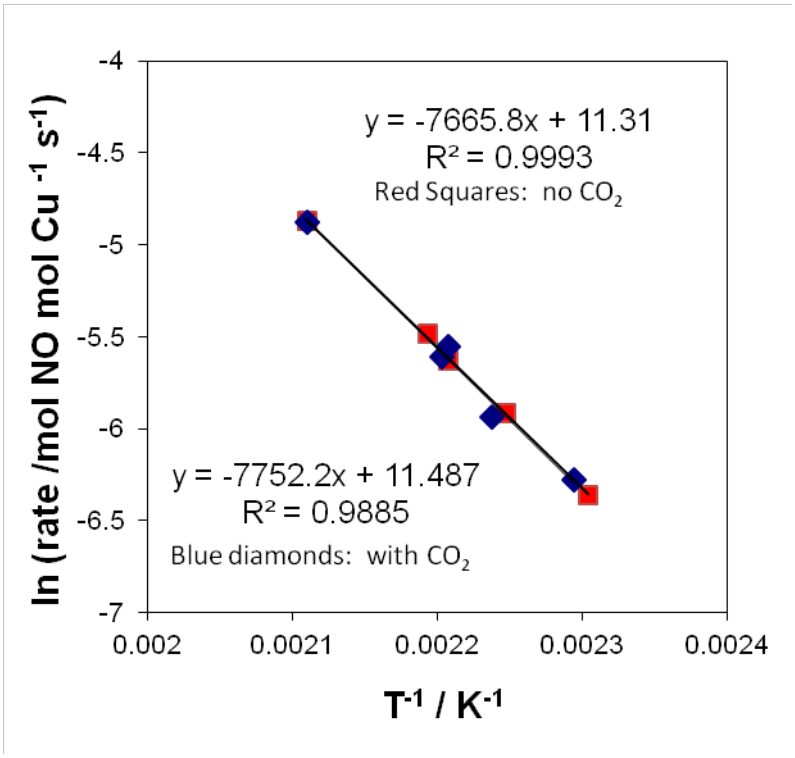

Figure A.4 Activation energy plot for a Cu-SSZ-13 (Cu:Al = 0.09) under standard SCR 320 ppm NO, 320ppm NH_3, 7% H_2O, 10% O_2, balance He with (blue diamonds) and without (red squares) 8% CO2 in the feed. Data were collected over 433-473 K at a total flow of ~1.5L min.-

Table A.2 Measured activation energy, pre-factor and rate for a Cu-SSZ-13 sample (Cu:Al = 0.09) under standard SCR gas conditions with and without CO_2 in the feed.

Sample	Ea / kJ mol^{-1}	A_o / 10^4 s^{-1}	Rate (473 K) / 10^{-3} mol NO mol Cu^{-1} s^{-1}
Standard SCR with CO_2	64	9.74	7.43
Standard SCR without CO_2	64	8.16	7.47

90% confidence interval for Ea and rate per mole Cu are ±5 kJ mol^{-1} and ±0.2 x 10^{-4} mol NO mol $Cu^{-1}s^{-1}$.

Additional information on the NH_3 Quantification Experiments

Scheme A.1 shows the three individual NH_3 species quantified. The first is a weakly bound NH_3 species which is found during the same NH_3 cutoff experiment in which the reactive NH_3 is quantified. The NH_3 concentration was monitored in the FTIR during the NH_3 cutoff.

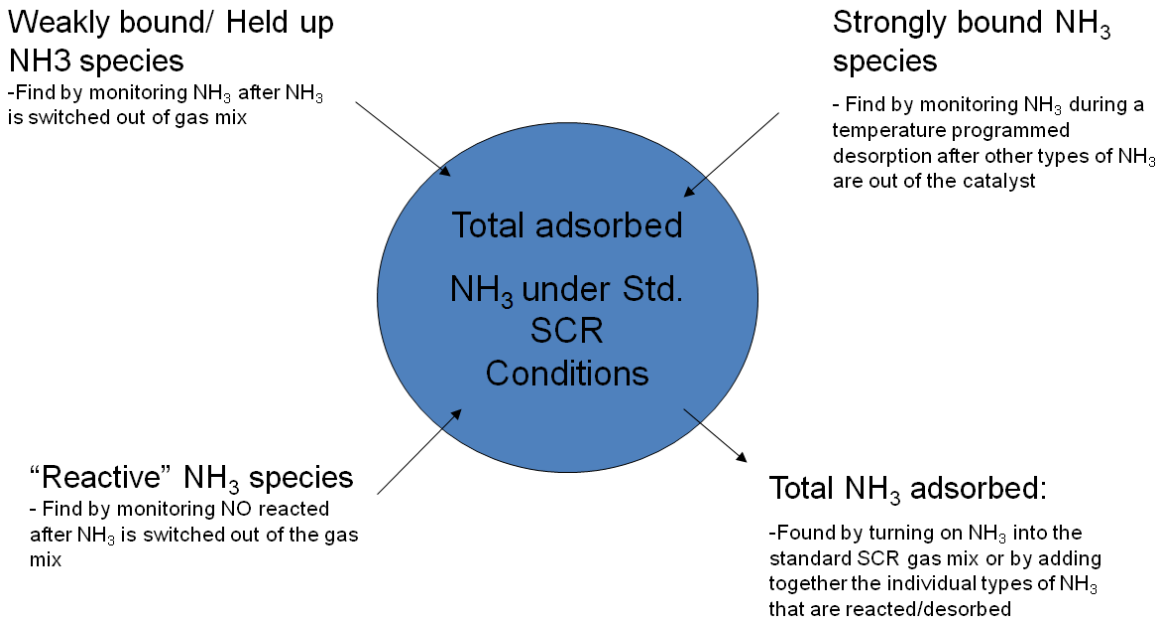

Scheme A.1 The overall NH_3 quantification flow diagram. The sum of weakly bound NH_3, reactive NH_3, and strongly bound NH_3 corresponded to the total adsorbed NH_3 present under standard SCR reaction conditions at 433 K. The total adsorbed NH_3 could also be determined separately as described in the scheme.

Figure A.4 shows an example for the Cu:Al = 0.09 sample. In the experiment shown, the NH_3 is removed from the gas phase within 5 – 7 minutes. Compared to the CO_2 tracer, there is a quantity of NH_3 that leaves when the NH_3 is removed from the gas phase. This may be a physisorbed species or NH_3 sticking in the lines of the system. At time zero, Figure A.4 shows the NH_3 starting at a lower concentration. At this point in time, the

valve had already been switched which caused a pressure spike in the IR; therefore, the real initial concentration was close to 300 ppm where the CO_2 was scaled.

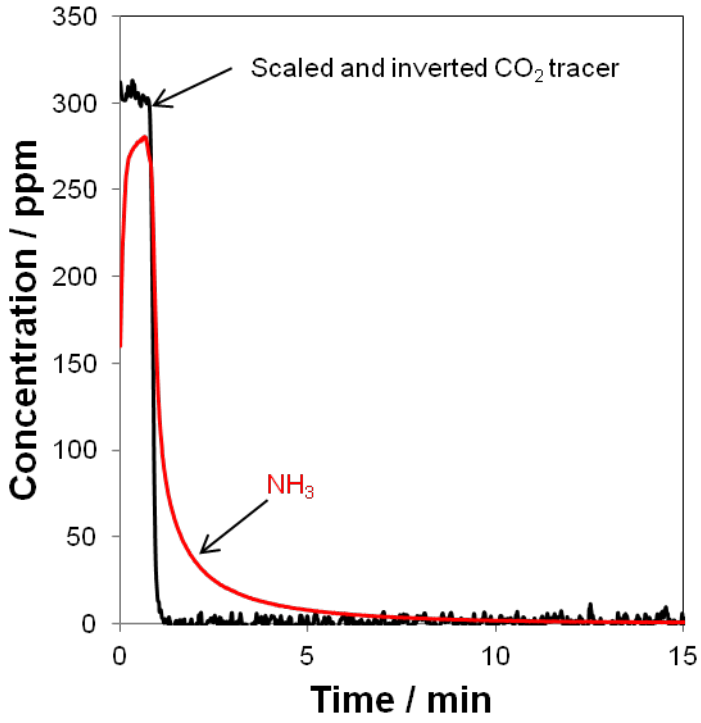

Figure A.5 NH_3 concentration over time as NH_3 was removed from the gas mixture and replaced with an equal flowrate of CO_2 for the Cu:Al = 0.09 Cu-SSZ-13 sample. The CO2 has been scaled and inverted to show the initial NH3 concentration as a comparison to see the lag in NH_3. Before NH_3 was removed, standard SCR conditions were present with 320 ppm NO, 320 ppm NH_3, 10% O_2, 6% H_2O, 8% CO_2, and balance Helium at 433 K. Total flowrate is 1.5 L min^{-1}.

Figure A.5 shows the weakly bound NH_3 determined over several Cu-SSZ-13 samples in this study. In general, a positive trend was observed as the Cu loading increased, indicating this weakly bound species may be related to an NH_3 associated with Cu; however, NH_3 from elsewhere cannot be ruled out.

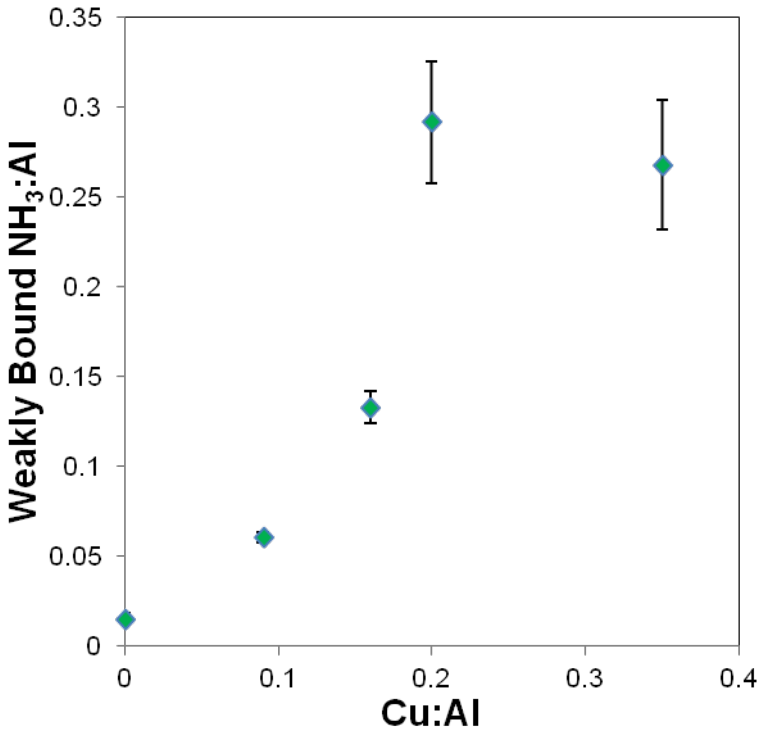

Figure A.6 The amount of weakly bound NH_3 determined in NH_3 cutoff experiments from standard SCR over different Cu:Al samples. Before NH_3 was removed, standard SCR conditions were present with 320 ppm NO, 320 ppm NH_3, 10% O_2, 6% H_2O, 8% CO_2, and balance Helium at 433 K. 90% confidence interval reported.

Figures 2.3 and A.6 show the data collected for the reactive NH_3 species, which was discussed in the main text of the study. Following that, Figures 2.3 and A.7-A.8 go through the TPD performed after the NH_3 cutoff experiment and flushing of the system.

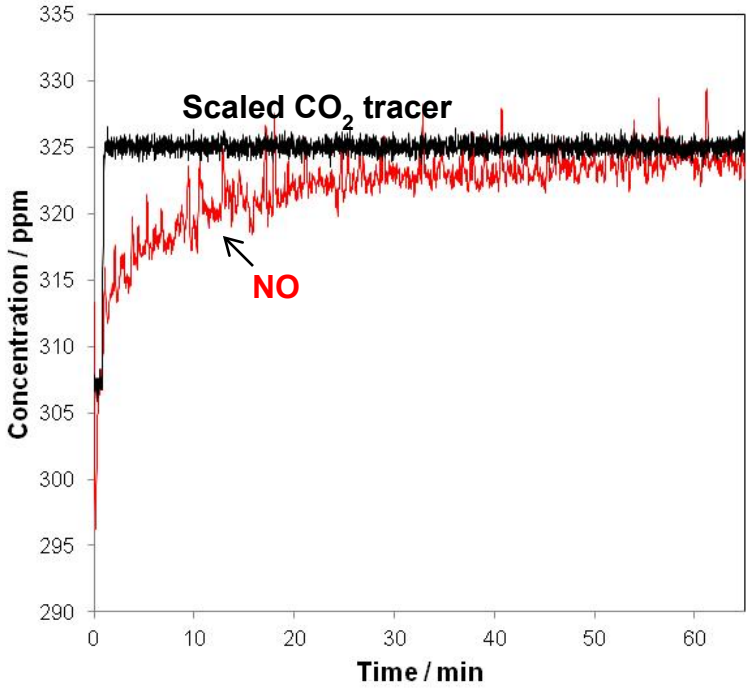

Figure A.7 Display of NO concentration over time as NH_3 was removed from the gas mixture and replaced with an equal flowrate of CO_2 for the Cu:Al = 0.09 Cu-SSZ-13 sample. The CO_2 is used as a tracer. Before NH_3 was removed, standard SCR conditions were present with 320 ppm NO, 320 ppm NH_3, 10% O_2, 6% H_2O, 8% CO_2, and balance Helium at 433 K. Total flowrate is 1.5 L min^{-1}.

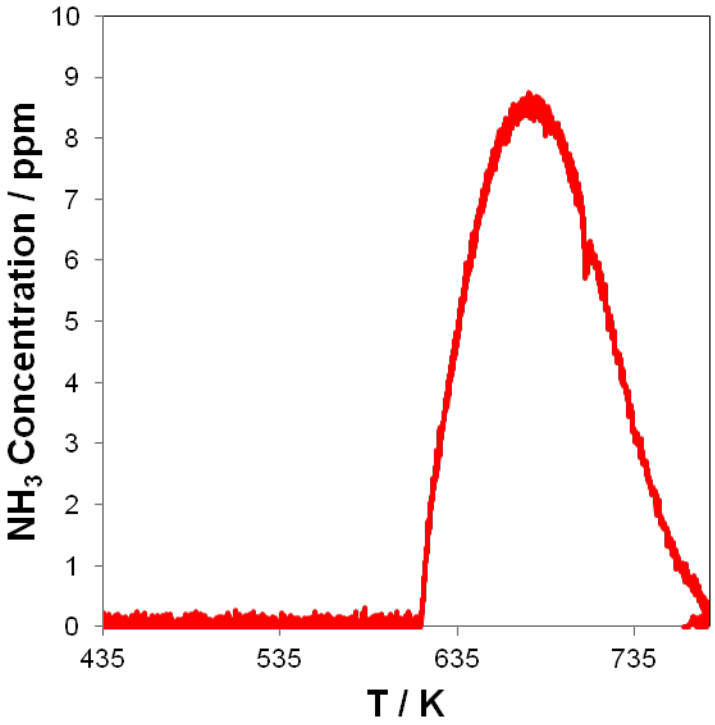

Figure A.8 NH_3 TPD following the NH_3 cutoff experiment from steady state standard SCR and a system flush for ~ 1hr with UHP helium for the Cu-SSZ-13 sample with Cu:Al = 0.09. The NH_3 observed has been called "strongly bound." The temperature ramp was 5 K min-1 starting from 433 K.

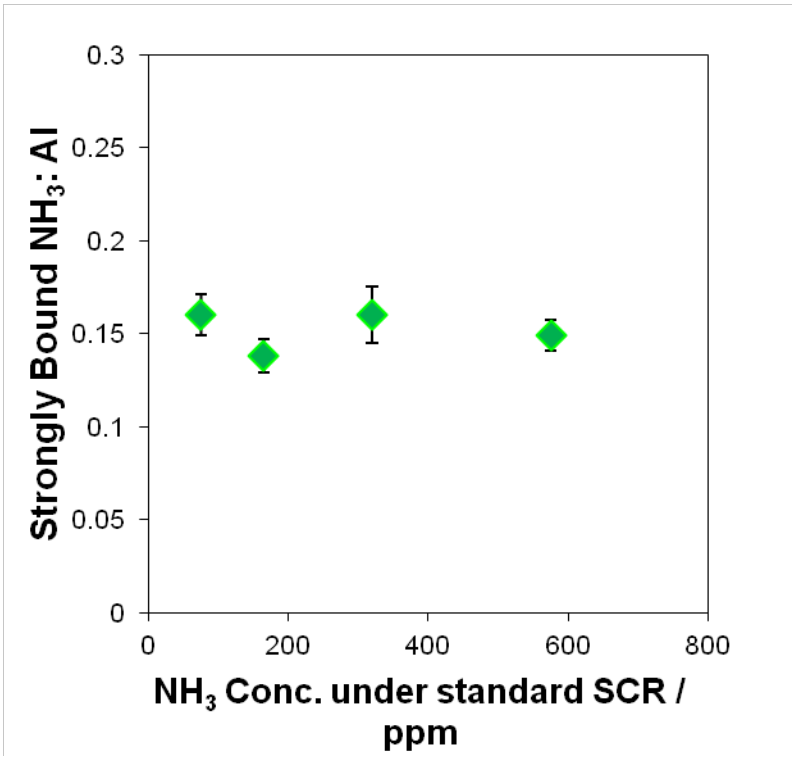

Figure A.9 The quantity of strongly bound NH_3 after different concentrations of NH_3 were used under steady state standard SCR conditions at 433 K for the Cu:Al = 0.09 Cu-SSZ-13 sample. NH_3 was then removed in a cutoff experiment and flushed for ~ 1hr in UHP He before the TPD was performed. 90% confidence interval reported.

The final step in the process was to quantify the total amount of NH_3 present under steady state standard SCR conditions, which can be used to compare to the sum of the three individual NH_3 species. This was performed starting with an NH_3-free catalyst surface with 320 ppm NO, 10% O_2, 6% H_2O, and an equal flow of CO_2 corresponding to the same flow of NH_3 which was removed in the earlier NH_3 cutoff experiment at 433 K. Ammonia was switched into the gas mixture and CO_2 removed. The result was an NH_3 adsorption curve shown in Figure A.9 which approached steady state standard SCR after ~ 30 minutes. The resulting area between the NH_3 and the scaled and inverted CO_2 tracer was integrated for the total NH_3 under standard SCR at 433 K. The sum of the individual NH_3 species was then compared to the total NH_3 adsorbed under standard SCR conditions at 433 K. The results can be seen in Figure A.10, where a good agreement

between all samples was observed except for the Cu:Al = 0.2 sample, which had significantly more NH_3 in the NH_3 adsorption experiment and was not characteristic of any of the other samples tested. One explanation of this was that in this particular set of adsorption experiments, some water had accumulated somewhere in the lines which was capturing some extra NH_3 and artificially inflating the value. Every time a new sample was loaded a significant amount of heating tape was used in the inlet and outlet of the reactor. If a cool spot was present, this was a plausible explanation.

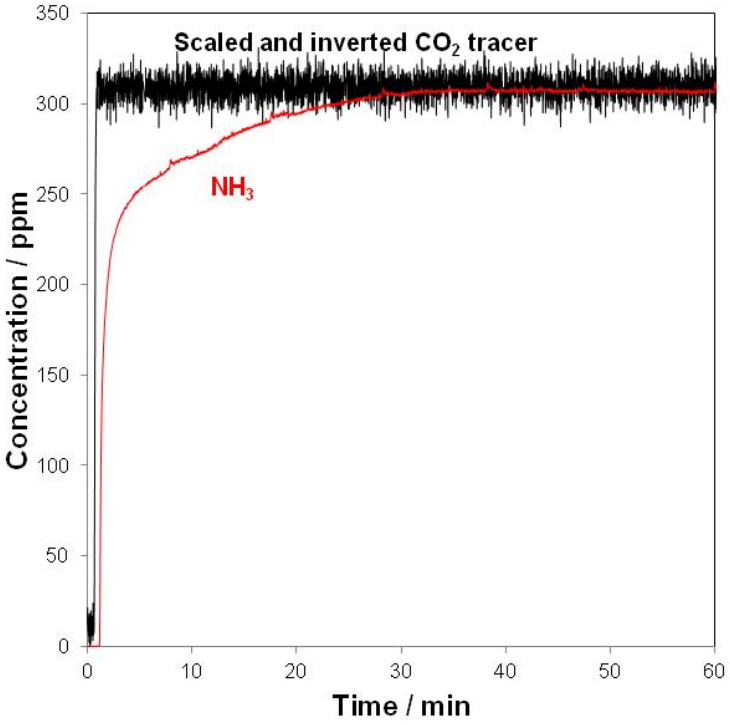

Figure A.10 Display of NH_3 concentration over time as NH_3 was added to the gas mixture and CO_2 removed for the Cu:Al = 0.09 Cu-SSZ-13 sample. The CO_2 has been scaled and inverted to show the initial NH_3 concentration as a comparison to see the lag in NH_3. Before NH_3 was added, an NH_3 free surface was obtained via TPD and standard SCR conditions minus NH_3 were present with 320 ppm NO, 10% O_2, 6% H_2O, 8% CO_2, and balance Helium at 433 K.

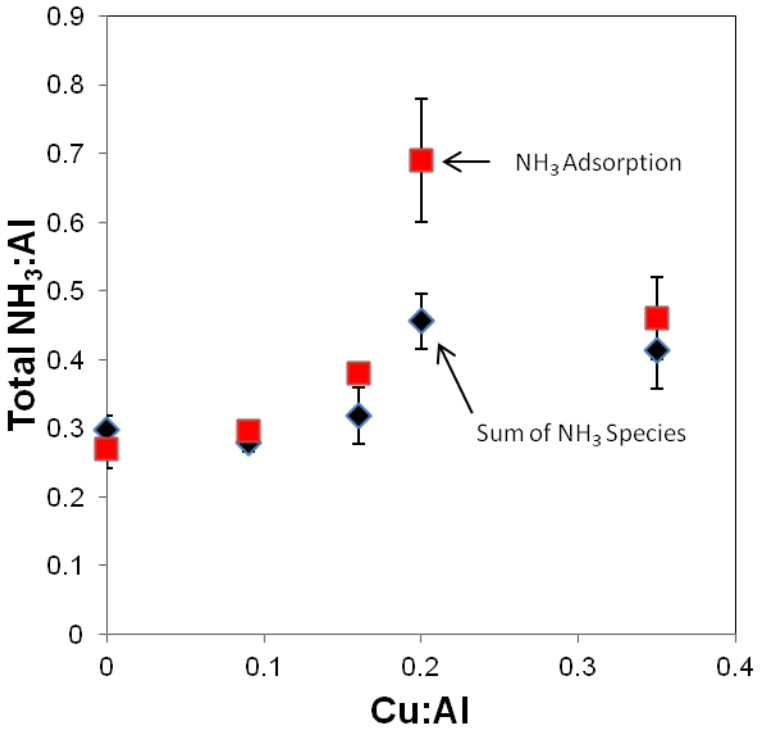

Figure A.11 Comparison of the total NH_3 present under standard SCR conditions at 433 K using two different methods. The sum of the individual NH_3 species is shown in black while the NH_3 from an adsorption experiment is shown in red. 90% confidence intervals are included.

UV-Vis-NIR Quantification of d-d transition for hydrated Cu(II)

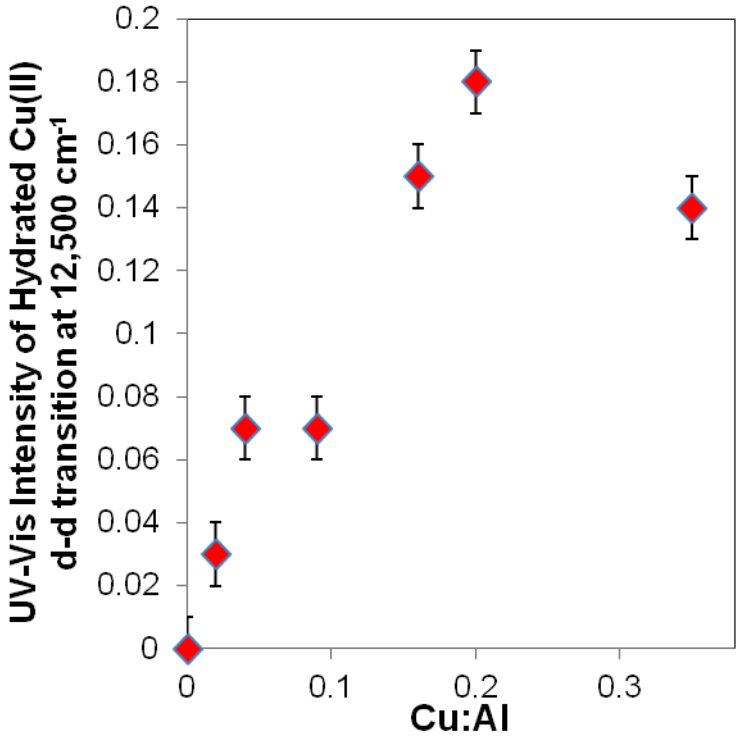

Figure A.12 UV-Vis-NIR intensity of the d-d transition for hydrated Cu(II) at 12,500 cm-1 in Kubelka-Munk units under ambient conditions. Cu:Al ranges from 0 to 0.35. 90% confidence intervals are included.

Additional XANES and EXAFS Spectra and analysis.

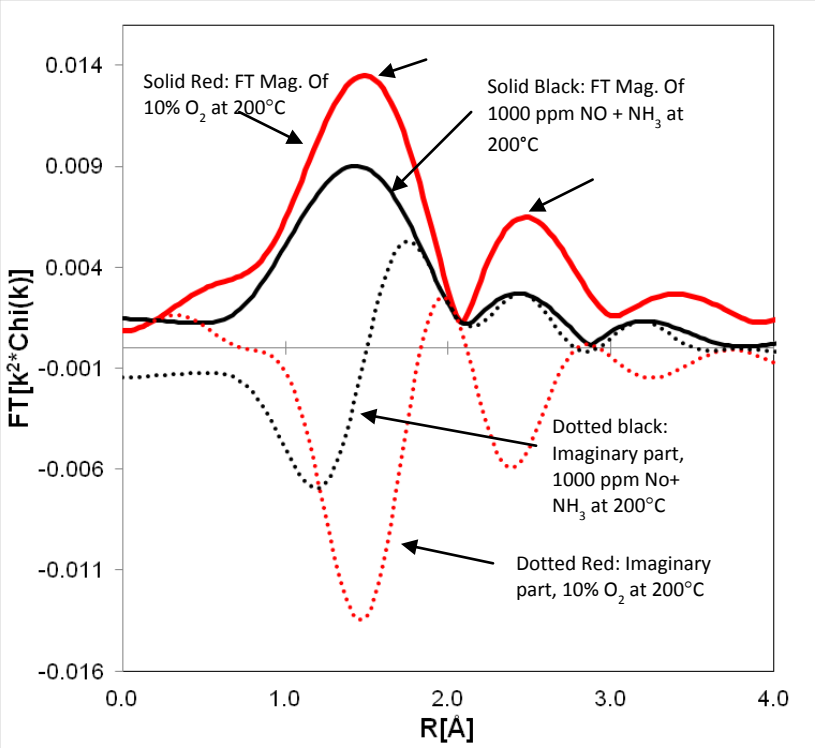

Figure A.13 EXAFS spectra for the isolated Cu(II) (red) and isolated Cu(I) (black) references. Solid lines indicate the Fourier transform magnitude. Dotted lines indicate the imaginary contribution.

Table A.1 EXAFS fit paremeters for isolated Cu(I) and isolated Cu(II).

0.31% Cu EXAFS of Cu-SSZ-13								
Sample	Treatment	XANES		Absorber-Scatter	N	R / Å	$\Delta\sigma^2$ (x 10^3)	E_o / eV
		Fraction Cu(II)	Fraction Cu(I)					
Cu(II)	RT, ambient	1.0	-	Cu-O	3.9	1.96	2.0	-8.5
Cu(II)	10% O_2 , 473 K	1.0	-	Cu-O	4.0	1.96	4.0	-7.5
Cu(I)	1000 ppm NH_3 + 1000 ppm NO, 473 K	-	1.0	Cu-O	2.2	1.85	4.0	-5.1

Table A.2 Linear combination XANES fits for all Cu-SSZ-13 samples in air at room temperature included in this study.

Sample	Cu:Al	Treatment	Cu(II)O	Isolated Cu(I)	Isolated Cu(II)	Hydrated Cu(II)
Cu-SSZ-13	0.02	in air, room temperature	4	0	0	96
Cu-SSZ-13	0.04	in air, room temperature	0	0	0	100
Cu-SSZ-13	0.08	in air, room temperature	0	0	0	100
Cu-SSZ-13	0.16	in air, room temperature	0	0	0	100
Cu-SSZ-13	0.2	in air, room temperature	0	0	0	100
Cu-SSZ-13	0.35	in air, room temperature	25	0	0	75

±5% error associated with linear combination XANES fits

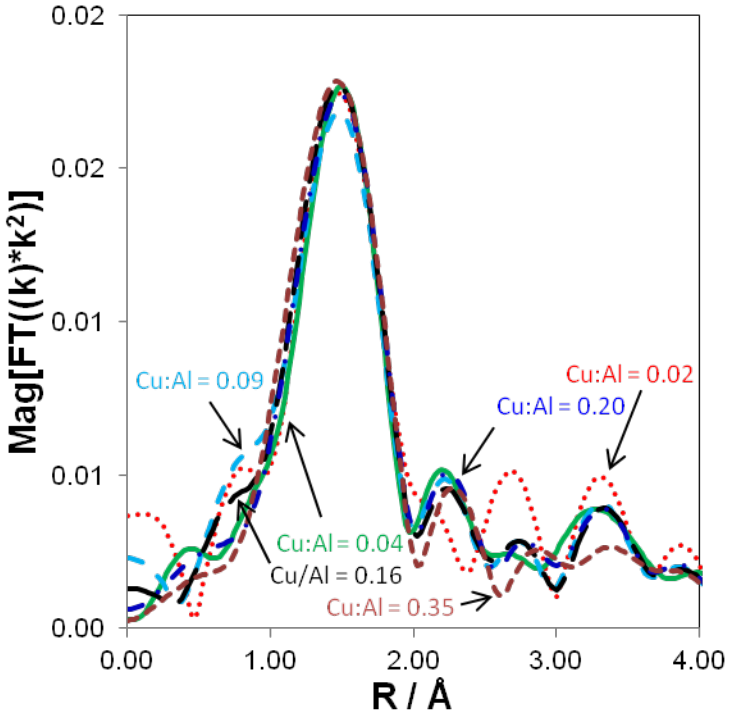

Figure A.14 EXAFS spectra all Cu-SSZ-13 samples in this study under ambient conditions (in air at room temperature).

Table A 3 EXAFS fit paremeters for all Cu-SSZ-13 samples in this study in air at room temperature.

Sample	Cu:Al	Treatment	Absorber - Scatter	CN	R / Å	$\Delta\sigma^2$ / 10^{-3} Å	E_o / eV
Cu-SSZ-13	0.02	in air, room temperature	Cu-O	4.0	1.94	2	-9.5
Cu-SSZ-13	0.04	in air, room temperature	Cu-O	3.9	1.94	2	-10.3
Cu-SSZ-13	0.08	in air, room temperature	Cu-O	3.9	1.94	2	-10.4
Cu-SSZ-13	0.16	in air, room temperature	Cu-O	4.1	1.94	2	-10.2
Cu-SSZ-13	0.2	in air, room temperature	Cu-O	4.1	1.94	2	-10.6
Cu-SSZ-13	0.35	in air, room temperature	Cu-O	4.3	1.94	2	-11.2

Table A.4 Linear combination XANES fits for Cu-SSZ-13 samples under standard SCR reaction conditions. Standard SCR conditions used were 320 ppm NO, 320 ppm NH_3, 10% O_2, 8% CO_2, 6% H_2O, and balance Helium at 453 K.

Cu:Al	Treatment	%Cu(II)O	% Isolated Cu(I)	% Isolated Cu(II)	% Hydrated Cu(II)	SCR Rate / 10^{-4} mol NO mol Cu^{-1} s^{-1} at 453 K
0.09	standard SCR, 453 K, operando XAS	0	37	57	5	43.0
0.09	standard SCR, 453 K, lab scale PFR	-	-	-	-	43.2
0.16	standard SCR, 453 K, operando XAS	0	26	71	3	46.6
0.16	standard SCR, 453 K, lab scale PFR	-	-	-	-	37.4

±5% error associated with linear combination XANES fits.

The pre-edge feature we have identified as isolated Cu(I) at 8983 eV in *operando* XAS has also been attributed to NH_3 adsorbed on Cu(II) at low temperature by Deka et al [15]. The Cu-tetraamine XANES spectrum (Figure A14) contains a dip in white line intensity with two features appearing at 8994 eV and 8998 eV, which when compared to the isolated Cu(I) reference and samples under standard SCR conditions in Figure 3.6 cannot be ruled out as a possible contributor to the shape of the XANES spectra. It would not be able to give an intense pre-edge feature at 8983 eV, which was observed in this study for the isolated Cu(I) reference. On this basis and because the linear combination XANES did not give any reasonable fits, it was not included as a reference.

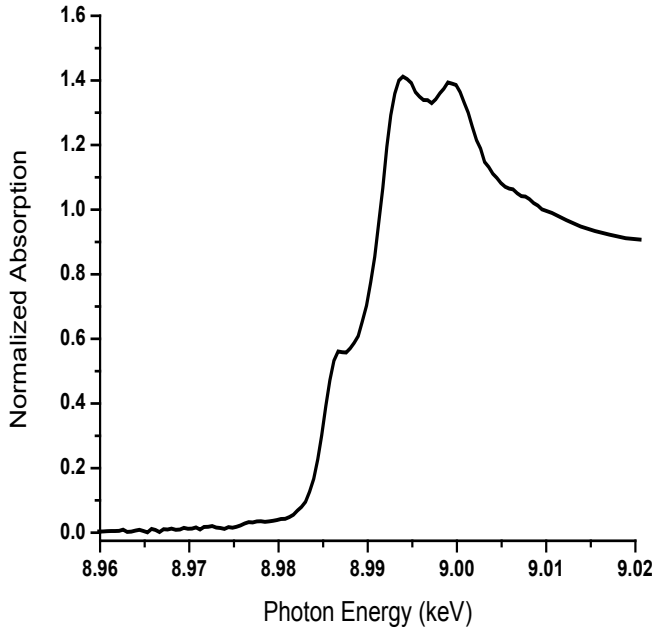

Figure A.15 XANES spectrum of the Cu(II)-tetraamine reference compound .

Details of stability of isolated Cu(II) cation

The optimized structure for relative stability of isolated Cu(II) in the SSZ-13 zeolite structure is shown in Figure below.

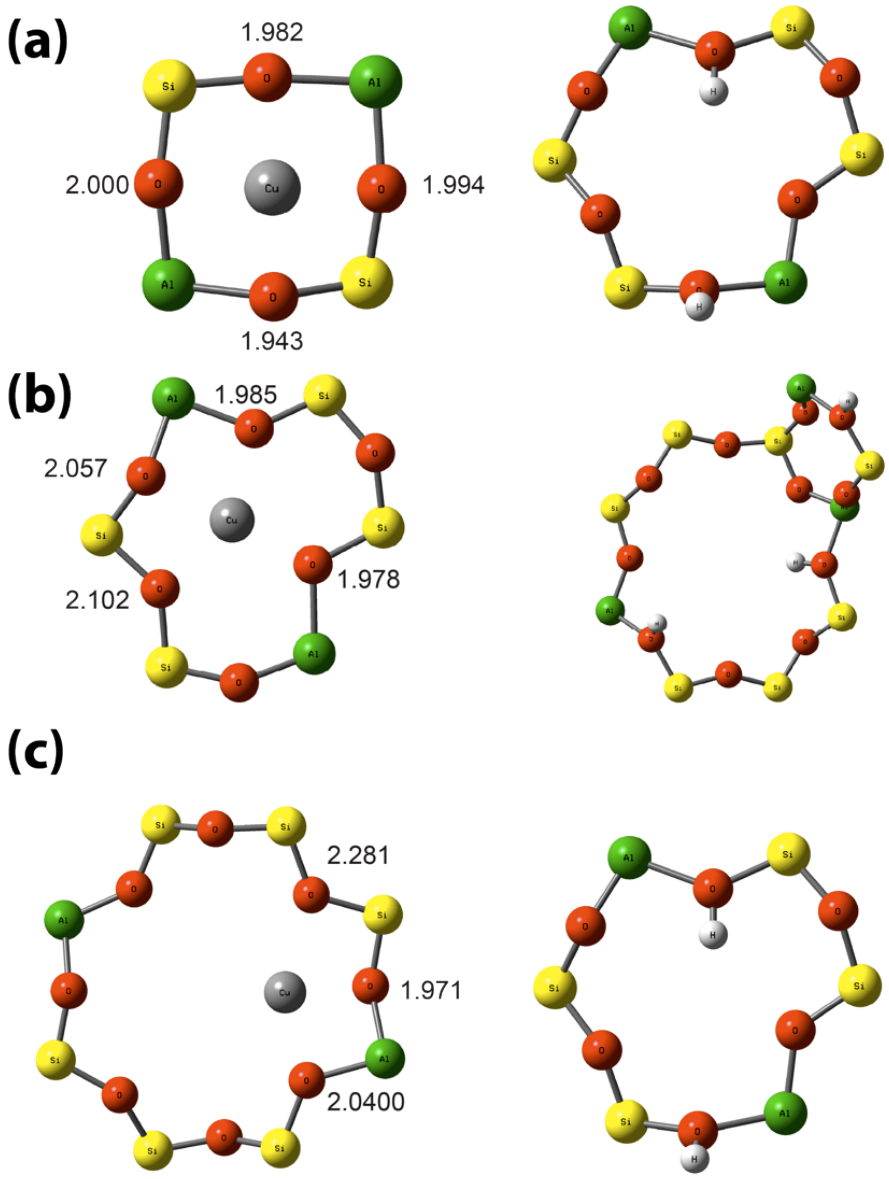

Figure A.16 Optimized structure of isolated Cu(II). (a) Isolated Cu(II) located in the 4-membered ring of SSZ-13 and two hydrogen attached to the oxygen in the 6-membered ring structure of the zeolite. (b) Isolated Cu(II) located in the 6-membered ring of SSZ-13 and two hydrogen attached to the oxygen in the 8-membered ring structure of the zeolite. (c) Isolated Cu(II) located in the 8-membered ring of SSZ-13 and two hydrogen attached to the oxygen in the 6-membered ring structure of the zeolite.

Exchange energy calculation for isolated Cu(II) in the 4-membered ring:

$Z_4H_4 + Cu(s)$	$\rightarrow Z_4H_2Cu + H_2$ (g)	ΔE= 3.31 eV	(DFT)
$Cu(II) + 2e^-$	$\rightarrow Cu(s)$	ΔG= -nFE = -2*1*0.34 eV	[155]
H_2 (g)	$\rightarrow 2H^+ + 2e^-$	ΔG= 0 eV	[155]
$Z_4H_4 + Cu^{2+}$	**$\rightarrow Z_4H_2Cu + 2\ H^+$**	**ΔE= 2.63 eV**	

Exchange energy calculation for isolated Cu(II) in the 6-membered ring:

$Z_4H_4 + Cu(s)$	$\rightarrow Z_4H_2Cu + H_2$ (g)	ΔE= 2.18 eV	(DFT)
$Cu(II) + 2e^-$	$\rightarrow Cu(s)$	ΔG= -0.68 eV	[155]
H_2 (g)	$\rightarrow 2H^+ + 2e^-$	ΔG= 0 eV	[155]
$Z_4H_4 + Cu^{2+}$	**$\rightarrow Z_4H_2Cu + 2\ H^+$**	**ΔE= 1.50 eV**	

Exchange energy calculation for isolated Cu(II) in the 8-membered ring:

$Z_4H_4 + Cu(s)$	$\rightarrow Z_4H_2Cu + H_2$ (g)	ΔE= 3.68 eV	(DFT)
$Cu(II) + 2e^-$	$\rightarrow Cu(s)$	ΔE= -0.68 eV	[155]
H_2 (g)	$\rightarrow 2H^+ + 2e^-$	ΔE= 0 eV	[155]
$Z_4H_4 + Cu^{2+}$	**$\rightarrow Z_4H_2Cu + 2\ H^+$**	**ΔE= 3.00 eV**	

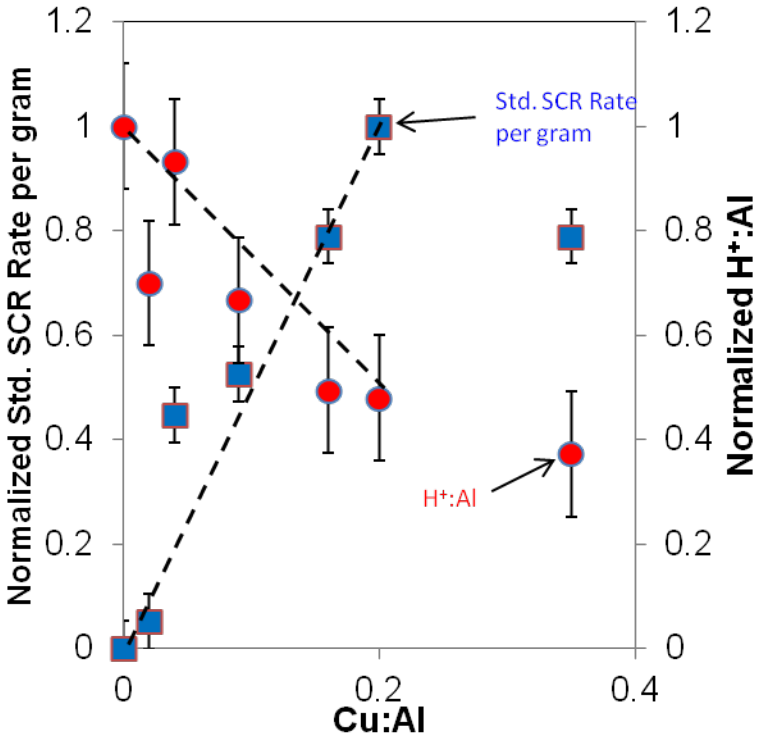

Figure A.17 Normalized Brønsted acid site count and normalized standard SCR rate per gram shown with respect to the Cu:Al in several Cu-SSZ-13 samples. 90% confidence intervals reported.

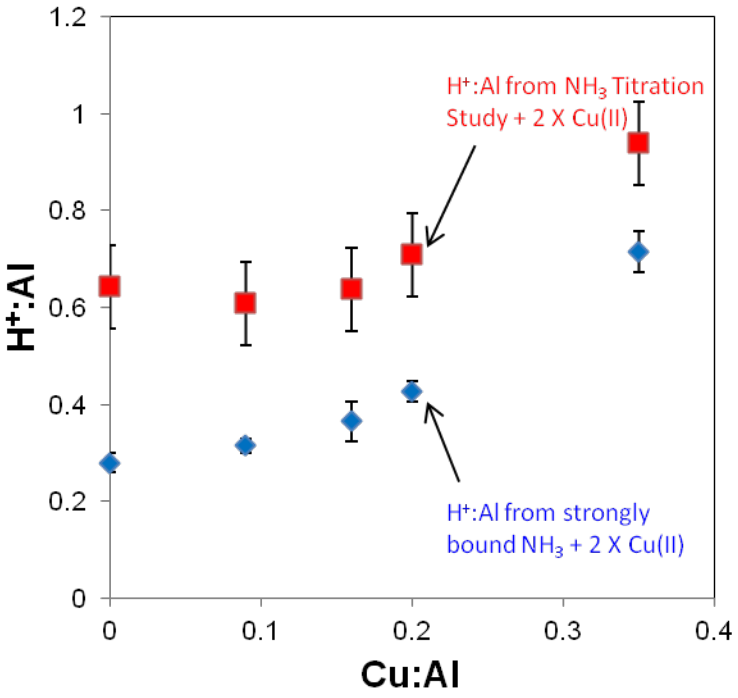

Figure A.18 The total number of Brønsted acid sites counted in a previous study using numbers from the NH_3 titration [26] and the strongly bound NH_3 in this study. Two Brønsted acid sites are added for each Cu(II) exchanged in the sample. 90% confidence intervals are reported.

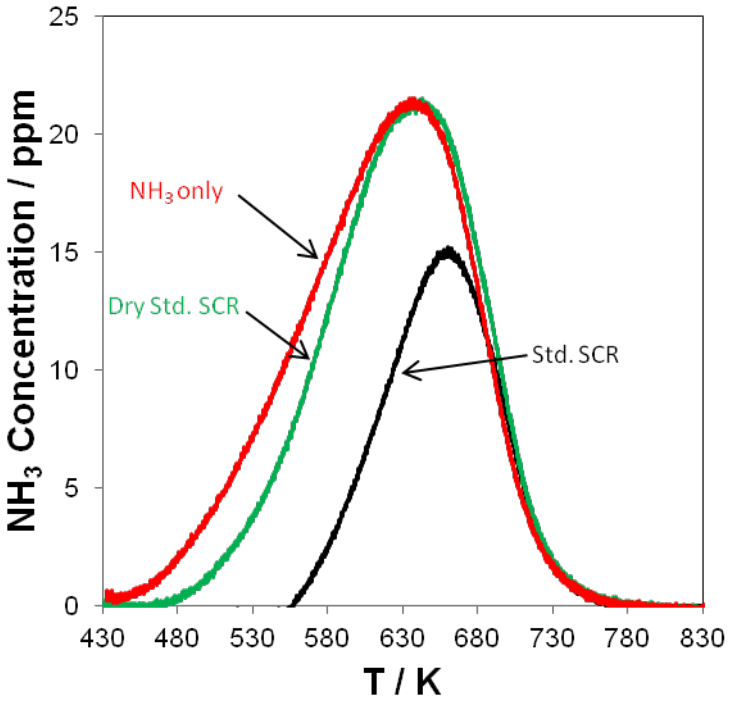

Figure A.19 TPDs following an NH_3 cutoff experiments at 433 K and system flush at 433 K. Conditions before the NH_3 cutoff are given in the labels.

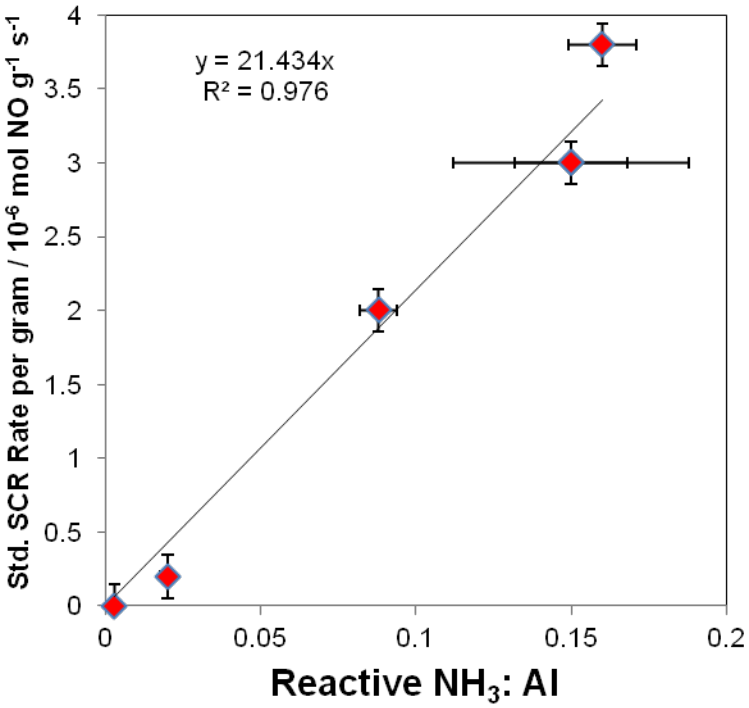

Figure A.20 Standard SCR rate per gram shown against the amount of reactive NH_3 per total Al in several Cu-SSZ-13 samples. 90% confidence intervals are reported.

Appendix B Appendix for Chapter 3

Table B.1 Summary of Cu-SSZ-13 catalysts used in this study

Copper Weight %	Si:Al ratio	Cu:Al ratio
0	4.5	0
0.31	4.3	0.02
0.82	4.3	0.04
1.74	4.5	0.09
3.04	4.5	0.16
3.75	4.5	0.2
5.64	4.5	0.31
6.39	4.5	0.35
7.4	4.5	0.39
18.93	4.5	1.6

Si, Cu and Al measured independently by atomic absorption spectroscopy. Error in measurement of Si:Al atomic = ± 0.03 and Cu:Al ratio = ± 0.03

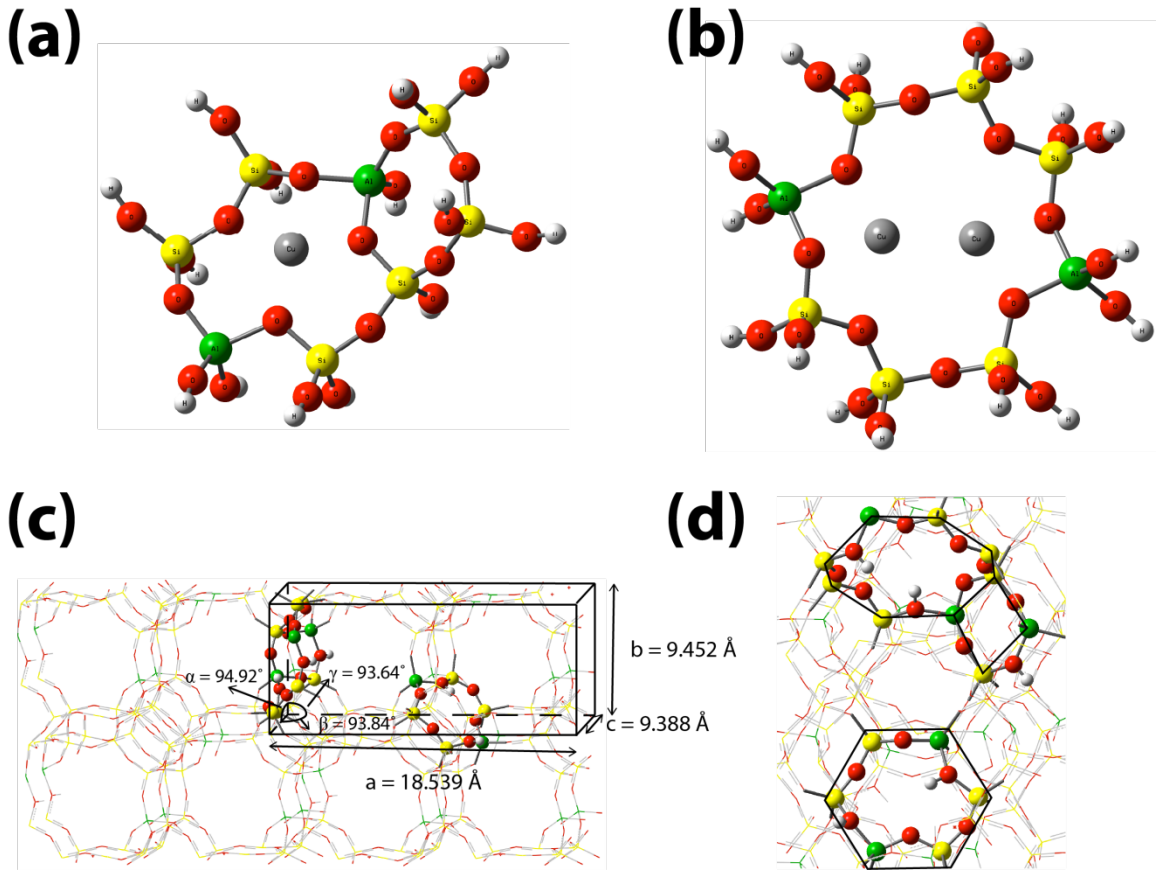

Figure B.1 Cluster models for SSZ-13 zeolite. (a) The Z_2Cu 6-ring cluster model with third-nearest-neighbor (3NN) Al sites. (b) The Z_2Cu_2 8-ring cluster model with fourth-nearest-neighbor (4NN) Al sites. (c) Periodic representations of 2×1×1 supercell of SSZ-13. (d) Zoom-in on a 2×1×1 Z_4H_4 supercell highlighting the 4-, 6-, and 8-rings containing 2NN, 3NN, and 4NN Al sites, respectively. Yellow spheres are Si, red spheres are O, grey spheres are Cu, green spheres are Al, and white spheres are H.

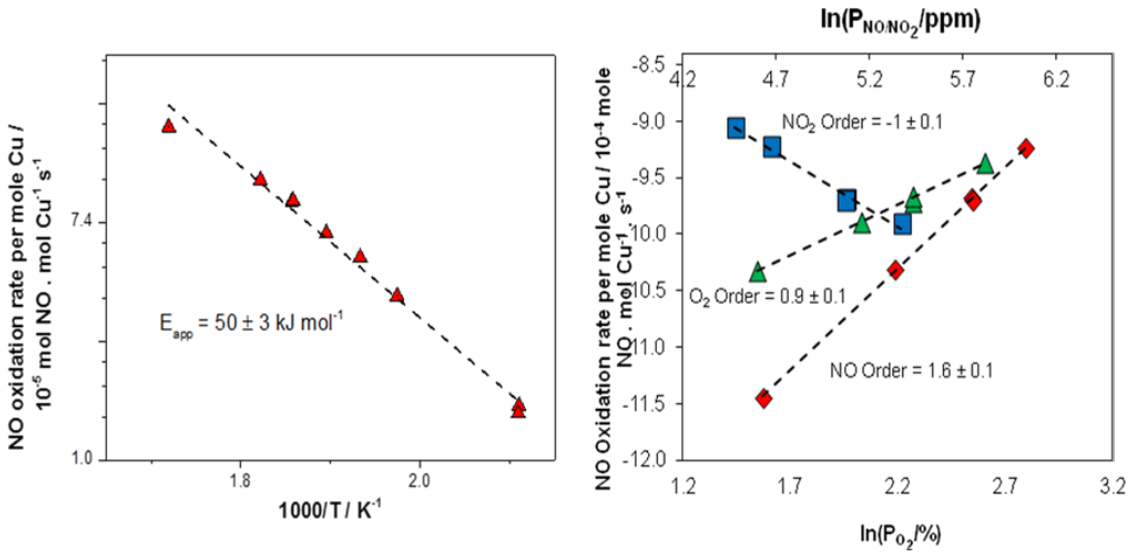

Figure B.2 (a) Variation of the rate of NO oxidation (per mole Cu) with temperature for a Cu/SSZ-13 catalyst with Cu/Al atomic ratio = 0.35. Feed conditions are 300 ppm NO, 150 ppm NO_2 and 10% O_2. (b) Variation of the rate of NO oxidation with gas concentrations for a Cu/SSZ-13 catalyst with Cu/Al_{tot} atomic ratio = 0.35. Feed for NO order = 150 ppm – 400 ppm NO, 150 ppm NO_2 and 10% O_2. Feed for O_2 Order = 5 –15% O_2, 300 ppm NO and 150 ppm NO_2. Feed for NO_2 order = 80 – 200 ppm NO_2, 300 ppm NO and 10% O_2.

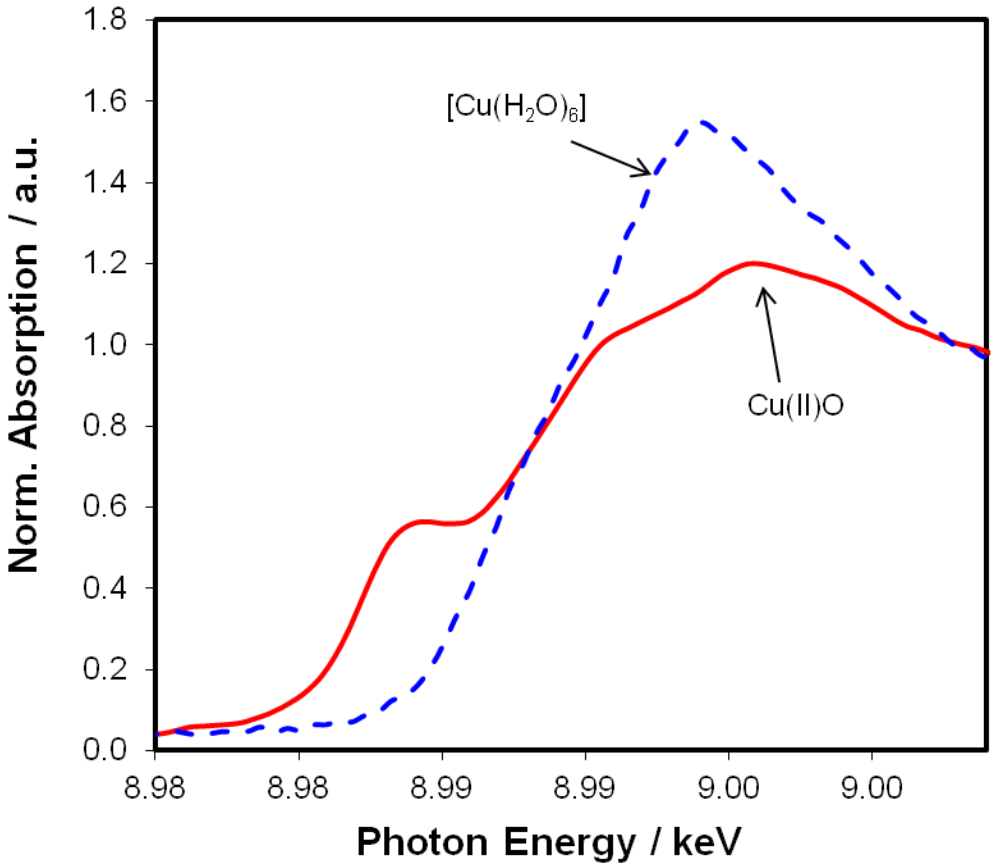

Figure B.3 XANES spectra of hexa-aquo Cu^{2+} ions in solution $[Cu(H_2O)_6]^{2+}$ and bulk copper oxide (Cu(II)O). Both copper compounds have a formal oxidation state of +2.

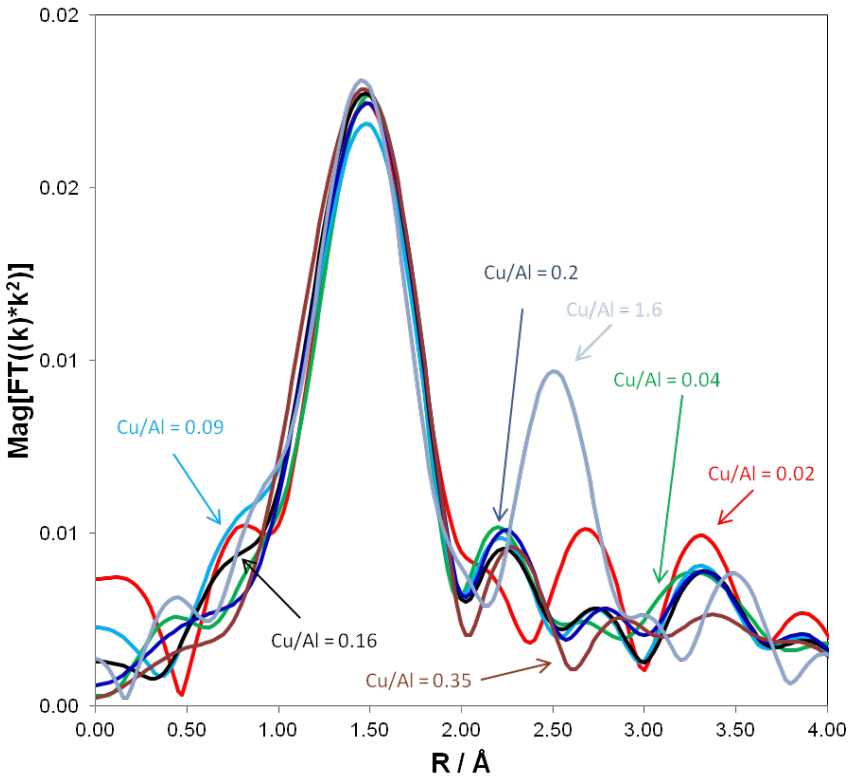

Figure B.4EXAFS spectra for all Cu/SSZ-13 samples in this study in air under ambient conditions.

Table B.2 The EXAFS fit parameters for all Cu-SSZ-13 samples in this study under ambient conditions (in air at room temperature).

Sample	Cu/Al_{tot} atomic ratio	Treatment	Absorber - Scatter	CN	R / Å	$\Delta\sigma^2$ / 10^{-3} Å	E_o / eV
Cu-SSZ-13	0.02	RT, ambient	Cu-O	4.0	1.94	2	-9.5
Cu-SSZ-13	0.04	RT, ambient	Cu-O	3.9	1.94	2	-10.3
Cu-SSZ-13	0.08	RT, ambient	Cu-O	3.9	1.94	2	-10.4
Cu-SSZ-13	0.16	RT, ambient	Cu-O	4.1	1.94	2	-10.2
Cu-SSZ-13	0.2	RT, ambient	Cu-O	4.1	1.94	2	-10.6
Cu-SSZ-13	0.35	RT, ambient	Cu-O	4.3	1.94	2	-11.2
Cu-SSZ-13	1.6	RT, ambient	Cu-O	3.3	1.77	2	6.26

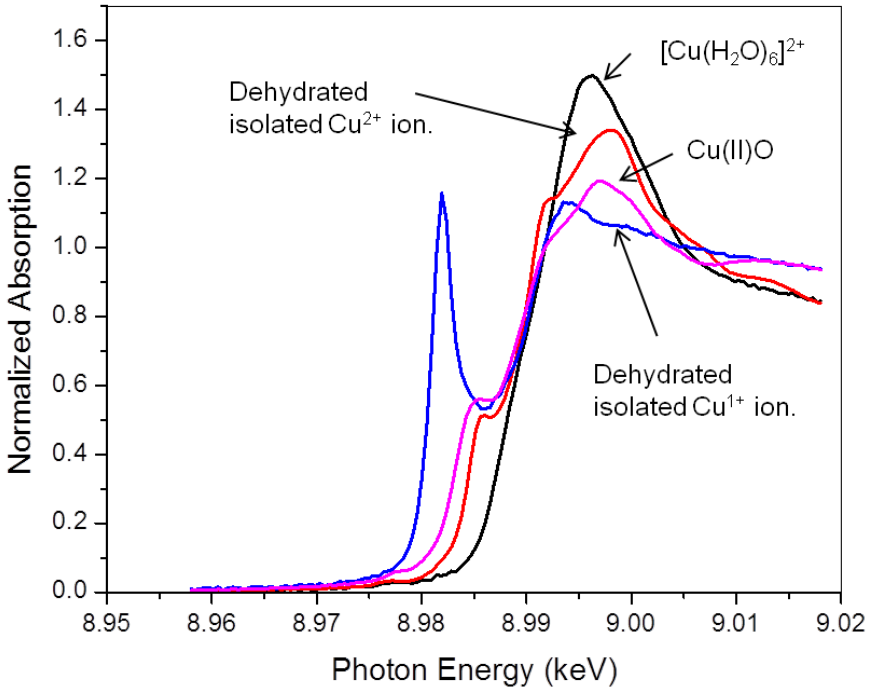

Figure B.5 XANES spectra for a series of references used. These include XANES on $[Cu(H_2O)_6]^{2+}$ ions dehydrated isolated Cu^{2+} ions in SSZ-13, dehydrated Cu^{1+} ions in SSZ-13, and bulk copper oxide (Cu(II)O)

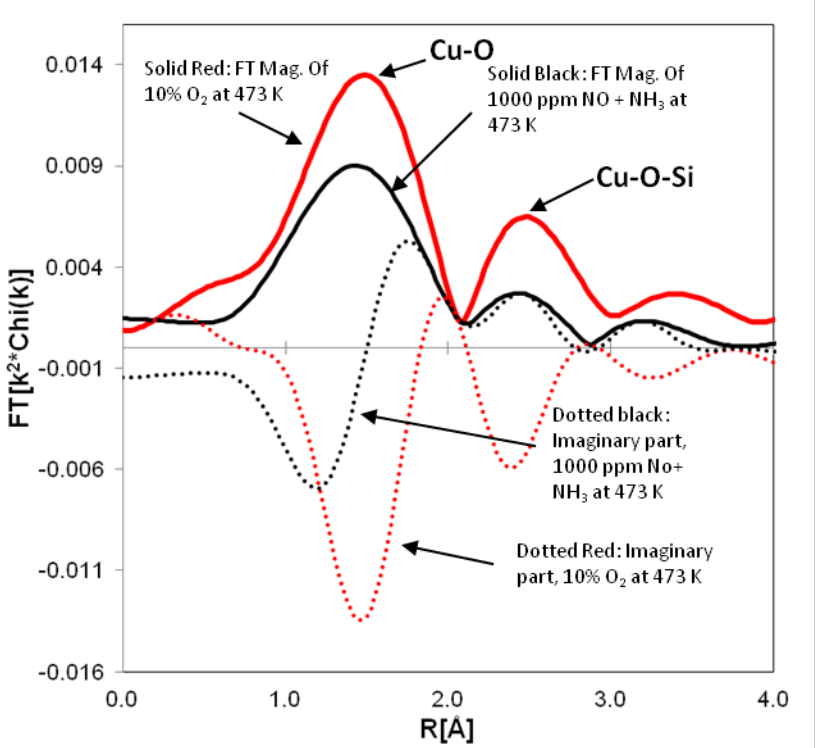

Figure B.6 FT-EXAFS for the isolated Cu^{2+} reference (in red) and isolated Cu^{1+} reference (in black). The isolated Cu^{2+} reference was generated by treating 0.3 wt% Cu-SSZ13 (Cu/Al atomic ratio =0.02) in 10% O_2 at 200°C. The first shell was identified as Cu – O scattering and the second shell was identified as Cu – Si scattering (Cu – O – Si). The isolated Cu^{1+} reference was generated by treating 0.3wt% Cu-SSZ13 (Cu/Al atomic ratio = 0.02) in 1000 ppm NO + 1000 ppm NH_3 at 200°C.

Table B.3 EXAFS fit parameters for isolated Cu(I) and isolated Cu(II).

0.31% Cu EXAFS of Cu/SSZ-13 (Cu/Al_{tot} = 0.02)								
Sample	Treatment	XANES		Scatter	N	R, Å	$\Delta\sigma^2$ (x 10^3)	Eo, eV
		Fraction Cu^{+2}	Fraction Cu^{+1}					
Cu(II)	RT, ambient	1.0	-	Cu-O	3.9	1.96	2.0	-8.5
Cu(II)	10% O_2 , 473 K	1.0	-	Cu-O	4.0	1.96	4.0	-7.5
Cu(I)	1000 ppm NH_3 + 1000 ppm NO, 473 K	-	1.0	Cu-O	2.2	1.85	4.0	-5.1

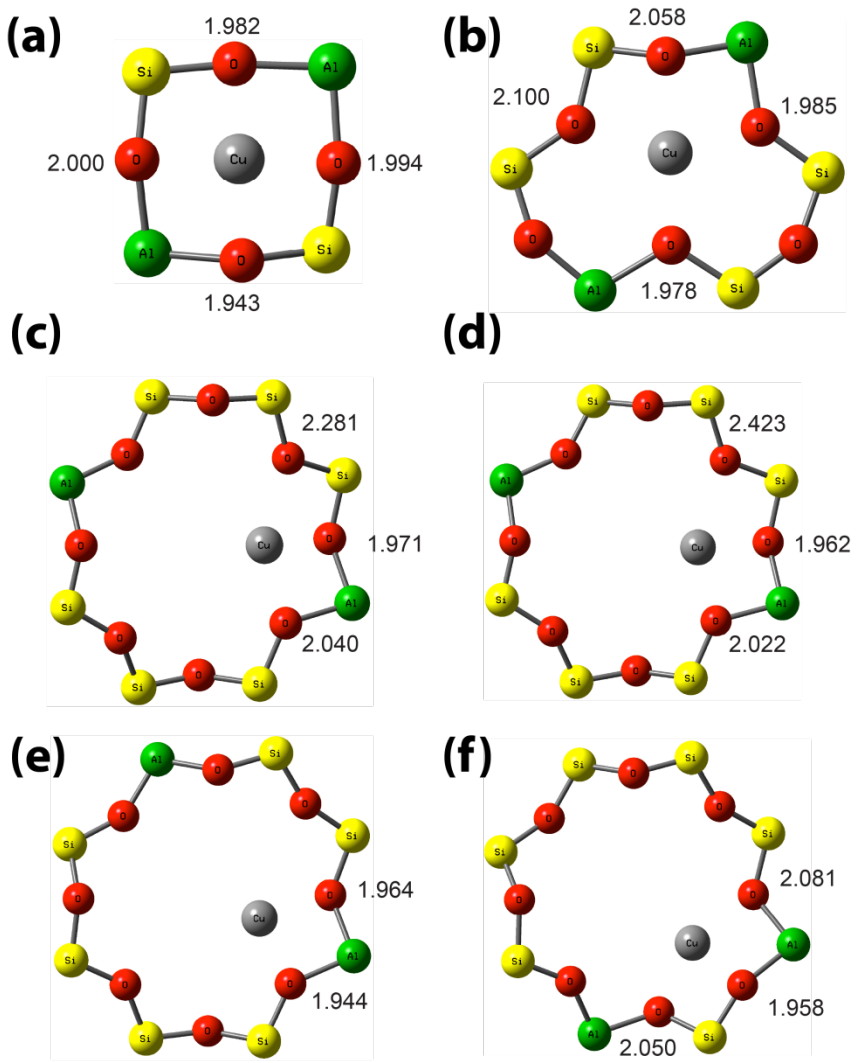

Figure B.7 Optimized structure of the isolated exchanged Cu^{2+} ion. (a) 2 × 1 × 1 supercell 4-ring 2NN Al site. (b) 2 × 1 × 1 supercell 6-ring 3NN Al site. (c) 2 × 1 × 1 supercell 8-ring site 4NN Al site. (d) 1 × 1 × 1 supercell 4NN 8-ring site. (e) 1 × 1 × 1 supercell 3NN 8-ring site. (f) 1 × 1 × 1 supercell 2NN 8-ring site. The sphere color coding is as in Figure S1. Number indicates optimized Cu-O distances in Å.

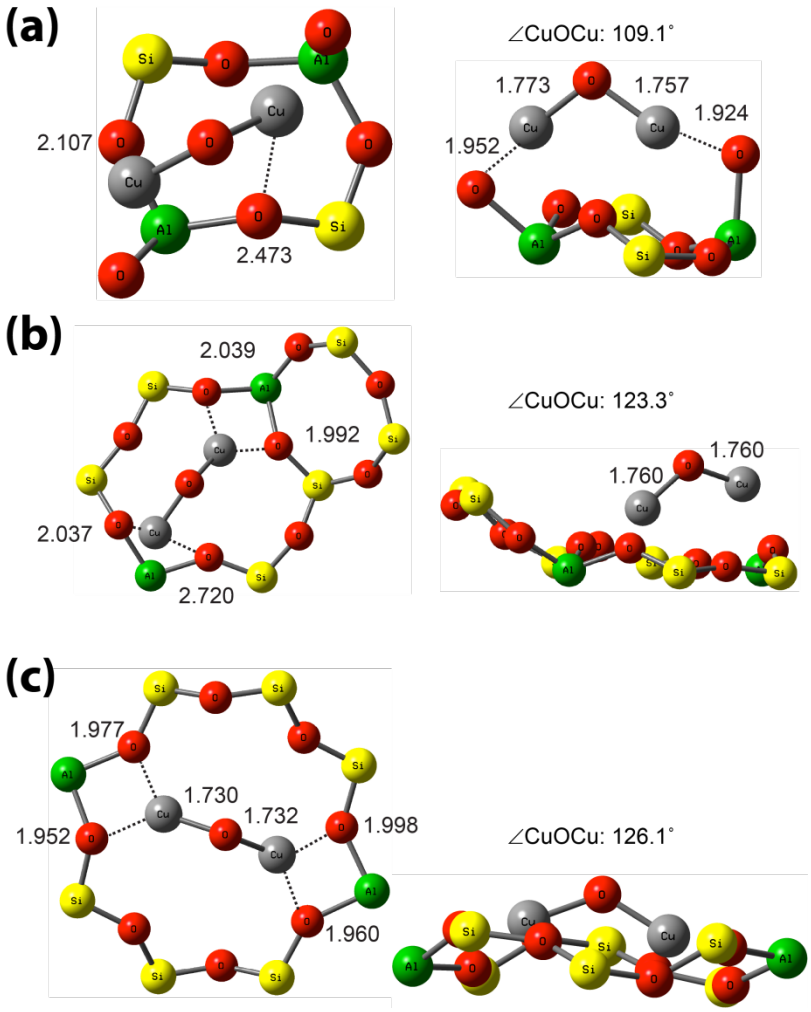

Figure B.8 Optimized Z_4H_2CuOCu structures in 2 × 1 × 1 supercell model. (a) $^3[CuOCu]^{2+}$ in the 4-ring 2NN Al site. (b) $^3[CuOCu]^{2+}$ in the 6-ring 3NN Al site. (c) $^1[CuOCu]^{2+}$ in the 8-ring 4NN Al site. Sphere color coding is as in Figure S1. Numbers indicate optimized Cu-O distances in Å.

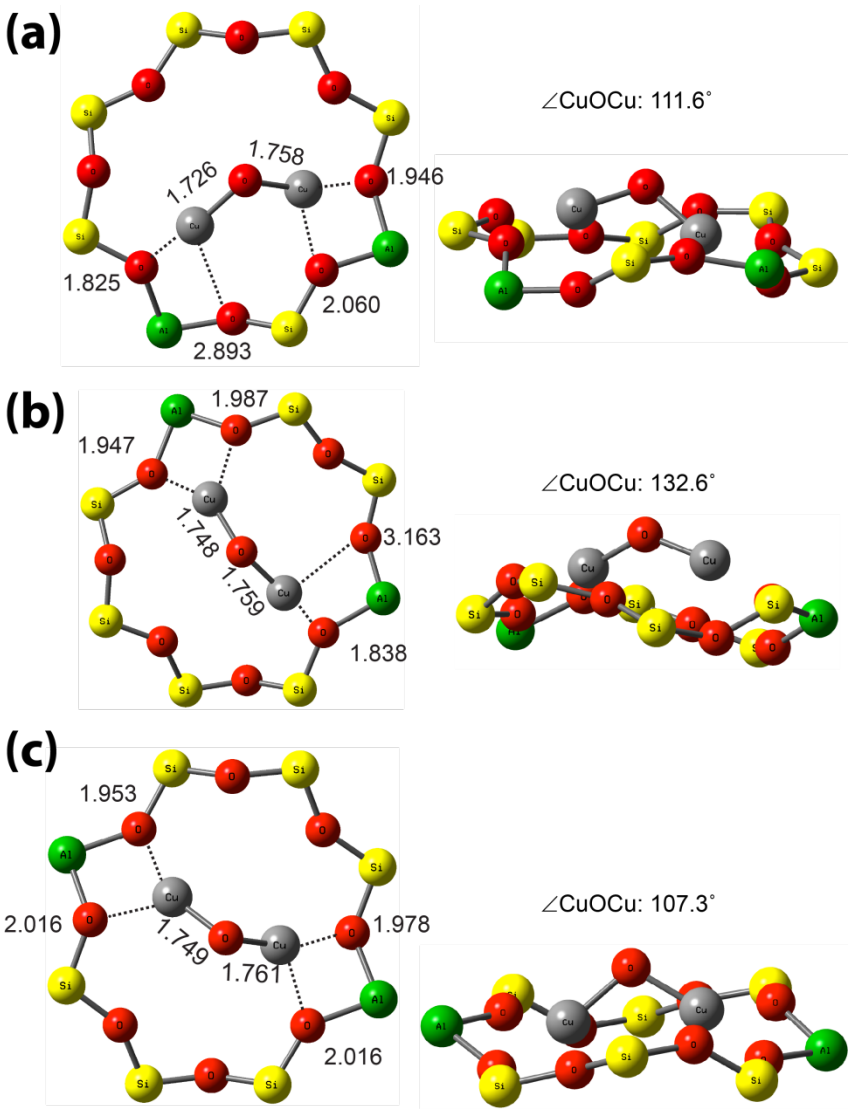

Figure B.9 Optimized ZCuOCuZ structures in 1 × 1 × 1 supercell model. (a) $^{3}[CuOCu]^{2+}$ in the 8-ring 2NN Al site. (b) $^{3}[CuOCu]^{2+}$ in the 8-ring 3NN Al site. (c) $^{3}[CuOCu]^{2+}$ in the 8-ring 4NN Al site. Sphere color coding is as in Figure S1. Numbers indicate optimized Cu-O distances in Å.

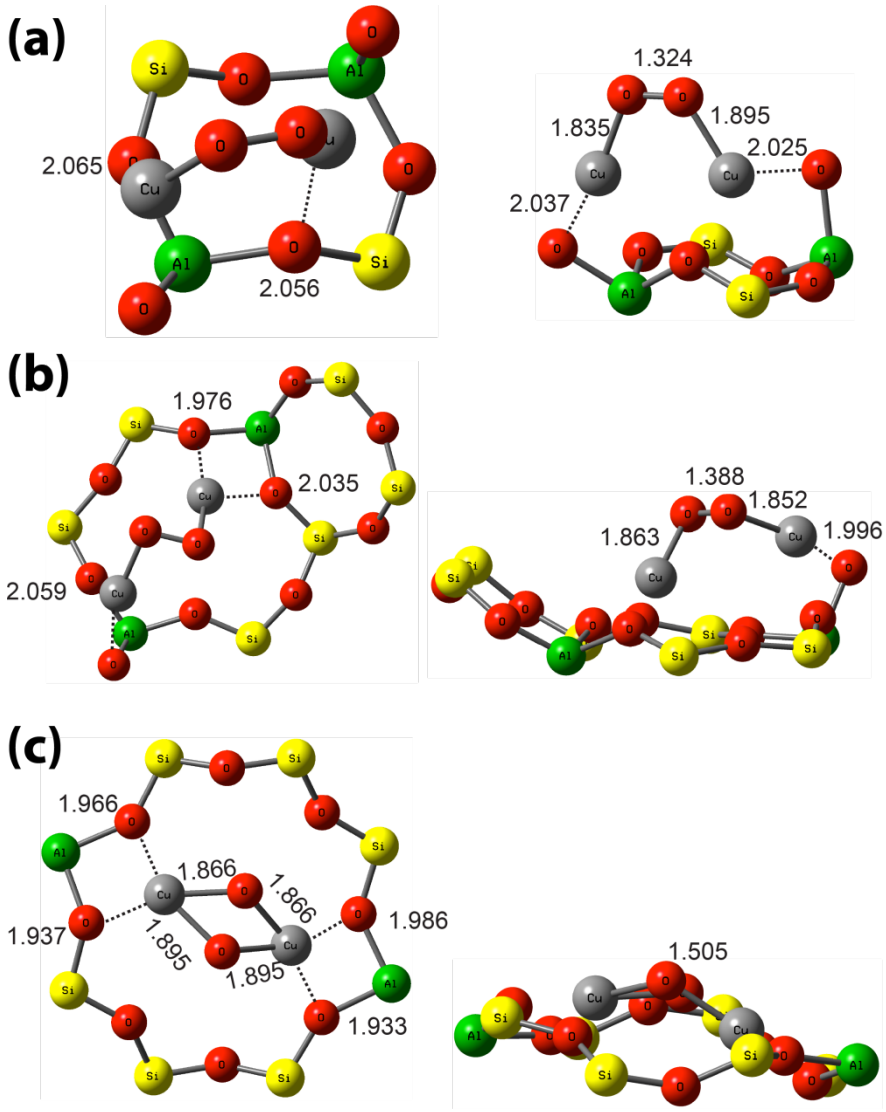

Figure B.10 Optimized $Z_4H_2CuO_2Cu$ structures in 2 × 1 × 1 model. (a) $^3[\mu\text{-}1,2\text{-}O_2Cu_2]^{2+}$ in 4-ring 2NN Al site. (b) $^3[\mu\text{-}1,2\text{-}O_2\ Cu_2]^{2+}$ in the 6-ring 3NN Al site. (c) $^1[\mu\text{-}\eta^2\text{:}\eta^2\text{-}O_2Cu_2]^{2+}$ in the 8-ring 4NN Al pair site. Sphere color coding is as in Figure S1. Numbers indicate optimized Cu-O distances in Å.

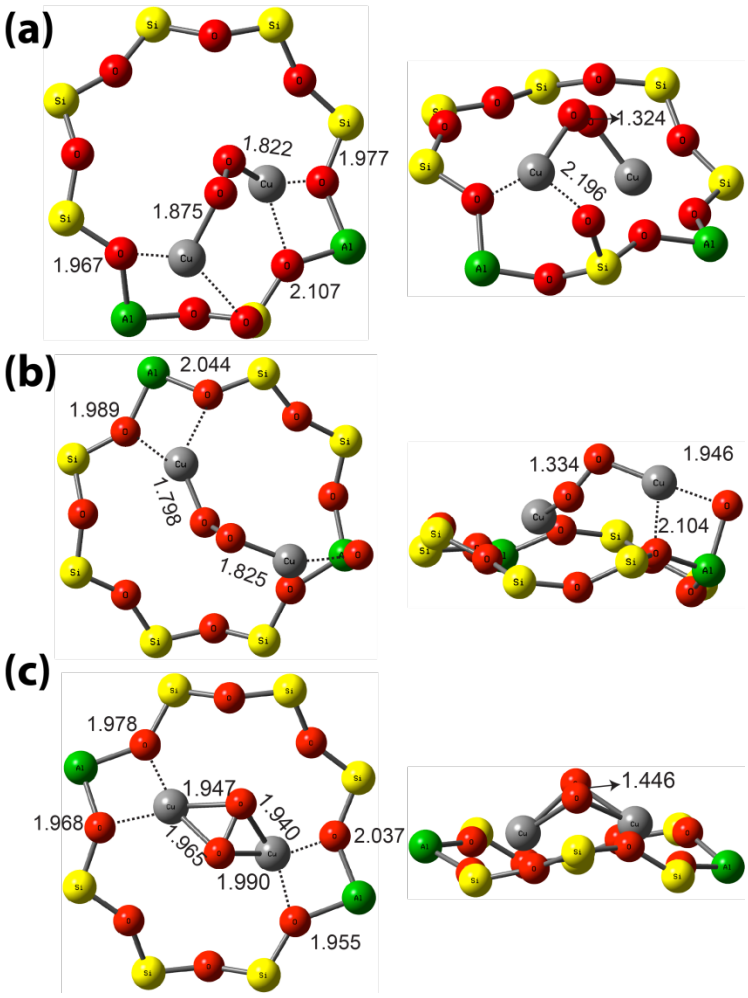

Figure B.11 Optimized $[CuO_2Cu]^{2+}$ structures corresponding to Figure 11. (a) $^3[\mu\text{-}1,2\text{-}O_2Cu_2]^{2+}$ in the 8-ring 2NN Al site. (b) $^3[\mu\text{-}1,2\text{-}O_2Cu_2]^{2+}$ in the 8-ring 3NN Al site. (c) $^3[\ \mu\text{-}\eta^2\text{:}\eta^2\text{-}O_2Cu_2]^{2+}$ in the 8-ring 4NN Al site. The sphere color coding is as in Figure S1. Numbers indicate optimized Cu-O distances in Å.

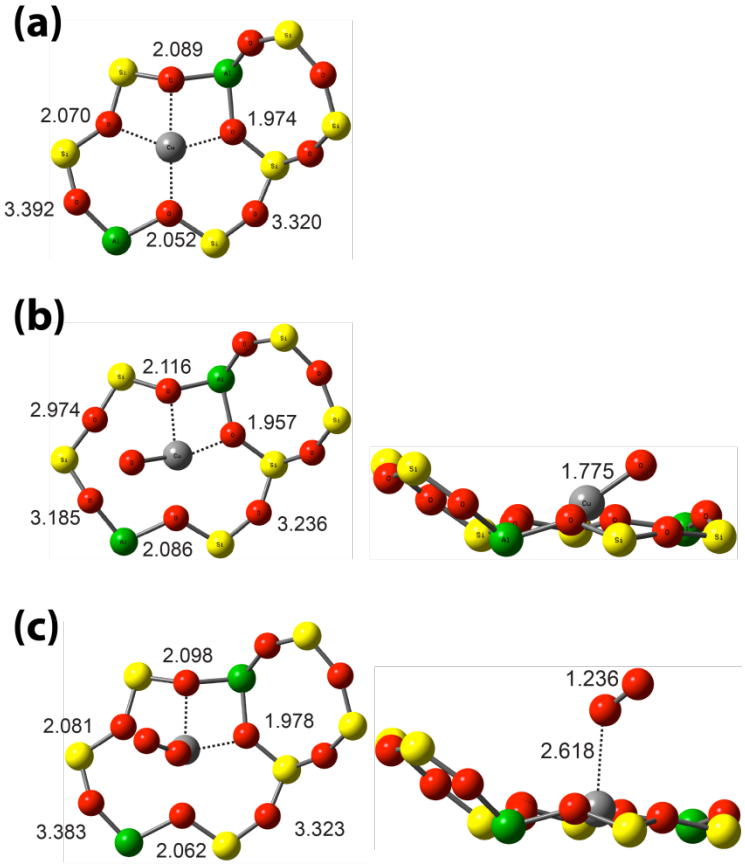

Figure B.12 Optimized Z_2Cu, Z_2CuO, and Z_2CuO_2 structures corresponding to Figure 11. (a) Z_2Cu in the 6-ring 3NN Al site. (b) ^4Z_2CuO in the same site. (c) $^2Z_2CuO_2$ in the same site. The sphere color coding is as in Figure S1. Numbers indicate optimized Cu-O distances in Å.

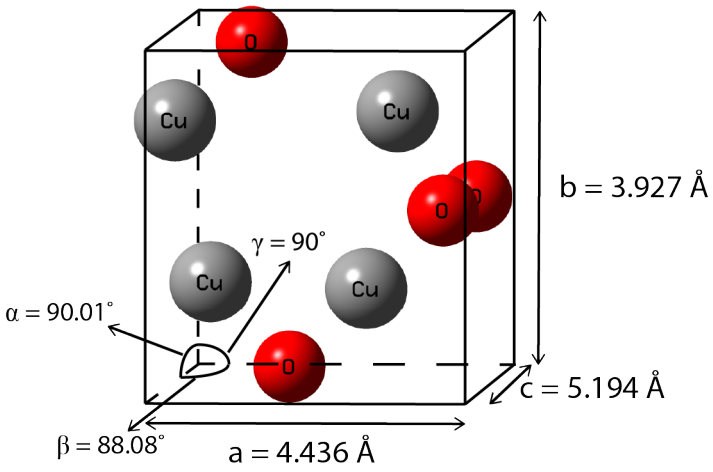

Figure B.13 GGA-computed bulk Cu(II)O lattice parameters. Atom color coding as in Figure B.1.

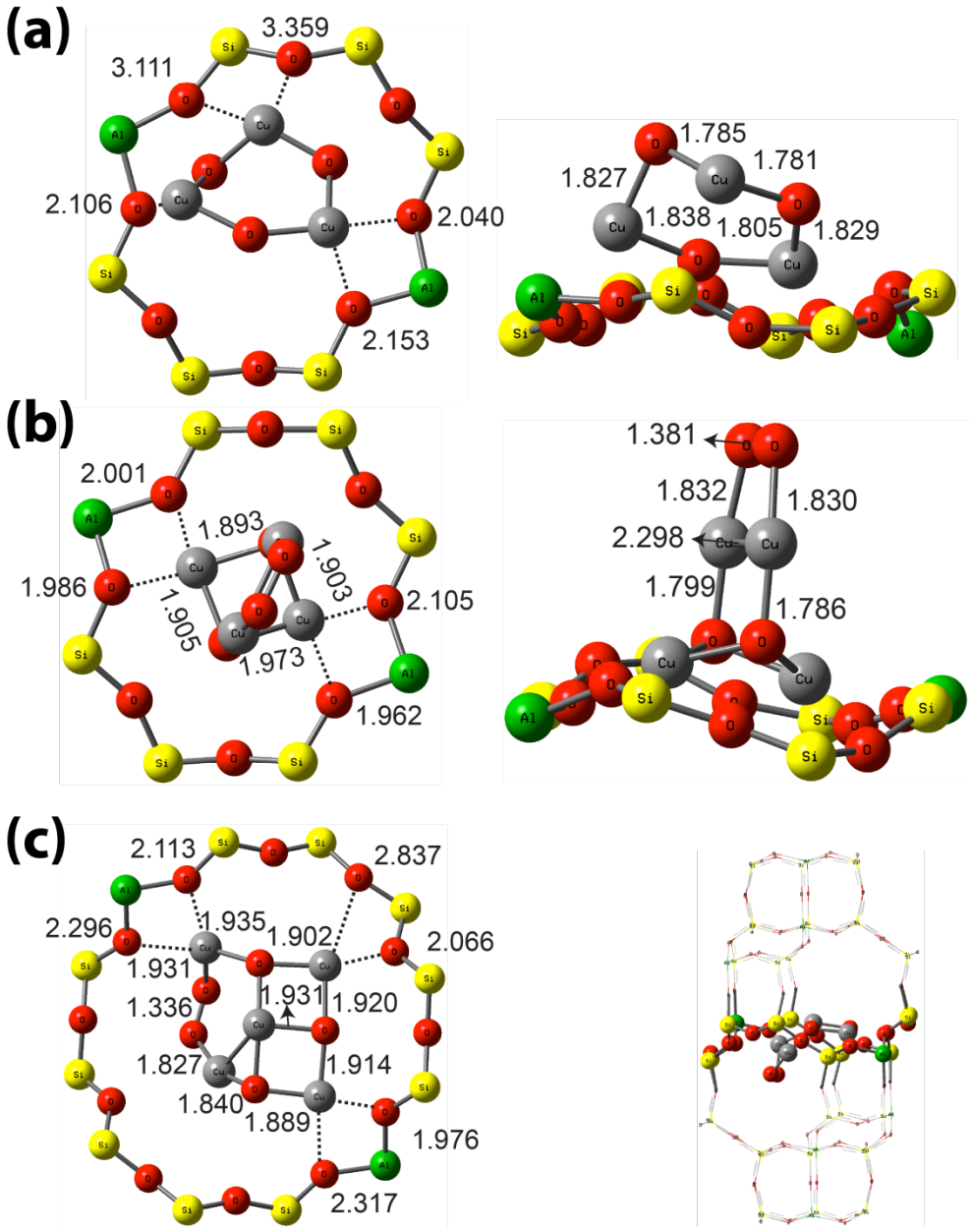

Figure B.14 Optimized $(CuO)_x^{2+}$ clusters (x = 3-5) inside the SSZ-13 zeolite cage. (a) $^4(CuO)_3$ cluster. (b) $^1(CuO)_4$ cluster. (c) $^2(CuO)_5$ cluster. The sphere color coding is as in Figure S1. Numbers indicate optimized Cu-O distances in Å.

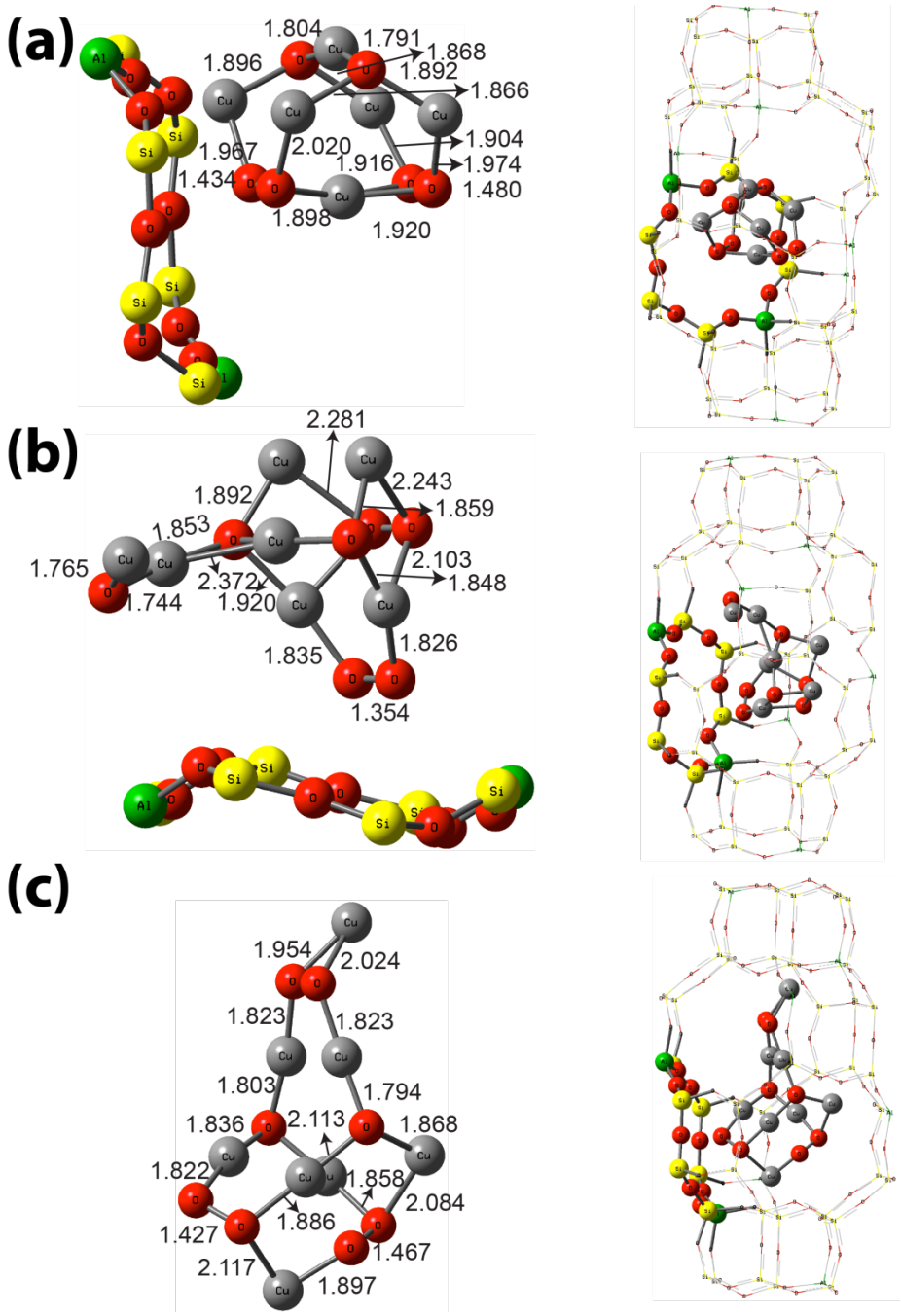

Figure B.15 Optimized $(CuO)_x^{2+}$ clusters (x = 6-8) inside the SSZ-13 cage. (a) $^1(CuO)_6$ cluster. (b) $^3(CuO)_7$ cluster. (c) $^4(CuO)_8$ cluster. The sphere color coding is as in Figure B.1

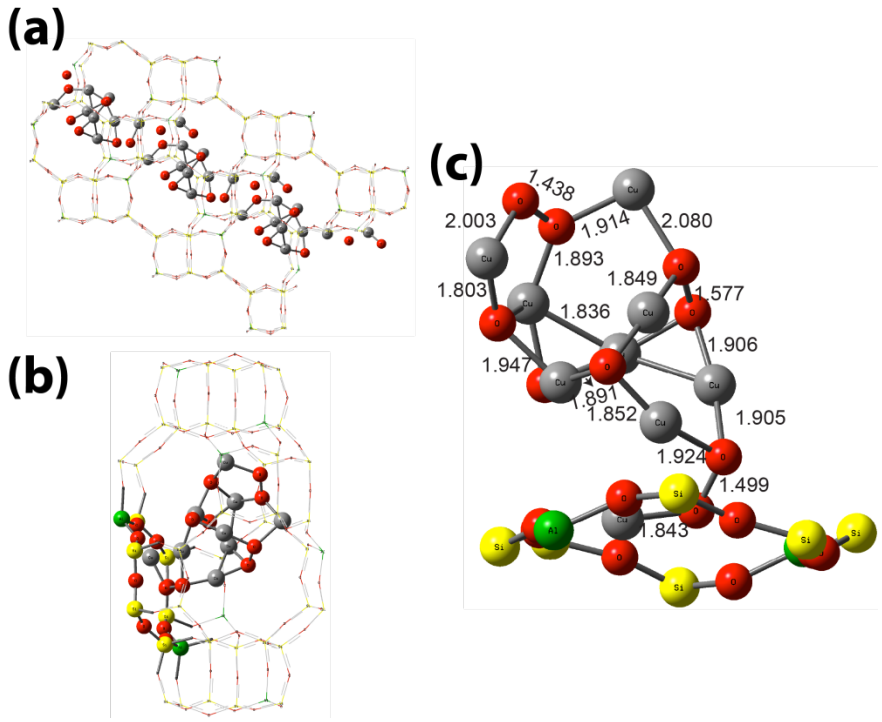

Figure B.16 $(CuO)_9$ cluster inside the SSZ-13 cate. (a) Percolation of $(CuO)_9$ across the zeolite cages. (b) $(CuO)_9$ inside one channel of SSZ-13. (c) Optimized $^2(CuO)_9$ cluster geometry values. The color coding for the spheres is as in Figure B.1.

Table B.4 Raw and Relative energies of isolated Cu(II) ions at different Al-pair locations. All energies are in eV.

Al-pair sites	From 2 × 1 × 1 supercell		From 1 × 1 × 1 supercell	
	Raw Energy	**Relative Energy**	**Raw Energy**	**Relative Energy**
4-Ring	-574.622	-0.37	-284.155	-0.37
6-Ring	-575.751	-1.51	-285.203	-1.42
8-Ring – 4NN	-574.246	0	-283.783	0
8-Ring – 3NN	N/A	N/A	-283.550	0.23
8-Ring – 2NN	N/A	N/A	-284.030	-0.25

Table B.5 Molecular oxygen adsorption energy on various sites within the SSZ-13 zeolite structures.

Model	Multiplicity	Cu-O	E_{ads} – GGA (eV)	E_{ads} – B3LYP corrected (eV)
$ZCuO_2$[a]	2.9	1.965, 1.966	-0.61	-0.38
Z_2CuO_2	2.0	2.618	-0.05	0.25
$Z_2Cu_2O_2$-2NN	3.0	1.822;1.874	-1.28	-0.67
$Z_2Cu_2O_2$-3NN	3.0	1.798;1.825	-1.91	-1.44
$Z_2Cu_2O_2$-4NN	3.0	1.947, 1.965; 1.940, 1.990	-2.05	-1.84
$Z_2Cu_2O_2$-4NN	1.0	1.865, 1.893; 1.866, 1.895	-2.06	-1.20

a: McEwen et al. [24]

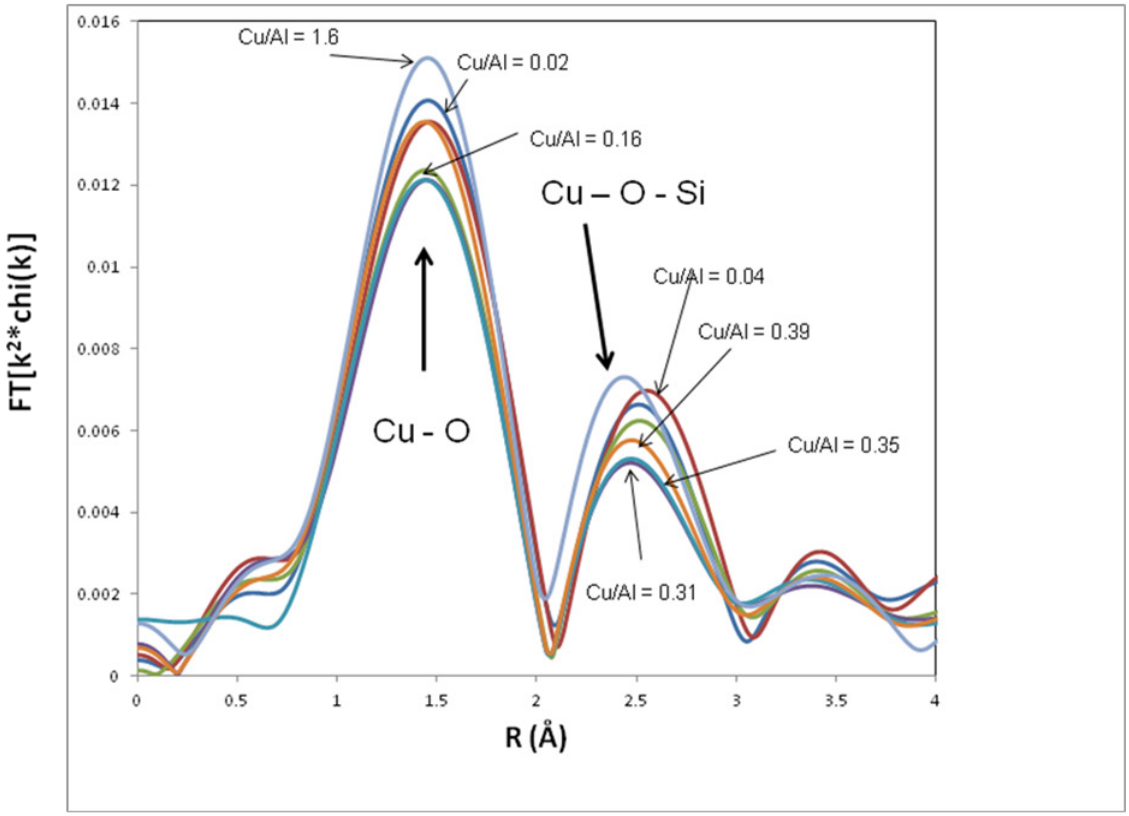

Figure B.17 EXAFS spectra for all Cu/SSZ-13 samples in this study under in-situ NO oxidation. Feed conditions: 300 ppm NO, 150 ppm NO_2 and 10% O_2.

Table B.6 EXAFS fit parameters for Cu-SSZ13 catalysts under NO oxidation

Sample	Scatter	N	R, Å	$\Delta\sigma^2$ (x 10^3)	Eo, eV
Cu/Al = 0.02	Cu-O	4.01	1.91	3.4	-12.5
Cu/Al = 0.04	Cu-O	3.75	1.93	3.4	-10.3
Cu/Al = 0.16	Cu-O	3.5	1.9	3.4	-11.3
Cu/Al = 0.31	Cu-O	3.22	1.9	3.4	-11
Cu/Al = 0.35	Cu-O	3.21	1.9	3.4	-11.65
Cu/Al = 0.39	Cu-O	3.6	1.9	3.4	-11.7
Cu/Al = 1.6	Cu-O	3.96	1.9	3.4	-11.32

Feed Conditions: 300 ppm NO, 150 ppm NO_2, 10% O_2 and 573 K

Determination of the rate expression for NO oxidation on Cu-SSZ-13 from the mechanism presented in Figure 3.11

The mechanistic steps from the visual representation in Figure 3.11, is presented in detail below. On the assumption of step 2 to be an irreversible forward reaction and the rate determining step *(R.D.S.), the rate of reaction can be derived as follows:*

$$1) O_2 + * \underset{}{\overset{K_1}{\rightleftharpoons}} O_2 *$$

$$2) NO + O_2 * \xrightarrow{k_2} O * + NO_2$$

$$3) NO + O * \underset{}{\overset{K_3}{\rightleftharpoons}} NO_2 *$$

$$4) NO_2 * \underset{}{\overset{K_4}{\rightleftharpoons}} NO_2 + *$$

Here,

* = A Cu-Cu pair without adsorbed oxygen.

L = Total number of Cu-Cu pairs available for NO oxidation catalysis.

The rate of NO removal (from step 3) $-r_{NO} = k_2[NO][O_2*]$

Expressing $[O_2*]$ in terms of [*] (Cu pair) using step 1, we get $[O_2*] = K_1[O_2][*]$

Thus, the rate of NO removal $-r_{NO} = k_2 K_1[NO][O_2][*]$

A mass balance on all the paired Cu sites, $L = [*] + [O*] + [O_2*] + [NO_2*]$

We will now evaluate $[O*]$ from step 3 $[O*] = \dfrac{K_3^{-1}K_4^{-1}[NO_2][*]}{[NO]}$

Using $[NO_2*] = K_4^{-1}[NO_2][*]$ from step 4

$$L = [*] + \frac{K_3^{-1}K_4^{-1}[NO_2][*]}{[NO]} + K_1[O_2][*] + K_4^{-1}[NO_2][*]$$

And, $$[*] = \frac{L[NO]}{[NO] + K_3^{-1}K_4^{-1}[NO_2] + K_1[O_2][NO] + K_4^{-1}[NO_2][NO]}$$

Substituting this in the final rate expression, we obtain:

$$-r_{NO} = \frac{k_2 K_1 L[NO]^2[O_2]}{[NO] + K_3^{-1}K_4^{-1}[NO_2] + K_1[NO][O_2] + K_4^{-1}[NO][NO_2]}$$

Defining the following surface coverage terms:

$$\theta_{O^*} = \frac{[O^*]}{L} = \frac{K_3^{-1}K_4^{-1}[NO_2]}{[NO] + K_3^{-1}K_4^{-1}[NO_2] + K_1[O_2][NO] + K_4^{-1}[NO_2][NO]}$$

$$\theta_{O_2^*} = \frac{[O_2^*]}{L} = \frac{K_1[O_2][NO]}{[NO] + K_3^{-1}K_4^{-1}[NO_2] + K_1[O_2][NO] + K_4^{-1}[NO_2][NO]}$$

$$\theta_{NO_2^*} = \frac{[NO_2^*]}{L} = \frac{K_4^{-1}[NO_2][NO]}{[NO] + K_3^{-1}K_4^{-1}[NO_2] + K_1[O_2][NO] + K_4^{-1}[NO_2][NO]}$$

$$\theta_* = \frac{[*]}{L} = \frac{[NO]}{[NO] + K_3^{-1}K_4^{-1}[NO_2] + K_1[O_2][NO] + K_4^{-1}[NO_2][NO]}$$

$\theta_* + \theta_{O^*} + \theta_{O_2^*} + \theta_{NO_2^*} = 1$ (Mass balance on all reactive sites)

By taking the derivative of $\ln(-r_{NO})$ with respect to $\ln(C_i)$ (where C_i is the concentration of NO, NO_2 or O_2), we obtain the following relations between the apparent reaction orders and surface coverage terms.

$$n_{NO} = 2 - \theta_* - \theta_{O_2^*} - \theta_{NO_2^*}$$

$$n_{O_2} = 1 - \theta_{O_2^*}$$

$$n_{NO_2} = -(\theta_{O^*} + \theta_{NO_2^*})$$

The experimental apparent reaction orders at 300°C are NO = 1.6 ± 0.2, NO_2 = -0.8 ± 0.1and O_2 = 0.9 ± 0.1 . Using these apparent reaction orders, we compute that the corresponding average reactive surface coverage terms are as follows:

$\theta_* = 0.1$, $\theta_{O_2^*} = 0.1$, $\theta_{NO_2^*} = 0.2$, and $\theta_{O^*} = 0.6$. These reactive surface coverage terms are consistent with the energetics of the mechanism proposed in Figure 11, i.e., O* is predicted to be the most stable intermediate during NO oxidation catalysis on Cu-SSZ-13 consistent with its average reactive surface coverage of 0.6 shown in the kinetic analysis above.

Appendix C Appendix for Chapter 4

Catalyst Preparation

The catalyst was prepared by ion exchange of $Cu(NO_3)_2$ into H-SSZ-13 zeolite powder. The H-SSZ-13 zeolite was synthesized in-house following the recipe published by Fickel *et al.*[30] based on the original synthesis of this zeolite by S. I. Zones [43]. The details of the zeolite synthesis, as well as comparisons with XRD in literature and atomic absorption spectroscopy (AA) characterization were discussed in a previous publication [25]. A solution of 970 mg of H-SSZ-13 in 40 mL of deionized (DI) H_2O was stirred and heated to 313 K for 30 min. After dropwise addition of a solution of 47 mg of $Cu(NO_3)_2$ (Alfa-Aesar) dissolved in 10 mL of DI H_2O; more DI H_2O was added to bring the total solution volume to 200 mL. The mixture was allowed to stir for 300 min while the pH was maintained between 5 and 5.2 by dropwise addition of 0.1 M NH_4OH (Sigma Aldrich, Cat. No. 221228-2L-A). The resulting slurry went through three centrifuge and rinse cycles with de-ionized (DI) water before vacuum drying for 540 min at ambient temperature. After drying, the catalyst was calcined with 80 sccm dry air (Comm. Grade, Indiana Oxygen) at 798 K for 360 min with a 0.5 K min^{-1} ramp rate. The zeolite was determined to have a silicon to aluminum atomic ratio (Si:Al) of 4.5 by atomic absorption spectroscopy, and the two samples tested in this study had 2.1 and 3.04 wt.% Cu corresponding to copper to aluminum atomic ratios (Cu:Al) of 0.11 and 0.16, respectively.

Operando XAS reactor

Operando XAS experiments were performed in a custom built, down-flow, fixed-bed, plug-flow reactor using a low X-ray absorbing vitreous carbon tube reactor. The design and implementation of the reactor have been discussed in detail in previous publications [25, 61]. The carbon tube reactor (10 mm x 4 mm x 200 mm OD x ID x L) was held inside an aluminum heater block which had 25 mm long x 2 mm wide slits cut into the side to let the X-ray beam pass through the block and sample within the tube. Four 5” long, 100W heat cartridges (Chromalux CIR-1051) were used to heat the block. A wire

mesh welded to a piece of 1/16" tubing was used to hold the catalyst bed in place. From bottom to top, the catalyst bed was composed of a layer of quartz wool on top of the wire mesh, a layer of glassy carbon beads, the same material as the reactor tube, to create a flat surface upon which the catalyst could sit, followed by 8 - 20 mg of catalyst powder sieved to 125-250 μm, then another layer of quartz wool followed by a layer of crushed quartz (< 60 mesh) to help break up gas flow. The catalyst bed height was roughly 3 mm, and while this bed size was small compared to the bed diameter, the quality of the kinetics was not affected. An extensive discussion and comparison of the *operando* reactor with a conventional, bench top laboratory reactor can be found in our previous publication [25].

Temperature was measured with a thermocouple fed into the reactor and placed into the top layer of quartz wool just above the catalyst bed. Gases were mixed and introduced into the reactor in precise order to prevent the formation of NH_4NO_3 and other side reactions. The ultra high purity He (Airgas, Inc.) carrier gas flowed through a heated shell-type humidifier (Perma Pure MH-Series) to introduce DI H_2O into the gas stream. All gas lines downstream of the humidifier were kept heated above 373 K to prevent H_2O condensation. After H_2O introduction, NO (3000 ppm in N_2; Matheson Tri-Gas) was introduced into the gas stream, followed by the introduction of O_2 (20% in He; Airgas, Inc.). The reaction mixture was then preheated to 473 K. The reactor was found to be well below the Mears criterion for radial heat transfer gradients within the catalyst bed [25, 156, 157]. Ammonia (3000 ppm in He; Matheson Tri-Gas) was introduced through a feed tube which injected the gas a few inches above the catalyst bed to minimize the chances of gas phase side reactions. When the feed gas concentrations were measured by bypassing the reactor, the NH_3 was switched such that it was introduced into the gas mixture moments before passing through a 7 μm stainless steel particulate filter and entering the gas analysis system. Gas concentrations were measured using an MKS Multi-Gas 2030 gas analyzer FTIR with a cell temperature of 464 K based on stock calibration files. A total flow rate of 500 sccm and a temperature of 473 K were maintained throughout all of the experiments. The Standard SCR contained 300 ppm NO,

300 ppm NH_3, 5% H_2O and 10% O_2. Contrary to our previous experiments, CO_2 was not included as a reactant, because it was used as a tracer in the cut-off experiments. The presence or absence of CO_2 as a reactant was found to have no effect on the catalyst kinetics. This is evident from Figure S1 and Table S1.

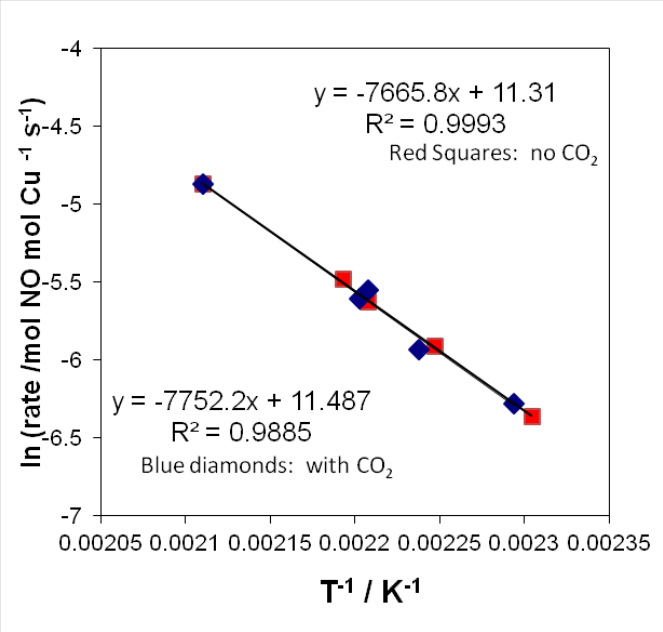

Figure C.1 Activation energy plot for a 1.7 wt.% Cu-SSZ-13 (Cu:Al = 0.09) under standard SCR 320 ppm NO, 320ppm NH_3, 7% H_2O, 10% O_2, balance He with (blue diamonds) and without (red squares) 8% CO_2 in the feed. Data were collected over 433-473 K at a total flow of ~1500 ml min^{-1}.

Table C.1Measured activation energy, pre-factor and rate for a 1.7% Cu-SSZ-13 (Cu:Al = 0.09) catalyst under standard SCR gas conditions with and without CO_2 in the feed.

Sample	Ea / kJ mol^{-1}	k_o / 10^4 s^{-1}	Rate (473 K) / 10^{-3} mol NO mol Cu^{-1} s^{-1}
Standard SCR with CO_2	64	9.7	7.43
Standard SCR without CO_2	64	8.2	7.47

The cutoff experiments were designed to dynamically isolate the reducing or oxidizing portion of the SCR reaction. Each portion of the SCR redox cycle was isolated by systematically cutting off individual reactants, and the state of the catalyst was observed through XANES in the new non catalytic steady state. For example, if redox of Cu were

central to the standard SCR reaction, the catalyst, which starts in a mixed Cu^{I} – Cu^{II} oxidation state under steady state standard SCR, should become more reduced when the oxidant is removed. Correspondingly, the catalyst should become more oxidized when a reductant is removed. Three different cutoff experiments were designed to test this hypothesis. For each experiment, the catalyst was first allowed to come to steady state under the standard SCR reaction, at which point steady state XAS and kinetic data were collected. After steady state data were collected, one of the reactants was cut off from the gas flow and the transient changes in catalyst and gas compositions were monitored by time-dependent XAS and the FTIR gas analyzer, respectively. Reactant addition experiments to enable standard SCR in the final steady state, were performed separately and the results were completely reversible. For these experiments, CO_2 was used as a tracer to track the exchange of gases throughout the gas holdup of the system upon cutoff of one of the reactants.

In the O2 cutoff experiment, O_2 was cut off from the standard SCR reaction mixture, isolating the reducing portion of the reaction, NO + NH_3. In the NO cutoff experiment, NO was cut off from standard SCR, interrupting the reducing portion of the reaction and only allowing oxidation by O_2 in the presence of NH_3. lastly, the NH_3 was removed to disrupt the reducing portion again and complete the series of reactant cutoffs from standard SCR. For all steady state standard SCR conditions, the catalyst was maintained under approximately differential conditions of less than 20% conversion of NO.

Only minor modifications to the gas manifold feeding the *operando* reactor needed to be made to allow for consistent switching. The most important aspect of the switch was to maintain the same total overall flow rate, so that gas concentrations remained unchanged. The gas switch was performed using an electronically actuated 2 position, 6-port switching valve (Valco Instrument Company, Inc.; Model E26UWE). In one position, the valve would feed the cutoff gas into the reactor. In the other position the valve would feed a mixture of CO_2 and He with the same total flow rate as the cutoff gas into the reactor.

Reaction rate reproducibility

In order to ensure that the Cu-SSZ-13 catalysts were performing as expected, we compared the rate of standard SCR, under differential conditions, between two reactors. The first reactor was a steady state plug flow system used to measure standard SCR kinetics in the laboratory. The second involved the *operando* XAS unit with a glassy carbon tube. The reaction rates for the catalyst in the glassy carbon tube were collected during spectroscopic measurements at the beamline. Figure S1 reports the variation of the rate of standard SCR per gram catalyst with Cu:Al (dark green squares) as measured by Bates et al.[135] A linear trend till Cu:Al = 0.2 which shows that the rate is directly proportional to the number of active sites, i.e. isolated Cu ions and by the Koros-Nowak test[70], this kinetic data-set is free of all mass transfer effects. This results in a constant turnover rate (TOR) among catalysts with Cu:Al < 0.2. Catalysts with Cu:Al = 0.09 and 0.16 were tested independently at the beam line in glassy carbon tubes and their rates are overlaid over the laboratory PFR data points in Figure S2. There is agreement in between the rates measured at the beam line and the rates measured in the laboratory, which indicates that the results are reproducible (Table S2). The standard feed conditions in both reactors were 300 ppm NO, 300 ppm NH_3, 10% O_2, 5% H_2O, 5% CO2, at 473K.

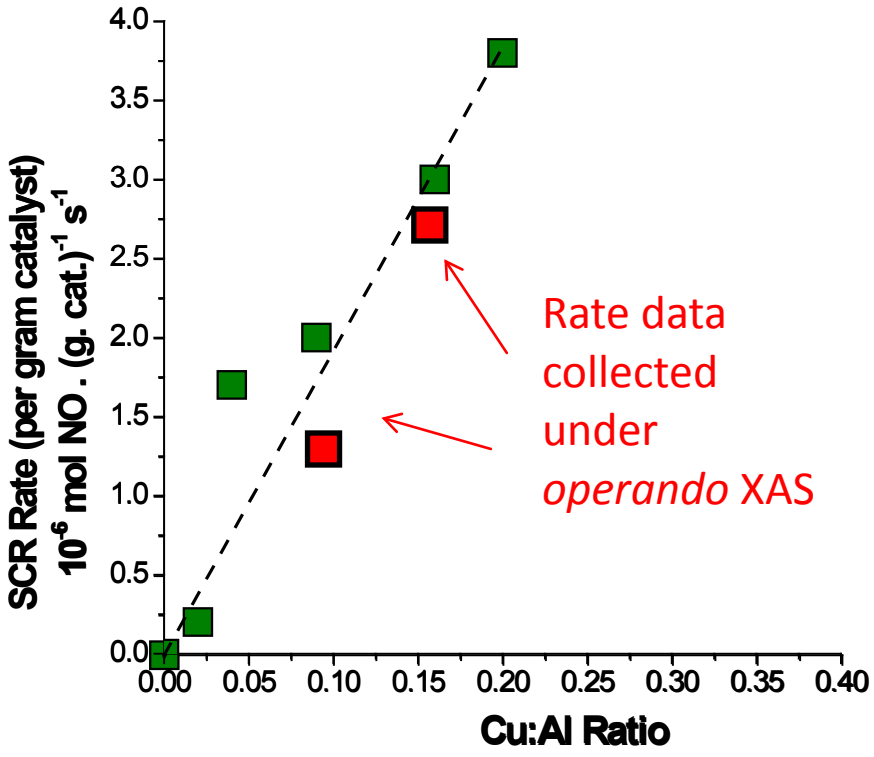

Figure C.2 Comparison of the standard SCR rate per gram catalyst on catalyst samples measured at the APS beamline (red squares) and in the laboratory (green squares). Feed conditions: 300 ppm NO, 300 ppm NH_3, 10% O_2, 5% H_2O, 5% CO_2, at 473K.

Table C.2 Comparison of standard SCR reaction rates for Cu-SSZ-13 catalysts tested in the laboratory and at the APS beam line

Sample	Rate (473 K) / 10^{-6} mol NO g cat^{-1} s^{-1}(Laboratory)	Rate (473 K) / 10^{-6} mol NO g cat^{-1} s^{-1}(Beamline)
Cu:Al = 0.11	2	1.4
Cu:Al = 0.16	2.9	2.6

Feed conditions: 300 ppm NO, 300 ppm NH_3, 10% O_2, 5% H_2O, 5% CO_2, at 473K.

X-ray Absorption Spectroscopy

X-ray absorption spectroscopy (XAS) experiments were performed at Sector 10 of the Advanced Photon Source, the Materials Research Collaborative Access Team (MR-CAT), of Argonne National Laboratory. The insertion device beamline at Sector 10 (10-ID) was necessary for the *operando* experiments due to the high photon flux available at the beamline. This capability allowed for time-dependent and positional measurements along the length of the catalyst bed with a 200 x 200 μm beam size without compromising data quality. Incident X-rays were measured in an ion chamber filled with 20% He in N_2 while the transmitted beam was measured in an ion chamber with 20% Ar in N_2 to obtain roughly 70% absorption of the beam after the sample. A third detector was used to simultaneously measure a Cu metal foil reference with each spectrum. The Cu metal foil, 8979 eV edge energy, was used to calibrate the X-ray beam for the Cu absorption K edge. All data was normalized with a 1st-order polynomial subtraction of the pre-edge and 3rd-order polynomial subtraction of the post edge backgrounds. Total absorption (μx) due only to the sample and carbon tube reactor was around 1.2-1.3, with a step height ($\Delta\mu x$) of around 0.9. Data was collected in quick scan mode with an energy range between 8730 to 9890 eV, and each spectrum took 2 min and 15 s or 2 min and 22 s to complete. The edge energy was reached approximately 32 s after the start of the scan. The Cu K-edge X-ray absorption near edge spectroscopy (XANES) has four distinct features indicative of the various electronic transitions in our samples. The different features represent Cu(I) and Cu(II) oxidation states, and since XAS is a bulk technique, the spectrum represents a linear combination of the spectra for each oxidation state. The first peak is centered at 8977 eV and is representative of the symmetry forbidden 1s → 3d transition of Cu(II) atoms which becomes an allowed transition when mixing of the 3d and 4p orbitals occurs [52]. The peak centered around 8983 eV (has been known to be present from 8982-8985 eV) represents the 1s → 4p transition of two-coordinate Cu(I) atoms and there is literature evidence for this in an array of environments including Cu-ZSM-5 in HC-SCR [53, 54] and NO decomposition [55, 56], Cu-Y-Zeolite [158], Cu-SAPO-5 and Cu-SAPO-11 in HC-SCR [58], as well as Cu(I) ammine complexes [59, 60] and a large number of ligated organic compounds [52]. The edge feature occurring at

8987 eV represents the 1s → 4p electronic transition of Cu(II) atoms [54]. Finally, the white line intensity is also indicative of Cu(II), with lower white line intensity corresponding to a loss of Cu(II).

References used for Linear Combination XANES Fits within this study

Three references were utilized. The first was a hydrated Cu^{II} species, $[Cu(H_2O)_6]^{2+}$, which we have observed to be the primary state of Cu in low loadings at room temperature in air, thus it was reasonable to include it in the references. The isolated Cu^{II} and isolated Cu^{I} were obtained with a 0.31 wt% Cu-SSZ-13 sample (Cu:Al = 0.02), which was the lowest we were able to achieve in the lab. The assumption for this sample was that it contained only the isolated Cu species at the very lowest loadings. The isolated Cu(II) reference was obtained *in situ* with 10% O_2/UHP He at 473 K. The isolated Cu^{I} reference was obtained *in situ* with 1000 ppm NO and 1000 ppm NH_3 at 473 K. Figure S3 shows the resulting XANES region used for linear combination fits. The EXAFS were observed to behave as expected in Figure S4 and Table S3. Under the reducing conditions of NO and NH_3, the Cu-O coordination was 2.2 (or 2, with error), which was what we expected for an isolated Cu^{I}. Additionally, the oxidizing environment of O_2 gave a coordination of 4, which was as expected as well.

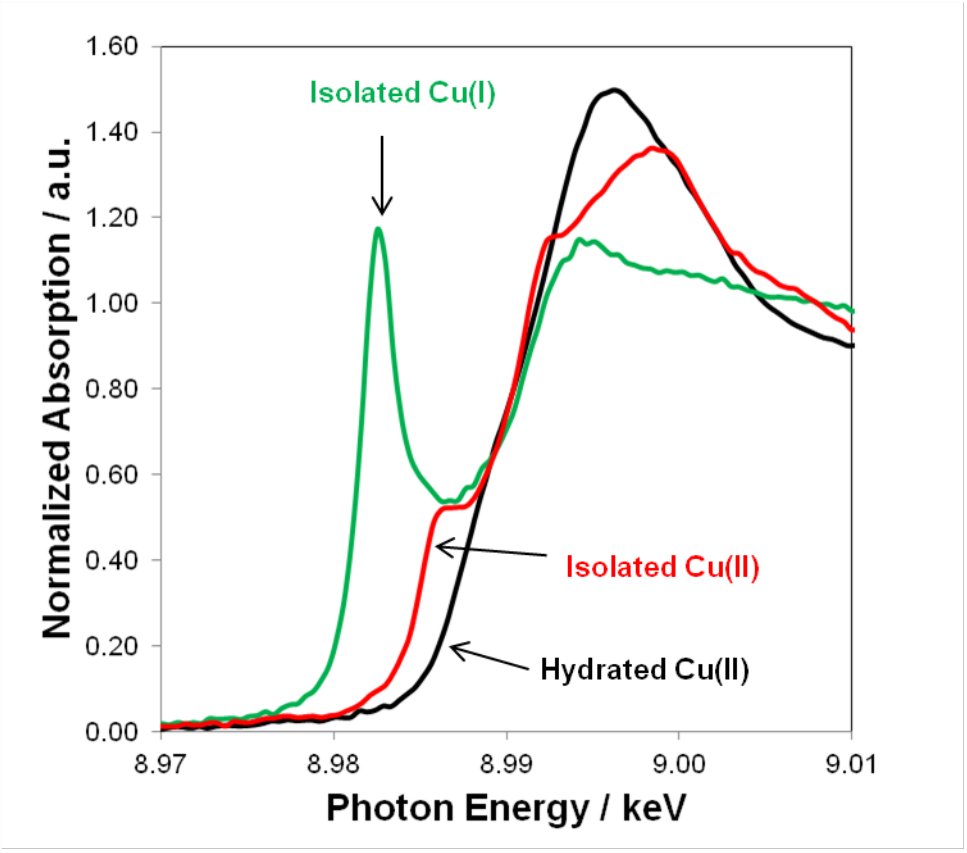

Figure C.3 Reference spectra used for linear combination XANES fits. Hydrated Cu^{II} corresponds to a solution of $[Cu(H_2O)_6]^{II}$ under ambient conditions. A 0.31 wt% Cu-SSZ-13 sample (Cu:Al = 0.02) was used for isolated Cu^{II} with 10% O_2 at 473 K and for the isolated Cu(I) with 1000 ppm NO + 1000 ppm NH_3 at 473 K.

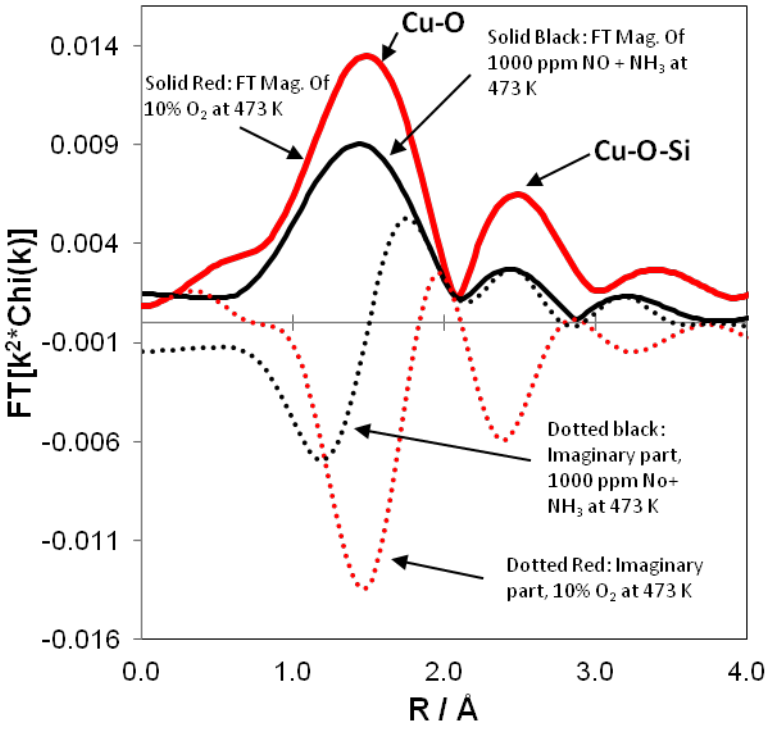

Figure C.4 EXAFS spectra for the isolated Cu^{II} (red) and isolated Cu^{I} (black) references. Solid lines indicate the Fourier transform magnitude. Dotted lines indicate the imaginary contribution.

Table C.3 EXAFS fit parameters for isolated Cu^{I} and isolated Cu^{II}.

EXAFS of 0.31% Cu-SSZ-13 (Cu:Al = 0.02)								
Sample	Treatment	XANES		Scatter	***N***	R / Å	$\Delta\sigma^2$ (x 10^3)	E_o / eV
		Fraction Cu^{II}	Fraction Cu^{I}					
Cu^{II}	RT	1.0	-	Cu-O	***3.9***	1.96	2.0	-8.5
Cu^{II}	10% O_2 , 473 K	1.0	-	Cu-O	***4.0***	1.96	4.0	-7.5
Cu^{I}	1000 ppm NH_3 + 1000 ppm NO, 473 K	-	1.0	Cu-O	***2.2***	1.85	4.0	-5.1

Operando XAS spectra for Cu-SSZ-13 catalysts under various gas conditions

XANES spectra as a function of time for NH_3 cut-off from standard SCR

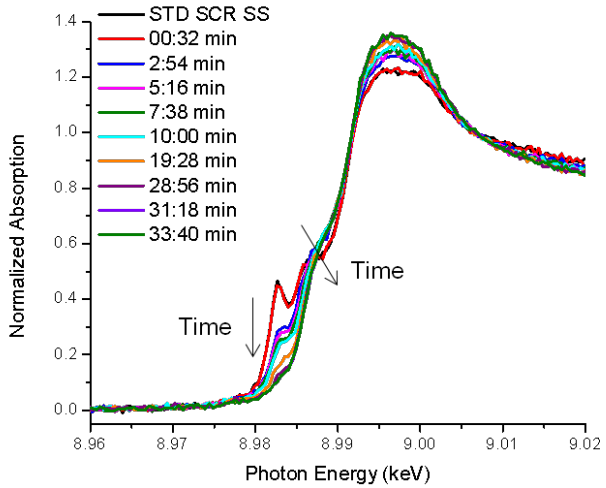

Figure C.5 Time resolved XAS of the Cu:Al = 0.16, Cu-SSZ-13 catalyst after NH_3 was cut off from the standard SCR reactant stream. To clearly present the data, spectra are not linear in time resolution.

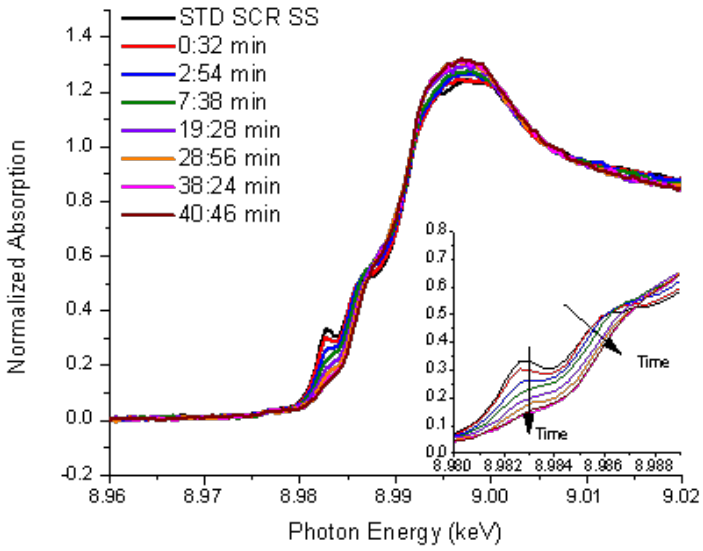

Figure C.6 Time resolved XAS of the Cu:Al = 0.11, Cu-SSZ-13 catalyst after NH_3 was cut off from the standard SCR reactant stream. Inset zooms in on the edge feature at

~9.9828 keV, the identifying feature of Cu^{I} species. To clearly present the data, spectra are not linear in time resolution.

XANES spectra as a function of time for NO cut-off from standard SCR

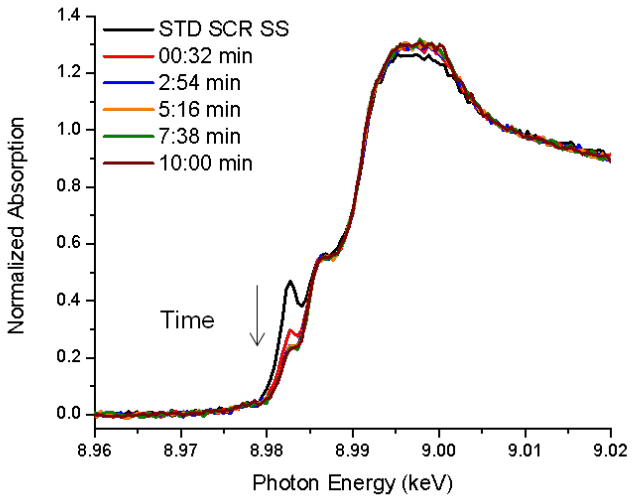

Figure C.7 Time resolved XAS of the Cu:Al = 0.16, Cu-SSZ-13 catalyst after NO was cut off from the standard SCR reactant stream.

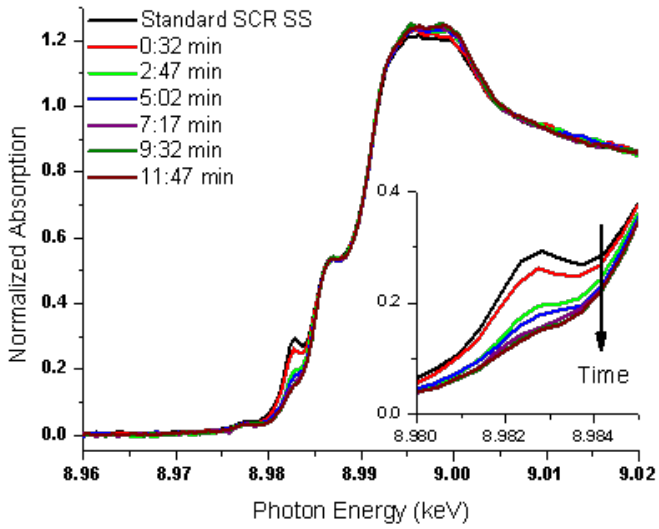

Figure C.8 Time resolved XAS of the Cu:Al = 0.11, Cu-SSZ-13 catalyst after NO was cut off from the standard SCR reactant stream. Inset zooms in on the edge feature at ~9.9828 keV, the identifying feature of Cu^{I} species.

XANES spectra as a function of time for O_2cut-off from standard SCR

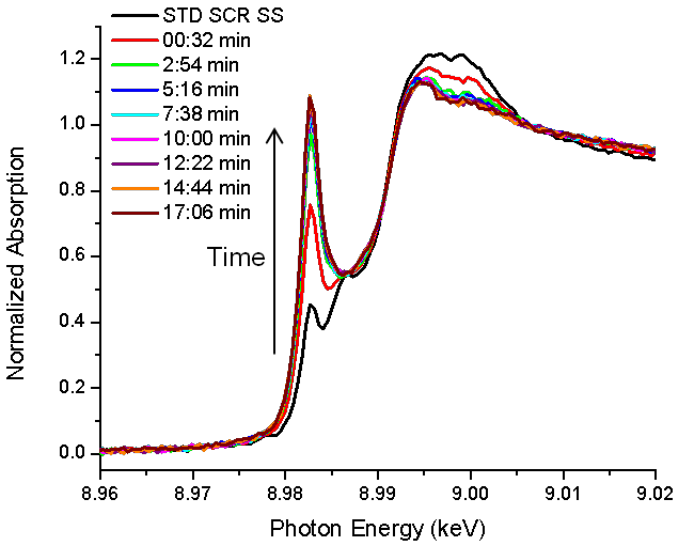

Figure C.9 Time resolved XAS of the Cu:Al = 0.16, Cu-SSZ-13 catalyst after O_2 was cut off from the standard SCR reactant stream.

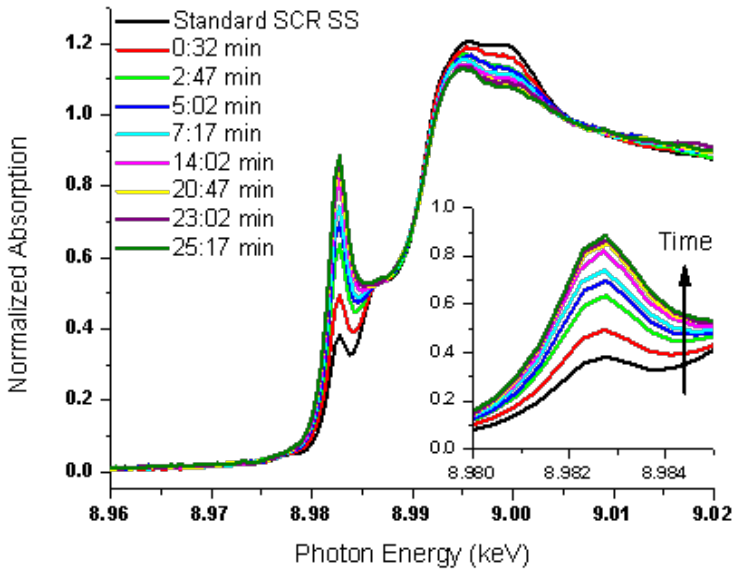

Figure C.10 Time resolved XAS of the Cu:Al = 0.11, Cu-SSZ-13 catalyst after O_2 was cut off from the standard SCR reactant stream. Inset zooms in on the edge feature at ~9.9828 keV, the identifying feature of Cu^I species. To clearly present the data, spectra are not linear in time scale.

Table C.4 Table of XANES linear combination fits for each reactant cutoff experiment. The conditions analyzed correspond to the steady state value (SS value) of standard SCR and the new SS value after the reactant is removed.

Cu:Al	Experiment	Condition	Hydrated Cu^{II} / %	Isolated Cu^{II} / %	Isolated Cu^{I} / %	Total Cu^{II} / %
0.11		SS Value	7	64	29	71
	O_2 Cutoff	After O_2 Cutoff	1	23	76	24
		SS Value	8	65	27	73
	NO Cutoff	After NO Cutoff	10	78	12	88
		SS Value	3	73	24	76
	NH_3 Cutoff	After NH_3Cutoff	41	55	4	96
0.16		SS Value	4	60	36	64
	O_2 Cutoff	After O_2 Cutoff	0	5	95	5
		SS Value	4	62	34	66
	NO Cutoff	After NO Cutoff	6	79	15	85
		SS Value	4	59	34	63
	NH_3 Cutoff	After NH_3 Cutoff	48	47	5	95

* ±5% error associated with each LC XANES fit.

Quantification of different Cu ion configurations during NH_3 cut-off from standard SCR for Cu:Al = 0.11

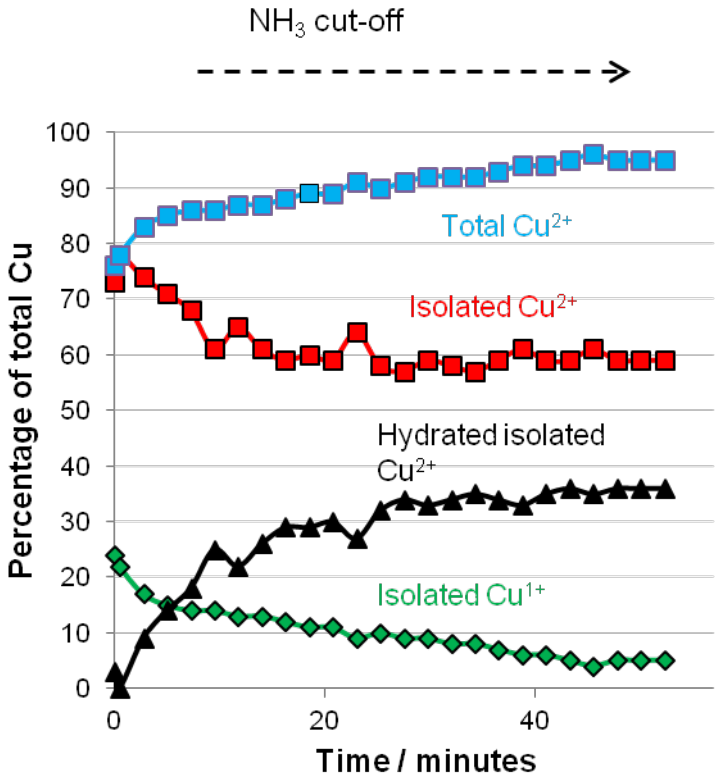

Figure C.11 Variation of the % of Cu present in different configurations as a function of time after NH_3 cut-off from steady state standard SCR over Cu-SSZ-13 with Cu:Al = 0.11

Counting available Brønsted acid sites on Cu-SSZ-13 with predominantly a Cu^{I} or Cu^{II} oxidation state.

From Figure 1, we have shown that isolated Cu ions in Cu-SSZ-13 can be made to attain predominantly Cu^{I} or Cu^{II} oxidation states, depending on an appropriate choice of gas conditions. The Cu^{II} oxidation state in Cu-SSZ-13 is achieved by pre-treating the catalyst with 10% O_2 at 473K for 120 minutes. Using separate XAS results (detailed in S5, supporting information), the Cu ions remain in the Cu^{II} oxidation state. Moreover, for these catalysts with Cu:Al < 0.2 (for Si:Al = 4.5), Cu^{II} ions require two Brønsted acid sites for stabilization[26]. There is, however, a measurable number of excess Brønsted acid sites which do not stabilize Cu ions and recently we devised methods to efficiently

count these excess Brønsted acid sites[26] on a predominantly Cu^{II} oxidation state of Cu-SSZ-13.

Results in this contribution point toward the reduction of isolated Cu^{II} ions to form predominantly isolated Cu^{I} ions by contacting them with an equimolar combination of NO and NH_3(results detailed in Figures 1 and S5). In particular, the Cu-SSZ-13 catalyst was contacted with 500 ppm NO + 500 ppm NH_3 in a balance of He gas (UHP grade, Indiana Oxygen, total flow rate = 350 ml min^{-1}) at 473 K for 120 minutes. This time period was enough to reduce the Cu^{II} to a predominantly Cu^{I} oxidation state. Moreover, the Cu ions in the Cu^{I} oxidation state require only one Brønsted acid site for stabilization, thus exposing the second Brønsted acid site, proximal to that Cu^{I} ion. Thus, based on the stoichiometry of Cu ion reduction, the number of excess Brønsted acid sites should be equal to the total number of isolated Cu^{I} ions (according to equation S1).

$$Cu^{II} \rightarrow Cu^{I} + H^{+} \text{ (S1)}$$

In order to stabilize NH_4^+ ions on these Brønsted acid sites, the temperature was reduced to 423 K under 500 ppm NO + 500 ppm NH_3 mixture. Subsequently, the NO + NH_3 mixture was replaced by 500 ppm NH_3, with the same flow of total gas (350 ml min^{-1}). This process was sustained for 120 minutes, after which NH_3 was shut-off and the catalyst was flushed with 350 ml min^{-1} of He for the next 480 minutes. This was done to retain only NH_4^+ ions on Brønsted acid sites. After the flush, a temperature programmed desorption (in He) was performed from 423 K to 820K (shown in Figure S12) and the total moles of NH_3 desorbed was quantified (Table S5). As verified by Bates et al.[26], the total moles of NH_3 desorbed were taken to be the total number of Brønsted acid sites on Cu-SSZ-13. Comparing this result with the correspondingNH$_3$ count from a TPD on the Cu^{II} oxidation state of Cu-SSZ-13 resulted in an excess number of Brønsted acid sites which was quantified and reported.

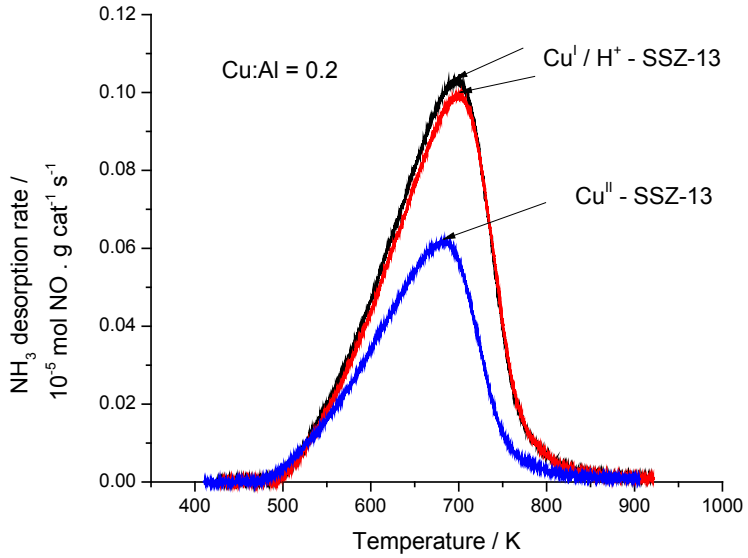

Figure C.12a The NH_3 desorption profile of the predominantly Cu^{I} and Cu^{II} oxidation states of Cu-SSZ-13, for Cu:Al = 0.2, Cu wt% = 3.75 %.

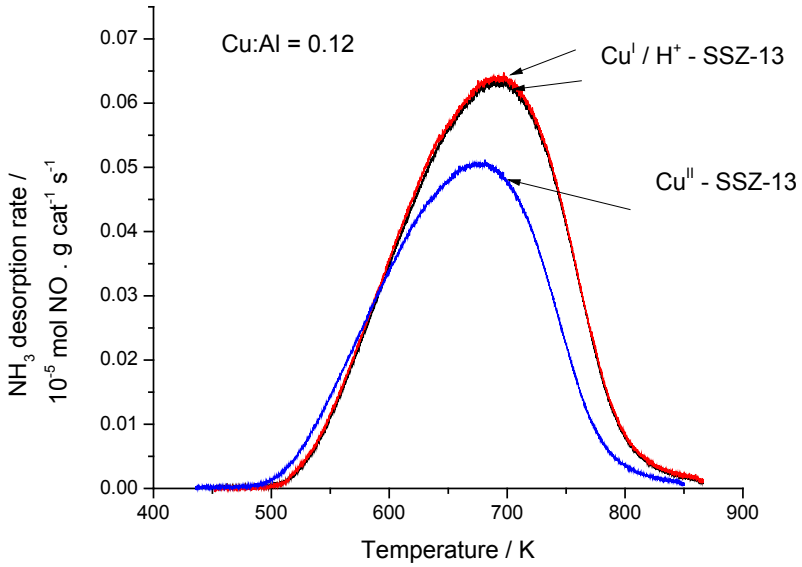

Figure C.13 The NH_3desorption profile of the predominantly Cu^{I} and Cu^{II} oxidation states of Cu-SSZ-13, for Cu:Al = 0.12, Cu wt% = 2.36 %.

A careful observation of the NO + NH_3 treatment of isolated Cu^{II} ions in SSZ-13 at 473 leads to a predominant amount of isolated Cu^{I}ions. This procedure, however, does not lead to a quantitative reduction of Cu ions. For example, from Figure 1 and Table S4, after the NO + NH_3 reduction, the percentage of Cu^{I} ions in Cu-SSZ-13 with Cu:Al = 0.11 is around 76%, while it is around 95% Cu^{I} ions for Cu:Al = 0.2. We would expect reduction of all Cu^{II} ions to Cu^{I}, but through *operando* XANES (Figure 1), a finite, non zero number of isolated Cu^{II} ions remain in the system. We would expect that the same protocol when applied to produce Cu^{I} ions in Cu-SSZ-13 catalysts with Cu:Al ratios similar to 0.11 and 0.16, would lead to reduction of less than 100% of Cu^{II} ions. This leads to excess H^{+} : Al counts which are lesser than the Cu^{II}:Al ratios. In fact, it would be equal to the Cu^{I} : Al ratios shown by the stoichiometry of Equation S1.

As a result, for Cu-SSZ-13 with Cu:Al = 0.12 (tested in this experiment), we would expect on an average, only 76% of Cu^{II} sites have reduced to Cu^{I}, thereby making the Cu^{I} : Al ratio to be 0.12 x 0.76 = 0.09. Similarly, for Cu:Al = 0.2, on average, 95% of Cu ions get reduced in the NO + NH_3 treatment, which leads to Cu^{I} : Al = 0.2 x 0.95 = 0.19. As a result, the Cu^{I} : Al ratios must match with the experimentally obtained excess H^{+} : Al ratios for each catalyst, which verifies the stoichiometry of Equation S1.

Table C.5 Quantification of H^{+}:Al for Cu-SSZ-13 catalysts prepared in such a way to stabilize either Cu^{II} ions or Cu^{I} ions predominantly.

Catalyst	**Cu^{II} : Al**	**% of Cu^{II} ions reduced to Cu^{I} ions[a]**	**Cu^{I} : Al**	**H^{+} : Al**	**Excess H^{+} : Al**
Cu^{II} – SSZ-13	0.2	--	--	0.32 ± 0.03	0.21 ± 0.03
Cu^{I} / H^{+} - SSZ-13	0.2	95%	0.19	0.53 ± 0.03	
Cu^{II} – SSZ-13	0.12	--	--	0.37 ± 0.03	0.09 ± 0.03
Cu^{I} / H^{+} - SSZ-13	0.12	76%	0.09	0.46 ± 0.03	

a : based on expectation from catalysts with similar Cu:Al ratios as shown in Figure 1 and Table S4

Computational Details

Structural Optimizations

Periodic density functional theory (DFT) calculations were performed using the Vienna ab-initio Software Package (VASP)[15]. Core states were treated using the projector augmented wave (PAW) method[16]. Structural optimizations were first performed using the PW91 exchange-correlation functional to give an initial structure guess for a HSE06 calculation. The HSE06[17] exchange-correlation functional was used with a screening parameter of HFSCREEN=0.2. The supercell used in this work is reported elsewhere [6]. Plane waves were included up to a cutoff of 400 eV and the Brillouin zone sampled at the gamma point. Electronic energies were converged to within 10^{-6} eV and optimized geometries relaxed until the forces minimized to less than 0.03 eV/Angstrom.

Frequency Calculations

Vibrational frequencies were obtained from the PW91 optimized structures using the PW91 exchange-correlation functional. These frequencies were used to calculate the zero-point vibrational energy of species and their vibrational contributions to the free energy at 473 K under the harmonic oscillator assumption (see S.12).

Ab-Initio Molecular Dynamics (AIMD)

AIMD calculations were performed using the Car-Parnello Molecular Dynamics software[18]. Born-Oppenheimer Molecular Dynamics at 473 K using a Nose-Hoover thermostat and a time-step of 0.5 femtoseconds for a duration of 20000 time steps in the

NVT ensemble was used to sample starting structures and for potential of mean force calculations. The supercell used for AIMD was equivalent to that used in VASP. The PBE exchange-correlation and ultrasoft pseudopotentials were used. A 30 Rydberg cutoff was used and energies converged to within $5x10^{-6}$ eV.

HSE06-optimized Structures

Si-Yellow Al-Green O-Red Cu-Gray N-Blue H-White

Cu

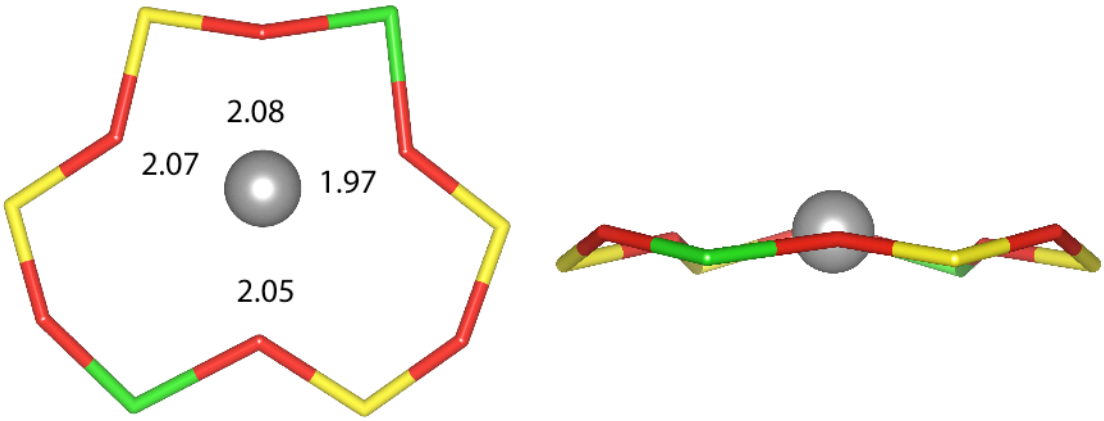

$CuNH_3$

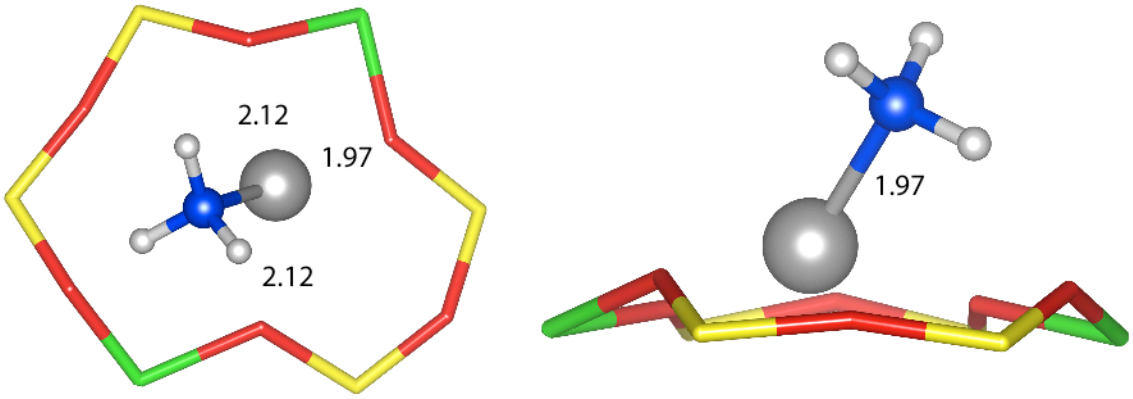

CuNO

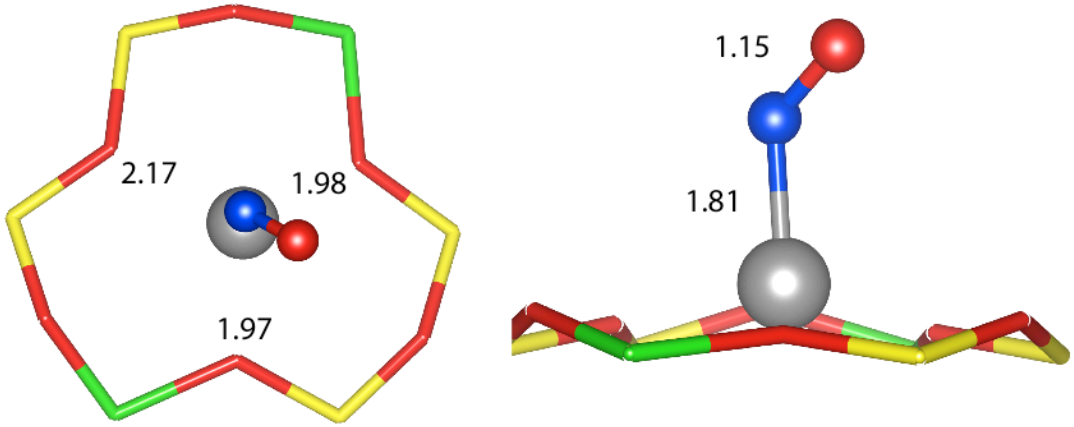

CuO_2

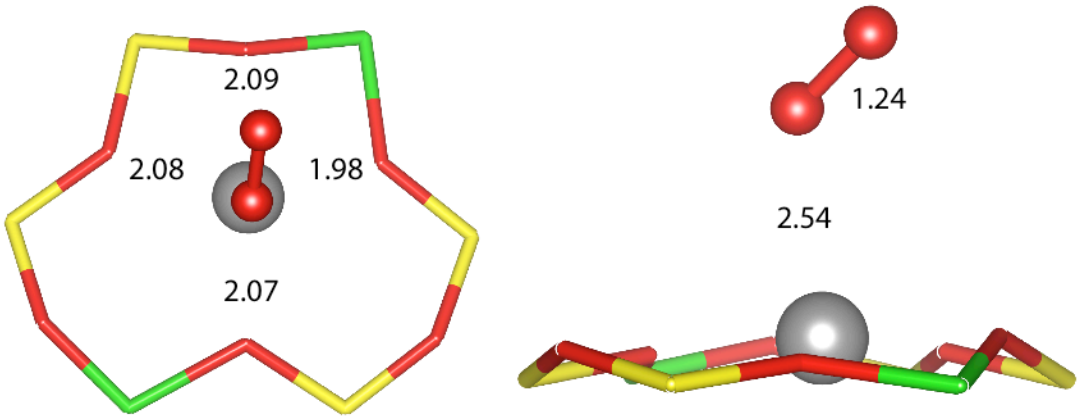

CuH_2O

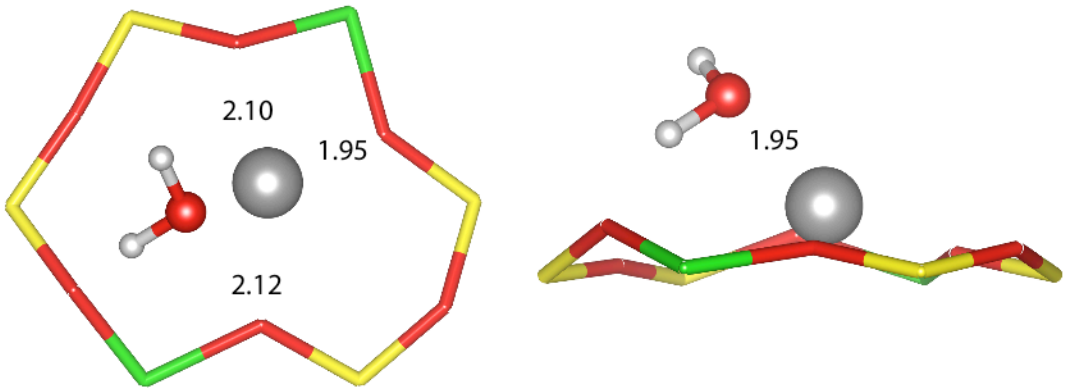

CuN_2

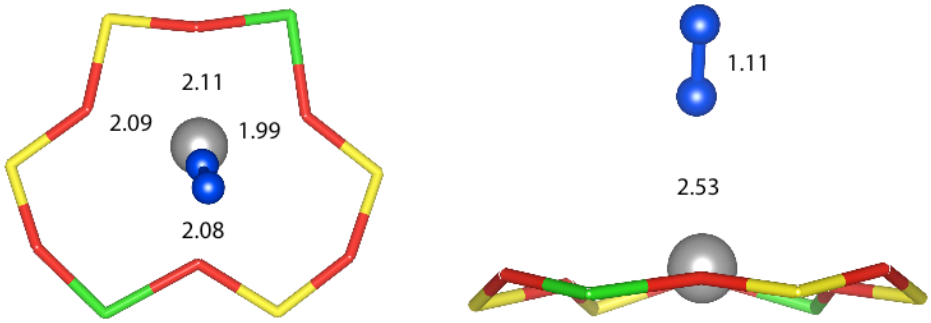

Cu/H

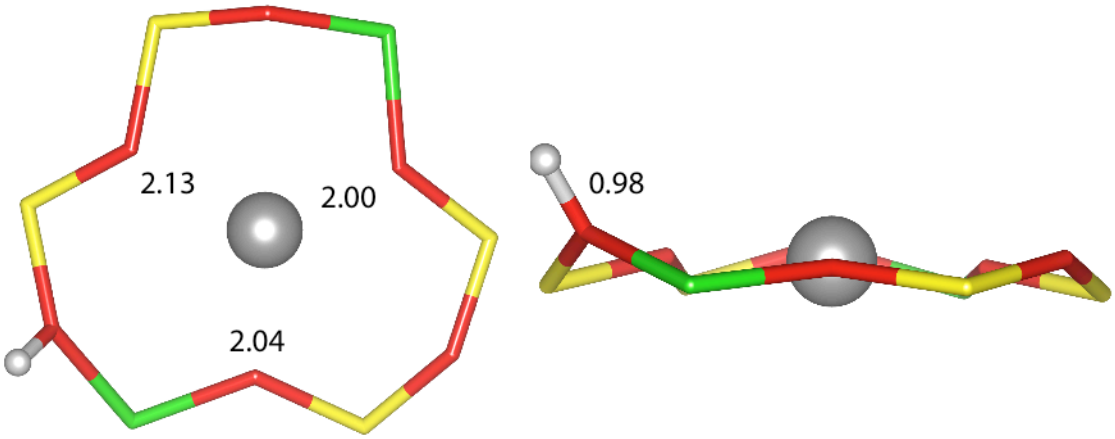

$CuNH_3$/H

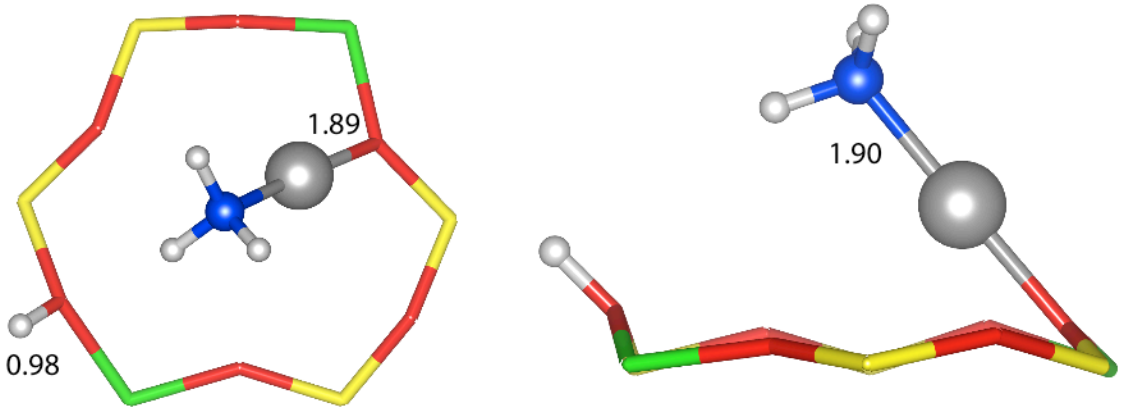

CuNO/H

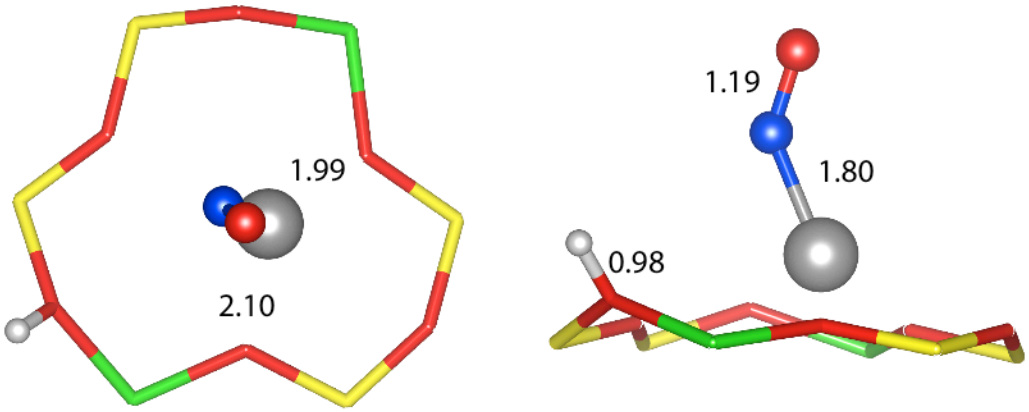

$CuNO_2$/H

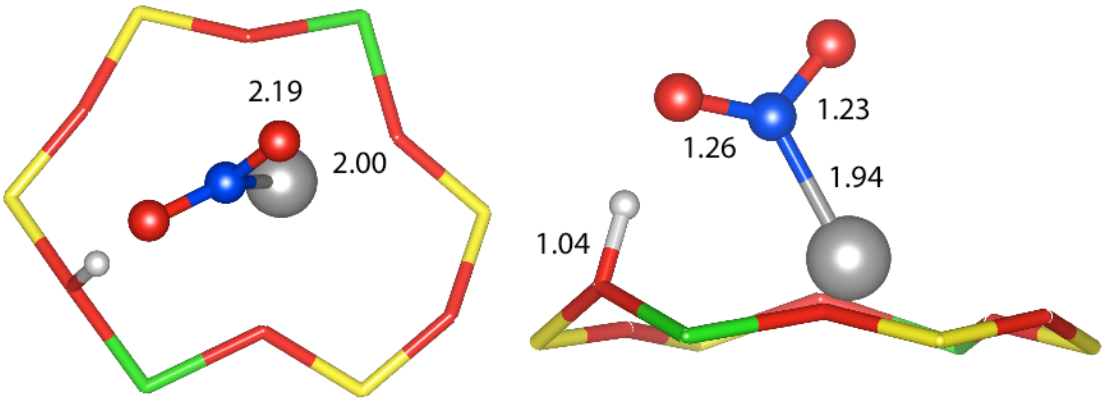

CuO_2/H

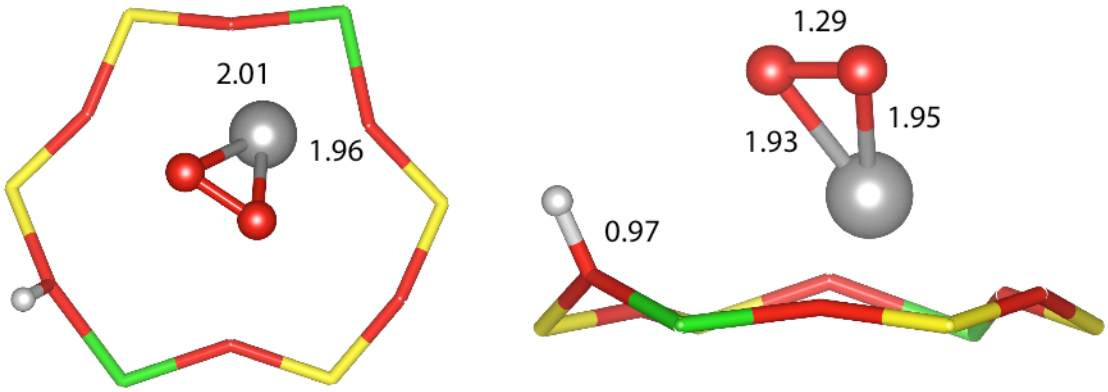

CuN_2/H

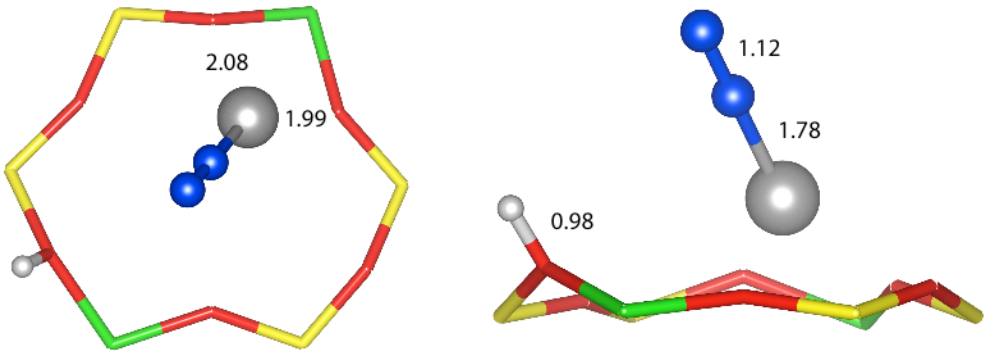

CuH_2O/H

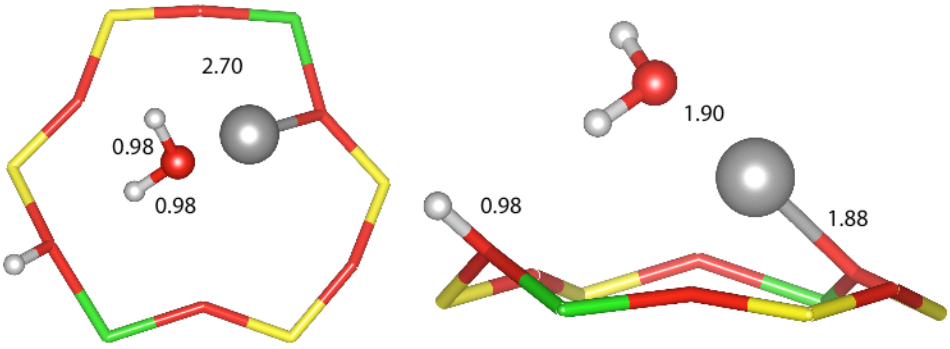

$Cu(OH)_2/H$

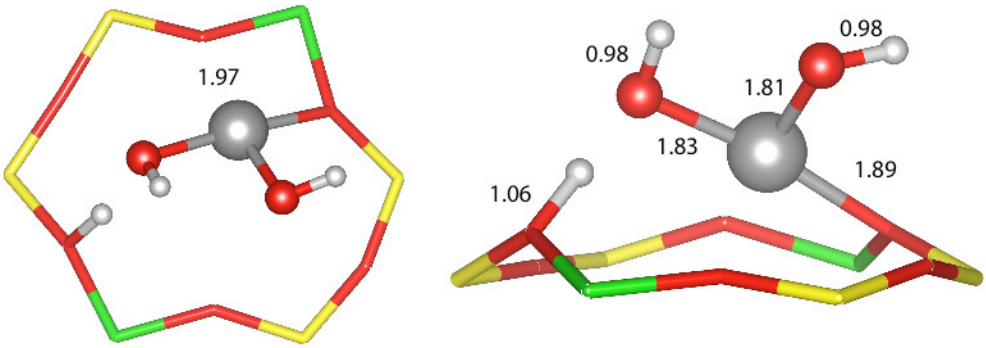

Cu/NH_4

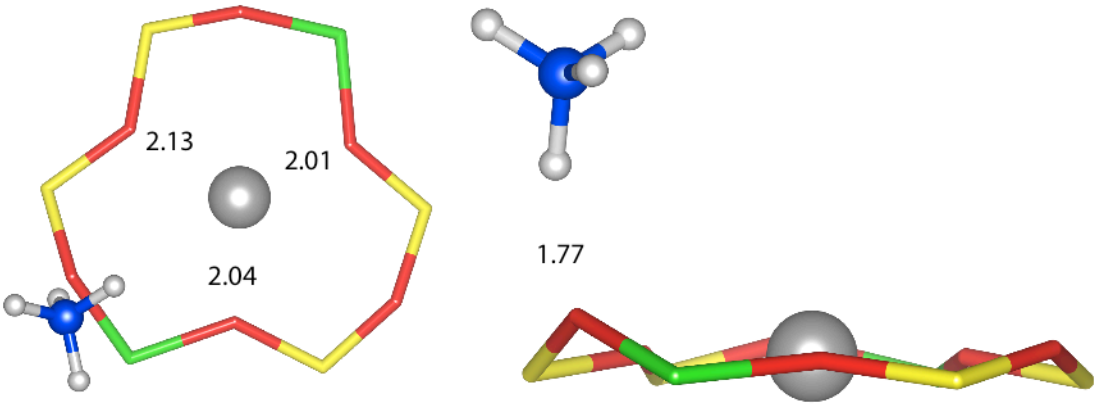

$CuNH_3/NH_4$

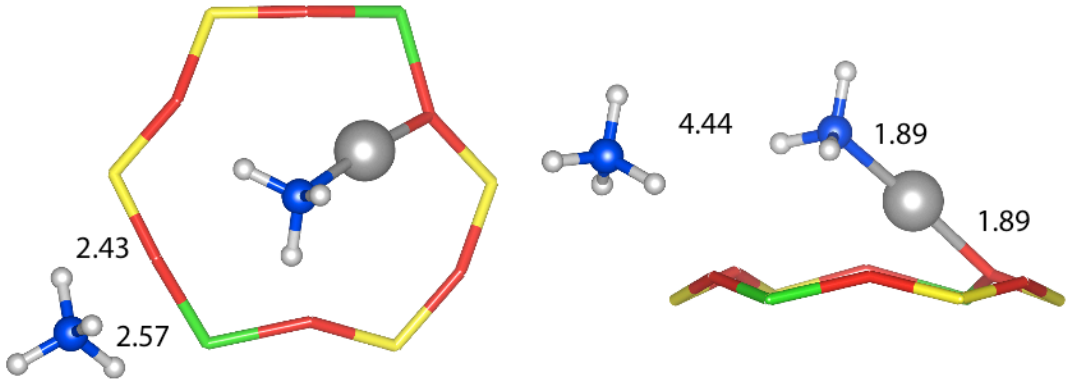

$CuNO_2/NH_4$

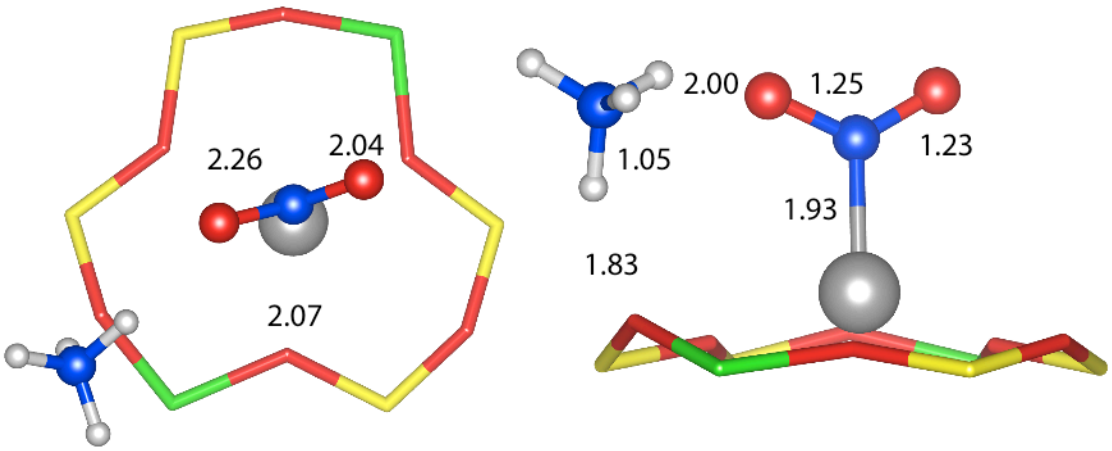

$CuNH_2$

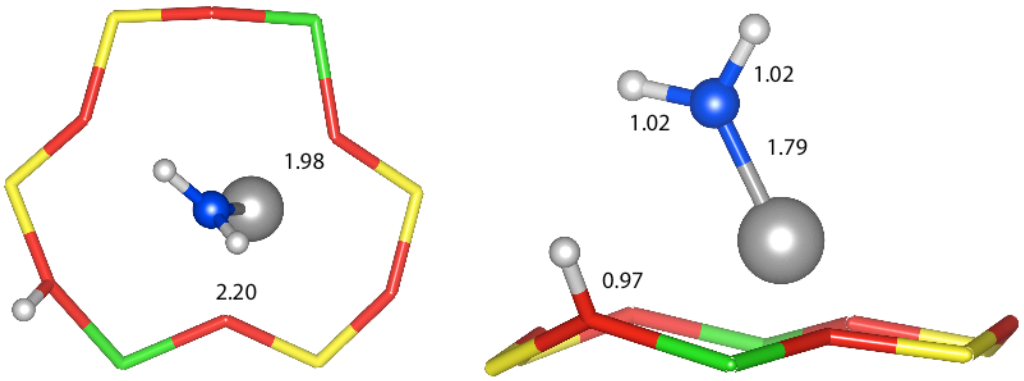

$CuNH_3$-NO

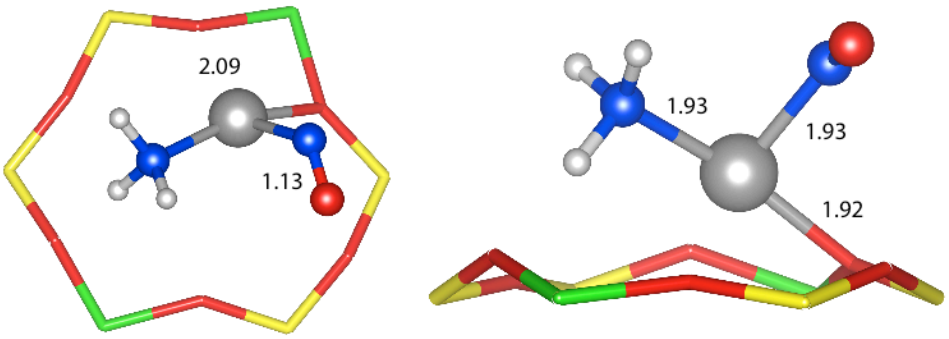

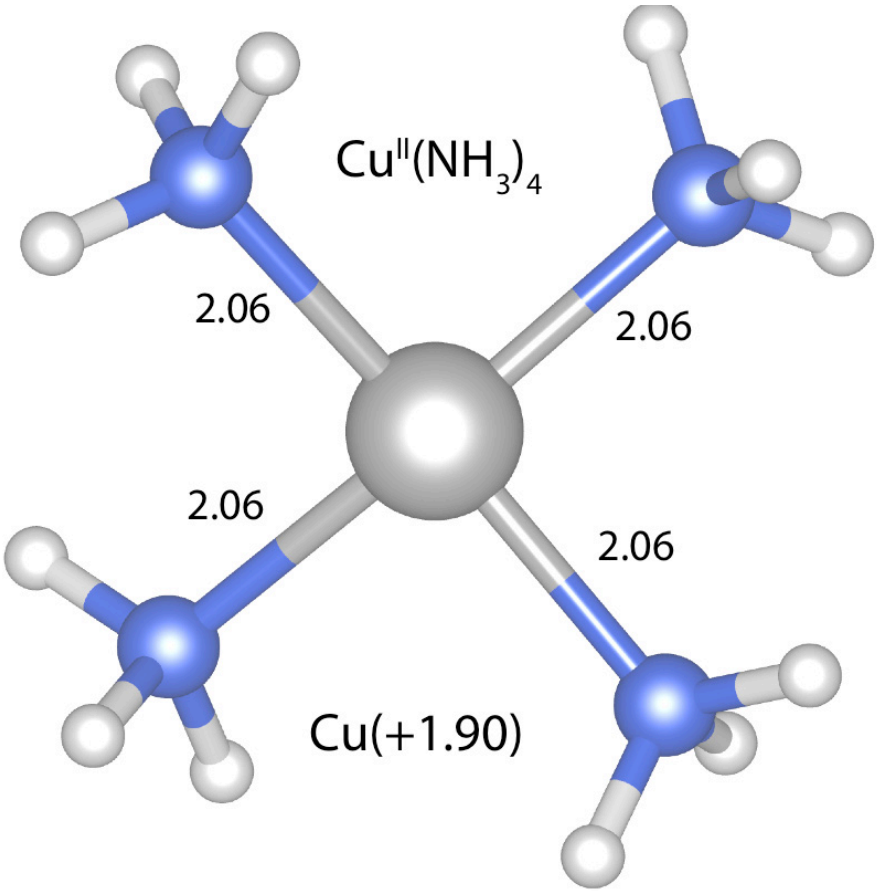

NH_3 Potential of Mean Force

To calculate the free energy of adsorption for NH3 on 6-MR Cu^{II}, 36 independent AIMD simulations were run using the previously reported computational details in addition to constraining the Cu-N distance at fixed 0.1 Angstrom intervals. The force associated with this constraint was sampled each time step and integrated over the distance to construct the potential of mean force. Error was estimated from block averaging.

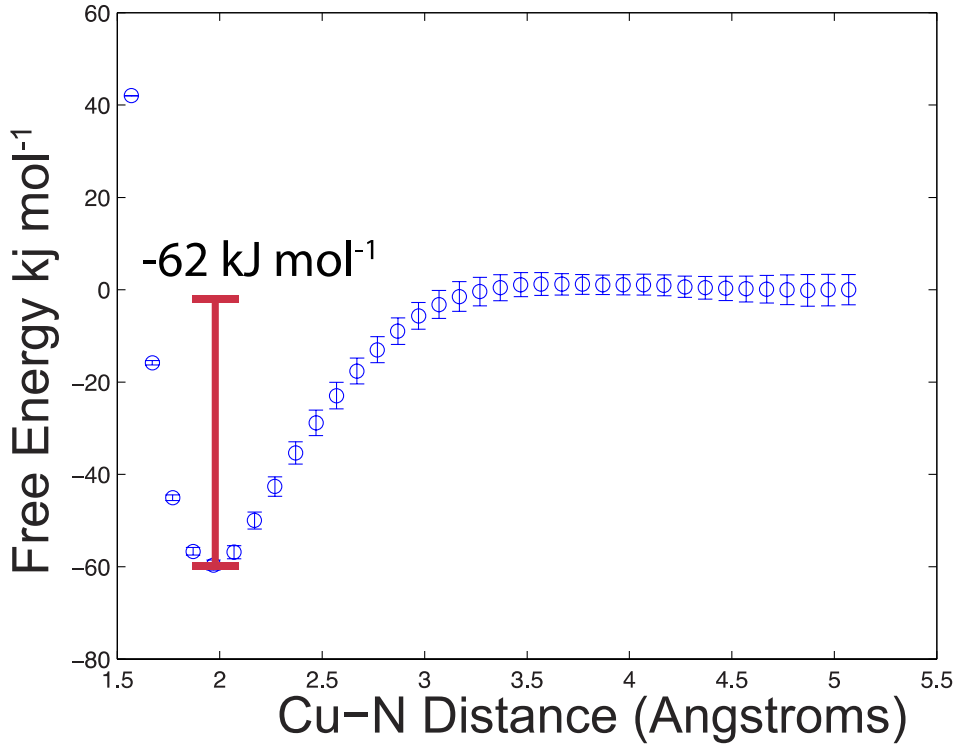

Density of States

Density of states for select adsorbed species. The charge reported in the lower right hand corner comes from the normalized Bader charge analysis.

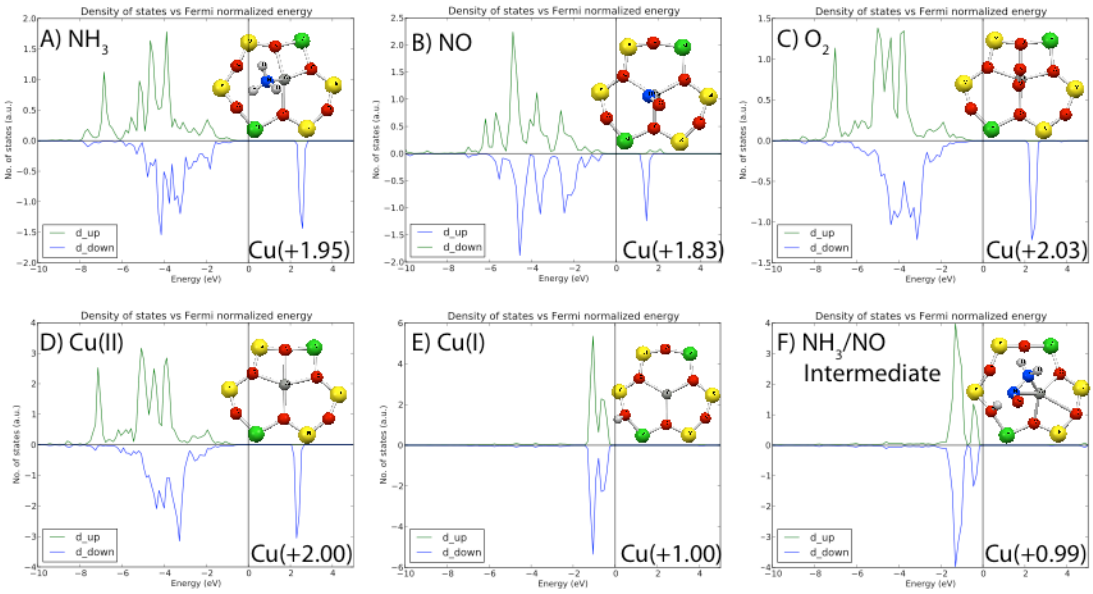
Density of states vs Fermi normalized energy
A) NH3
Cu(+1.95)
B) NO
Cu(+1.83)
C) O2
Cu(+2.03)
D) Cu(II)
Cu(+2.00)
E) Cu(I)
Cu(+1.00)
F) NH3/NO
Intermediate
Cu(+0.99)
d_up
d_down
No. of states (a.u.)
Energy (eV)

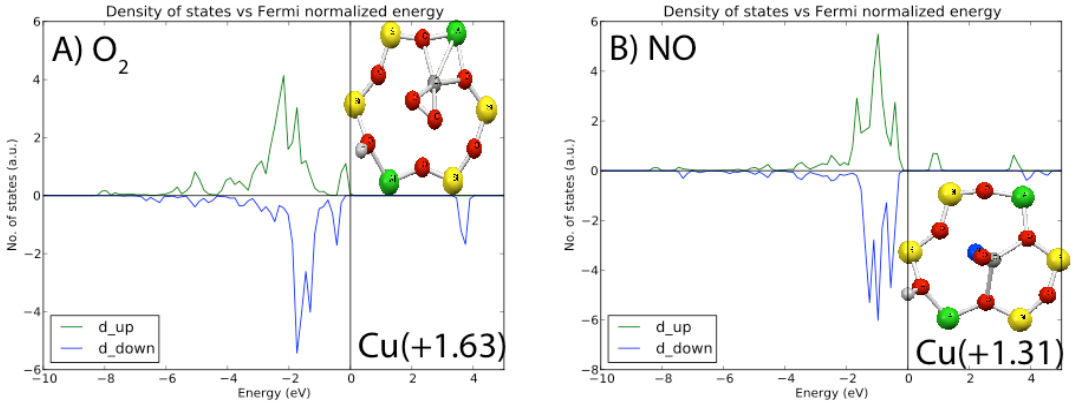
Density of states vs Fermi normalized energy
A) O2
Cu(+1.63)
B) NO
Cu(+1.31)
d_up
d_down
No. of states (a.u.)
Energy (eV)

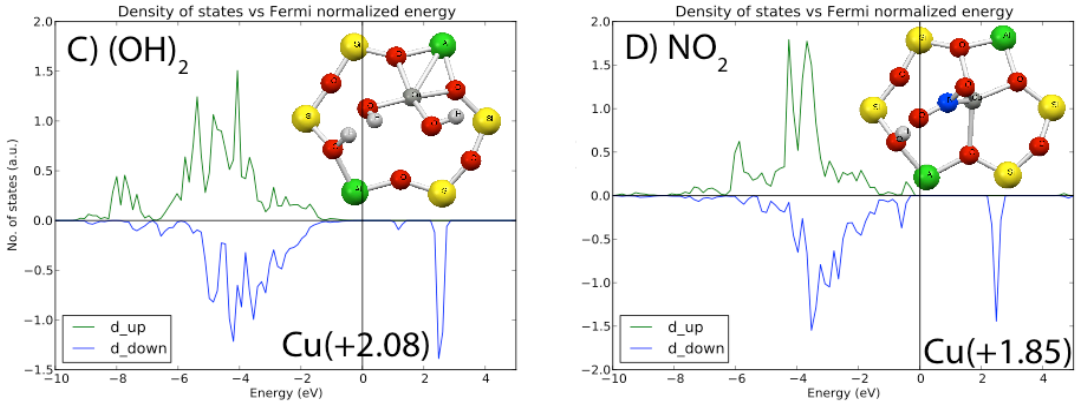
Density of states vs Fermi normalized energy
C) (OH)2
Cu(+2.08)
D) NO2
Cu(+1.85)
d_up
d_down
No. of states (a.u.)
Energy (eV)

Free Energy Calculations

Gas phase free energies were calculated using the ideal gas, rigid rotor, and harmonic oscillator approximations. Adsorbed species vibrational free energy calculations were computed under the harmonic oscillator assumption. In the mobile case the two lowest vibrational modes associated with the adsorbed species were discarded. The mobile model assumes that adsorbed gas species retain 2/3 of their gas phase translational entropy as calculated by the Sackur-Tetrode equation. The immobile model assumes the adsorbed species retains only harmonic vibrational contributions to entropy.

Adsorption on Isolated Cu^{II} :

Free energies (G) were calculated using both the mobile and immobile approximations described above and are listed in columns 2 and 3. In column 4 E represents the HSE06 calculated 0K binding energy. The normalized Density of States (DOS) and Bader Charge calculated on the Cu after adsorption are listed in columns 5 and 6.

Adsorbate	ΔG_{ads} (Immobile)	ΔG_{ads} (Mobile)	ΔE	DOS (d)	Bader Charge
NH_3	+10	-32	-95	2.04	1.95
H_2O	+15	-27	-70	2.02	2.05
$O_2^{(3)}$	+93	+49	-2	2.02	2.03
N_2	+94	+50	-10	2.02	2.03
NO	+126	+82	+3	1.78	1.83
$Z_2Cu(II)$	0	0	0	2	2
$Z_2HCu(I)$	-	-	-	1	1

Adsorption on Isolated Cu^{I}:

Free energies (G) were calculated using both the mobile and immobile approximations described above and are listed in columns 2 and 3. In column 4 E represents the HSE06 calculated 0K binding energy. The normalized Density of States (DOS) and Bader Charge calculated on the Cu after adsorption are listed in columns 5 and 6.

Adsorbate	ΔG_{ads} (Immobile)	ΔG_{ads} (Mobile)	ΔE	DOS (d)	Bader Charge
NH_3	-3	-45	-97	1.22	0.92
H_2O	+26	-16	-48	1.10	1.01
O_2	+41	-4	-30	1.51	1.63
NO	+43	-1	-57	1.51	1.31
N_2	+50	+6	-39	1.2	1.22
$NO + \frac{1}{2}O_2$	-10	-76	-164	1.87	1.85
$H_2O + \frac{1}{2}O_2$	+112	+48	-12	1.98	1.99
$Z_2Cu(II)$	0	0	0	2	2
$Z_2HCu(I)$	-	-	-	1	1

Reaction Mechanism Energies

Reaction Scheme Energies:

Calculated reaction free energies and standard state (1 atm) reaction free energies for Scheme 1 are listed in columns 2 and 3. The HSE06 calculated 0K reaction energies are listed in column 4. The equilibrium constants corresponding to the appropriate standard state reaction free energies are listed in column 5.

Reaction	ΔG_{ads} (Mobile)	ΔG°_{ads} (Mobile)	ΔE	K_{eq}
$Z_2Cu + NH_3 \longrightarrow Z_2CuNH_3$	-32	-64	-95	1.08×10^{7}
$Z_2CuNH_3 + NO \longrightarrow Z_2HCuN_2H_2O$	+44	+12	-9	4.36×10^{-2}
$Z_2HCuN_2H_2O \longrightarrow Z_2HCu + N_2 + H_2O$	-288	-238	-202	1.88×10^{26}
$Z_2HCu + NH_3 \longrightarrow Z_2NH_4Cu$	-78	-110	-122	1.30×10^{12}
$Z_2NH_4Cu + NO + \frac{1}{2}O_2 \longrightarrow Z_2NH_4CuNO_2$	-47	-84	-144	1.72×10^{9}
$Z_2NH_4CuNO_2 \longrightarrow 2\,H_2O + N_2$	-279	-217	-122	9.48×10^{23}

Rate Determining Step Results

I. Case 1: NH_3 assisted dissociation RDS

A.

$$* + NH_3 \overset{K_1}{\rightleftharpoons} *NH_3 \quad (1)$$

$$*NH_3 + NO \xrightarrow{k_2} * H|N_2H_2O \quad (2)$$

$$* H|N_2H_2O \overset{K_3}{\rightleftharpoons} * H| + N_2 + H_2O \quad (3)$$

$$* H| + NH_3 \overset{K_4}{\rightleftharpoons} * NH_4| \quad (4)$$

$$* NH_4| + NO + \frac{1}{2}O_2 \overset{K_5}{\rightleftharpoons} * NH_4|NO_2 \quad (5)$$

$$* NH_4|NO_2 \overset{K_6}{\rightleftharpoons} * + N_2 + 2\,H_2O \quad (6)$$

$$* NH_4| + NH_3 \overset{K_7}{\rightleftharpoons} * NH_4|NH_3 \quad (7)$$

B. Rate:

$$\frac{k_2K_1K_3K_4K_5K_6NH_3{}^2NO^2\sqrt{O_2}}{H_2O^3N_2{}^2 + K_3H_2O^2N_2\left(1 + K_4NH_3\left(1 + K_7NH_3 + K_5NO\sqrt{O_2}\right)\right) + K_3K_4K_5K_6NH_3\left(1 + K_1NH_3\right)NO\sqrt{O_2}}$$

C. Rate Orders

NO:

$$n_{NO} = 2 - \theta_{NH_4|NO_2} - \theta_v - \theta_{NH_3}$$

O_2:

$$n_{O_2} = \frac{1}{2}\left(1 - \theta_{NH_4|NO_2} - \theta_v - \theta_{NH_3}\right)$$

NH_3:

$$n_{NH_3} = 2 - 2\theta_{NH_4|NH_3} - \theta_v - 2\theta_{NH_3} - \theta_{NH_4} - \theta_{NH_4|NO_2}$$

D. Coverage:

$$\theta_{NH_3} \approx 1$$

II. Case 2: N_2H_2O decomposition RDS

A.

$$* \mathrm{H}|\,\mathrm{N_2H_2O} \xrightarrow{k_3} * \mathrm{H}| + \mathrm{N_2} + \mathrm{H_2O} \tag{8}$$

(9)

B. Rate:

$$\frac{k_3 K_1 K_2 K_4 K_5 K_6 \mathrm{NH_3}^2 \mathrm{NO}^2 \sqrt{\mathrm{O_2}}}{\mathrm{H_2O}^2 \mathrm{N_2} \left(1 + K_4 \mathrm{NH_3} \left(1 + K_7 \mathrm{NH_3} + K_5 \mathrm{NO}\sqrt{\mathrm{O_2}}\right)\right) + K_4 K_5 K_6 \mathrm{NH_3 NO} \left(1 + K_1 \left(\mathrm{NH_3} + K_2 \mathrm{NH_3 NO}\right)\right) \sqrt{\mathrm{O_2}}}$$

C. Rate Orders
NO:

$$n_{\mathrm{NO}} = 2 - \theta_{\mathrm{NH_4|NO_2}} - \theta_v - \theta_{\mathrm{NH_3}} - 2\theta_{\mathrm{H|N_2H_2O}}$$

O_2:

$$n_{\mathrm{O_2}} = \frac{1}{2}\left(1 - \theta_{\mathrm{NH_4|NO_2}} - \theta_v - \theta_{\mathrm{NH_3}} - \theta_{\mathrm{H|N_2H_2O}}\right)$$

NH_3:

$$n_{\mathrm{NH_3}} = 2 - 2\theta_{\mathrm{NH_4|NH_3}} - \theta_v - 2\theta_{\mathrm{NH_3}} - \theta_{\mathrm{NH_4}} - \theta_{\mathrm{NH_4|NO_2}} - 2\theta_{\mathrm{H|N_2H_2O}}$$

D. Coverage:

$$\theta_{\mathrm{NH_3}} \approx 1$$

III. Case 3: NO_2 formation RDS

A.

$$* NH_4| + NO + \frac{1}{2}O_2 \xrightarrow{k_5} * NH_4|NO_2 \tag{10}$$

(11)

B. Rate:

$$\frac{k_5 K_1 K_2 K_3 K_4 K_6 NH_3{}^2 NO^2 \sqrt{O_2}}{H_2O^3 N_2{}^2 + K_1 K_2 K_3 K_6 NH_3 \left(1 + K_4 NH_3 \left(1 + K_7 NH_3\right)\right) NO + H_2O K_6 N_2 \left(1 + K_1 NH_3 + K_2 NH_3 NO\right)}$$

C. Rate Orders
NO:

$$n_{NO} = 2 - \theta_{NH_4|NH_3} - \theta_v - \theta_H - \theta_{H|N_2H_2O} - \theta_{NH_4}$$

O_2:

$$n_{O_2} = \frac{1}{2}$$

NH_3:

$$n_{NH_3} = 2 - 3\theta_{NH_4|NH_3} - \theta_{NH_3} - 2\theta_{NH_4} - \theta_H - \theta_{H|N_2H_2O}$$

D. Coverage:

$$\theta_{NH_4|NH_3} \approx 1$$

IV. Case 4: NH_4NO_2 decomposition RDS

A.

$$* NH_4|NO_2 \xrightarrow{k_6} * + N_2 + 2H_2O \tag{12}$$

B. Rate:

$$\frac{k_6 K_1 K_2 K_3 K_4 K_5 {NH_3}^2 NO^2 \sqrt{O_2}}{H_2ON_2\left(1 + K_1\left(NH_3 + K_2 NH_3 NO\right)\right) + K_1 K_2 K_3 NH_3 NO\left(1 + K_4 NH_3\left(1 + K_7 NH_3 + K_5 NO\sqrt{O_2}\right)\right)}$$

C. Rate Orders
NO:

$$n_{NO} = 2 - \theta_{NH_4|NH_3} - 2\theta_{NH_4|NO_2} - \theta_H - \theta_{H|N_2H_2O} - \theta_{NH_4}$$

O_2:

$$n_{O_2} = \frac{1}{2}\left(1 - \theta_{NH_4|NO_2}\right)$$

NH_3:

$$n_{NH_3} = 2 - 3\theta_{NH_4|NH_3} - \theta_{NH_3} - 2\theta_{NH_4} - \theta_H - \theta_{H|N_2H_2O} - 2\theta_{NH_4|NO_2}$$

D. Coverage:

$$\theta_{NH_4|NH_3} \approx 0.14, \qquad \theta_{NH_4|NO_2} \approx 0.86$$

Appendix D Permissions for Reprint.

Chapter 2 & Appendix A has been reprinted with permission from (S.A. Bates, A.A. Verma, C. Paolucci, A.A. Parekh, T. Angarra, A. Yezerets, W.F. Schneider, J.T. Miller, W.N. Delgass, and F.H. Ribeiro, Identification of The Active Cu Site in Standard Selective Catalytic Reduction with Ammonia on Cu-SSZ-13, J. Catal., 312 (2014) 87 – 97) Copyright (2014) Elsevier Inc.

Chapter 3 & Appendix B has been reprinted with permission from (A.A. Verma, S.A. Bates, T. Angarra, C. Paolucci, A.A. Parekh, K. Kamasamudram, A. Yezerets, J.T. Miller, W.N. Delgass, W.F. Schneider, and F.H. Ribeiro, NO Oxidation : A Probe Reaction on Cu-SSZ-13, J. Catal., 312 (2014) 179 – 190). Copyright (2014) Elsevier Inc.

Chapter 4 and Appendix C has been reprinted with permission from C. Paolucci, A.A. Verma, S.A.Bates, V.F.Kispersky, J.T.Miller, R. Gounder, W. Nicholas Delgass, F.H. Ribeiro, and W.F. Schneider, Isolation of the Copper Redox Steps in the Selective Catalytic Reduction on Cu-SSZ-13, Angew. Chem.. doi 10.1002/ange.201407030

Chapter 5 is currently under preparation to be submitted as a research note in ACS catalysis.

Reprint permission for Chapter 2

This is a License Agreement between Anuj A Verma ("You") and Elsevier ("Elsevier") provided by Copyright Clearance Center ("CCC"). The license consists of your order details, the terms and conditions provided by Elsevier, and the payment terms and conditions.

All payments must be made in full to CCC. For payment instructions, please see information listed at the bottom of this form.

Supplier	Elsevier Limited The Boulevard,Langford Lane Kidlington,Oxford,OX5 1GB,UK
Registered Company Number	1982084
Customer name	Anuj A Verma
Customer address	Office 2166 WEST LAFAYETTE, IN 47906
License number	3439411318284
License date	Jul 31, 2014
Licensed content publisher	Elsevier
Licensed content publication	Journal of Catalysis
Licensed content title	Identification of the active Cu site in standard selective catalytic reduction with ammonia on Cu-SSZ-13
Licensed content author	Shane A. Bates,Anuj A. Verma,Christopher Paolucci,Atish A. Parekh,Trunojoyo Anggara,Aleksey Yezerets,William F. Schneider,Jeffrey T. Miller,W. Nicholas Delgass,Fabio H. Ribeiro
Licensed content date	April 2014
Licensed content volume number	312
Licensed content issue number	n/a
Number of pages	11
Start Page	87
End Page	97
Type of Use	reuse in a thesis/dissertation
Intended publisher of new work	other
Portion	full article
Format	both print and electronic
Are you the author of this Elsevier article?	Yes
Will you be translating?	No
Title of your thesis/dissertation	Fundamental Studies on Copper Zeolites for Catalytic NOx Abatement

Reprint permission for Chapter 3

This is a License Agreement between Anuj A Verma ("You") and Elsevier ("Elsevier") provided by Copyright Clearance Center ("CCC"). The license consists of your order details, the terms and conditions provided by Elsevier, and the payment terms and conditions.

All payments must be made in full to CCC. For payment instructions, please see information listed at the bottom of this form.

Supplier	Elsevier Limited The Boulevard,Langford Lane Kidlington,Oxford,OX5 1GB,UK
Registered Company Number	1982084
Customer name	Anuj A Verma
Customer address	Office 2166 WEST LAFAYETTE, IN 47906
License number	3439411195772
License date	Jul 31, 2014
Licensed content publisher	Elsevier
Licensed content publication	Journal of Catalysis
Licensed content title	NO oxidation: A probe reaction on Cu-SSZ-13
Licensed content author	Anuj A. Verma,Shane A. Bates,Trunojoyo Anggara,Christopher Paolucci,Atish A. Parekh,Krishna Kamasamudram,Aleksey Yezerets,Jeffrey T. Miller,W. Nicholas Delgass,William F. Schneider,Fabio H. Ribeiro
Licensed content date	April 2014
Licensed content volume number	312
Licensed content issue number	n/a
Number of pages	12
Start Page	179
End Page	190
Type of Use	reuse in a thesis/dissertation
Portion	full article
Format	both print and electronic
Are you the author of this Elsevier article?	Yes
Will you be translating?	No
Title of your thesis/dissertation	Fundamental Studies on Copper Zeolites for Catalytic NOx Abatement
Expected completion date	Dec 2014
Estimated size (number	200

Reprint permission for Chapter 4

This is a License Agreement between Anuj A Verma ("You") and John Wiley and Sons ("John Wiley and Sons") provided by Copyright Clearance Center ("CCC"). The license consists of your order details, the terms and conditions provided by John Wiley and Sons, and the payment terms and conditions.

All payments must be made in full to CCC. For payment instructions, please see information listed at the bottom of this form.

License Number	3471711284594
License date	Sep 18, 2014
Licensed content publisher	John Wiley and Sons
Licensed content publication	Angewandte Chemie
Licensed content title	Isolation of the Copper Redox Steps in the Standard Selective Catalytic Reduction on Cu-SSZ-13
Licensed copyright line	© 2014 WILEY-VCH Verlag GmbH & Co. KGaA, Weinheim
Licensed content author	Christopher Paolucci,Anuj A. Verma,Shane A. Bates,Vincent F. Kispersky,Jeffrey T. Miller,Rajamani Gounder,W. Nicholas Delgass,Fabio H. Ribeiro,William F. Schneider
Licensed content date	Sep 12, 2014
Start page	n/a
End page	n/a
Type of use	Dissertation/Thesis
Requestor type	Author of this Wiley article
Format	Print and electronic
Portion	Full article
Will you be translating?	No
Title of your thesis / dissertation	Fundamental Studies on Copper Zeolites for Catalytic NOx Abatement
Expected completion date	Dec 2014
Expected size (number of pages)	200
Total	0.00 USD
Terms and Conditions	

VITA

VITA

Anuj A. Verma
Graduate School, Purdue University

Education
B.S., Chemical Engineering, 2010, Institute of Chemical Technology (formerly known as UDCT or UICT), Mumbai, Maharashtra, India
M.S., Technology, 2013, Purdue University, West Lafayette, Indiana
Ph.D., Engineering, 2014, Purdue University, West Lafayette, Indiana

Anuj Verma was born on 11 December 1988 to Asha Verma and Arun Verma. He was born in Mumbai, India and did his schooling in Maneckji Cooper Education Trust school (MCET). His interest in chemistry enabled him to join UDCT in 2006 where he read chemical engineering for four years. While at UDCT, Anuj was ranked 1 in the university and received the prize for the best chemical design project among undergraduates by the Indian Institute of Chemical Engineers (IIChE), 2010. After finishing the undergraduate program, Anuj chose to pursue a PhD in Chemical Engineering under the guidance of Fabio H. Ribeiro and W. Nicholas Delgass. He investigated the kinetics of $NO/NH_3/O_2$ reactions on copper exchanged zeolites from 2011 till 2014 and published his work in the Journal of Catalysis and Angewandte Chemie Int. Ed. He also presented his work in leading conferences like the AIChE annual meeting in 2012 (on an Eastman Travel grant), 23rd North American Meeting of NACS, and the spring symposium of the Michigan Catalysis Society (2013). He was awarded an outstanding poster presentation at

the Spring symposium of the Chicago Catalysis Club at the B.P. research center at Naperville (2012). He also received the best presentation award at the GSO Symposium, 2013, Purdue University. Anuj graduated with a PhD in Chemical Engineering in September 2014 and will join Abbvie Inc., North Chicago, as a Senior Engineer in the Global Process R&D division.